



**HAL**  
open science

# Multi-scale modeling of fiber orientation in coupled fiber-reinforced viscous polymer systems

Nazih Assaad Al Ayoubi

► **To cite this version:**

Nazih Assaad Al Ayoubi. Multi-scale modeling of fiber orientation in coupled fiber-reinforced viscous polymer systems. Mechanics of materials [physics.class-ph]. École centrale de Nantes, 2024. English. NNT : 2024ECDN0008 . tel-04673561

**HAL Id: tel-04673561**

**<https://theses.hal.science/tel-04673561v1>**

Submitted on 20 Aug 2024

**HAL** is a multi-disciplinary open access archive for the deposit and dissemination of scientific research documents, whether they are published or not. The documents may come from teaching and research institutions in France or abroad, or from public or private research centers.

L'archive ouverte pluridisciplinaire **HAL**, est destinée au dépôt et à la diffusion de documents scientifiques de niveau recherche, publiés ou non, émanant des établissements d'enseignement et de recherche français ou étrangers, des laboratoires publics ou privés.

# MEMOIRE DE DOCTORAT DE

## L'ECOLE CENTRALE DE NANTES

ECOLE DOCTORALE N° 602

*Sciences de l'Ingénierie et des Systèmes*

Spécialité : *Mécanique des Solides, des Matériaux, des structures et des surfaces*

Par

**Nazih ASSAAD AL AYOUBI**

## **Multi-scale modeling of fiber orientation in coupled fiber-reinforced viscous polymer systems**

Projet de recherche doctoral présenté et soutenu à Ecole Centrale de Nantes le 26 Mars 2024

Unité de recherche : UMR 6183, Institut de Recherche en Génie Civil et Mécanique (GeM)

### **Rapporteurs avant soutenance :**

Julien BRUCHON  
Emmanuelle ABISSET-CHAVANNE

Professeur de l'École des Mines - IMT, HDR, Mines Saint-Étienne  
Professeure des universités ENSAM Bordeaux

### **Composition du Jury :**

Président :  
Julien FÉREC

Professeur des universités, Université Bretagne-Sud

Examineurs :  
Julien BRUCHON  
Emmanuelle ABISSET-CHAVANNE

Professeur de l'École des Mines - IMT, HDR, Mines Saint-Étienne  
Professeure des universités ENSAM Bordeaux

Directeur de recherches doctorales:  
Sébastien COMAS-CARDONA

Professeur des universités, Ecole Centrale de Nantes

Co-dir. de recherches doctorales :  
Christophe BINETRUY

Professeur des universités, Ecole Centrale de Nantes

Co-enc.de recherches doctorales :  
Hugues DIGONNET

Maître de conférences, Ecole Centrale de Nantes



---

وَقُلْ رَبِّ زِدْنِي عِلْمًا

and say, “My Lord, increase me in knowledge.”

Taha, verse 144

سورة طه، الآية 114

---



## Acknowledgments

I would like to express my sincere gratitude to all the people who have supported me throughout my doctoral journey. This thesis would not have been possible without their guidance, encouragement, and friendship.

My sincere thanks go to my thesis reviewers, Julien Bruchon, Emmanuelle Abisset-Chavanne, and Julien Férec, for their meticulous review and insightful feedback. I am particularly indebted to my thesis supervisor, Sébastien Comas-Cardona. His unwavering support, invaluable advice, and exceptional teaching have been instrumental in bringing this thesis to fruition. I am equally grateful to Luisa Rocha Da Silva for her unwavering belief in me, both personally and professionally. Her guidance has been a constant source of inspiration. I am also grateful to Christophe Binetruy for his mentorship. His ability to simplify complex concepts and his knack for effective communication have been truly enriching. I am particularly grateful for his willingness to accommodate my schedule despite his demanding role as Vice President of Nantes Université. My sincere thanks to Hugues Digonnet for his dedicated support and his willingness to make time for me despite his busy schedule. His ingenious ideas have greatly enhanced the originality of this work, and his insightful suggestions have enriched my thought process. I am also grateful to Françoise Foucher for entrusting me with teaching responsibilities, an experience I thoroughly enjoyed. I extend my gratitude to FORVIA, represented by Benedikt Eck and Thierry Renault, for their trust and financial support.

I am immensely grateful to the wonderful team at the lab, especially Pierre-Emmanuel Guerin and Pablo Bondia-Luttiau, for their unwavering involvement in my work, particularly during the challenges faced with launching simulations on Nautilus. My thanks to my colleagues Onkar, Lorys, Manisha, Lucas, Gianni, Yassine, John, Kiran, and Yohann for the camaraderie, laughter, and meaningful conversations we shared. I also extend my gratitude to my colleagues from other teams, too numerous to mention individually, for making my lab experience truly enjoyable.

I am so grateful to my "Nantes family," both those who remain and those who have moved on: Simo, Anas, Ilhame, Bader, Ahmad, Joud, Kareem, Abdelrahman, Abdelhamid, Soukaina & Abdelhay, Nabila & Maarouf, Batul & Hussein. With them, I shared countless moments of joy, from playing games to enjoying meals and celebrating birthdays.

I extend my deepest gratitude to my beloved in-laws for their unwavering love and support, especially during the challenging times of writing my thesis. Their unwavering encouragement has been a source of strength and solace.

My heartfelt gratitude goes to my dear parents, Salam and Mohamad, for their unwavering dedication to my upbringing and their immense love and affection. I hope they find in the completion of this work the culmination of their efforts and my deepest appreciation. Thank you for always being so proud of me.

Finally, I extend my deepest love and gratitude to my wife, Imane, who has supported me throughout this journey. Her unwavering love, both personal and professional, has been my guiding light. Thanks to her, I have been able to overcome the challenges of these past four years and continue to push myself to achieve my goals. Her patience, positivity, and strength have inspired me beyond measure.

# Contents

<b>List of Acronyms</b>	<b>v</b>
<b>I State of art</b>	<b>1</b>
I.1 Industrial motivation . . . . .	2
I.2 Composite materials . . . . .	2
I.2.1 The reinforcement . . . . .	4
I.2.2 The matrix . . . . .	5
I.2.3 Fiber-matrix interface . . . . .	5
I.2.4 Short summary . . . . .	6
I.3 Injection molding process . . . . .	6
I.3.1 Two-shot molding . . . . .	7
I.3.2 Insert molding . . . . .	7
I.3.3 Overmolding . . . . .	8
I.3.4 Short summary . . . . .	10
I.4 Fiber orientation mechanism in suspension media . . . . .	11
I.4.1 Analysis of flow-induced fiber orientation . . . . .	11
I.4.2 Analysis of parameters influencing fiber orientation . . . . .	13
I.4.3 Fiber orientation modeling . . . . .	15
I.4.4 Short summary . . . . .	26
I.5 Conclusion and research plan . . . . .	26
I.5.1 A synopsis . . . . .	26
I.5.2 Industrial context . . . . .	27
I.5.3 Study objectives and approach . . . . .	27
I.5.4 Thesis structure . . . . .	28
<b>II Solving Fokker-Planck equation</b>	<b>29</b>
II.1 Introduction . . . . .	30
II.2 Mathematical modeling . . . . .	32
II.2.1 Fokker-Planck equation . . . . .	32
II.2.2 Reformulation of Fokker-Planck Equation . . . . .	33
II.2.3 Discretization of Fokker-Planck equation . . . . .	37
II.2.4 Short summary . . . . .	41
II.3 Numerical results . . . . .	41
II.3.1 Validation tests . . . . .	41
II.3.2 Numerical convergence analysis and computational efficiency . . . . .	47
II.3.3 Fiber orientation-flow . . . . .	51
II.3.4 Short summary . . . . .	53
II.4 Discussion . . . . .	53
II.5 Conclusion . . . . .	55

<b>III Fiber-Flow coupling</b>	<b>57</b>
III.1 Introduction . . . . .	58
III.2 Rheological models of fiber suspensions . . . . .	60
III.2.1 Newtonian matrix suspensions . . . . .	60
III.2.2 Non-Newtonian matrix suspensions . . . . .	65
III.2.3 Short summary . . . . .	67
III.3 Multiscale modeling for injection molding process . . . . .	67
III.3.1 Generalities on the resolution of the flow-fiber coupling problem	67
III.3.2 Construction of the physical model . . . . .	68
III.3.3 Finite element approach to resolving a flow-fiber coupling model	70
III.3.4 Solution algorithm . . . . .	74
III.3.5 Short summary . . . . .	76
III.4 Numerical results . . . . .	76
III.4.1 Parallel computing . . . . .	76
III.4.2 Effect of rheological coupling coefficient $N_p$ on flow and fiber orientation . . . . .	79
III.4.3 Effect of interaction coefficient $C_I$ on fiber orientation . . . . .	87
III.4.4 Short summary . . . . .	89
III.5 Conclusion . . . . .	90
<b>IV Application: complex geometries</b>	<b>91</b>
IV.1 Introduction . . . . .	91
IV.2 Configurations of fluid-fiber coupling in diverse geometries . . . . .	93
IV.2.1 Complex shape models . . . . .	93
IV.2.2 Numerical results . . . . .	95
IV.2.3 Short summary . . . . .	114
IV.3 Problem setup for a real-case injection molding scenario . . . . .	114
IV.3.1 Two-phase flow model . . . . .	114
IV.3.2 Numerical results . . . . .	117
IV.3.3 Short summary . . . . .	124
IV.4 Conclusion . . . . .	124
<b>V Conclusion and perspectives</b>	<b>127</b>
V.1 Synthesis and conclusion . . . . .	127
V.2 Perspectives and improvements . . . . .	130
<b>Bibliography</b>	<b>133</b>

# List of Acronyms

<b>CNC</b>	computer numerical control . . . . .	7
<b>MFD</b>	mold flow direction . . . . .	12
<b>FEM</b>	finite element method . . . . .	28
<b>DNS</b>	direct numerical simulation . . . . .	29
<b>PDF</b>	probability distribution function . . . . .	33
<b>FPE</b>	Fokker-Planck equation . . . . .	28
<b>PETSc</b>	Portable, Extensible Toolkit for Scientific computation . . . . .	41
<b>SUPG</b>	streamline upwind Petrov–Galerkin . . . . .	39
<b>RSC</b>	reduced strain closure . . . . .	22
<b>ARD</b>	anisotropic rotary diffusion . . . . .	23
<b>DNS</b>	direct numerical simulation . . . . .	29
<b>CFL</b>	Courant-Friedrichs-Lewy . . . . .	39
<b>MPI</b>	message passing interface . . . . .	31
<b>CAD</b>	computer-aided design . . . . .	131



---

## Multi-scale modeling of fiber orientation in coupled fiber-reinforced viscous polymer systems

**Abstract:** Overmolding, a technique involving the injection of short fiber thermoplastics (SFT) over a continuous fiber reinforced thermoplastic composite insert, is gaining traction across various industries, including automotive, aeronautics, and electronics. However, the precise prediction of insert displacement and fiber orientation during overmolding requires robust numerical simulation tools. This study proposes a multi-scale fiber-flow model that incorporates mesoscopic fiber orientation dynamics into macroscopic flow equations.

To address the challenges of fiber orientation modeling, the direct solver technique is introduced, employing the Fokker–Planck equation to describe the evolution of fiber orientation probability density. This approach captures the intricate relationship between fiber orientation and flow kinematics. The proposed technique involves two types of discretization: angular discretization over an unit circle (2D) and spatial discretization. The computed orientation tensor is integrated into the Stokes equations to form a coupled multi-scale fiber-flow model. Additionally, a spatial advection equation is solved to track the dynamic motion of fibers within the domain, providing insights into fiber-flow interactions. The research extends to developing a two-phase flow model, accurately simulating real-world overmolding scenarios. This multi-scale model aims to enhance the accuracy of industrial simulations, enabling process optimization and design optimization.

**Keywords:** Overmolding process, numerical simulation, multiphase flow, fiber suspension, fiber orientation, multiscale modeling, finite element method

---

---

## Modélisation multi-échelle de l'orientation des fibres dans des systèmes polymères visqueux

**Résumé:** L'injection de plastiques thermoplastiques à fibres courtes (SFT) sur un insert composite thermoplastique renforcé par des fibres continues, communément appelée surmoulage, est une technique en plein essor dans divers secteurs industriels, notamment l'automobile, l'aéronautique et l'électronique. Cependant, la prédiction précise du déplacement de l'insert et de l'orientation des fibres pendant le procédé de surmoulage nécessite des outils de simulation numérique robustes. Cette étude propose un modèle multi-échelle de fibre-écoulement qui intègre la dynamique de l'orientation des fibres à l'échelle mésoscopique dans les équations de l'écoulement à l'échelle macroscopique.

Pour relever les défis de la modélisation de l'orientation des fibres, la technique de résolution directe est introduite, en utilisant l'équation de Fokker-Planck pour décrire l'évolution de la densité de probabilité d'orientation des fibres. Cette approche capture la relation complexe entre l'orientation des fibres et la cinématique de l'écoulement. La technique proposée implique deux types de discrétisation : la discrétisation angulaire sur un cercle unité (2D) et la discrétisation spatiale. Le tenseur d'orientation calculé est intégré aux équations de Stokes pour former un modèle multi-échelle de fibre-écoulement couplé. De plus, une équation d'advection spatiale est résolue pour suivre le mouvement dynamique des fibres dans le domaine, fournissant des informations sur les interactions fibre-écoulement. La recherche s'étend au développement d'un modèle d'écoulement biphasique, capable de simuler avec précision des scénarios de surmoulage réels. Ce modèle multi-échelle vise à améliorer la précision des simulations industrielles, permettant l'optimisation des processus et la conception des produits.

**Mots clés:** Procédé de surmoulage, simulation numérique, écoulement multiphasique, suspension de fibres, orientation des fibres, modélisation multiéchelle, méthode des éléments finis

---

# State of art

---

## Contents

<b>I.1</b>	<b>Industrial motivation</b>	<b>2</b>
<b>I.2</b>	<b>Composite materials</b>	<b>2</b>
I.2.1	The reinforcement	4
I.2.2	The matrix	5
I.2.3	Fiber-matrix interface	5
I.2.4	Short summary	6
<b>I.3</b>	<b>Injection molding process</b>	<b>6</b>
I.3.1	Two-shot molding	7
I.3.2	Insert molding	7
I.3.3	Overmolding	8
I.3.4	Short summary	10
<b>I.4</b>	<b>Fiber orientation mechanism in suspension media</b>	<b>11</b>
I.4.1	Analysis of flow-induced fiber orientation	11
I.4.2	Analysis of parameters influencing fiber orientation	13
I.4.3	Fiber orientation modeling	15
I.4.4	Short summary	26
<b>I.5</b>	<b>Conclusion and research plan</b>	<b>26</b>
I.5.1	A synopsis	26
I.5.2	Industrial context	27
I.5.3	Study objectives and approach	27
I.5.4	Thesis structure	28

---

The plastics processing industry is in constant progress despite the effects of the cycle due to the lack of stability of raw materials and the very strong pressure exerted downstream by the customer markets, which are the major contractors. This relatively young industry is developed mainly after the Second World War. However, according to the different professional branches, there are some differences of evolution. In 2000, plastic packaging, elements for the building industry and even technical parts such as reinforced materials have might experienced sustained growth despite the increase in raw materials. Only a few miscellaneous consumer products have suffered competition from countries with low labor costs for several years. For composite materials (reinforced materials), the positioning of the market in France is rather on the high end due to the significant weight of aeronautics (22% in value) just behind the automotive industry (31%) but ahead of building

and construction (14%) and electricity (10%). These four markets represent around 75% of the use of composites in France. Chapter I is devoted to the presentation of the essential bibliographic concepts necessary for the study of fiber suspensions. The injection process and its impact on the induced microstructure are described. Special attention is also paid to orientation descriptors, the main models used for its prediction, and a selection of mesoscopic simulation approach.

## I.1 Industrial motivation

The thesis work is a part of an industrial chair collaboration between Centrale Nantes and Faurecia (Forvia Group). Faurecia is a french global automotive supplier and automotive parts manufacturer for vehicle interiors and emission control technology. Overmolding process is used at Faurecia, in order to not be limited with thermo-stamping where a trimming part edge for the latter can be needed which causes a loss of materials to produce vehicle components with complex shapes made by composites. The premier process is preferable to the company as it eliminates costly assemblies, captures one composite part inside another without fasteners and adds flexibility to rigid parts areas. Overmolding is done by injecting molten thermoplastics with short/long fibers over a continuous fiber reinforced composite insert. A Moldflow numerical software is used by Faurecia as simulation tool to track the injection's flow in the mold and to analysis the residual stresses and the deformation at the interface to the thermo-stamped continuous fiber reinforcement sheet due the fibers orientation. A numerical model is developed at Ecole Centrale de Nantes using Stokes equation, assuming a type of fluid flow where advective inertial forces are small compared with viscous forces, coupled with Fokker-Planck equation, as the latter describes the dynamic motion of fibers during the injection phase. The solver is implemented using ICI-Tech library that is built inside the lab. A study is done on numerical and theoretical sides to understand the physical behaviour of fluid injected represented by the molten thermoplastics at macro and microscales in order to tackle the problem caused by the defects such as deformation, displacement and penetration that come out at the interface between the molded composite materials affecting the mechanical properties of the final product.

## I.2 Composite materials

The modern use of composites began in the mid-1960s and mainly in the aeronautical industry, its aim of which is to lighten structures and reduce costs. Over the decades and until today, these new composites have revolutionized the field and are starting gradually to replace the metallic materials. A remarkable rise in power of composites in the aeronautical field is also observed in the automotive industry. Thus, composite materials have gained popularity and their shares increased in the market especially in the aeronautical fields where major companies such Airbus and Boeing nowadays launch scientific programs in order to study and improve these materials where they seek for high-performance products that need to be lightweight, yet strong enough to take harsh loading conditions. Also, the automotive industries

have witnessed the revolution in the use of composite materials over the last few years to create components that have unique characteristics, such as being strong and light as the trend in using composites is accelerating to meet light-weighting requirements to meet the next generation of fuel economy standards. So, composite materials have invested heavily in the automotive field for parts that do not undergo significant mechanical loads (bodywork, interior trim, tailgate, front end). For example, carbon fiber composites are now used widely in many of the Formula

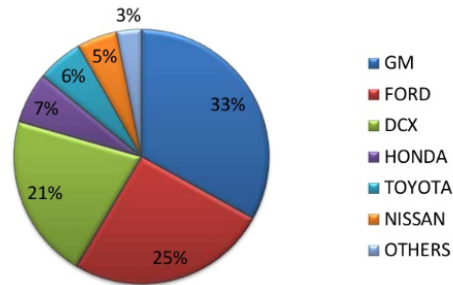


Figure I.1: The use of composites in automotive companies [1]

F1 components as almost 85 percent of the volume of a typical F1 race car is made up of them where technological advancements in materials have enabled the racing cars to become lighter, safer and faster. As well, Boeing has expanded the use of composites, particularly in the highly tension-loaded environment of the airplane's fuselage, which greatly reduces the maintenance due to fatigue when compared with an aluminum structure. Also Airbus, with introducing the composites into its manufacturing process, expresses that an aircraft's airframe can be both sturdier and lighter. Meanwhile, like how Boeing points out, less maintenance is also required for the frame when in service due to reduced wear down. For instance, the A350 requires 50% fewer structure maintenance tasks. Classically, composite materials are

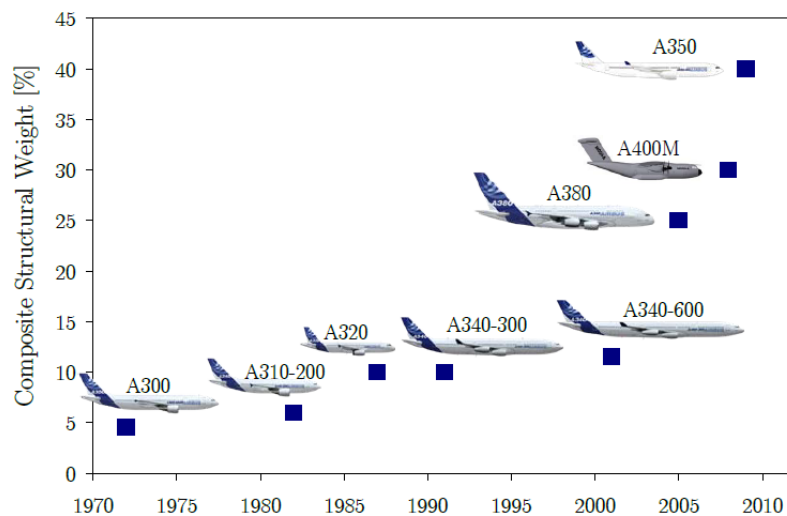


Figure I.2: The use evolution of composites in commercial aircrafts Airbus [2]

defined as the constitution of the assembly of two or more materials of different nature, complementing each other and making it possible to achieve a material whose overall performance is superior to that of the components taken separately. In general, it also consists of one or more discontinuous phases distributed in a continuous phase. The continuous phase is called the matrix. The discontinuous phase called the reinforcement or reinforcing material which is mainly in fibrous or filamentary form, has usually mechanical properties (rigidities and resistances) superior to those of the matrix. The properties of composite materials result from the properties of the constituent materials, the geometric distribution of the reinforcements, the volume ratio of reinforcement, the nature of the reinforcement/matrix interfaces, and the manufacturing process. The matrix acts as a binder in order to protect the

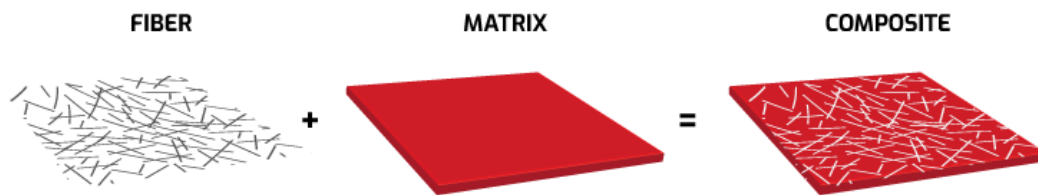


Figure I.3: A Fiber-Reinforced Polymer composite[3]

reinforcement from the environment, to maintain it in its initial position and to ensure the transmission of forces. Composite materials can be classified according to the nature of their matrix: composite material with organic matrix, composite material with ceramic matrix or composite material with metal matrix. Between the reinforcement and the matrix, there is a connection zone called the interface. A composite material is mostly heterogeneous and anisotropic.

### I.2.1 The reinforcement

In general, the reinforcements are fibers such as fiberglass (which is the most common), carbon fiber, aramid fiber or even vegetable fiber (which is renewable). The reinforcement can also take the form of particles. Reinforcements make the material even more efficient. Glass fibers are the most commonly used reinforcements for composite materials [4]. It is an inexpensive reinforcement assembled in the form of a wick containing about 200 fibers having a diameter of  $15 \mu\text{m}$  and a length of 25 mm on average. Due to their quick processing times and simplicity of production in complex geometries, short fibers are more frequently employed as reinforcement. Short fibers help to resist impact loads [7, 8], however because of their structural imperfections, it can be difficult to achieve other mechanical qualities, such as tensile and bending capabilities. Tensile and bending strength are closely related to continuous fiber reinforcement [9]. The reinforcement can be alone within a matrix (homogeneous composite) or combined with a reinforcement of a different nature (hybrid composite).

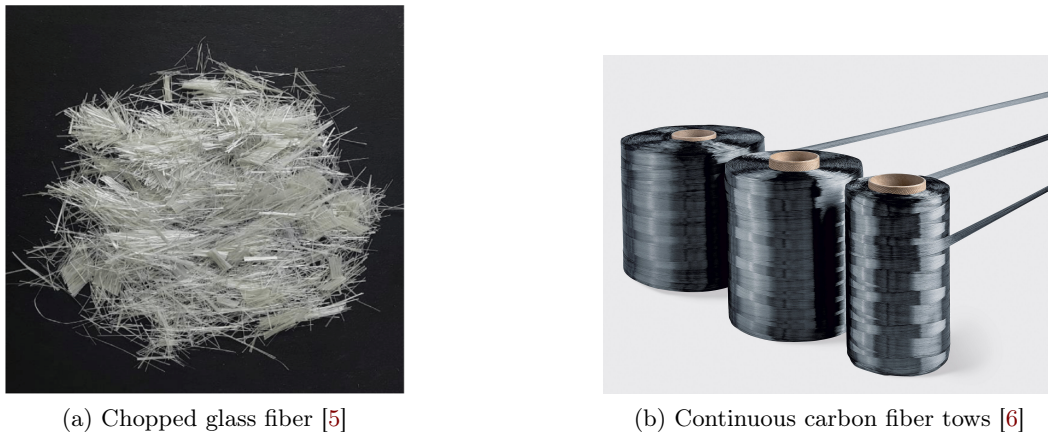


Figure I.4: Different types of reinforcement

### I.2.2 The matrix

Another very important component of a composite material is the matrix which is a light and deformable organic material. The main roles of a matrix are the protection of the loads, the distribution of the mechanical load on the reinforcements and the cohesion of the loads which has a very important role for the homogenization of the composite [10, 11, 12], as it also determines the shape and surface finish of the composite component. In general, organic matrices are classified into two groups which are thermosetting and thermoplastic matrices. Most matrices are made of polymers (mainly utilized for fiber reinforced plastics):

- **Thermoset polymers** [13, 14] are cured polymers that take on a solid form and can never revert to their uncured state. Thermoset matrices are used to create robust composites with excellent fatigue resistance. They have low impact-toughness making and are quite fragile. Due to the thermoset matrix's resistance to melting unlike thermoplastics, they are frequently utilized in high-heat applications. Thermoset composites are exceedingly challenging to recycle because they cannot be remolded or reshaped.
- **Thermoplastic polymers** [15, 16] may be shaped, melted, and remolded without losing their physical characteristics. In comparison to thermosets, thermoplastic matrix composites are tougher and less brittle, with excellent impact resistance and damage tolerance. Composite materials can be more easily repaired, remolded, and recycled since the matrix can be melted. Because they are less dense than thermosets, thermoplastic composites are a good choice in applications where weight is an important factor.

### I.2.3 Fiber-matrix interface

The importance of the bond between fiber and matrix is so crucial for the properties of the composite material and its lifetime [18, 19] to the point that it is considered as a third constituent of a composite material although its volume fraction is theoretically zero or practically low. Indeed, it allows the transfer of stresses while

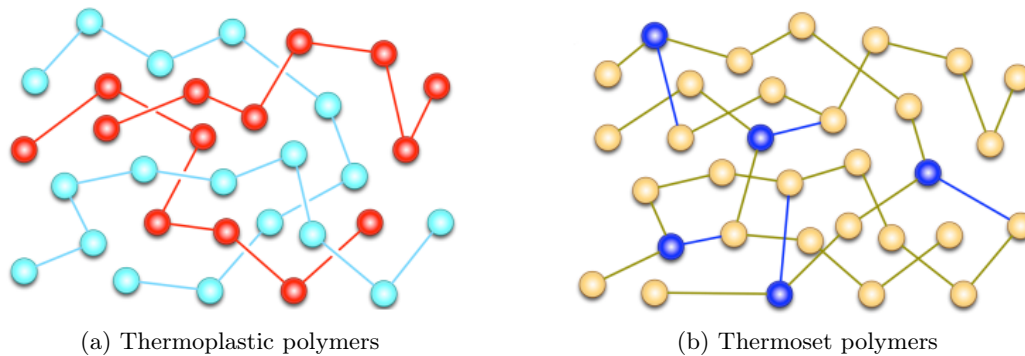


Figure I.5: Polymer intermolecular structures [17]

avoiding the relative displacement of one in relation to the other, as the interfacial bond strength must be strong enough. Therefore, the Young's modulus, interlaminar shear strength, bending stiffness, compressive strength, and many features of composite behavior can all be influenced by the interfacial bond [20].

#### I.2.4 Short summary

- ✓ Composite materials stand out for their lightness and ease of use. Their mechanical strength, physics and chemistry offers a wide range of possibilities in terms of use, design, geometry and integration functions.
- ✓ From a mechanical point of view, they offer excellent tensile, bending, compression, plane shear and excellent shock absorption. Their mechanical strength combined with their low density make it an essential element of current designs, whether structural or not.
- ✓ The automotive industry, alongside aerospace, remains a major field of investigation for composite materials. To date, more than 30000 tons plastics and composites are used for the manufacture of body parts, in particular in bumpers, wings, side doors, rear doors, parts under hood and seats.

### I.3 Injection molding process

In the development of making parts from composites, different process have been applied in order to get well finished complex shapes. One of the most significant procedures in the manufacturing sector is known by the general name "injection molding" [21, 22]. This procedure calls for a mold, which is commonly made of metal and has a cavity formed to the shape of the desired object. The mold is filled with molten plastic, which is then ejected [23, 24]. To create thousands of identical pieces, the process is repeated. Given the various advantages of adopting injection molding for production, it is safe to assume that every large-volume plastic compo-

ment on the market was produced using an injection molding machine. Therefore, the vast majority of consumer products use it, a flexible and affordable manufacturing production technique that also includes the sub-processes of two-shot molding, insert molding and overmolding. Comparing injection molding to other production processes like computer numerical control (CNC) machining and even 3D printing, it frequently delivers the lowest cost per part [25].

### I.3.1 Two-shot molding

Double shot molding, also known as two-shot molding, is a manufacturing technique that involves molding plastic around a prefabricated metal or plastic insert to create complex molded parts from two different materials. The procedure is rather

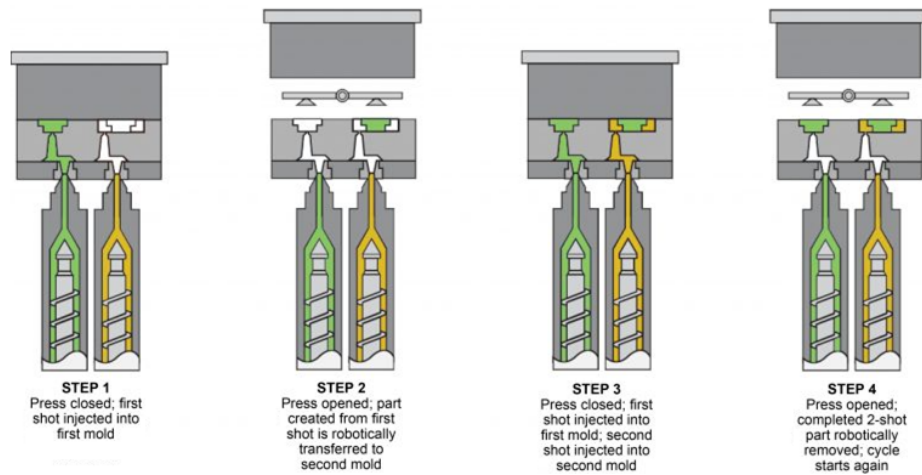


Figure I.6: Two-Shot molding process [26]

straightforward: once one material is injected into a mold to create the product's initial component, another substance that is compatible with the original material is injected into the mold once more. Then, the multi-resin molded part is cooled and ejected, following the formation of a molecular link between the two plastic resins. Particularly in a scenario of a high-volume manufacturing, double shot molding is an exemplary technique for complicated, multi-material, and multi-colored plastic products.

### I.3.2 Insert molding

The technique of forming or molding plastic pieces around non-plastic parts, or inserts, is known as insert injection molding. It is mainly considered as a subset of injection molding processes, in which metal components are inserted into a mold cavity prior to the injection of plastic. Either manually or with the help of a robotic arm, the insert is carefully placed into the mold. A single part is then produced once the mold closes and plastic is formed over the insert. There are several advantages to using insert molding, like improving component reliability and its strength and structure. It renders the final part combine the features of both plastic and metal

materials as for example metal inserts can be utilized when stiffness and strength are needed, while to reduce the weight, the rest of the part can be made of plastic.

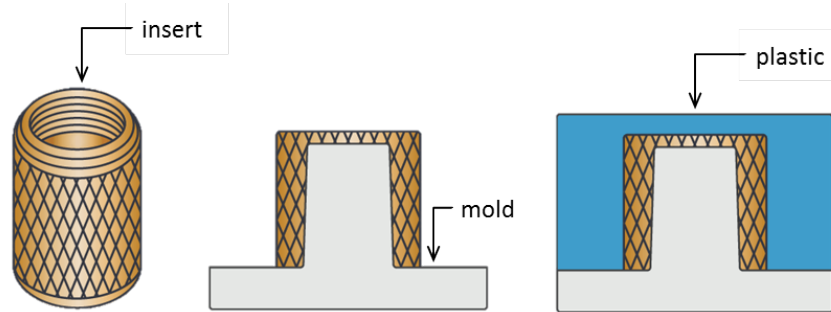


Figure I.7: Insert Molding Process [27]

### I.3.3 Overmolding

In essence, overmolding is a form of insert molding. Overmolding, as opposed to

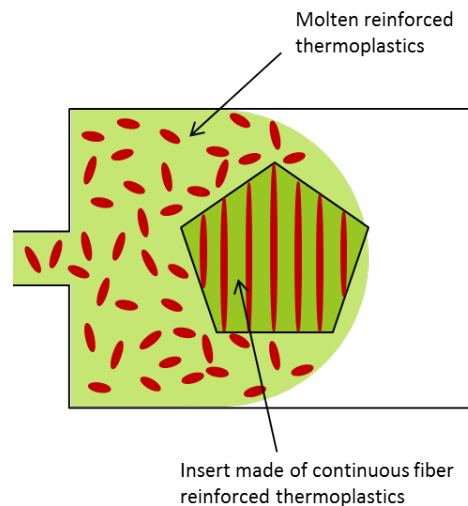


Figure I.8: Overmolding process

insert molding, involves molding plastic over another molded part. So as part of the first step, a plastic substrate is either molded or thermoformed, then a second step involves the injection of another layer of plastic on top and around of the first layer in order to create one product. Using this technique, multiple plastics are combined for either practical or aesthetic reasons. As figure I.8 depicted, the case that will be mainly studied is the overmolding phase where molten short fiber-reinforced thermoplastics are injected onto a pre-molded insert made of continuous fiber-reinforced thermoplastics in order to investigate on the defects of this process occurred at this point. So consequently, as it is mentioned, the bases of overmolding are close to those of conventional molding, but with constraints due to the nature of the insert and the need to use suitable molds and / or presses. We may thus encounter

problems such as: displacement of insert, deformation of insert and penetration of polymer.

- The displacement of the insert can be caused by unequal force transmission and the pressure gradient applied on the insert surface of the flowing molten thermoplastics injected into the mold's cavity. Therefore it is due to injection

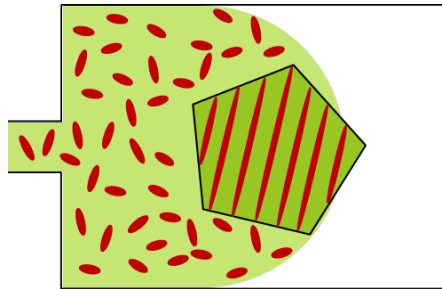


Figure I.9: Displacement of insert

pressure. In other word, core shift can be defined as the spatial deviation of the position of the mold inserts caused by the imbalance of polymer pressure and from asymmetric filling during injection molding.

- Deformation can be caused as stated in the previous paragraph and by variations in shrinkage throughout the insert, while varying pressure and temperature as main parameters coupled with the frozen layer growth to determine it. Knowing that the insert is made of continuous fiber reinforced thermoplastics, it affects significantly its ways of deformation. A continuous fiber reinforced composite insert acts as an insulator and delays the cooling and solidification of the injected polymer in the cavity which affects the temperature and pressure fields, thus affecting the deformation. Therefore, the injected plastic can

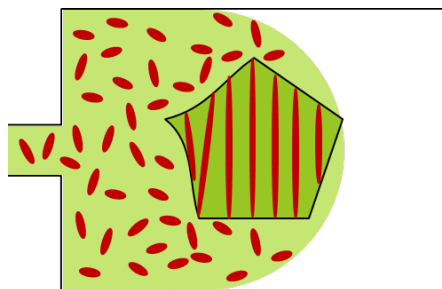


Figure I.10: Deformation of insert

solidify around the insert while still being hotter than the insert. The subsequent differential shrinkage between the injected polymers and anisotropic composite inserts becomes a source of warpage and deformation for injection over-molded parts. And if the insert is thermoformed by the closing action of the mold, residual stresses in the insert itself may influence the final part shape after ejection. The analysis of the deformation in this sequential over-molding probably results from thermal residual stresses. In addition, due to

the molten injected thermoplastics with high temperature, it causes to soften the composite insert that leads to some sort of deformation.

- A penetration into the insert is a typical defect which appears when short fiber reinforced thermoplastic is injected over continuous fiber reinforced thermoplastic part and it is able to pass through the thermoformed plastic insert to reach the aesthetic side of the part. A combination of a minimum injection

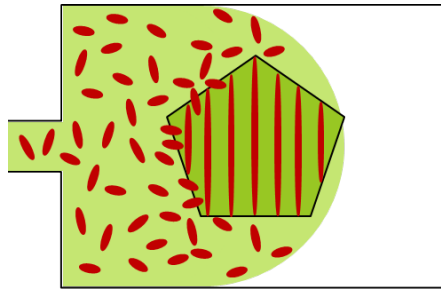


Figure I.11: Penetration of polymer

tion temperature and minimum injection pressure in the exact point in which defect appears, can characterize the penetration.

#### I.3.4 Short summary

- ✓ The injection molding process makes it possible to obtain parts of various geometrical sizes and complexities and remains an economical process, well adapted to large series, giving dimensional tolerances generally sufficient to avoid machining operations.
- ✓ Overmolding is the most common method used to make two-material parts with stiffness and flexibility. In addition, overmolding has many advantages, such as low tooling costs and short cycle times. Some defaults are displacement, deformation or penetration of the insert during overmolding.
- ✓ The anisotropy, induced by the presence of the fibers, is an important property that it must be taken into account when designing the parts and the mold. Indeed, the fiber has a major role in the strength and rigidity of a part. At the same time, the heterogeneity induced by a length distribution of the fibers and non-homogeneous concentration in the flow is often a source of defects which may lead to parts being warped which is difficult to predict or which may induce early fatigue of the composite material.
- ✓ It therefore seems essential to monitor or at least to provide for the orientation of the fibers during the shaping phase. Numerical simulation finds its place in this research, given its ability to predict the flow of matter and therefore the orientation of the fibers in the mold.

## I.4 Fiber orientation mechanism in suspension media

Based on the fiber orientation distribution, the anisotropic mechanical properties of a discontinuous fiber reinforced polymer can be interpreted. This orientation distribution of fiber has in most cases strong impact on the final micro-structure of the manufactured part, which at the same time controls its mechanical performance. A description of the orientation of the particles in a suspension during the shaping process is detailed. More specifically, the mechanisms that govern the orientation of the fibers during the filling phase is described. The first part is devoted to the qualitative analysis of the different orientation mechanisms encountered during the filling phase. Thereafter, an analyze is made to characterize all the parameters likely to influence the orientation of the fibers. Then, mathematical expressions, as well as the main models that describe the evolution of short fiber orientation at different scales, are introduced.

### I.4.1 Analysis of flow-induced fiber orientation

From the aforementioned section, injection is a process that involves different physical phenomena. It is carried out in a non-isothermal manner with a free boundary and generally in tools of complex geometry. During this process, fiber orientation and flow are coupled. In fact, the fluid applies stresses to the fibers and transports them. On the other hand, the presence of the fibers disturbs the flow profile around them. The flow present during injection is a generally mixed flow that combines elongation and shear. Those two latter act as stresses that will preferentially orient the fibers during the filling step. Shear is present mainly in the injection gate, a section of the melt flowing passage from the nozzle of the injection molding machine to the cavity, or in the thin cavities. On the other hand, elongation is locally dominant in certain regions such as the injection gate, at the front of the material during injection or in some 3D regions. Therefore, during the filling process, the fibers will orient in preferred directions as a function of the applied stress. In order to understand the phenomena that govern the orientation of the fibers, illustrations focusing on the description of the movement of a fiber subjected to a shear and elongation flow, respectively, are made.

- Studies made in [28, 29, 30] point out that a single isolated fiber, in shear flow with a Newtonian fluid, has an infinite periodic rotational motion in an extended period of time in the direction of flow. This period  $T$  is inversely proportional to the generalized shear rate and approximately proportional to the aspect ratio  $\beta$  of the fiber, defined as the ratio between the length and the diameter of the fiber:

$$T = \frac{2\pi}{\dot{\gamma}} \beta(1 + \beta) \quad (\text{I.1})$$

The rotational speed of the fiber is not constant, it becomes maximum when the fiber is perpendicular to the direction of flow as shown in figure I.12. With a non-Newtonian fluid, the fiber also undergoes a rotational movement. However, the rotation period increases strongly with the pseudo-plasticity of the fluid [31].

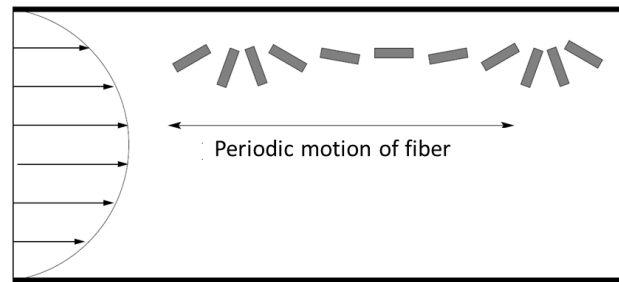


Figure I.12: Motion of a single fiber induced by a Poiseuille flow [30]

- Contrary to the latter finding, in elongational flow, the fiber orientation depends on whether the rate of elongation is negative or positive. So during a

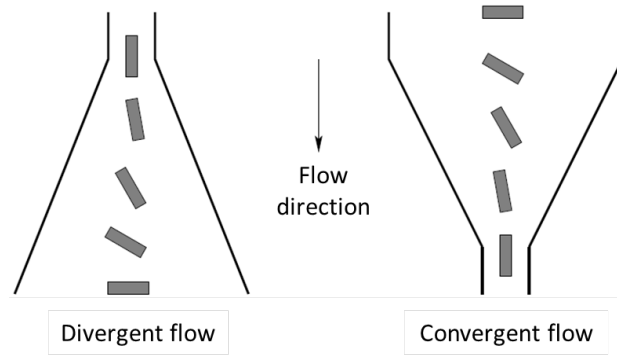


Figure I.13: Motion of a single fiber induced by an elongational flow [30]

pure elongation flow, a fiber tends towards a stable equilibrium position parallel to the flow for a case of a convergent nozzle and perpendicularly for a case of a divergent nozzle, figure I.13.

The flows involved in the injection processes combine and sometimes oppose shear and elongation. The orientation of the fibers, for a thermoplastic filled with short glass fibers, then presents a rather particular structure in the thickness of the part, as the micro-structure of the injected parts is highly heterogeneous as a function of the thickness and shows a characteristic aspect of the injection process known as a skin-shell-core formation. As shown in figure I.14, the micro-structure obtained is arranged in layers in a symmetrical manner:

- A **skin layer**: thin and randomly oriented. During filling, in contact with the cold walls of the mold, a solidified layer develops due to the high temperature gradient. Consequently, the fibers solidify with an isotropic orientation, as the shear effect is neglected due to the restricted time before the solidification. This layer is thin in relation to the others and therefore difficult to observe, its thickness depends on the filling time and on the thermal conductivity of the polymer.
- A **shell layer**: it is relatively thick and contains fibers oriented parallel to mold flow direction (MFD).

- A **core layer**: it is located in the central zone whose fibers are oriented perpendicular to the flow. At core, the generalized shear rate is very low, so the elongational flow diverging around the injection gate is maintained and the fibers align transversely to the flow.
- A **intermediate transition layer**: it is located between the skin and the heart and constitutes the transition between them. For this reason, it is characterized by a random distribution of the orientation of the fibers.

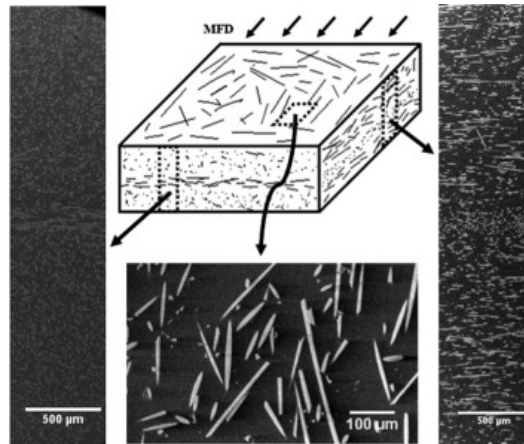


Figure I.14: Skin-shell-core micro-structure formation [32]

## I.4.2 Analysis of parameters influencing fiber orientation

From the previous section, it is deduced that the mold fill parameters control the mechanisms of formation of the micro-structure layers and orientation. These are related to design and injection parameters and the nature of the matrix, some of which are listed below.

### I.4.2.1 Influence of main process parameters of injection molding

To ensure the quality of plastic parts and stable qualification, the influence of temperature, pressure and injection speed play a big role. The orientation of the fibers is governed by the latter variables related to the injection process. Various studies have been conducted in the literature [33, 34, 30] to understand their influence on the final orientation of fibers.

- The **injection speed**: studies [35, 36] have shown that a higher injection rate results in a larger core area and a reduced shell area. On the other hand, the shell layer becomes thinner since the fibers do not have time to orient. In addition, for high injection rates, the area of shell affected by the fountain effect is reduced, thus shifting the region with a high generalized shear rate towards the walls of the mold.
- The **mold temperature**: a reduction in the mold temperature increases the solidified polymer layer, which induces maximum shear values offset towards

the center of the molded part. This reduction in temperature thus leads to an increase in the thickness of the shell layer [37], where the fibers are generally considered to be aligned in the direction of flow. The phenomena observed are mainly related to the fountain effect, which is accentuated by the rate of cooling of the polymer.

- The **packing pressure**: Following a complete cavity filling, pressure distribution affects fiber orientation. At the point of full filling, packing pressure aims to lessen the degree of fiber alignment in the flow direction [38], thus increasing the thickness of the core area [39].

#### I.4.2.2 Influence of reinforcement and matrix

The main focus has been on the three essential parameters that can influence the orientation of the fibers in a molded part by injection: the rheology of the matrix, the fiber concentration and the aspect ratio of the fibers.

- The **matrix rheology**: The nature of the velocity profile in the mold results from the rheothinning nature of the polymers used. The pseudo-plastic nature of the polymers gives rise to a flow characterized by a velocity profile which is much more flattened than in the case of Newtonian fluids. It appears that the thickness of the core zone is an increasing function of the pseudo-plasticity index of the polymer. At the same time, the addition of fibers will contribute to increasing the pseudo-plasticity of the matrix [40]. It should also be noted that, in the vast majority of cases, these studies remain qualitative.
- The **fiber concentration and its aspect ratio**: An in-depth study of glass fiber reinforced polypropylene (short and long) with several reinforcing rates revealed that the width of the core layer increases with fiber concentration and length [41]. In the case of a low fiber percentage (<15% by mass), the core-skin structure can completely disappear and leave its place to an isotropic microstructure over the entire thickness of the part. Another study [42], carried out on a glass fiber reinforced polypropylene with different fiber lengths (fibers initially of 4 and 12 mm), also showed an increase in the width of the core zone with the aspect ratio of the fibers.

#### I.4.2.3 Influence of mold design

The geometry of the flow such as the injection gate and the mold cavity, is an important parameter and has a major role on the orientation of the fibers [43].

- The **injection molding gate**: It appears that the presence of the injection gate governs the initial orientation of the fibers which are transported during the flow in the core layer because the generalized shear rate there is practically zero [44]. The flow around the injection gate governs the initial orientation that will be transported to the core layer. In fact, when a rectangular part is injected into a sheet, a shear flow is established from the start of filling, giving rise to an orientation at the core in the direction of the flow. On the

other hand, in the case of a point injection, a radial elongation flow is initially established, inducing a transverse orientation to the core.

- The **mold cavity**: The geometry of the mold cavity plays an important role in defining the orientation. Qualitative microscopic observations [45, 46] show that the orientation of the fibers in the core zone may be affected by a reduction in the thickness of the cavity. So a reduction in the thickness of the cavity by factor of two results in a direction that is almost in line with the flow. On the other hand, a reduction in the thickness of the cavity also has the effect of reducing the thickness of the core layer. In fact, the flows in thin parts create high generalized shear rates which are the site of a quasi-unidirectional orientation in the direction of flow.

### I.4.3 Fiber orientation modeling

The bibliographic work has highlighted the complexity of the phenomena that govern the orientation of fibers. By definition, a fiber suspension is a complex fluid consisting of a non-miscible mixture of a solid phase (fibers) with a liquid phase (polymer). The study of these suspensions cannot be carried out without introducing certain definitions related to orientation and concentration. In order to understand these mechanisms, this section also covers the mathematical description that stands behind the study of the modeling of the orientation of the fibers.

#### I.4.3.1 Representation of a single fiber orientation

A single fiber is classically modelled as an axisymmetric particle. In a 3D coordinate system  $(x, y, z)$ , its orientation is described by means of a unit vector  $\mathbf{p}$  carried by its main axis, as illustrated in figure I.15. This vector is expressed by equation (I.2) using the angles  $(\theta, \phi)$ . The angle  $\theta$ , called the angle of inclination, is the angle formed from the  $z$ -axis to the fiber direction, while the angle  $\phi$ , called the azimuthal angle, is the angle formed from the  $x$  axis at the projection of the fiber direction in the plane  $(x, y)$ . Knowing that no convention is made on the definition of the ends of

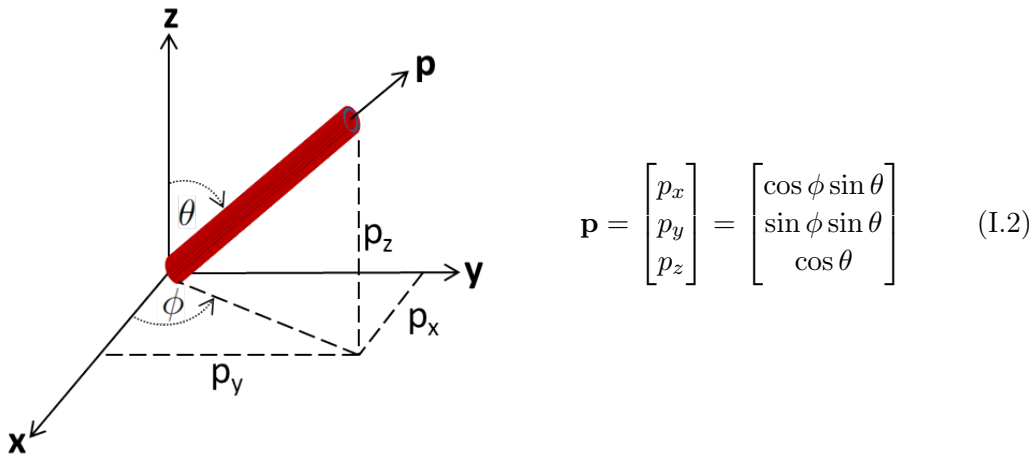


Figure I.15: 3D description of fiber orientation

the fiber, the direction of  $\mathbf{p}$  is completely arbitrary. For this reason,  $\theta$  and  $\phi$  belong to the intervals  $[0; \pi]$  and  $[-\pi/2; \pi/2]$ , respectively, and equation (I.2) confirms that  $\mathbf{p}$  remains unchanged by the operations  $\theta \rightarrow \pi - \theta$  and  $\phi \rightarrow \phi + \pi$ . Similarly, a 2D representation of a fiber orientation can be also described through only one angle  $\theta$ . So each orientation vector is contained in a sphere (3D) or in a circle (2D) of unitary radius. Hence, each possible state of orientation corresponds to a point located on the surface of the unit sphere or circle. Thus, to study the movement of the fiber, it is necessary to follow the evolution of the angles  $(\theta, \phi)$  running through time [47].

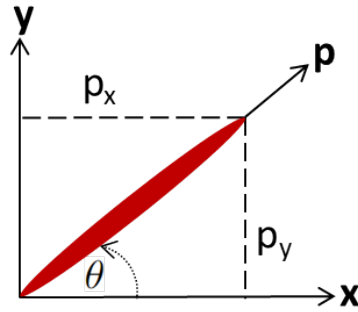


Figure I.16: 2D description of fiber orientation

### I.4.3.2 Orientation distribution function

In a fiber reinforced thermoplastic, the particles can orient in different directions. A first study was made in [48], that focus on particle orientation statistics by defining an orientation distribution function. Indeed, a complete description of the orientation state of the composite requires the call of an orientation distribution function  $\varphi(\mathbf{p}, t)$  or equivalently  $\varphi(\theta, \phi)$  which expresses the probability of obtaining a fiber having a certain orientation between  $(\mathbf{p}$  and  $d\mathbf{p})$  at time  $t$ . So the probability is written as follows:

$$P = \int_{\mathbf{p}}^{\mathbf{p}+d\mathbf{p}} \varphi(p) d\mathbf{p} \quad (\text{I.3})$$

In other words, depending on the angles  $(\theta, \phi)$   $P$  is written:

$$P(\theta_1 \leq \theta \leq \theta_1 + d\theta, \phi_1 \leq \phi \leq \phi_1 + d\phi) = \int_{\theta}^{\theta+d\theta} \int_{\phi}^{\phi+d\phi} \varphi(\theta, \phi) \sin(\theta) d\theta d\phi \quad (\text{I.4})$$

The orientation distribution function  $\varphi$  is an even function (i.e., unchanged by  $\mathbf{p} \rightarrow -\mathbf{p}$  transformation) whose integral over all possible orientations is equal to 1.

### I.4.3.3 Introduction to orientation tensors

The distribution function  $\varphi$  provides a general and precise description of the orientation state of a suspension at a given material point. However, its use in an industrial setting proves very complicated to set up since the resolution of the equations of

motion involving this distribution function requires the use of significant computer resources. To calculate the fiber orientation and its evolution for industrial applications, a more compact description is needed [49]. This can be achieved by using the notion of orientation tensors. These latter are used to describe the orientation state of a fiber population using a reduced number of discrete values.

Knowing that the function  $\varphi$  must satisfy some conditions such as periodicity, normalization and continuity condition, these tensors are obtained by integrating the tensor products of the vector  $\mathbf{p}$  with itself over the orientation space and by using  $\varphi$  as a weighting function. Since  $\varphi$  is even, only even order tensors are non-zero. An orientation tensor, commonly noted  $\mathbf{a}_2$ , is introduced expressing the spatial mean of the double tensor product of  $\mathbf{p}$  [50], by:

$$\mathbf{a}_2 = \int \varphi(\theta, \phi) \mathbf{p} \otimes \mathbf{p} d\mathbf{p} \quad (\text{I.5})$$

Orientation tensors have interesting properties, they are completely symmetrical ( $a_{xy}=a_{yx}$ ), all the more so, therefore at the normality property of  $\varphi$ , their trace is unitary ( $a_{xx}+a_{yy}+a_{zz} = 1$ ). The diagonal terms of  $\mathbf{a}_2$  express the alignment of the fibers with respect to the directions  $\mathbf{x}$ ,  $\mathbf{y}$ ,  $\mathbf{z}$ , while the extra diagonal terms quantify the asymmetry of the distribution of the orientations. In other words, if  $a_{xx} = 1$  all fibers are aligned along the  $\mathbf{x}$ -axis, while if  $a_{xx} = 0$  all fibers are located in the plane  $(\mathbf{y}, \mathbf{z})$ . Figure I.17 illustrates, for a three-dimensional configuration, some examples of tensor and the micro-structures associated therewith. For instance, if

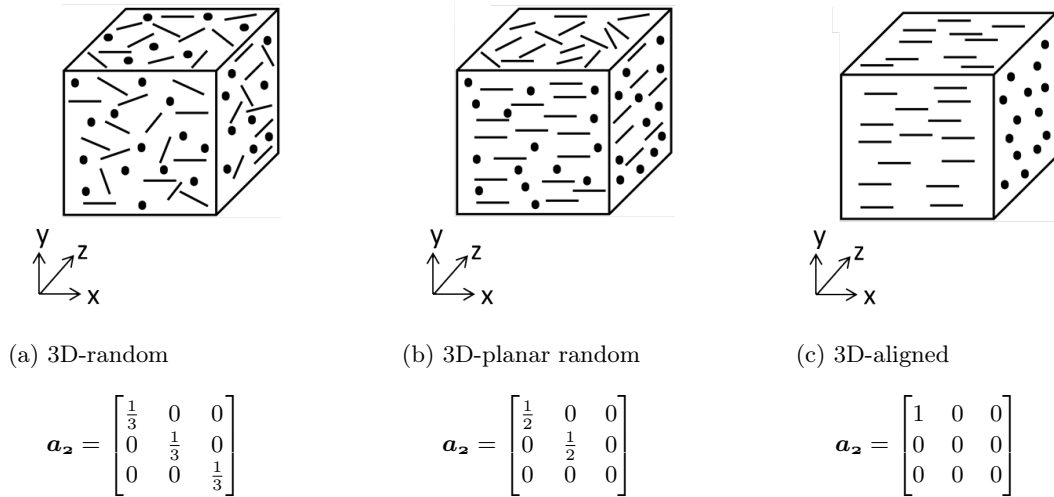


Figure I.17: 3D orientation tensor representation

( $a_{xx}=a_{yy}=a_{zz}=1/3$ ), the tensor is called isotropic as it represents a random orientation of the fibers, as shown in figure I.17a. In the two-dimensional case, the isotropy results in diagonal components equal to  $1/2$ , where the extra-diagonal components being zero. So like any average description, the definition of a tensor representation derived from the orientation distribution function  $\varphi$  results in a loss of information and prevents a complete description of the orientation state. To improve this description, the use of a fourth order orientation tensor  $\mathbf{a}_4$  defined by equation (I.6)

is common in the literature [50, 51, 49]. The tensor  $\mathbf{a}_4$  increases the number of parameters describing the orientation. Of its 81 components, it has 14 independent components and it also contains all the information of second order tensor  $\mathbf{a}_2$ .

$$\mathbf{a}_4 = \int \varphi(\theta, \phi) \mathbf{p} \otimes \mathbf{p} \otimes \mathbf{p} \otimes \mathbf{p} d\mathbf{p} \quad (\text{I.6})$$

To approximate the loss of information related to tensor descriptions, different studies in [49, 52, 53] propose different methods for reconstructing the  $\varphi$  function from the orientation tensors. The results were compared with experimental orientation distribution measures. None of the methods can be described as more precise than another, regardless of the nature of the probability function taken for the identification (spherical harmonic functions or others). Indeed, the reliability of the reconstructions depends strongly on the orientation state of the micro-structure, on the other hand, the reconstitution of  $\varphi$  is all the better in the case of the involvement of tensor of order greater than 2.

#### I.4.3.4 Concentration regimes

A suspension is characterized, among other things, by its concentration of particles, in this case fibers. It is essential to define and differentiate the different concentration regimes that characterize fiber suspensions in order to construct a domain of validity for the laws of behavior used. Fiber suspensions are typically classified into three concentration regimes: dilute, semi-dilute, and concentrated. These regimes are presented as concentration regimes based on their volume fraction and fiber aspect ratio [54]. Most of the composites usually have a high volume fraction of fibers,

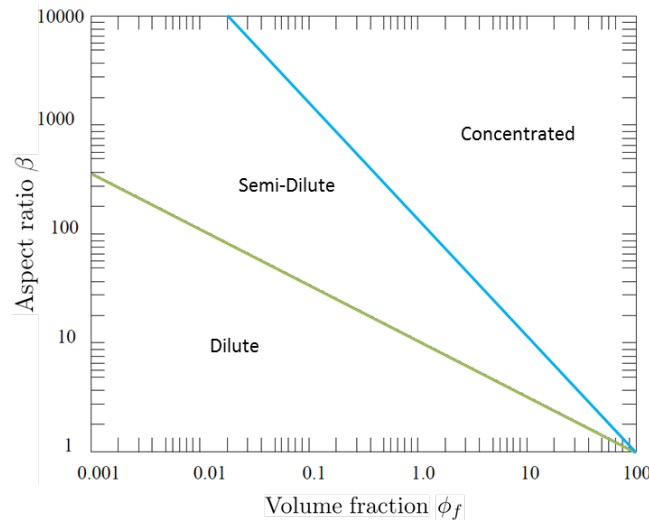


Figure I.18: Different areas of concentration regimes for fiber suspensions [55]

which is the ratio between the total volume of the fibers and the volume of the suspension, that typically ranges from 0.005 to 0.5 with a high aspect ratio  $\beta = L/D$  that typically ranges from 10 to  $10^3$  [56], where  $L$  and  $D$  are the characteristic fiber length and diameter, respectively, and with random to quasi-ordered fiber orientations. Indeed, if the fiber is considered as a cylindrical particle of length  $L$

and diameter  $D$ , the volume fraction of fibers  $\phi_f$ , in the case of a unit volume using number  $n$  as fiber density in a volume  $V$ , can be expressed as follows:

$$\phi_f = n\pi \frac{D^2 L}{4} \quad (\text{I.7})$$

The three regimes can be defined from the following conditions represented in table I.1. Figure I.18 summarizes the criteria used to distinguish each regime and illus-

Dilute	Semi-dilute	Concentrated
$\phi_f \leq \frac{1}{\beta}$	$\frac{1}{\beta^2} \leq \phi_f \leq \frac{1}{\beta}$	$\phi_f > \frac{1}{\beta}$
$n \leq \frac{1}{L^3}$	$\frac{1}{L^3} \leq n \leq \frac{1}{DL^2}$	$n > \frac{1}{L^3}$

Table I.1: Conditions of concentration regimes [46]

trates the hypothetical boundaries drawn between them. This figure highlights the close relationship between the aspect ratio  $\beta$  and the fraction  $\phi_f$  in the definition of the concentration regime. For a given  $\phi_f$ , the suspension is considered to be more concentrated if the aspect ratio of the fibers is greater. The characteristics of each regime can be briefly outlined as follows:

- The **dilute regime**: There is no interaction between the fibers as they move independently due to the fact that the distance between a fiber and its nearest neighbor is therefore greater than or equal to the length of the fiber. As a result, flow is governed simply by fluid-fiber interactions.
- The **semi-dilute regime**: The fiber can be displaced in the direction of its axis of rotation and the distance between a fiber and its nearest neighbor therefore varies from the length of a fiber to its diameter. Thus, the fibers interact with each other [57], most of the time, through hydrodynamic forces, but also, with a small occurrence, contact interactions can take place.
- The **concentrated regime**: The orientation of the fiber population tends towards a unidirectional distribution for concentrated regime and the average distance between fibers is smaller than the diameter of the fibers and the latter can no longer move without entanglement.

It should be noted that some studies [58] also define a hyper-concentrated regime for which the average distance between the axes of the fibers is less than twice their diameter. The disorientation of a fiber with respect to the mean direction is very limited. The periodic movement of the fibers encountered in shear flow is no longer possible.

#### I.4.3.5 Orientation evolution models

For the structural simulation of the fabricated part, the final fiber orientation induced by the manufacturing process plays a big role as an important parameter. Therefore, this section provides an overview of the several so-called fiber orientation evolution models at different scales that have been developed in recent years.

### Microscale model: Jeffery equation

At this scale, a single fiber orientation evolution model is adopted as the dynamic motion of each fiber is investigated separately, where the effect of fibers intersection is not introduced in this model (case of dilute regime). So, a study done in [47], was one of the first to describe the orientation dynamics of a particle. It provides a relatively correct description of the movement of an ellipsoidal object (whether prolate or oblate) in a flow, and consequently coming out with an equation for the evolution of orientation for dilute solutions of rigid spheroidal particles. Since then, this description has been considered essential for all work on the study of orientation phenomena despite its many restrictive assumptions. Indeed, in this work [47], numerous assumptions have been made about particle, flow, and contact. It considers first that the particle is rigid ellipsoidal, its center of gravity moving at the same speed of translation as the fluid. Also, the dimensions of the particle are small so that the velocity field of deformation is homogeneous at a large distance. The flow is known, stationary and homogeneous (except for a zone of disturbance around the particle) and occurs in an infinite medium formed by an incompressible Newtonian fluid. Lastly, the contact between the fluid and the particle is sticky, thus making it possible to connect the kinematics of the fluid to that of the particle. Solving the Stokes equations, the following model for the evolution of the orientation vector is proposed:

$$\dot{\mathbf{p}} = -\boldsymbol{\omega} \cdot \mathbf{p} + \lambda(\mathbf{E} \cdot \mathbf{p} - \mathbf{E} : \mathbf{p} \otimes \mathbf{p} \otimes \mathbf{p}) \quad (\text{I.8})$$

where  $\dot{\mathbf{p}}$  is material derivative of  $\mathbf{p}$ ,  $\mathbf{E}$  and  $\boldsymbol{\omega}$  are the strain rate and vorticity tensors respectively and  $\lambda$  is the shape factor which depends on the geometry of the fiber, defined by:

$$\lambda = \frac{\beta^2 - 1}{\beta^2 + 1} \quad (\text{I.9})$$

Equation (I.8) shows two contributions, the first is the rotational movement about the axis of vorticity expressed by the term  $\boldsymbol{\omega} \cdot \mathbf{p}$  and the second term  $\mathbf{E} \cdot \mathbf{p} - \mathbf{E} : \mathbf{p} \otimes \mathbf{p} \otimes \mathbf{p}$  presents the movement which tends to align the fibers in the direction of the velocity.

### Analytical solution: application in the case of a simple shear flow

In the case of a simple shear flow governed by a velocity field  $\mathbf{u}=(\dot{\gamma}y,0,0)$ , where  $(\dot{\gamma}>0)$  is the generalized shear rate, the Jeffery equation accepts at time  $t$  the following analytical solution for a fiber initially collinear to the  $x$ -axis:

$$\mathbf{p} = \frac{1}{\sqrt{\cos^2(\frac{2\pi t}{T}) + \frac{1-\lambda}{1+\lambda} \sin^2(\frac{2\pi t}{T})}} \begin{bmatrix} \cos(\frac{2\pi t}{T}) \\ -\frac{\sqrt{1-\lambda^2}}{1+\lambda} \sin(\frac{2\pi t}{T}) \\ 0 \end{bmatrix} \quad (\text{I.10})$$

The fiber is oriented by an angle of  $\theta$ , as shown in the figure I.19: Figure I.20 shows that the particle (fiber) undergoes a periodic rotational movement, “tumbling”, which depends on the aspect ratio  $\beta$ , the generalized shear rate  $\dot{\gamma}$  and the initial orientation, thus highlighting the trajectory of the particle commonly known as Jeffery’s orbit.

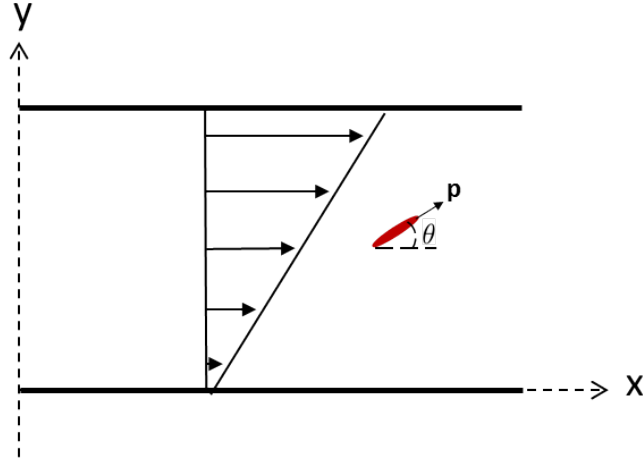
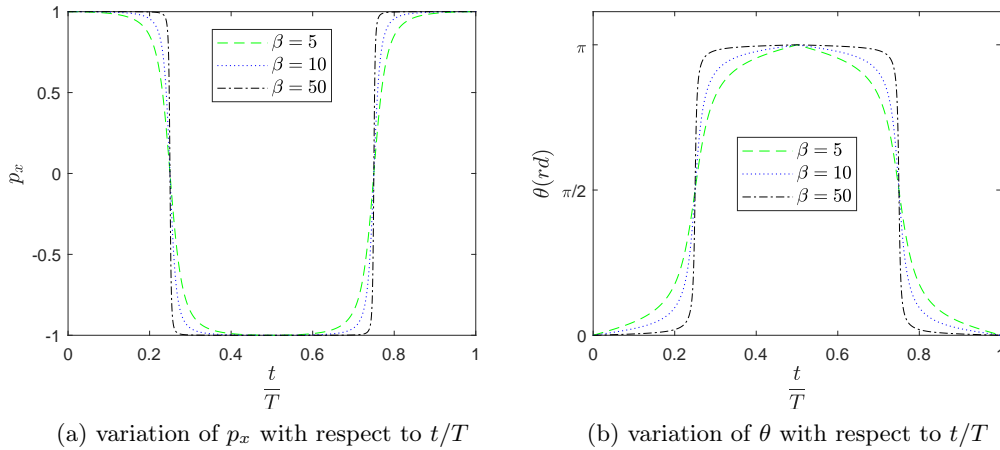


Figure I.19: Simple shear flow case

Figure I.20: Jeffery solution in a simple shear flow: effect of  $\beta$  on fiber orientation

It can be also found that the fiber spends most of the time oriented in the direction of the flow velocity. Its residence time in this direction is greater as the generalized shear rate is smaller and the aspect ratio  $\beta$  is larger. Thus, the solution also indicates that if  $\beta \rightarrow \infty$ , then the trajectory of the particle becomes stable. So, the time taken by the particle during rotation is small compared with the time elapsed when the particle remains aligned with the current lines.

### Mesoscale model: Fokker-Planck equation

As already discussed above, Jeffery's model is only valid for diluted suspensions, which is far from being the case for the majority of industrial suspensions involving fibers. It is imperative to take into account at least the interactions between fibers which strongly influence the state of orientation. Hence, an evolution model describing the orientation of a population of fibers is needed, where it is more reasonable to group fibers within an angle range, rather than tracking the angle variation of

each fiber individually. The mesoscopic scale is an intermediate scale between the part and the particle. Consequently, the fibers are not considered individually, but the fiber population is taken into account through its statistical distribution  $\varphi$ . A study done in [59] describes the evolution of the orientation distribution function  $\varphi$  by adapting the Fokker-Planck equation to fiber suspensions as follows:

$$\frac{D\varphi}{Dt} = -\nabla_{\mathbf{p}} \cdot (\varphi \dot{\mathbf{p}}) + D_r \nabla_{\mathbf{p}}^2 \varphi \quad (\text{I.11})$$

where  $(D/Dt)$  is the material derivative and  $D_r$  is the rotational diffusion coefficient. The latter has been introduced to represent hydrodynamic interactions that induce an effect similar to that of a Brownian diffusion, however, the choice of the value of this parameter is rather tricky. Thus, although  $\varphi$  allows a complete description of the state of orientation, the study of its evolution through the resolution of equation (I.11) has long been avoided in the literature. The multidimensional nature of this equation made its treatment inadequate by standard discretization methods except for simple problems. In contrast, in recent decades, many studies [60, 61] have shown the possibility of solving this equation by different methods, under certain conditions. Afterwards the macroscopic model is presented briefly, while the mesoscopic method will be detailed in the following chapter.

### Macroscale model: Folgar and Tucker equation and its improvements

Modeling of fiber orientation in a semi-concentrated medium has been the subject of some studies [62]. In contrast, there are very few macroscopic models that can account for the evolution of fiber orientation during flow. To model particle motion in semi-concentrated solutions, macroscopically, the orientation state is described by a phenomenological approach that allows the evolution of the tensor  $\mathbf{a}_2$  to be tracked. Thus, the degree of finesse of the representation of physics is reduced in favor of the speed of calculation. The most famous model is represented in [59] and described by equation (I.12).

$$\frac{D\mathbf{a}_2}{Dt} = \underbrace{-(\mathbf{a}_2 \cdot \boldsymbol{\omega} - \boldsymbol{\omega} \cdot \mathbf{a}_2) + \frac{1}{2} \lambda (\mathbf{E} \cdot \mathbf{a}_2 + \mathbf{a}_2 \cdot \mathbf{E} - 2\mathbf{E} : \mathbf{a}_4)}_{\text{Hydrodynamic contributor}} + \underbrace{2C_I \dot{\gamma} (\mathbf{I} - 3\mathbf{a}_2)}_{\text{Isotropic rotary diffusion contributor}} \quad (\text{I.12})$$

Many studies were done later in order to improve the model since the simulated orientation of the fiber shows a deviation from the experimentally determined orientation of the fiber, as the first model had an inexact prediction with a faster response rate of fiber orientation. Thereby a work made in [63] proposed a reduced strain closure (RSC) model based on the decomposition of the eigenvalue  $\lambda$  and the eigenvector  $\mathbf{e}$ , written as follows:

$$\frac{D\mathbf{a}_2}{Dt} = \frac{1}{2} (\boldsymbol{\omega} \cdot \mathbf{a}_2 - \mathbf{a}_2 \cdot \boldsymbol{\omega}) + \frac{1}{2} \lambda (\mathbf{E} \cdot \mathbf{a}_2 + \mathbf{a}_2 \cdot \mathbf{E} - 2[\mathbf{a}_4 + (1 - k)(\mathbf{L}_4 - \mathbf{M}_4 : \mathbf{a}_4)] : \mathbf{E}) + 2kC_I \dot{\gamma} (\mathbf{I} - 3\mathbf{a}_2) \quad (\text{I.13})$$

where  $k \in [0, 1]$  is a constant slow-down factor fit by experimental data,  $\mathbf{M}_4$  and  $\mathbf{L}_4$  are fourth order tensors which depend on the eigenvalues and eigenvectors, expressed

as:

$$\begin{aligned}\mathbf{M}_4 &= \sum_{i=3}^3 \mathbf{e}_i \mathbf{e}_i \mathbf{e}_i \mathbf{e}_i \\ \mathbf{L}_4 &= \sum_{i=3}^3 a_i \mathbf{e}_i \mathbf{e}_i \mathbf{e}_i\end{aligned}\tag{I.14}$$

The anisotropic rotary diffusion (ARD) model was later introduced in [64], where the isotropic rotary diffusion contribution in (I.12) was modified by replacing  $C_I$  with anisotropic rotary tensor  $\mathbf{C}$ . The ARD model is then given as:

$$\begin{aligned}\frac{D\mathbf{a}_2}{Dt} &= \frac{1}{2}(\boldsymbol{\omega} \cdot \mathbf{a}_2 - \mathbf{a}_2 \cdot \boldsymbol{\omega}) + \frac{1}{2}\lambda(\mathbf{E} \cdot \mathbf{a}_2 + \mathbf{a}_2 \cdot \mathbf{E} - 2\mathbf{E} : \mathbf{a}_4) \\ &+ \dot{\gamma}(2\mathbf{C} - 2\text{tr}(\mathbf{C})\mathbf{a}_2 - 5(\mathbf{C} \cdot \mathbf{a}_2 + \mathbf{a}_2 \cdot \mathbf{C}) + 10\mathbf{a}_4 : \mathbf{C})\end{aligned}\tag{I.15}$$

where  $\mathbf{C}$  can be computed based on different modeling approaches that are found in [65, 66, 64]. At present, many commercial injection molding simulation softwares, such as Moldex 3D and Autodesk Moldflow have integrated a ARD-RSC model [67] which is developed by combining equations (I.13) and (I.15):

$$\begin{aligned}\frac{D\mathbf{a}_2}{Dt} &= \frac{1}{2}(\boldsymbol{\omega} \cdot \mathbf{a}_2 - \mathbf{a}_2 \cdot \boldsymbol{\omega}) + \frac{1}{2}\lambda(\mathbf{E} \cdot \mathbf{a}_2 + \mathbf{a}_2 \cdot \mathbf{E} - 2[\mathbf{a}_4 + (1-k)(\mathbf{L}_4 - \mathbf{M}_4 : \mathbf{a}_4)] : \mathbf{E}) \\ &+ \dot{\gamma}(2[\mathbf{C} - (1-k)\mathbf{M}_4 : \mathbf{C}] - 2k\text{tr}(\mathbf{E})\mathbf{a}_2 - 5(\mathbf{C} \cdot \mathbf{a}_2 + \mathbf{a}_2 \cdot \mathbf{C}) \\ &+ 10[\mathbf{a}_4 + (1-k)(\mathbf{L}_4 - \mathbf{M}_4 : \mathbf{a}_4)] : \mathbf{C})\end{aligned}\tag{I.16}$$

Nevertheless, there are two major difficulties in solving these models. In addition to the first mentioned for equation (I.11), which is linked to the choice of the parameter modeling the degree of interaction, and it is also observable that the evaluation of the equation of orientation tensor must contain the next higher even-order tensor, so the presence of the orientation tensor  $\mathbf{a}_4$  of order 4 is added. The latter can only be solved by means of its evolution equation which involves a tensor of order 6 and so on. For that reason, a standard approach is brought in form of a closure approximation which is needed to close the set of the evolution equations of the orientation tensors. The approach is defined in a way that the fourth order tensor is approximated as function of the second order orientation tensor.

In the literature, there are several forms for these closure methods [68, 69, 70, 71], but none of them is conclusive in predicting the direction of actual flows. For this reason, identifying a closure approximation presents a challenge that continues to motivate researchers to date. Despite these difficulties, this tensor description remains the most used, especially in an industrial context. For this reason, some researches are still made in order to improve the accuracy of their uses [72, 73]. For an injected part, equation (I.12) makes it possible to predict the orientation in the shell zone well, but this is far from the case for the core zone where significant differences in prediction are observed. A review of objective and non-objective models for improving the results from equation (I.12) is presented in [74]. Some examples of closure equations that can be incorporated into a calculation code to predict the orientation state of the fibers are concisely explained.

- The **linear approximation**: It was first introduced in [49], and known as one of the simplest closure approaches. It is represented as a summation of all products of orientation tensor  $a_{ij}$  and kronecker delta function  $\delta_{ij}$ , as the symmetry and normalization conditions are applied:

$$a_{ijkl}^{LIN} = \frac{1}{7}(a_{ij}\delta_{kl} + a_{ik}\delta_{jl} + a_{il}\delta_{jk} + a_{kl}\delta_{ij} + a_{jl}\delta_{ik} + a_{jk}\delta_{il}) - \frac{1}{35}(\delta_{ij}\delta_{kl} + \delta_{ik}\delta_{jl} + \delta_{il}\delta_{jk}) \quad (I.17)$$

- The **quadratic approximation**: A study made in [75] has implemented an exact quadratic closure approximation for flows that orient fibers in a single direction. It takes the following form:

$$a_{ijkl}^{QUAD} = a_{ij}a_{kl} \quad (I.18)$$

The quadratic closure equation is widely used for its compact expression, however it does not respect all the symmetry conditions of the fourth order tensor. Furthermore, it is known to overestimate the alignment of the fibers in the direction of flow.

- The **orthotropic approximation**: The orthotropic closure approximations had been developed in the literature [69], [76]. The orthotropic closure satisfies the full symmetry condition. It is built on that all fourth-order closure formulas are necessarily orthotropic, with principal axes that match the principal axes of the second order tensor. In the orthotropic closure, three independent components of  $\mathbf{a}_4$  ( $A_1$ ,  $A_2$ , and  $A_3$ ) in the eigenspace system, are taken to depend on the eigenvalues of  $\mathbf{a}_2$  as follows:

$$A_k = C_K^1 + C_K^2 a_1 + C_K^3 (a_1)^2 + C_K^4 a_2 + C_K^5 (a_2)^2 + C_K^6 a_1 a_2 \quad (I.19)$$

where ( $K \in [1,3]$ ). Two largest eigenvalues of  $\mathbf{a}_2$  are represented by  $a_1$  and  $a_2$ , and  $C_K^i$ , where ( $i \in [1,6]$ ), are eighteen fitting parameters. Several versions of the orthotropic closure approximations were developed in order improve the accuracy and to overcome some nonphysical behaviors of the original model. From numerical aspect, an additional computation is required for tensor transformations between the global coordinate and the principal coordinate, which is its drawback in terms of the computational efficiency.

- The **neural-network based approximation**: The neural-network based closure approximation was developed recently, which assumes two-layer neural network between the second and fourth order orientation tensors as follows:

$$\mathbf{a}_4 = f_2(\mathbf{W}_2 f_1(\mathbf{W}_1 \mathbf{a}_2 + \mathbf{b}_1) + \mathbf{b}_2) \quad (I.20)$$

where ( $f_1$ ,  $f_2$ ) are transfer functions which can be linear or tangent hyperbolic and ( $\mathbf{W}_1$ ,  $\mathbf{W}_2$ ) are weighting coefficients, and ( $\mathbf{b}_1$ ,  $\mathbf{b}_2$ ) are bias coefficients. The neural network closure is accurate for a wide range of the flow fields, and also its computational time is a lot decreased compared to the orthotropic closures.

- **The Invariant-based optimal fitting (IBOF) approximation [68]:** It is a fitted closure derived from the natural closure (NAT) [77] that expands the fourth-order tensor  $a_{ijkl}$  in terms of the second-order orientation tensor,  $a_{ij}$ , and the velocity gradient,  $L_{ij}$  [77]. It was developed to address the singularity problems encountered with the natural closure and to improve its accuracy. IBOF achieves this by employing principal invariants, which can be readily calculated in any coordinate system, rather than eigenvalues.

$$a_{ijkl}^{IBOF} = \beta_1 S(\delta_{ij}\delta_{kl}) + \beta_2 S(\delta_{ij}a_{kl}) + \beta_3 S(a_{ij}a_{kl}) + \beta_4 S(\delta_{ij}b_{kl}) \\ + \beta_5 S(a_{ij}b_{kl}) + \beta_6 S(b_{ij}b_{kl}) \quad (\text{I.21})$$

where  $b_{ij} = a_{im} \cdot a_{mj}$  and  $\beta_i, i=1, \dots, 6$  are functions of  $a_{ij}$ .

#### I.4.4 Short summary

- ✓ During the phase of flow of the charge into the mold, each fiber is transported by the flow and its orientation changes as a function of the stresses imposed by the matrix, the other particles and the walls of the mold. This results in a distribution of complex orientation, varying considerably in the workpiece, in particular according to the thickness, thus affecting the mechanical properties: the elastic modulus, the breaking strength, and the impact strength will depend on this distribution of orientation but also on the local concentration of the fibers and on the heterogeneity of the length distribution of the fibers.
- ✓ The Jeffery equation provides a description of particle orientation for a dilute fiber solution that supports several experimental studies. The Jeffery model hypotheses are rather restrictive (Newtonian fluid, dilute solution of fibers, neglected hydrodynamic interactions).
- ✓ The most widely used model in the industrial field is that of Folgar and Tucker. In this model, variables are the moment tensors derived from the fiber distribution function whose equation describes the evolution of the second order orientation tensor with respect to time.
- ✓ A closure approximation is needed for Folgar and Tucker equation where a dependency of the lower even order fiber orientation tensor on the tensor of the next higher even-order is recurred, but often resulting in inaccuracy and loss of information.
- ✓ Fokker-Planck equation resolution, is required in order to predict without approximations the fiber orientation.

### I.5 Conclusion and research plan

#### I.5.1 A synopsis

Throughout this chapter, some notions on the definition and concepts in the field of composite materials have been given. Some general information on the different types of composite materials, the different types of fibers and their mechanical properties as well as their use in industry, and the difference between the thermoplastic and the thermosetting polymers were presented. The main terminology relating to the field of injected fiber suspensions has been introduced. This chapter have also discussed the highly anisotropic microstructure generated by the flow involved in the production of a composite with discontinuous reinforcement. In fact, it has defined the parameters of the process as well as the rheology that govern this microstructure. The difficulty of predicting such a microstructure was also reported and special attention was paid to Jeffery's theory on which all orientation models are based.

### I.5.2 Industrial context

Recalling that this work is held within an industrial research chair between Centrale Nantes and Faurecia, its focus is made on understanding at first the overmolding process which is used at Faurecia company as technique to fabricate parts with complex shapes made of composite materials, where it targets to manufacture lightweight automotive parts with better mechanical properties. So the company aims to understand the drawbacks of the overmolding technique causing the deformation, displacement and penetration of the insert that are explained detailedly (see section I.3.3) in order to manage fixing them by controlling the machine parameters during the filling stage such as pressure. Thus, depending on the defects that occur during overmolding and the needs of the company, it is important to have a code that performs simulations to calculate the displacement and deformation at the interface between the molten injected thermoplastics and the insert. This will make it easier for the company to predict defects in order to ensure a better final shape of the manufactured composite parts.

### I.5.3 Study objectives and approach

The purpose of the thesis is to develop a numerical method enriching ICI-Tech library that is capable to simulate the filling stage of overmolding, as figure I.21

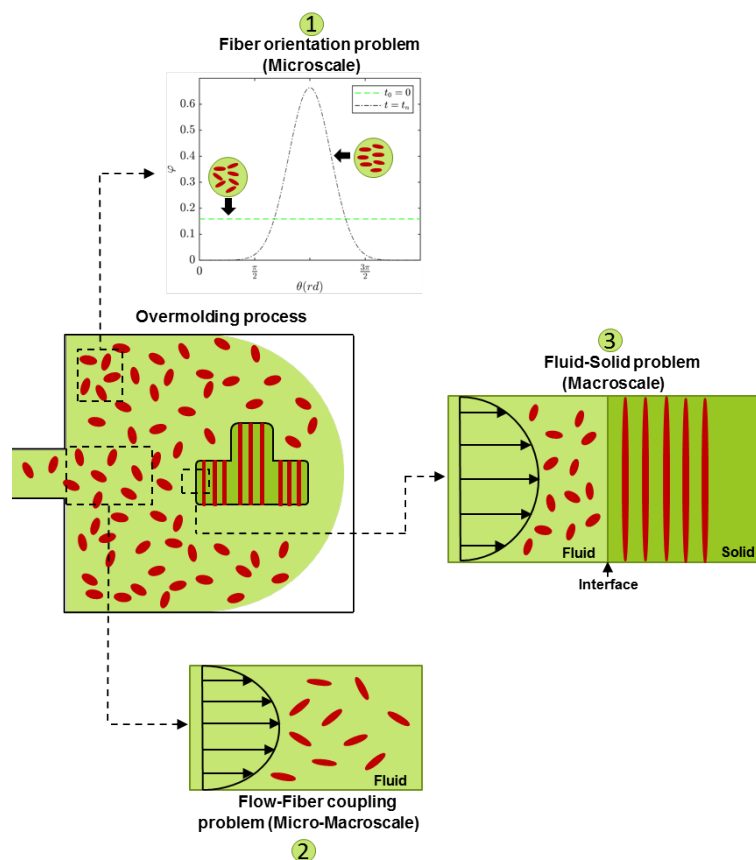


Figure I.21: Illustration on the research methodology conduction

depicts the research plan in the logical order. It therefore seems essential to control or at least to provide at first for the orientation of the fibers during the shaping phase as this can be achieved through the resolution of the Fokker-Planck equation (FPE) (see chapter II). So the numerical simulation finds its place in this research, given its ability to predict the flow of the material and thus the orientation of the fibers in the mold where the stress constitutive equation, representing the behavior of the material, is then needed to be constructed (see chapter III). Thus, the stress field of the material is expressed as a function of the orientation distribution. A fluid/solid model is then built, where the constitutive relation, that takes into account the fiber orientation, is implemented for the two phases in order to compute the stress and strain deformation, thereby getting information on what happens on the interface between the injected molten thermoplastics (phase 1: fluid) and the insert (phase 2: solid).

#### I.5.4 Thesis structure

This thesis is mainly structured around three parts, each of which contributes to the understanding of orientation mechanisms via numerical simulation and their effect on the mechanical properties of the final fabricated part.

- **Chapter II:** It is dedicated to the description of the microscopic model for the modeling of the mechanisms of orientation of fibers in flow. Its aim is to develop a new numerical method to study the orientation of fibers by solving the Fokker-Planck equation using the finite element method (FEM) in the orientation space.
- **Chapter III:** It details the constitutive laws generally used to model the behavior of a suspension loaded with fibers. So it will be devoted to the description of the numerical model used in the context of the resolution of the coupling problem of evolution of the orientation and the law of rheological behavior at the macroscale level. It is therefore mainly dedicated to the coupling between rheology and fiber orientation.
- **Chapter IV:** It provides an extension of the analysis of the fiber-flow coupling problem to more complex domains. Additionally, it delves into the construction of a two-phase flow-fiber coupling model aimed at simulating real-case scenarios, such as overmolding process.

# Solving Fokker-Planck equation

---

## Contents

---

<b>II.1 Introduction</b> . . . . .	<b>30</b>
<b>II.2 Mathematical modeling</b> . . . . .	<b>32</b>
II.2.1 Fokker-Planck equation . . . . .	32
II.2.2 Reformulation of Fokker-Planck Equation . . . . .	33
II.2.3 Discretization of Fokker-Planck equation . . . . .	37
II.2.4 Short summary . . . . .	41
<b>II.3 Numerical results</b> . . . . .	<b>41</b>
II.3.1 Validation tests . . . . .	41
II.3.2 Numerical convergence analysis and computational efficiency	47
II.3.3 Fiber orientation-flow . . . . .	51
II.3.4 Short summary . . . . .	53
<b>II.4 Discussion</b> . . . . .	<b>53</b>
<b>II.5 Conclusion</b> . . . . .	<b>55</b>

---

In the complex fluid family, including polymer-short fiber suspensions, materials have characteristic lengths that are significantly larger than those of simple fluids. The coupling between microstructures (fiber concentration and orientation) and flows often leads to specific rheological behaviours. Short fiber suspensions are extensively involved in the composite industry. Knowledge of the final microstructure of the parts is essential for predicting mechanical properties. Similarly, the prediction of such a microstructure can also be used to optimize the processes in order to obtain the desired final properties. The quality of such a prediction depends on mastering many different aspects. One of these aspects, which is covered in the following chapter, is the mechanical modeling of the suspension, in other words, the resolution of the fiber angular motion. To predict the fiber orientation, a macroscopic model based on Folgar and Tucker equation [59], which defines so-called orientation tensors, was introduced. For this model, closure approximations were needed to solve the equation, but these methods usually result in implicit errors. Chapter II presents a direct numerical simulation (DNS) technique which is applied in order to overcome the mentioned inaccuracies. It discusses in detail the simulation of the fiber orientation through a finite element approach to solve the Fokker-Planck equation at mesoscale level.

## II.1 Introduction

From the aforementioned chapter, thermoplastics reinforced with short fibers are popular engineered materials, particularly in the automotive sector. These materials make it possible to meet the challenges of massive weight reduction and reduction in manufacturing costs, while optimizing the characteristics and mechanical behavior [78, 79]. The latter depend closely on the microstructure induced by the manufacturing process [80]. In the case of injected parts, the orientation distribution of short fibers plays an important role [81, 82]. It influences the mechanical properties of the final molded composite part, such as its tensile strength. Therefore, predicting orientation using numerical approaches has been a topic of significant research interest [46, 83].

Many theoretical formulations have been established to describe the orientation of a fiber population [49, 84, 85]. The probability distribution function (PDF),  $\varphi(\mathbf{x}, \mathbf{p}, t)$ , allows to describe more widely the state of orientation of a population of fibers at a material point [49], since it is not feasible to study the motion of each fiber in a part. The PDF  $\varphi(\mathbf{x}, \mathbf{p}, t)$  presents at a time  $t$  and a position  $\mathbf{x}$  the probability  $P$  of finding fibers orienting in the direction  $\mathbf{p}$  where the latter is defined as a unit vector that describes the orientation of each fiber. This distribution function is a complete and accurate representation of the orientation state of the fibers, it is expressed in equation (I.3). As early as 1922, the motion of a rigid ellipsoidal particle immersed in an incompressible Newtonian fluid was well predicted thanks to the work of Jeffery [47]. Since then, several authors have studied the impact of the geometry of the particle [86] and the behaviour of the suspending flow on the evolution of its motion. However, flows arising in industrial applications are more complex than the diluted cases described above, where interactions between fibers must be taken into account. Nevertheless, in the early 90s, solving a model that describes fiber dynamics whose governing equation is analogous to Fokker-Planck equation was impracticable on existing computing resources due to the large numbers of unknowns to be determined at each spatial node. The latter equation is introduced by the rate of change of the PDF with respect to time  $t$  and fiber direction  $\mathbf{p}$ .

For an industrial application, a more compact description is needed to calculate the evolution of the fiber orientation in a medium. The concept of orientation tensor was introduced in [50, 51, 49] to condense the information contained in  $\varphi$  and thus obtain a representation of the orientation state of the fibers which depends only on position and time. The most widely used model in this case is that of Folgar and Tucker [59], introducing a diffusion coefficient inspired by considerations of Brownian motion [87] with a determination that remains rather delicate. In this model, variables are the moment tensors derived from the fiber distribution function whose equation describes the evolution of the second order orientation tensor with respect to time, it is expressed in equation (I.12). Thus, a closure approximation is needed where a dependency of the lower even order fiber orientation tensor on the tensor of the next higher even-order is recurred, as the fourth order tensor in the Folgar and Tucker equation is a function of a six order tensor and so forth. Hence, different closure approximations have been proposed in the literature [68, 69, 70, 71], but often resulting in inaccuracy and loss of information [88, 89].

To circumvent these drawbacks, Fokker-Planck equation resolution, is required in order to predict without approximations the fiber orientation. Advani and Tucker [90] attempted to solve the Fokker-Planck equation using a finite difference technique with a central differencing scheme to approximate the differential operator with respect to  $\mathbf{p}$  and an implicit time derivative. At each time step, Gauss-Seidel relaxation method was set to compute the solution in the orientation and physical spaces. It was required to re-normalize the PDF  $\varphi(\mathbf{p},t)$  at each time iteration, due to imposed boundary conditions where  $\varphi$  is assumed to be zero at angles 0 and  $\pi$ . This means that the probability of finding fibers orientated in both angles is negligible, which is not always true. Thus, the conservation properties of the PDF were not preserved. Chinesta et al. [60] applied the meshless particle method to discretize the advection-dominated Fokker-Planck equation. This technique has also been adopted to address a convection-diffusion equation with the diffusive term modeled by random motions [91, 92]. However, its use was restricted to quite slight diffusion effects due to the massive number of particles needed in order to maintain a good stabilization of the solution, which makes this method useless for complex industrial applications. On the other hand, a spherical harmonic Galerkin approach was proposed in [93, 94] in order to solve the Fokker-Planck equation. In case of a negligible or weak Brownian motion, which corresponds to a high Peclet number  $P_e$  (generalized shear rate/rotary diffusivity), the probability distribution function  $\varphi$  could feature a high gradient in the solution which requires additional degrees of freedom in the orientation space to better describe the PDF and obtain more accurate results. Also, solutions up to a certain  $P_e$  could be non-achievable due to the ill-conditioning of the modal matrix. Therefore this method is limited and only applicable for strong Brownian motion. Férec et al. [61] and Johnson et al. [95] also used an approximation method by implementing Fokker-Planck resolution in a finite volume framework, as their methods were only applied in the case of a homogeneous flow.

This chapter focuses only on the numerical simulation of orientation mechanisms and not on their impacts on the induced mechanical performance. Its aim is to present a new numerical method that is developed to study the orientation of fibers by solving the Fokker-Planck equation using the FEM in the orientation space as for the physical space. This approach is meant to ease the transition of the problem, solving from meso to macro-scale and the implementation of message passing interface (MPI) based parallel simulation algorithm using Open MPI library. The outline of chapter II is as follows. Section II.2 describes the methodology developed to compute the evolution equation of the probability distribution function on a 2D domain. Hence, the reformulation and the discretization through a full FEM of the Fokker-Planck equation are explained. Then, numerical results are presented in section II.3, where simple tests illustrate the solution obtained with our method. Furthermore, results on more advanced cases are shown to check the flow-induced fiber orientation. Finally before concluding, the physical interpretation and the prediction of the fiber motion determined from solving Fokker-Planck equation are discussed, as well as the influence of some parameter on its behaviour and evolution.

## II.2 Mathematical modeling

Several evolutionary equations are used to model the suspensions of short fibers. From a microscopic point of view, the evolution of fiber orientation in a Newtonian fluid is described by the Jeffery Equation (I.8). Nevertheless this equation does not take into account fiber interactions. Therefore, a model in [59] introduces the Fokker-Planck equation adapted to fiber suspensions that describes the evolution of the orientation distribution. The physical interpretation of this equation is detailed in the following sections.

### II.2.1 Fokker-Planck equation

Generally, in statistical mechanics, the Fokker-Planck equation is defined as a partial differential equation that describes the temporal evolution of the probability density function of the particle's velocity under the impact of drag forces. In short fiber reinforced thermoplastic processing, fibers can orient in different directions induced by the injection flow. Prager [48] was the first to get interested in the statistics of particle orientations by defining an orientation distribution function. In kinetic theory, a complete description of the orientation state of the composite requires calling an orientation distribution function  $\varphi(\mathbf{p}, t)$  which, as discussed above, expresses the probability of a fiber for having a certain orientation  $\mathbf{p}$  at time  $t$ . From Bird et al. [96], if  $\dot{\mathbf{p}}$  ( $d\mathbf{p}/dt$ ) denotes the material time derivative of  $\mathbf{p}$ , then the conservation equation of  $\varphi$  is written, neglecting the Brownian motion of the fibers as follows:

$$\frac{\partial \varphi}{\partial t} = -\nabla_{\mathbf{p}} \cdot (\dot{\mathbf{p}}\varphi) \quad (\text{II.1})$$

This equation is valid in the particular case of dilute fiber suspensions. On the other hand, in the case of semi-diluted or concentrated fiber suspensions, the hydrodynamic type interactions should be taken into account by adding in equation (II.1) a term analogous to a pseudo-Brownian diffusivity. In order to take into account fiber interactions, Folgar and Tucker [59] added to the Jeffery equation a phenomenological diffusion term. Consequently, the time evolution of particles can be expressed generally as [49]:

$$\dot{\mathbf{p}}_{\text{FT}} = \underbrace{-\boldsymbol{\omega} \cdot \mathbf{p} + \lambda(\mathbf{E} \cdot \mathbf{p} - \mathbf{E} : \mathbf{p} \otimes \mathbf{p} \otimes \mathbf{p})}_{\dot{\mathbf{p}}_{\text{Jeffery}}} - \frac{D_r}{\varphi} \nabla \varphi \quad (\text{II.2})$$

where  $\mathbf{E}$  and  $\boldsymbol{\omega}$  are the strain rate and vorticity tensors respectively,  $\dot{\gamma}$  is the scalar magnitude of strain tensor rate known as the generalized shear rate,  $\lambda$  is the shape factor, expressed in equation (I.9), which depends on the geometry of the fiber and  $\beta$  is the aspect ratio of the fiber (length/diameter).

$$\begin{aligned} \mathbf{E} &= \frac{1}{2}(\nabla \mathbf{u} + \nabla \mathbf{u}^T) \\ \boldsymbol{\omega} &= \frac{1}{2}(\nabla \mathbf{u}^T - \nabla \mathbf{u}) \\ \dot{\gamma} &= \sqrt{2\mathbf{E} : \mathbf{E}} \end{aligned} \quad (\text{II.3})$$

By combining equation (II.1) with equation (II.2), a new well known Fokker-Planck equation is introduced as:

$$\frac{\partial \varphi}{\partial t} = -\nabla_{\mathbf{p}} \cdot (\dot{\mathbf{p}}\varphi) + D_r \nabla_{\mathbf{p}}^2 \varphi \quad (\text{II.4})$$

where  $\dot{\mathbf{p}}$  is the orbital velocity and  $D_r$  is the rotary diffusivity coefficient. The expression of the latter is given in [49]:

$$D_r = C_I \dot{\gamma} \quad (\text{II.5})$$

where  $C_I$  is the interaction coefficient which is empirically determined and describes the rate of interaction. After all the Fokker-Planck equation (II.4) expresses the rate of change for the probability distribution function (PDF), using the Jeffery equation for a single fiber (I.8) and the continuity equation (II.1). Fibers are modeled as independent random variables with identical distribution and zero mean. Each interaction results in a change of orientation in both fibers. So the right hand side of equation (II.4) is the sum of two contributions: the convection and the diffusion parts. An illustration of PDF time evolution is shown in figure II.1.

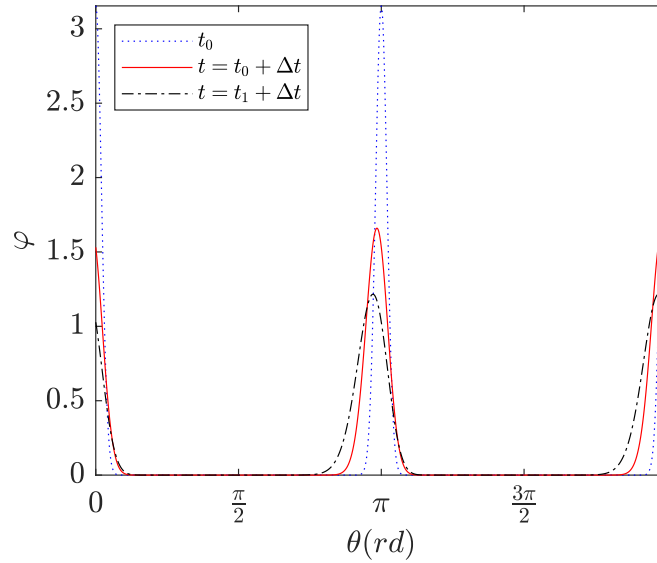


Figure II.1: Illustration: time evolution of PDF with  $\Delta t = 0.5s$ ,  $\dot{\gamma} = 1s^{-1}$ ,  $\lambda = 0.8$ , and  $C_I = 0.01$

## II.2.2 Reformulation of Fokker-Planck Equation

This model poses difficulties in the evaluation of the parameters and the large number of particles required leads to calculation costs that are often too high. For that in this section, the methodology used in order to reduce the complexity of equation (II.4) is described, which leads to minimize the computational cost of its resolution. Nonetheless, it should be pointed out that Fokker-Planck equation is resolved for one spatial node.

### II.2.2.1 Equation recasting

So at first, equation (II.4) is reformulated. By knowing that the divergence is a linear operator and employing the product rule that can be derived from the ordinary differentiation rules of calculus [97], the convective term is expanded and re-written in this form:

$$\nabla_{\mathbf{p}} \cdot (\dot{\mathbf{p}}\varphi) = \dot{\mathbf{p}} \cdot (\nabla_{\mathbf{p}}\varphi) + \varphi \nabla_{\mathbf{p}} \cdot \dot{\mathbf{p}} \quad (\text{II.6})$$

Noting that the orientation of the vector is defined as the angle that its line segment makes with the horizontal axis, an orientation of a single fiber is represented, as it is mentioned above, by the normal direction vector  $\mathbf{p}$ . So  $\mathbf{p}$  defined in a polar

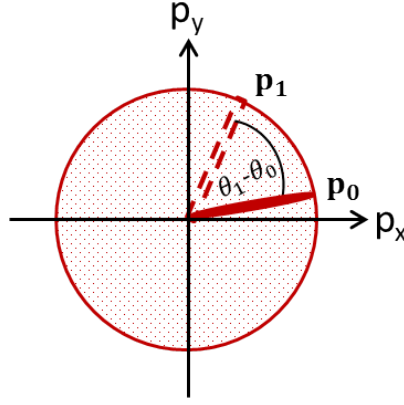


Figure II.2: 2D polar domain where all the possibilities of a fiber orientation exist

coordinates is described as function of angles ( $\theta$  in 2D) and ( $\theta, \phi$  in 3D) and radius ( $r = 1$ ). Let us consider a fiber which is initially orientated at an angle  $\theta_0$  and gradually rotated to an angle  $\theta_1$ . As depicted in figure II.2,  $\mathbf{p}_0$  and  $\mathbf{p}_1$  describe the fiber at  $\theta = \theta_0$  and  $\theta = \theta_1$ , respectively. Determining the slope (gradient) of  $\mathbf{p}$  through trigonometric expressions related to the polar angle, the change of  $p$  direction representing the fiber orientation corresponds to the change of its angle of rotation. Therefore, a link between  $\mathbf{p}$  and  $\theta$  is established under the forms  $\nabla_{\mathbf{p}} \mapsto \nabla_{\theta}$  and  $\mathbf{p} \mapsto \theta$ . Thus, in 2D,  $\varphi$  can also be expressed as a function of the orientation angle  $\theta$ . So combining the latter expression with equation (II.6), the reformulated Fokker-Planck equation is obtained:

$$\frac{\partial \varphi}{\partial t} + \dot{\theta} \cdot (\nabla_{\theta} \varphi) + \varphi \cdot \nabla_{\theta} \cdot \dot{\theta} - D_r \nabla_{\theta} \cdot (\nabla_{\theta} \varphi) = 0 \quad (\text{II.7})$$

### II.2.2.2 Angular velocity calculation

The orbital velocity  $\dot{\mathbf{p}}$  contributes to fiber motion, both in terms of rotation and deformation. Thus, the first term in equation (I.8) leads to pure rotation of the fibers, the second term generates deformation (elongation) which causes also a rotation and the third term contributes to only elongation. This can be mathematically proven by simple calculations of each term of  $\dot{\mathbf{p}}$ . Taking for example a simple 2D shear flow

in the x direction, its velocity profile can be given by:

$$\mathbf{u} = \begin{bmatrix} u_x \\ u_y \end{bmatrix} = \dot{\gamma} \cdot \begin{bmatrix} y \\ 0 \end{bmatrix} \quad (\text{II.8})$$

where  $\mathbf{u}$  has one non-zero component,  $u_x$ , whose gradient is perpendicular to the velocity itself and equal to  $\dot{\gamma}$ . For that case, this implies that equation (II.7) can be solved separately for each single spatial node as the velocity gradient is constant over the domain, which means that all fibers orient themselves with the same rotation rate. Firstly, vorticity and deformation tensors are computed from expressions (II.3), knowing that  $(\nabla u)_{ij}$  is expressed as  $\partial u_i / \partial x_j$  in index notation (with  $i, j \in [x, y]$ ), and then plugged into Jeffery's part of equation (II.2) to calculate each term of  $\dot{\mathbf{p}}$ , respectively. The components of the vector  $\mathbf{p}$  are expressed in polar coordinates, and the expressions of the first two terms in equation (II.2) can be determined:

$$\begin{aligned} \mathbf{E} \cdot \mathbf{p} &= \frac{1}{2} \begin{bmatrix} 0 & \dot{\gamma} \\ \dot{\gamma} & 0 \end{bmatrix} \cdot \begin{bmatrix} \cos \theta \\ \sin \theta \end{bmatrix} = \frac{1}{2} \dot{\gamma} \begin{bmatrix} \sin \theta \\ \cos \theta \end{bmatrix} \\ \boldsymbol{\omega} \cdot \mathbf{p} &= \frac{1}{2} \begin{bmatrix} 0 & -\dot{\gamma} \\ \dot{\gamma} & 0 \end{bmatrix} \cdot \begin{bmatrix} \cos \theta \\ \sin \theta \end{bmatrix} = \frac{1}{2} \dot{\gamma} \begin{bmatrix} -\sin \theta \\ \cos \theta \end{bmatrix} \end{aligned} \quad (\text{II.9})$$

The third term is re-written in a simpler manner form to facilitate its calculation, without necessarily computing the third order tensor resulting from the tensor product between the three unit vectors  $\mathbf{p}$ :

$$\mathbf{E} : \mathbf{p} \otimes \mathbf{p} \otimes \mathbf{p} = (\mathbf{p}^T \cdot \mathbf{E} \cdot \mathbf{p}) \cdot \mathbf{p} \quad (\text{II.10})$$

where  $\mathbf{p}^T$  is the transposed vector of  $\mathbf{p}$ . Then, similarly:

$$(\mathbf{p}^T \cdot \mathbf{E} \cdot \mathbf{p}) \cdot \mathbf{p} = \dot{\gamma} (\cos \theta \sin \theta) \cdot \begin{bmatrix} \cos \theta \\ \sin \theta \end{bmatrix} \quad (\text{II.11})$$

A vector field is defined as a function that maps points to vectors, thus the fields in equations (II.9) (II.11) which describe the physical motions of a fiber, can be sketched by plugging some coordinates of different points as shown in the following table:

fields \ $\theta$	0	$\pi/4$	$\pi/2$	$\pi$
$\mathbf{E} \cdot \mathbf{p}$	$(0, \zeta)$	$(\zeta \frac{\sqrt{2}}{2}, \zeta \frac{\sqrt{2}}{2})$	$(\zeta, 0)$	$(0, -\zeta)$
$\boldsymbol{\omega} \cdot \mathbf{p}$	$(0, \zeta)$	$(-\zeta \frac{\sqrt{2}}{2}, \zeta \frac{\sqrt{2}}{2})$	$(-\dot{\gamma}, 0)$	$(0, -\zeta)$
$(\mathbf{p}^T \cdot \mathbf{E} \cdot \mathbf{p}) \cdot \mathbf{p}$	0	$(\gamma \frac{\sqrt{2}}{2}, \gamma \frac{\sqrt{2}}{2})$	0	0

Table II.1: Representation of vector fields

where  $\zeta = \dot{\gamma}/2$  and  $\gamma = \dot{\gamma}(\cos \theta \sin \theta)$ . So starting from the configuration presented in figure II.2, contributions of the three terms on the vector fields are drawn in figure II.3. Furthermore, the vector field corresponding to equation (II.11) and the unit vector  $\mathbf{p}$  are shown to be collinear, physically meaning that the fiber experiences

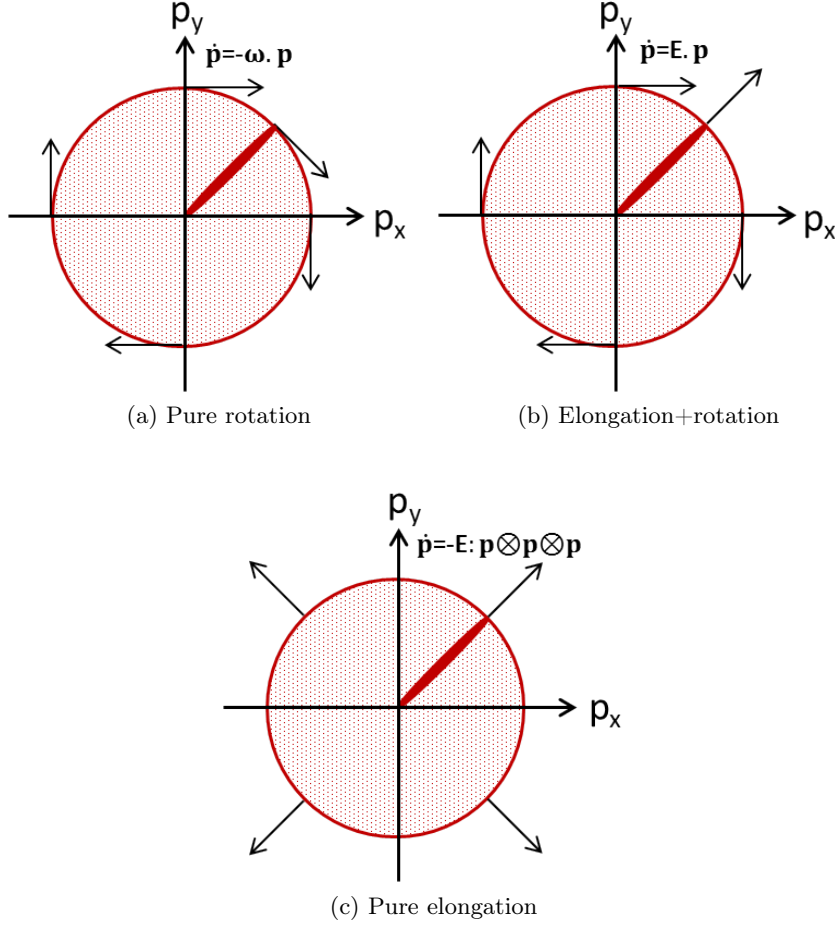


Figure II.3:  $\dot{\mathbf{p}}$ -effect applied to fiber motion: (a) pure rotation (equation (II.9)); (b) elongation+rotation (equation (II.9)); (c) pure elongation (equation (II.10))

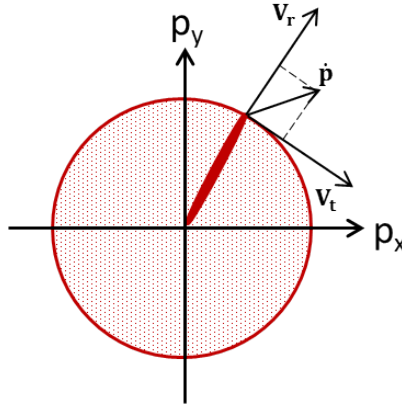
only deformation considering the effect of (II.11). This implies that this term can be negligible if fibers are very stiff. Hence, equation II.5 is recast as follows:

$$\dot{\mathbf{p}} = -\boldsymbol{\omega} \cdot \mathbf{p} + \lambda(\mathbf{E} \cdot \mathbf{p}) \quad (\text{II.12})$$

With the help of equation (II.3), equation (II.12) is written in the index notation where  $\mathbf{E}_{ij}$  and  $\boldsymbol{\omega}_{ij}$  are the components of the strain rate and the vorticity tensors respectively. This results in:

$$\dot{\mathbf{p}} = \begin{bmatrix} \cos \theta (\lambda E_{xx} - \omega_{xx}) + \sin \theta (\lambda E_{xy} - \omega_{xy}) \\ \cos \theta (\lambda E_{yx} - \omega_{yx}) + \sin \theta (\lambda E_{yy} - \omega_{yy}) \end{bmatrix} \quad (\text{II.13})$$

where ( $\omega_{xx} = \omega_{yy} = 0$ ). As aforementioned, the rotational effect of  $\dot{\mathbf{p}}$  is only sought in order to predict the fiber orientation. Thus, the angular velocity  $\dot{\theta}$ , which is the rate of change of angle in time, is determined in order to compute the fiber rotation. As seen in figure II.4,  $\dot{\mathbf{p}}$  can be decomposed into radial and tangential orientation velocities by projecting it on unit vectors  $\mathbf{V}_r$  and  $\mathbf{V}_t$  respectively. So, the projection

Figure II.4: Projection of  $\dot{\mathbf{p}}$ 

of  $\dot{\theta}$  is determined from the following formula:

$$proj_{\mathbf{v}_t} \dot{\mathbf{p}} = \left( \frac{\dot{\mathbf{p}} \cdot \mathbf{v}_t}{\|\mathbf{v}_t\|^2} \right) \cdot \mathbf{v}_t \quad (\text{II.14})$$

where ( $\|\mathbf{v}_t\|^2=1$ ) in case of the unit circle. Equation (II.13) is plugged into expression (II.14),  $\dot{\mathbf{p}}$  is projected and  $\dot{\theta}$  is computed as follows:

$$\dot{\theta} = \cos^2 \theta (\lambda E_{xy} - \omega_{yx}) - \sin^2 \theta (\lambda E_{xy} - \omega_{yx}) + \lambda \cos \theta \sin \theta (E_{yy} - E_{xx}) \quad (\text{II.15})$$

The final form of the reformulated Fokker-Planck equation, which will be later discretized in the  $\theta$ -space, is:

$$\frac{\partial \varphi}{\partial t} + \varphi \nabla_{\theta} \cdot \dot{\theta} + \dot{\theta} (\nabla_{\theta} \varphi) - D_r \nabla_{\theta} \cdot (\nabla_{\theta} \varphi) = 0 \quad (\text{II.16})$$

## II.2.3 Discretization of Fokker-Planck equation

### II.2.3.1 2D-1D configuration

Initially, the configurational domain is represented by a unit circle in the 2D plane, to reduce the complexity and the computational effort. The 2D domain is converted into a 1D domain by projecting the unit circle into a 1D segment whose length is  $2\pi$ , as shown in figure II.5. As seen in table II.2, the numbers of nodes and elements are equal, where the last node is connected to the first node.

### II.2.3.2 Finite element approach

As mentioned previously, there are a large number of studies in the literature concerning the numerical calculation of fiber orientation by solving FPE. On the contrary, few of them were able to get an accurate solution while maintaining its stabilization. The discretization of the geometries plays a key role for an accurate resolution of the FPE. The initial step is the definition of a proper computational domain (see figure II.5), representing as good as possible the characteristics and shape of the simulated problem. Also the choice of a formulation for the FPE also has a big impact on the accuracy of the results obtained.

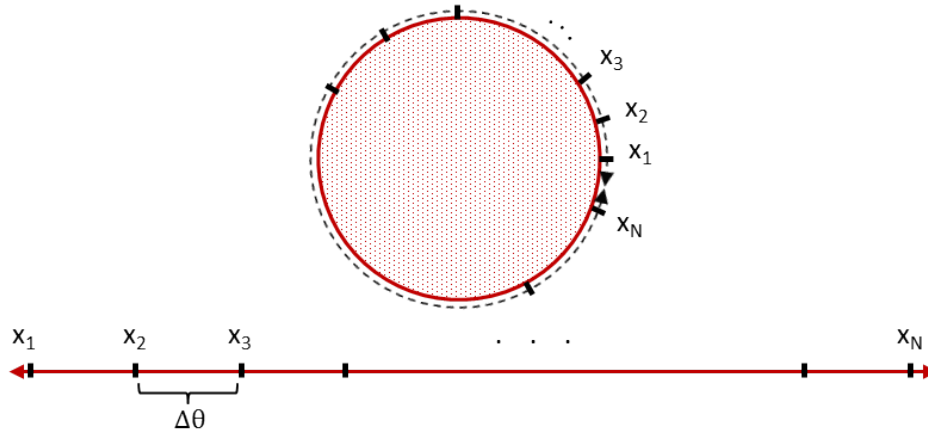


Figure II.5: Projecting 2D to 1D discretization domain

Element	Topology
1	1,2
2	2,3
⋮	⋮
⋮	⋮
⋮	⋮
N	N-1,N
N	N 1

Table II.2: Nodal connectivity matrix

Thus, the **FEM** was used in this work to compute the **FPE** which allows theoretical studies such as uniqueness, existence, consistency, and stability of solution to be performed, due to its strong mathematical developments. Also it assists in taking advantages from techniques like parallelization, a technique that use full capacity of the modern day computers for obtaining quick results, which have also been developed for enhancing in particular the **FEM** discretization technique; the parallelization technique will be advantageous especially in the coupling problem (see chapter III).

So **FEM** considers cells for its resolution, as the equations are written on a whole element. The approach is based on linearization of the solution on each element, using basis functions for interpolation and the solutions at each node of the mesh. The strong formulation which consists of mathematical equations and boundary conditions for a physical system, is not directly solved in **FEM**. Weak formulations, an alternative version of the problem, is constructed from the integral on a strong formulation element multiplied by the arbitrary functions. The entire problem, exercised to all the elements simultaneously, is written in a matrix formulation and solved, as **FEM** meshes can be structured (in this case) or unstructured. It is worth to be mentioned that the accuracy of the results is linked directly to the number of grid points set (see section II.3.2) or to the order of interpolation.

The existence of a time derivative in the **FPE** requires a time discretization. The

FPE problem is solved at different instants of the time, separated by a time step  $\Delta t$ . The choice of  $\Delta t$  at each instant needs to be well thought to capture the time rate of change of fiber orientation required by both the the variational formulation and  $\theta$ -space discretization. Different temporal discretization techniques can be found in the literature [98], where the choice of a method depends on its implementation complexity, its computational time and its accuracy. For example, the algorithm of the forward Euler (explicit) method is considered to be faster than the backward Euler (implicit) but it introduces some limitations to the size of  $\Delta t$ . In section II.3.2, three approaches (Rosenbrock, backward Euler and Crank-Nicolson) were chosen for the convergence study. The resolution of the  $Ax = b$  system for the two latter at time step  $n+1$  is written:

$$\begin{aligned} \mathbf{x}_{n+1} &= (\mathbf{I} - \Delta t \mathbf{A})^{-1} \mathbf{x}_n + (\mathbf{I} - \Delta t \mathbf{A})^{-1} \mathbf{b} && \text{(Backward Euler)} \\ (\mathbf{M}_1 + \mathbf{M}_2) \mathbf{x}_{n+1} &= (\mathbf{M}_1 - \mathbf{M}_2) \mathbf{x}_n + 2\mathbf{b} && \text{(Crank-Nicolson)} \end{aligned} \quad (\text{II.17})$$

where  $\mathbf{M}_1 = (\mathbf{I} - 0.5\Delta t \mathbf{A})^{-1}$  and  $\mathbf{M}_2 = (\mathbf{I} + 0.5\Delta t \mathbf{A})^{-1}$ . It should be noted that the temporal discretization has commonly a big effect on the accuracy of the simulation for solving a non-linear problem in time. So as known, the numerical schemes can provide some convergence issues when the chosen  $\Delta t$  is significantly large. For that the Courant-Friedrichs-Lewy (CFL) condition is required to guarantee the convergence. It is written in our case as follows:

$$\Delta t \sum_i \frac{\dot{\theta}_{x_i}}{h_i} < C_{max} \quad (\text{II.18})$$

where  $h_i$  is the mesh size and  $C_{max}$  is a constant parameter depending on the scheme used. So in order to solve equation (II.16), the streamline upwind Petrov-Galerkin (SUPG) approach [99] instead of the standard Galerkin method, as the latter either produces excessive numerical diffusion, or non-physical oscillations as a first order differential operator also appears for FPE. The SUPG consists in disturbing the test functions for the convection terms by adding a term which is similar to the artificial diffusion:

$$\tilde{\varphi}_{supg} = \tilde{\varphi} + \gamma \dot{\theta} \cdot \nabla \tilde{\varphi} \quad (\text{II.19})$$

where  $\gamma$  is a stabilizing coefficient that controls the artificial diffusion, expressed as:

$$\gamma = \frac{h}{(2|\dot{\theta}| + 2\frac{D_r}{h})} \quad (\text{II.20})$$

To begin with, the various spaces needed to express the weak formulation of FPE's physical problem, are introduced. The spaces used in ICI-tech are recalled:

- $\mathcal{C}^0(\Omega_\theta)$ : the space of functions continuous on  $\Omega_\theta$
- $\mathcal{P}^1(\Omega_\theta)$ : the space of polynomials of degree 1 on  $\Omega_\theta$
- $\mathcal{L}^2(\Omega_\theta)$ : the Lebesgue space of square-integrable functions on  $\Omega_\theta$

$$\mathcal{L}^2(\Omega_\theta) = \left\{ w, \int_{\Omega_\theta} w^2 d\Omega_\theta \right\} \quad (\text{II.21})$$

- $\mathcal{H}^1(\Omega_\theta)$ : the Sobolev space of functions whose order 1 derivatives belong to  $\mathcal{L}^2(\Omega_\theta)$

$$\mathcal{H}^1(\Omega_\theta) = \{w \in \mathcal{L}^2(\Omega_\theta), Dw \in \mathcal{L}^2(\Omega_\theta)\} \quad (\text{II.22})$$

Thus, the spaces for the PDF and its arbitrary function are defined as:

$$\begin{aligned} \mathcal{V} &= \{\varphi \in \mathcal{H}^1(\Omega_\theta)\} \\ \mathcal{W} &= \{\tilde{\varphi} \in \mathcal{H}^1(\Omega_\theta), \dot{\theta} \cdot \nabla \tilde{\varphi} \in \mathcal{H}^1(\Omega_\theta)\} \end{aligned} \quad (\text{II.23})$$

Galerkin's variational (or weak) formulation of the problem is then constructed by multiplying the equation (II.16) by the test function  $\tilde{\varphi}(x) \in \mathcal{W}$  and integrating over the entire domain  $\Omega_\theta$ , results in:

$$\begin{aligned} (\partial_t \varphi, \tilde{\varphi}) + (\gamma \dot{\theta} \cdot \partial_t \varphi, \nabla_\theta \tilde{\varphi}) + (\nabla_\theta \dot{\theta} \cdot \varphi, \tilde{\varphi}) + (\dot{\theta} \cdot \nabla_\theta \varphi, \tilde{\varphi}) \\ + (\dot{\theta} \cdot \nabla_\theta \varphi, \gamma \dot{\theta} \cdot \nabla_\theta \tilde{\varphi}) + D_r(\nabla_\theta \varphi, \nabla_\theta \tilde{\varphi}) = 0 \end{aligned} \quad (\text{II.24})$$

where the notation  $(\cdot, \cdot)$  defines the scalar product in the sense of the  $\mathcal{L}^2(\Omega_\theta)$ :

$$\forall (u, v) \in \mathcal{L}^2(\Omega_\theta), (u, v) = \int_{\Omega_\theta} uv d\Omega_\theta \quad (\text{II.25})$$

To solve this problem, the domain is discretized and broken down into simplices  $\mathcal{K}$  formed by 1D-elements (see figure II.5). Thus, the preceding spaces of continuous functions are approximated on  $\mathcal{K}$  by discrete sub-spaces of finite dimensions constituted by piece-wise continuous linear functions.

$$\begin{aligned} \mathcal{V}_h &= \{\varphi_h | \varphi_h \in \mathcal{C}^0(\Omega_\theta), \forall \mathcal{K}, \varphi_h|_{\mathcal{K}} \in \mathcal{P}^1(\mathcal{K})\} \\ \mathcal{W}_h &= \{\tilde{\varphi}_h | \tilde{\varphi}_h \in \mathcal{V}_h\} \end{aligned} \quad (\text{II.26})$$

The full-discrete Galerkin problem consists of finding  $\varphi_h \in \mathcal{V}_h$  such as  $\tilde{\varphi}_h \in \mathcal{W}_h$  for the following problem:

$$\begin{aligned} (\partial_t \varphi_h, \tilde{\varphi}_h) + (\gamma \dot{\theta} \cdot \partial_t \varphi_h, \nabla_\theta \tilde{\varphi}_h) + (\nabla_\theta \dot{\theta} \cdot \varphi_h, \tilde{\varphi}_h) + (\dot{\theta} \cdot \nabla_\theta \varphi_h, \tilde{\varphi}_h) \\ + (\dot{\theta} \cdot \nabla_\theta \varphi_h, \gamma \dot{\theta} \cdot \nabla_\theta \tilde{\varphi}_h) + D_r(\nabla_\theta \varphi_h, \nabla_\theta \tilde{\varphi}_h) = 0 \end{aligned} \quad (\text{II.27})$$

The approximation of the solution on an element is determined using the values at the nodes. Then the solution is approached by:

$$\begin{aligned} \varphi_h|_{\mathcal{K}} &= \sum_{i=1}^{D_{\mathcal{K}}} \varphi_i(t) N^i(x) \\ \tilde{\varphi}_h|_{\mathcal{K}} &= \sum_{j=1}^{D_{\mathcal{K}}} \tilde{\varphi}_j(t) N^j(x) \end{aligned} \quad (\text{II.28})$$

where  $i$  represents the node,  $N(x)$  the shape function on that node and  $D_{\mathcal{K}}$  the number of nodes in the  $\mathcal{K}$ -simplex. It is also noted that the accuracy of the results is directly linked to the order of interpolation, i.e, the degree of the polynomials  $N(x)$ . Eventually equation (II.28) is introduced into equation (II.27), which generates a

linear system of algebraic equations.

So once the stabilized weak formulation is well written, the equivalent matrix formulation is deduced. In ICI-tech, the method adopted for the resolution of the system is an iterative method of conjugate gradient type resolution. To do this, the library Portable, Extensible Toolkit for Scientific computation (**PETSc**) is used. **PETSc** [100] is a library of algorithms for solving linear and non-linear systems, both sequentially and in parallel, using iterative numerical methods. In the context of solving partial differential equations such as ours, **PETSc** offers interesting methods including preconditioners. Local arrays are created in ICI-tech as local solvers. Subsequently, **PETSc** supports them for preconditioning. A preconditioner, using an incomplete factorization method called the decomposition  $ILU(k)$  of a matrix  $\mathbf{A}$  in the form  $\mathbf{A}=\mathbf{LU}$ , is used. The parameter  $k$  makes it possible to control the filling ratio of the hollow matrix (sparse matrix), thus making it possible to solve even problems of a poorly conditioned nature. It should be noted that the resolution time with such an iterative process varies according to the number of iterations performed at the end of the resolution. C++11 is used as a programming language to write the **FEM** code of solving the probability distribution function.

#### II.2.4 Short summary

- ✓ The Fokker-Planck equation depends on kinematic parameters.
- ✓ For simplicity, 1D domain is discretized representing a 2D configuration of fiber orientation.
- ✓ The angular velocity of fiber correlated with the generalized shear rate in the field of the flow is determined.
- ✓ The Fokker-Planck equation is solved at each spatial grid independently in a finite element framework.

## II.3 Numerical results

### II.3.1 Validation tests

Within this section, a validation test was carried out using a simple shear flow case characterized by a constant generalized shear rate ( $\dot{\gamma} = 1s^{-1}$ ). The primary objectives of this validation are to confirm the accuracy of the computed angular velocity obtained from the equation (II.15) and to verify the reliability of the numerical solution of the Fokker-Planck equation. The validation process involves checking the normalization condition and examining the impact of the shape factor  $\lambda$  and the interaction coefficient  $C_I$  parameters on the numerical results.

#### II.3.1.1 Normalization condition

The 2D orientation distribution function is introduced, as described above, to represent the probability of finding a fiber between the angles  $(\theta$  and  $\theta + d\theta)$ , given

as:

$$P = \int_{\theta}^{\theta+d\theta} \varphi(\theta)d\theta \quad (\text{II.29})$$

Moreover, the integral over all possible orientations of the distribution function must

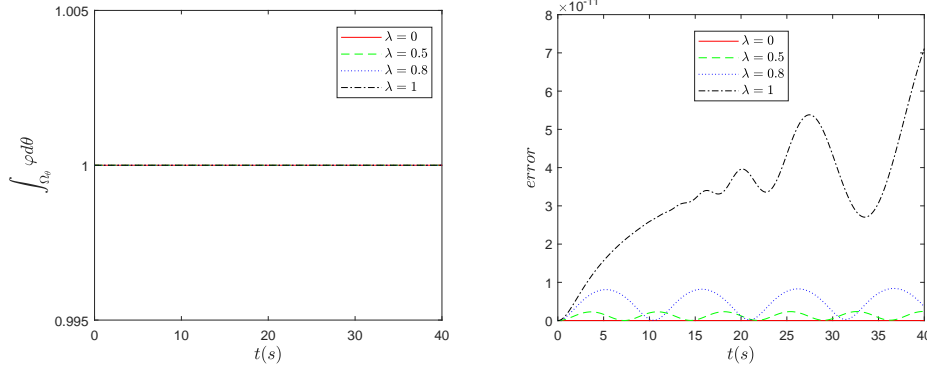


Figure II.6: Time evolution and error analysis of  $\varphi$  integral for different  $\lambda$ : ensuring normalization

be equal to unity satisfying the normalization condition induced by the definition of a probability:

$$P = \int_0^{2\pi} \varphi(\theta)d\theta = 1 \quad (\text{II.30})$$

The latter expression has been checked, as illustrated in figure II.6. When solving a pure convection Fokker-Planck equation ( $D_r = 0$ ) across the entire domain  $\Omega_\theta$ , the integral of the probability distribution function exhibits remarkable constancy, remaining close to 1 throughout varying time  $t$  for different shape factors  $\lambda$ . Upon analyzing figure II.6, it is evident that the error is extremely small, fluctuating within the order of  $10^{-11}$  for varying shape factors  $\lambda$ . A distinct pattern emerges in the error plot when  $\lambda = 1$ , exhibiting significant fluctuations in contrast to other shape factors. This observed behavior results from the physical phenomenon of fiber concentration or a high gradient in the resolution of the Fokker-Planck equation. Under such circumstances, the fibers tend to align at a specific moment, leading to a concentration of the solution at a particular orientation angle. Nevertheless, despite these fluctuations, the error magnitude remains remarkably small and within the order of  $10^{-11}$  for all shape factor values. This observation serves to emphasize the effectiveness of the Streamline-Upwind/Petrov-Galerkin (SUPG) finite element method in stabilizing critical convection-dominated cases, ensuring the preservation of the normalization condition.

### II.3.1.2 Influence of $\lambda$ -parameter

Figure II.8 shows the variation of the angular velocity for different values of  $\lambda$  parameter. When  $\lambda=0$ , the fiber is represented by a circular shape (figure II.7), and it rotates with an uniform circular motion as the angular velocity remains constant at any angle  $\theta$ . The fibers will keep subsequently rotating over themselves with a

steady velocity if fibers do not intersect. As for  $\lambda=1$ , the case where the fibers are assumed quasi-infinite, the angular velocity is zero at 0 and  $\pi$ . Therefore, the fibers

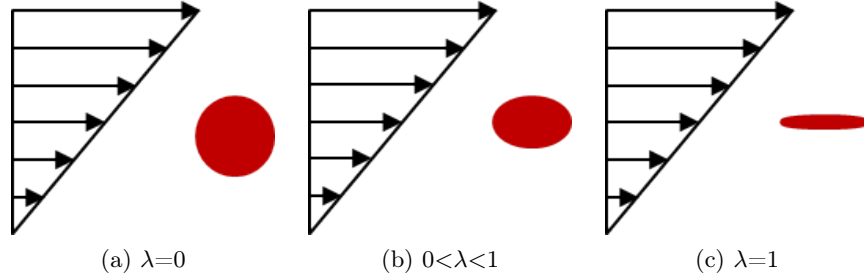


Figure II.7:  $\lambda$ -effect on fibers shape

that are oriented in the direction of the velocity field will not rotate. This is logical as the velocity gradient along the y-axis does not affect the rotation of fibers as their thickness tends to be zero. Therefore, we conclude that fibers initially oriented at a small angle with respect to the flow, will take longer to rotate in the case of shear flow if  $\lambda$  value is close to 1. In other words, it could be verified that the angular velocity values will be the highest for  $\lambda=1$  when  $\theta \in ]\pi/4, 3\pi/4[ \cup ]5\pi/4, 7\pi/4[$ . It is also noticeable that the maximum angular velocity is always at  $\pi/2$  and  $3\pi/2$  where the torque exerted by the flow on a fiber is at its maximum and the latter state is perpendicular to the velocity streamlines.

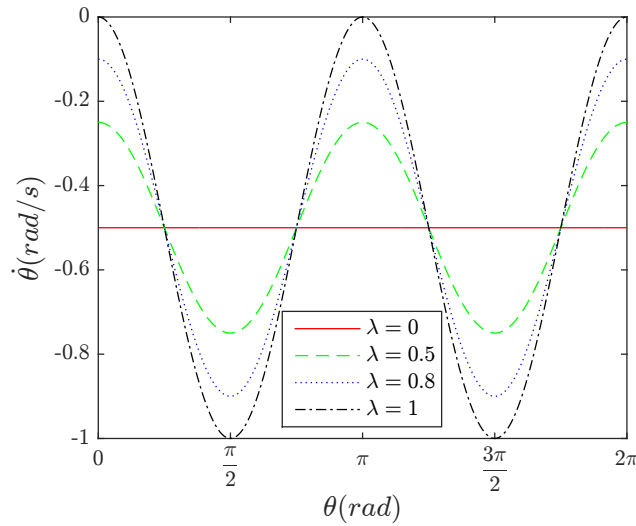


Figure II.8: Variation of  $\dot{\theta}$  versus  $\theta$

The Fokker-Planck equation has been computed in order to determine the probability distribution function that evolves over time *to* understand the change of fiber orientation with respect to time. The Fokker-Planck equation is an advection-diffusion equation, where the advection term represents the deterministic dynamics of the fibers, and the diffusion term represents the stochastic effects due to the interaction between the fibers. When examining the Fokker-Planck equation, the

initialization of a probability distribution function at  $t = 0$  corresponds to a scenario of fiber alignment, as depicted in figure II.9. This range accounts for the periodicity in the domain at angle 0, where  $2\pi - \Delta\theta$  returns to 0, signifying that the angle  $2\pi$  is equivalent to the angle 0. Thus, the complete representation of the total probability for this alignment scenario is defined by the integral equation:

$$P_{total\_alignment} = P(\theta \leq 0 + c\Delta\theta) + P(\theta \geq 2\pi - \Delta\theta(1 + c)) + P(\pi + c\Delta\theta \geq \theta \leq \pi + c\Delta\theta) \quad (\text{II.31})$$

Then, the Fokker-Planck equation is resolved, and from its solution of the proba-

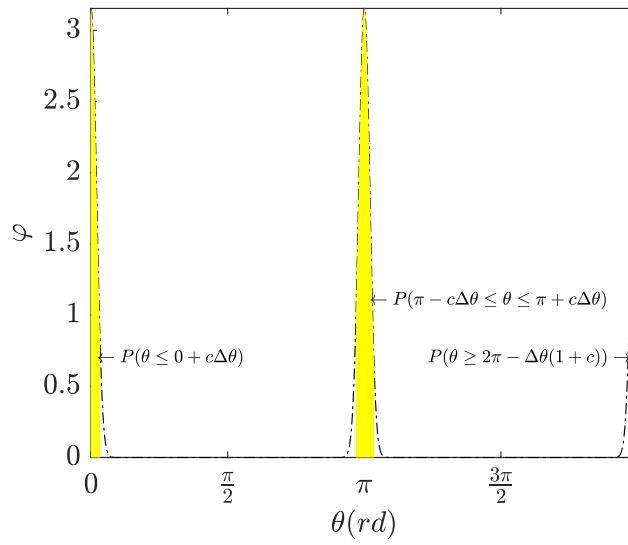


Figure II.9: Initialization of probability distribution function at  $t=0$  with  $c=32$  and  $\Delta\theta=\frac{2\pi}{2048}$

bility distribution function, the probability of finding fibers oriented around angles 0 and  $\pi$  is computed at each time step. The range is deliberately kept small with ( $c=32$  and  $\Delta\theta=\frac{2\pi}{2048}$ ) in order to effectively capture the variation of the probability of finding aligned fibers over time. The shape factor of fibers plays a significant role in the evolution of the probability distribution function over time as it is shown in figure II.10. Starting with an initial distribution function that depicts a unidirectional fiber orientation case, where most of the fibers (about 90%) are oriented with angles spanning both 0 and  $\pi$ , the probability distribution function decreases proportional to different values of shape factor of fibers over time. Physically, the fibers tend to orient faster around 0 and  $\pi$  as the shape factor gets smaller ( $\lambda \rightarrow 0$ ) representing a more circular shape of fibers, compared to fibers with a shape factor approaching 1, which is consistent with previous results (see figure II.8). This is due to the fact that with shape factors ( $\lambda \rightarrow 1$ ) represent more elongated fibers, they have a greater tendency to remain aligned and oriented in the direction of the flow, in this case in both 0-direction and  $\pi$ -direction, for a longer period of time. Conversely, fibers with small shape factors tend to orient slower than fibers with quasi-infinite shape factors when far from angles 0 and  $\pi$ , which leads to a slower

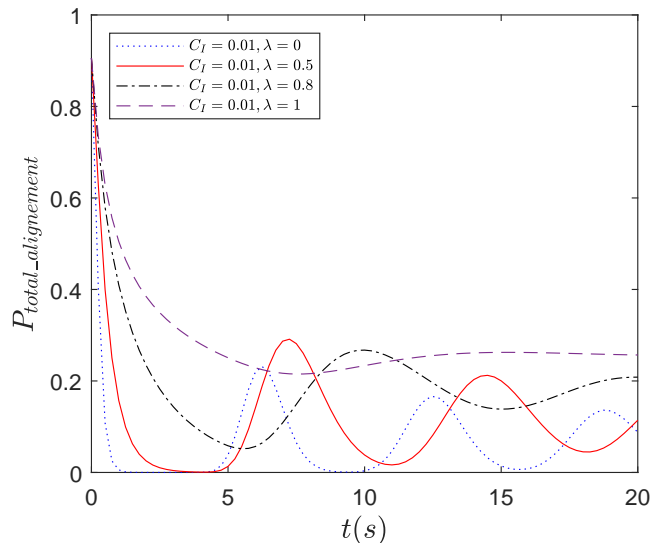


Figure II.10: Time evolution of the total probability of finding fibers oriented around angles 0 and  $\pi$  for different  $\lambda$

alignment with the initial angles 0 and  $\pi$ . This interpretation holds true in the absence of the diffusion term. However, when the diffusion term is included, depicted in figure II.10, fibers with shape factors closer to zero undergo subsequent rotation until the probability distribution function becomes more uniform, indicating a more isotropic orientation. In contrast, fibers with a shape factor ( $\lambda=1$ ) tend to remain aligned with angles 0 and  $\pi$ , serving as a counterforce to the diffusion term, even though a decrease of the peak of the probability distribution function near angles 0 and  $\pi$  occurred, but still resulting in a higher probability of finding fibers oriented in both angles 0 and  $\pi$  compared to the case of shape factors less than 1. These results demonstrate the important role of the shape factor in the evolution of fiber orientation over time.

### II.3.1.3 Influence of $C_I$ -parameter

An analysis is also done on the effect of the diffusion term on the fiber orientation to understand how it affects the probability distribution function. Thus, figure II.11 represents the evolution of the probability distribution centered around 0 and  $\pi$  with some degree of spread  $c\Delta\theta$  with ( $c=32$  and  $\Delta\theta=\frac{2\pi}{2048}$ ) by solving the full Fokker-Planck equation (advection-diffusion equation), with different interaction coefficients  $C_I$  to investigate their effects on the solution of the Fokker-Planck equation. The initial probability distribution function represents a scenario where a large majority of fibers (approximately 90%) are oriented around angles of 0 and  $\pi$ . The diffusion term arises from the Brownian motion of fibers and causes the distribution to spread out over time, resulting in a decrease in the peak of the distribution. This behavior can be observed by comparing the solutions of the Fokker-Planck equation with and without the diffusion term. Figure II.11 demonstrates the effect of the interaction coefficient on the evolution of the probability of finding fibers oriented around angles 0 and  $\pi$ . When the  $C_I$  is set to zero, the probability exhibits a periodic behavior

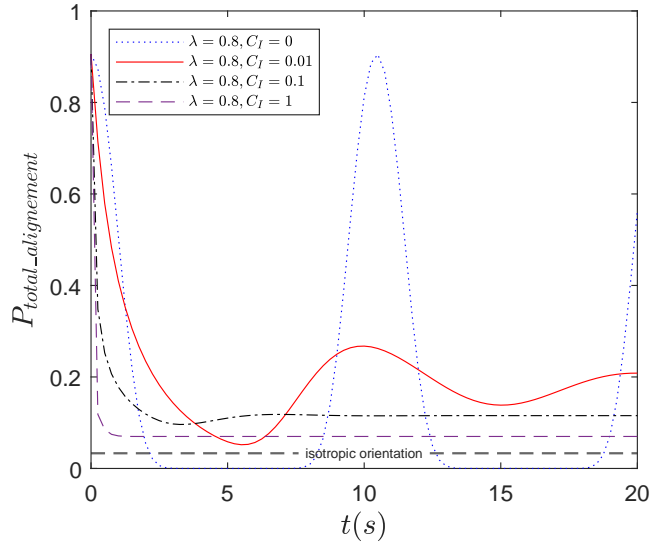


Figure II.11: Time evolution of the total probability of finding fibers oriented around angles 0 and  $\pi$  for different  $C_I$

where it returns to its initial value after a fixed period of time. However, when the  $C_I$  is increased, the probability evolves in a way that results in a decrease in the peak value before flattening out as it is illustrated in figure II.12. This is because

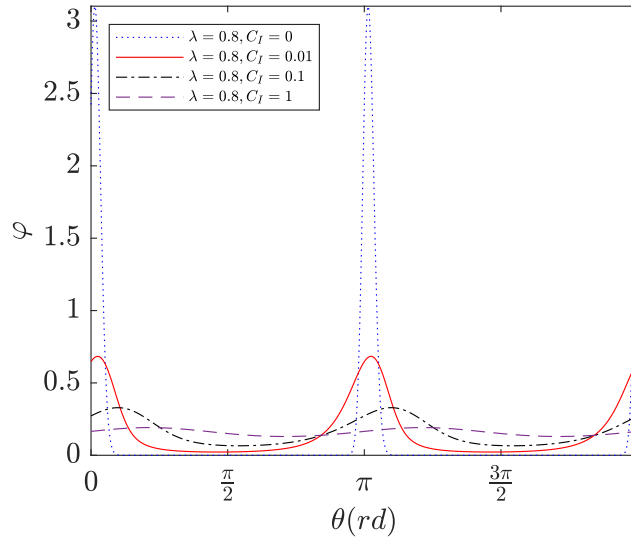


Figure II.12: Variation of the probability distribution function  $\varphi$  at time  $t=10s$  for different  $C_I$

diffusion acts to smooth out fluctuations in the fiber orientation and promotes a more uniform distribution of orientations indicates an isotropic distribution. As a result, the probability distribution becomes less peaked and more scattered, indicating that the fibers will be oriented in a wider range of angles meaning that there is no preferred orientation and the orientation of the fibers is considered to be random.

This effect is particularly evident in the long-term behavior of the system, where the probability distribution tends to approach a steady state that is less sensitive to the initial conditions. Thus, knowing that the diffusion term in the Fokker-Planck equation captures the stochasticity of the system and describes how the probability density evolves over time due to random fluctuations, the diffusion term plays a role in the stabilization phenomenon, by allowing the system to explore different orientations of the fiber and eventually converge to a stationary distribution, as the diffusion term represents the stochastic effects of the fiber-fiber interactions.

### II.3.2 Numerical convergence analysis and computational efficiency

In this section, we present numerical results regarding the resolution of the Fokker-Planck equation within the context of a Poiseuille flow scenario. This scenario is characterized by a position-dependent generalized shear rate, denoted as  $\dot{\gamma}$ , which varies spatially along the  $y$ -axis. Its specific form is expressed as:

$$\dot{\gamma} = \frac{y}{H^2} V_{max} \quad (\text{II.32})$$

where  $H$  is the distance between the two horizontal parallel plates,  $V_{max}$  is the maximum axial velocity. Throughout this section, the parameter values remain consistent, with  $H$  set to 1m,  $V_{max}$  set to 10m/s, while the shape factor  $\lambda$  is assigned a value of 0.98, and the interaction coefficient  $C_I$  is held at 0. The scope of these numerical results encompasses a thorough convergence analysis, focusing on both mesh refinement and time discretization schemes. Furthermore, a comprehensive comparison is drawn to discern the distinct impact of these schemes on computational efficiency.

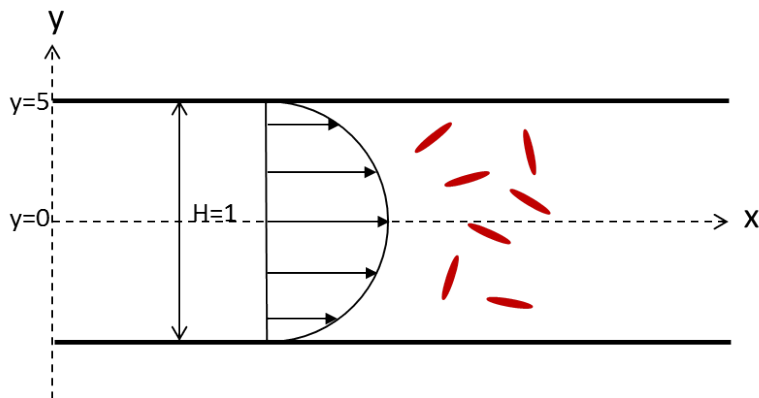


Figure II.13: Fibers orientation for the Poiseuille flow case

#### II.3.2.1 Convergence study: mesh and time discretization schemes

Knowing that function  $\varphi$  must satisfy some conditions such as periodicity, normalization and continuity and by integrating dyadic products with the PDF function, the even order orientation tensors ( $a_2, a_4, \dots, a_{2N}$ ) can be calculated. An orientation

tensor, commonly noted  $\mathbf{a}_2$ , has been proposed to express the spatial mean of the double tensor product of  $\mathbf{p}$ , by [50]:

$$\mathbf{a}_2 = \int_{\Omega_\theta} \varphi(\theta) \mathbf{p} \otimes \mathbf{p} d\mathbf{p} \quad (\text{II.33})$$

Thus, by computing  $\varphi(\theta)$  using equation (II.16), the planar orientation of the second order tensor is determined from equation (II.33), which describes the fiber orientation state in the direction of the main flow without a loss of accuracy due to the use of a closure approximation. So the components of the  $\mathbf{a}_2$  tensor can be written:

$$\begin{aligned} a_{xx} &= \sum_{i=1}^N \varphi_i \cos^2(\theta_i) \\ a_{yy} &= \sum_{i=1}^N \varphi_i \sin^2(\theta_i) \end{aligned} \quad (\text{II.34})$$

where the alignment of the fibers is expressed by  $a_{xx}$  and  $a_{yy}$  with respect to the main directions.

In pursuit of a comprehensive numerical convergence assessment, depicted in figure II.14, the time evolution of the orientation tensor  $\mathbf{a}_2$  is computed at  $y=0.5$ , corresponding to a generalized shear rate  $\dot{\gamma}=5s^{-1}$  based on equation (II.32). The initial condition is set to represent an isotropic state, with  $a_{xx}=a_{yy}=0.5$ , and the period of its evolution is  $T=4\pi s$ . To validate the results, a comparative analysis is performed, involving a comparison between the obtained numerical results and the analytical solution derived in [101].

A comparative study, depicted in figure II.14a, is initially conducted using various temporal discretization schemes, seeking to assess the sensitivity of the obtained numerical solution to various time discretization approaches. This study reveals that the employment of the backward Euler scheme "*beuler*", recognized as a first-order technique, results in significant loss of information and introduces inaccuracies that amplify over time, compared to the analytical solution. In contrast, the Crank-Nicolson scheme "*cn*" and the Rosenbrock-W scheme "*rosu*" exhibit improved performance. The observed discrepancies can be attributed to the inherent limitations of the backward Euler method in accurately capturing swift variations or oscillatory patterns. The Crank-Nicolson and Rosenbrock-W methods, distinguished by their respective local truncation errors of second and third order [102, 103], exhibit similar solution trends, apparent from the overlapping curves. Despite this, they yield better solutions with less damping, with their curves approaching the analytical solution and displaying smaller errors.

Figure II.14b examines the influence of altering  $\Delta t$  on the time evolution solution of  $a_{xx}$ . Employing the Crank-Nicolson time discretization scheme, the time step order is adjusted across the range of ( $2 \times 10^{-2}$  to  $2 \times 10^{-4} s$ ). Interestingly, decreasing the time step does not contribute to the convergence or enhancement of solution accuracy. This observation may be attributed to the circumstance that in situations where dominant effects are associated to convection or rapid changes, reducing the time step might not result in significant improvements, particularly if the underlying numerical scheme already provides adequate accuracy.

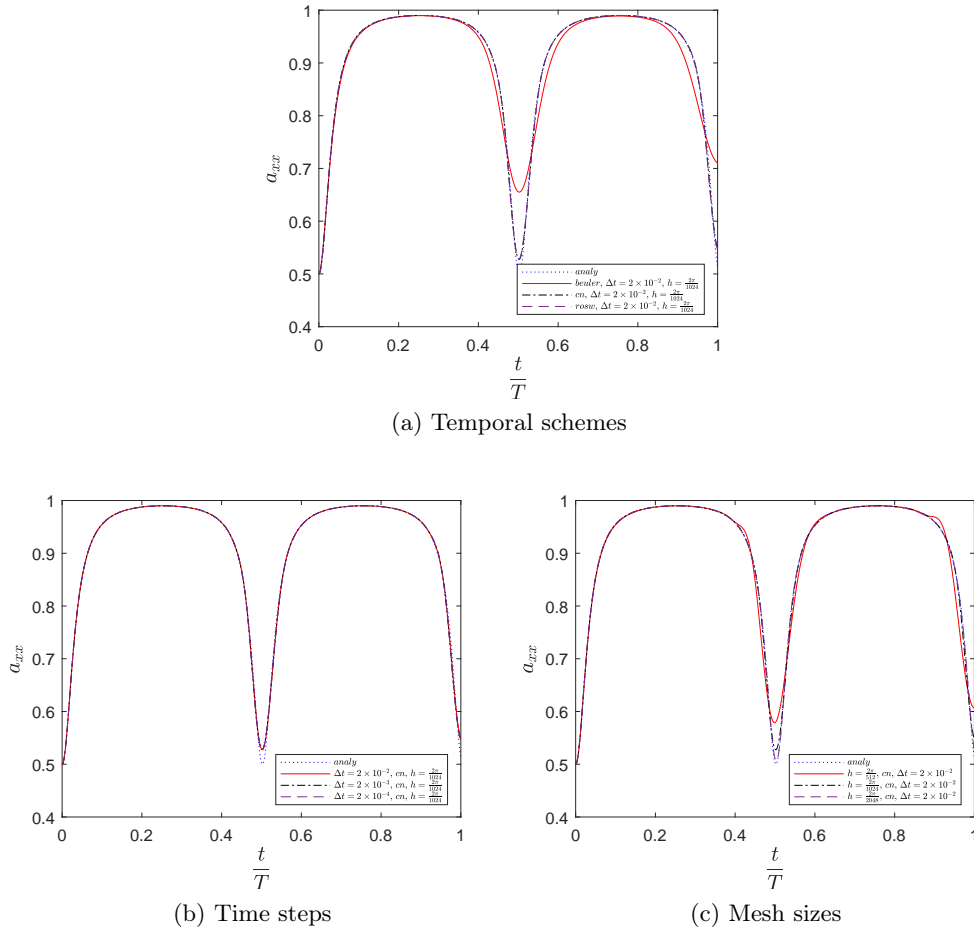


Figure II.14: Numerical convergence analysis: second Order orientation evolution with varied temporal schemes, time steps, and mesh sizes

Lastly, an investigation into mesh convergence is conducted, as illustrated in Figure II.14c, involving a range of mesh sizes from  $(\frac{2\pi}{512}$  to  $\frac{2\pi}{2048})$ . The objective is to address damping effects in the results. The plot demonstrates that as mesh refinement is undertaken, the numerical results progressively align with the analytical solution. Notably, for the case of a mesh size of  $h = \frac{2\pi}{2048}$ , the curves of the analytical and numerical results coincide, signifying the importance of mesh refinement to mitigate damping. This necessity arises due to the solution of the Fokker-Planck equation, which encompasses a probability distribution function with sharp gradients occurring at different time points around angles  $\theta = 0$  and  $\theta = \pi$ . Thus, neglecting mesh refinement can lead to compromised solution accuracy. So to demonstrate the origins of the damping phenomenon, figure II.15 captures the evolution of  $\varphi$  at half the period ( $t = 2\pi s$ ), corresponding to the state of  $a_{xx}$  at its minimum value ( $a_{xx} = 0.5$ ), representing randomly oriented fibers. Notably, as the mesh size is reduced, the oscillations in the probability distribution function become more stabilized, approaching a constant value of  $1/(2\pi)$  with refined meshes. This trend aligns with the isotropic orientation distribution state, thereby converging toward the analytical solution.

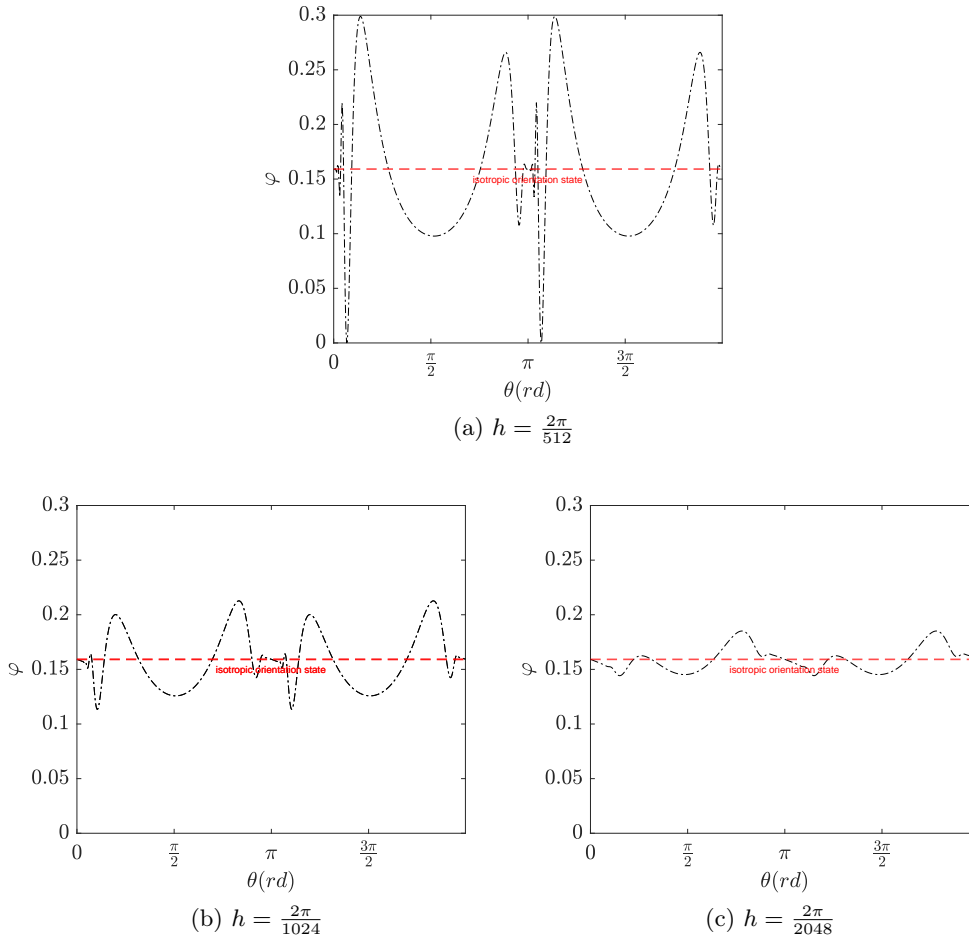


Figure II.15: Evolution of  $\varphi$  at isotropic orientation state ( $\frac{t}{T} = 0.5$ ) with varying mesh refinement

### II.3.2.2 Computational efficiency: impact of refinement and higher order temporal discretization schemes

A comprehensive computational cost analysis has been conducted, covering a comparison of various mesh sizes  $h$  and distinct time discretization schemes. Notably, the examination of different time steps has been excluded, as evidenced by the findings in figure II.14b, where it was established that altering the time step does not significantly affect the accuracy of Fokker-Planck equation resolution. As a result, the focus of the time computation comparative study will remain on a fixed time step of  $\Delta t = 2 \times 10^{-2}$ , ensuring a thorough exploration of the impact of mesh refinement and time discretization schemes on computational efficiency.

It is worth noting that the computation time for solving the Fokker-Planck equation on one spatial node (fluid domain) is relatively small. To better understand the effects of mesh refinement and time schemes, the comparative study will be conducted relative to the last case, where the time discretization scheme is considered Rosenbrock-W and the mesh size  $h$  is  $\frac{2\pi}{2048}$ , representing the largest computational time ( $t_{computed} = 0.915$  s). This approach provides a comprehensive overview of the computational time impact, serving as a baseline for the work related to coupling

problems (see chapter III), where the Fokker-Planck equation will be computed for all spatial nodes in the fluid domain.

<b>h</b> \ <b>Scheme</b>	<i>beuler</i>	<i>cn</i>	<i>rosw</i>
512	0.16	0.172	0.365
1024	0.24	0.265	0.524
2048	0.423	0.469	1

Table II.3: Computational cost analysis: comparison of mesh sizes and time discretization schemes for Fokker-Planck equation resolution

Table II.3 presents first the relative computational time variations resulting from transitioning from the backward Euler (*beuler*) scheme to the Crank-Nicolson (*cn*) scheme and the Rosenbrock-W (*rosw*) scheme. Interestingly, the shift to the Crank-Nicolson scheme leads to a slight increase in computational time compared to the Rosenbrock-W scheme, observed across all three distinct mesh sizes. Conversely, with the refinement of the mesh via a decrease in  $h$ , a substantial increase in relative computational time is evident, scaling by a factor of approximately 1.7 for all cases of temporal schemes. The combined insights from figure II.14 and the data within table II.3 indicate that opting for higher accuracy in solution while maintaining computational efficiency is best achieved by employing a mesh size of  $h = \frac{2\pi}{2048}$  coupled with the Crank-Nicolson time discretization scheme. Notably, the Crank-Nicolson scheme demonstrates enhanced accuracy results with nearly equivalent computational time compared to the backward Euler scheme, and it significantly outperforms the Rosenbrock-W scheme, by consuming almost half the computational time for providing the same accuracy. Furthermore, for  $h = \frac{2\pi}{2048}$ , despite its relatively higher computation time, it offers notably better results compared to the other two mesh sizes. It is noteworthy that the computational time discrepancy can be managed through the implementation of mesh adaptive methods, which strategically refine the mesh in specific regions of interest, thereby effectively mitigating the increased computational time associated with finer mesh sizes.

### II.3.3 Fiber orientation-flow

In this section, the domain considered to perform the flow simulations is a square of dimension 1. Figure III.4 illustrates the solution of the velocity as a no-slip condition is applied at the upper and lower walls, and a pressure ( $P_0 = 10 Pa$ ) is imposed at the inlet while it is kept zero at outlet to get a pressure-driven flow. The fluid dynamic viscosity  $\eta$  is set to 0.25 Pa.s. The advection term ( $v_f \cdot \nabla_{\mathbf{x}} \varphi$ ), where  $v_f$  is the fluid velocity and  $\nabla_{\mathbf{x}}$  is the spatial derivative, is not added to the Fokker-Planck equation (FPE). This implies that fibers are considered as fixed particles in the spatial domain, rotating on their own axis without being convected by the flow. Here, the effect of generalized shear rate  $\dot{\gamma}$  on the fiber orientation is studied. Thus, Stokes equation is solved first to compute  $\dot{\gamma}$  over the domain for a fine mesh (3250 triangular elements) and then the transient FPE is solved at each spatial node on its discretized domain of 1024 nodes independently. Knowing that

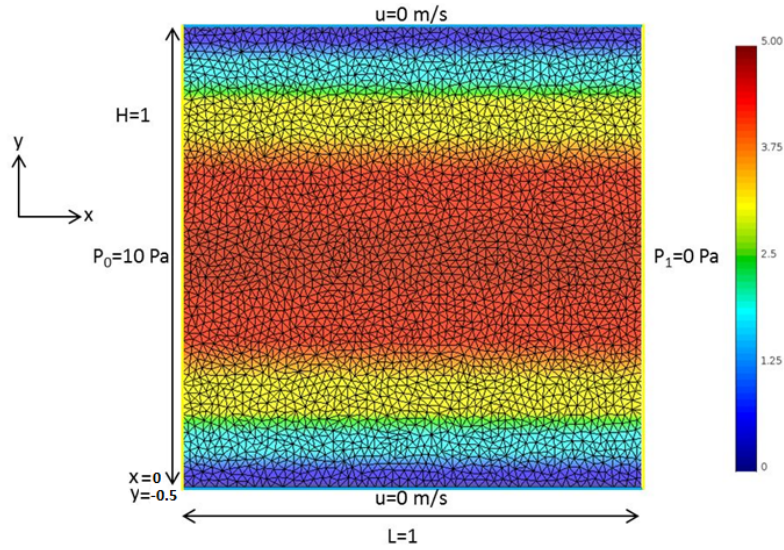
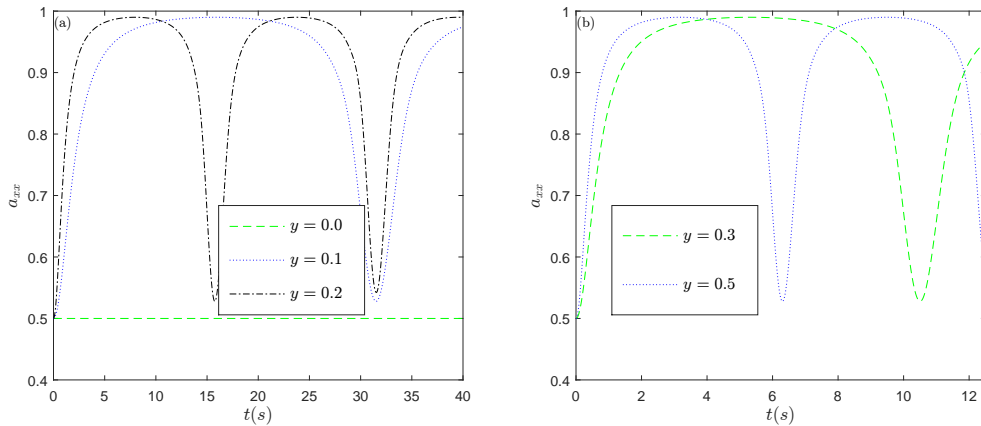


Figure II.16: Solution of the velocity on the square domain

Figure II.17: generalized shear rate effect on the variation of  $a_{11}$  with respect to time : (a) fiber orientation near the center region ; (b) fiber orientation near the boundary region

the rate of deformation of the fluid is not homogeneous in the flow, therefore the orientation velocity of the fibers is different from one point to another. Starting with an isotropic orientation ( $a_{xx} = a_{yy} = 0.5$ ), figure II.17 shows a fairly slow reorientation of the fibers at the center of the domain and much faster for the fibers close to the bounding walls. Indeed, fibers located in the center have a maximum velocity, as the generalized shear rate experienced in this zone is low, which explains the slow orientation of the fibers. Fibers located close to the upper and lower edges have relatively low velocity and the corresponding generalized shear rate is maximum, consequently the fibers orient more quickly. The fibers are therefore oriented according to the flow field and the generalized shear rate they undergo. Note that the entry conditions, governed in particular by the initial orientation of the fibers at time  $t=0$ , affect the orientation of the fibers in the core.

### II.3.4 Short summary

- ✓ The kinematics problem is governed by the classical fluid dynamics equations, while the microscopic problem is governed by a Fokker-Planck equation.
- ✓ Shape factor plays an important role in limiting the rotation of fibers, as for slender fibers ( $\lambda=1$ ), they tend to align with the flow direction after a relatively short period of time.
- ✓ A mesh refinement is needed for accuracy in order to well capture the solution with a high gradient.
- ✓ The resolution of the microscopic problem makes it possible to calculate directly the orientation tensor of order 4 which is taken up in the kinematic calculation (see in chapter III).

## II.4 Discussion

The anticipation of fiber orientation in industrial contexts, as previously elucidated, relies upon a constructed model employing a tensorial framework. This entails the resolution of the Folgar-Tucker equation to calculate the temporal evolution of  $\mathbf{a}_2$  [104, 105, 106, 107, 108]. However, the computational advantage of directly addressing the Fokker-Planck equation lies in its capacity to compute the higher-order orientation tensor  $\mathbf{a}_4$  without necessitating recourse to closure approximations. Thus,  $\mathbf{a}_4$  is considered to be a better choice than a second-order tensor  $\mathbf{a}_2$ , as it provides more detailed information on the distribution of fiber orientations within the material, which can be used to well understand the changes in fiber orientation over time and its influence on the flow during the injection process. As a result, using the fourth-order tensor is likely to be more effective in order to resolve the complex coupling problem in the upcoming work (see section III.2).

In a manner analogous to the computation of the second order orientation tensor  $\mathbf{a}_2$  in (section II.3.2.1), we proceeded to calculate the fourth order orientation tensor  $\mathbf{a}_4$ , defined as follows:

$$\mathbf{a}_4 = \int_{\Omega_\theta} \varphi(\mathbf{p}, t) \mathbf{p} \otimes \mathbf{p} \otimes \mathbf{p} \otimes \mathbf{p} d\mathbf{p} \quad (\text{II.35})$$

To validate the numerical results, an analytical solution from [101] was employed for comparison. The comparative analysis was carried out under the conditions of a simple shear flow with a generalized shear rate  $\dot{\gamma} = 1 \text{ s}^{-1}$ , an interaction coefficient  $C_I = 0$ , and two different shape factor values:  $\lambda = 1$  and  $\lambda = 0.98$ . The initial orientation was set to an isotropic state. For the numerical Fokker-Planck resolution, following the insights obtained in (section II.3.2.2), the Crank-Nicolson scheme was used for time discretization, with a time step  $\Delta t$  of  $2 \times 10^{-2}$  and a mesh size  $h$  of  $\frac{2\pi}{1024}$ .

The results, depicted in figure II.18 for the  $\lambda = 1$  case demonstrate a high level of

accuracy, evidenced by the nearly seamless alignment between the analytical and numerical solutions for all plotted components of  $\mathbf{a}_4$ . As for the results presented in figure II.19, they highlight the behavior of the numerical solutions for the  $\lambda = 0.98$  case. A notably small error is observed when comparing it with the analytical solution, particularly within the periodicity zone of the time evolution of  $\mathbf{a}_4$ , where each period of evolution is completed. As previously discussed in section II.3.2.1, this error is attributed to the damping phenomenon, which can be mitigated through mesh refinement. Contrary, this damping phenomenon is absent in the  $\lambda = 1$  case, where the time evolution of  $\mathbf{a}_4$  exhibits non-periodic behavior, and the fibers tend to align over time.

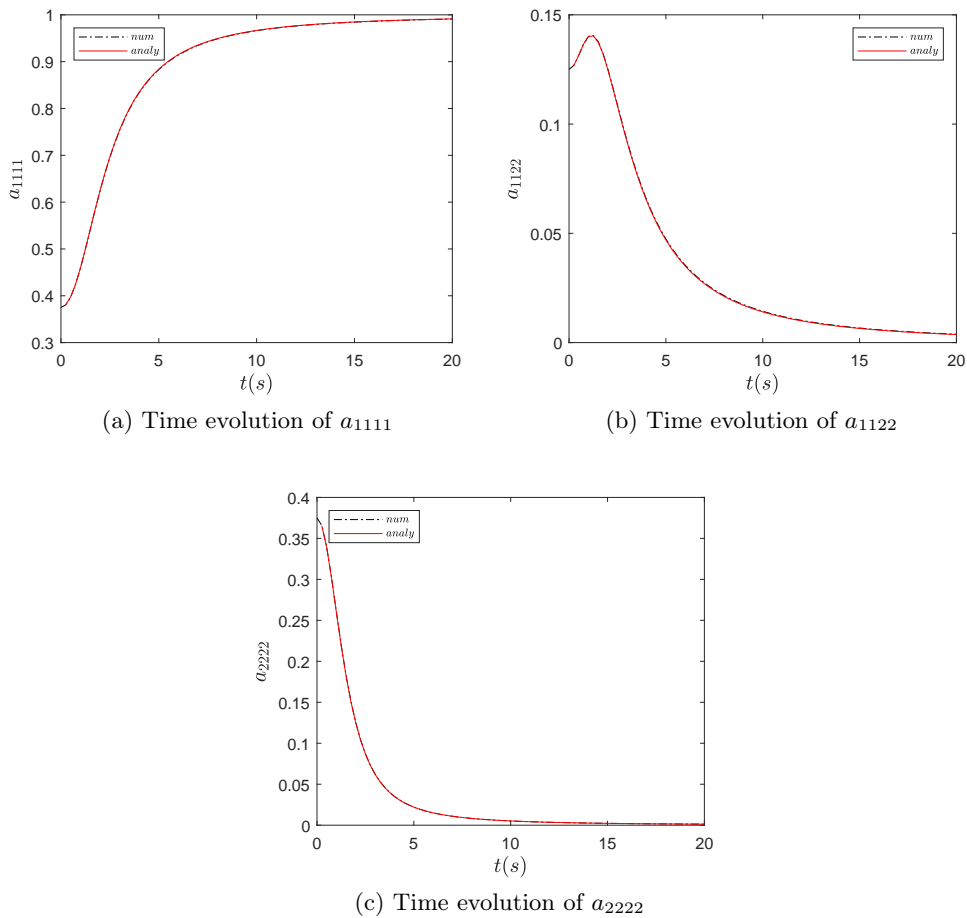


Figure II.18: Analytical vs numerical: a comparative study of fourth order fiber Orientation tensor solutions for  $\lambda=1$  and  $C_I=0$

Thus, in both cases of  $\lambda=0.98$  and  $\lambda=1$ , the computed results exhibited significantly improved accuracy with minimal error when compared to the results obtained from solving the Folgar and Tucker equation using closure approximations as demonstrated in [101]. This validates the effectiveness of the direct solver approach using the finite element method FEM-SUPG to solve the Fokker-Planck equation for determining the evolution of the fiber fourth-order orientation tensor. The results also

provide confidence in the ability of the approach to accurately capture the complex coupling between fiber orientation and flow in the injection process.

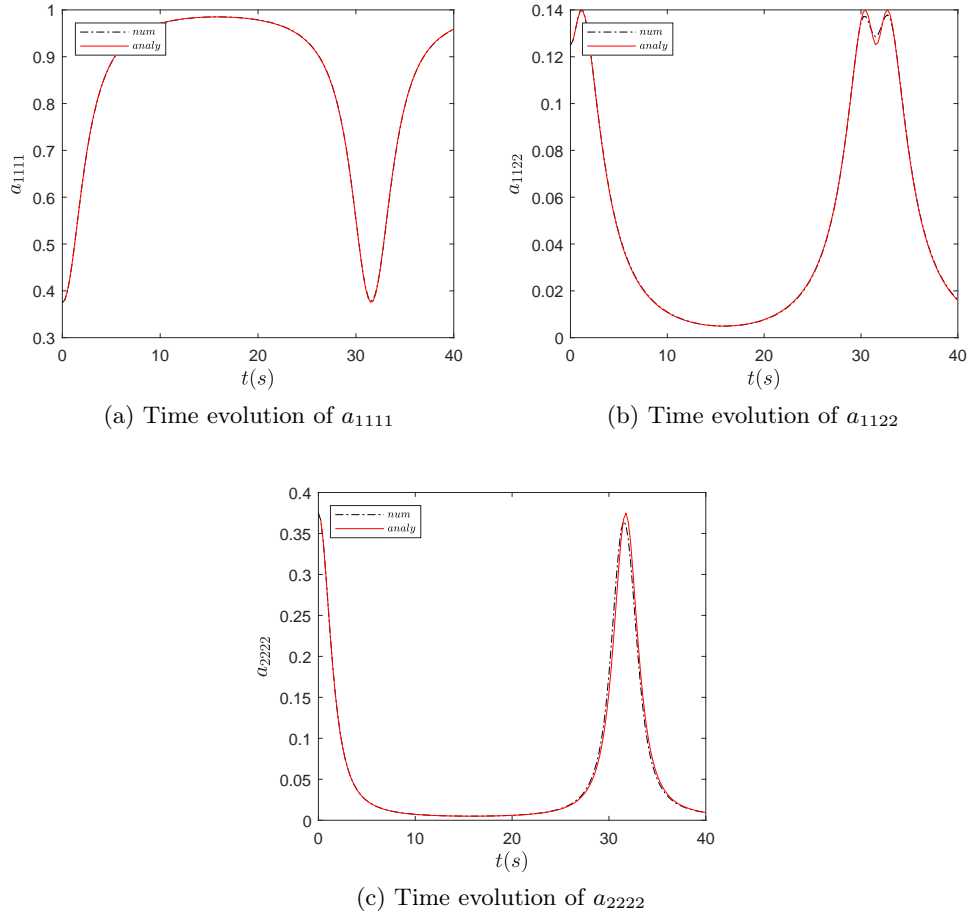


Figure II.19: Analytical vs numerical: a comparative study of fourth order fiber Orientation tensor solutions for  $\lambda=0.98$  and  $C_I=0$

## II.5 Conclusion

A 2D numerical model has been constructed, embedded within a finite element framework employing the SUPG method as an alternative to the standard Galerkin method. This model is tailored to explore the intricate motion of fibers, with the potential for future integration into the broader context of flow-fiber coupling, particularly within the scope of molten thermoplastics during the injection phase within mold cavities. The devised Direct Numerical Simulation (DNS) approach is specifically aimed at resolving the Fokker-Planck equation, providing a deeper insight into fiber orientation at the mesoscopic scale. Unlike conventional methods reliant on pre-averaged quantities like the second and fourth order orientation tensors ( $\mathbf{a}_2$ ,  $\mathbf{a}_4$ ), which often introduce inaccuracies and information loss due to closure approximations, this DNS approach offers a more accurate and detailed representation of fiber

orientation dynamics.

The numerical approach accuracy is validated, as a series of rigorous validation tests were conducted. The normalization condition, ensuring the integral of the probability distribution function equals 1, was consistently met. Exploration of parameter dependencies, such as  $\lambda$  and  $C_I$ , yielded results consistent with established expectations. A comprehensive convergence study identified optimal mesh sizes and time steps, striking a balance between accuracy and computational efficiency. Furthermore, comparisons with existing literature, including analytical solutions, underscored the proposed solver's better precision and remarkable agreement with theoretical predictions, affirming its robustness and effectiveness. Some tests of fiber orientation in a case of Poiseuille flow have been also studied. Furthermore, we have meticulously computed the fourth-order tensor  $\mathbf{a}_4$  and compared it with analytical solutions. This comparison serves as compelling evidence of the effectiveness of our resolution method for the Fokker-Planck equation. The computed  $\mathbf{a}_4$  tensor plays a pivotal role in our work, as it is integrated later with the fluid problem (see chapter III). This integration forms the cornerstone of constructing a comprehensive model for a full flow-fiber coupling problem.

# Fiber-Flow coupling

## Contents

<b>III.1 Introduction</b> . . . . .	<b>58</b>
<b>III.2 Rheological models of fiber suspensions</b> . . . . .	<b>60</b>
III.2.1 Newtonian matrix suspensions . . . . .	60
III.2.2 Non-Newtonian matrix suspensions . . . . .	65
III.2.3 Short summary . . . . .	67
<b>III.3 Multiscale modeling for injection molding process</b> . . . . .	<b>67</b>
III.3.1 Generalities on the resolution of the flow-fiber coupling problem	67
III.3.2 Construction of the physical model . . . . .	68
III.3.3 Finite element approach to resolving a flow-fiber coupling model	70
III.3.4 Solution algorithm . . . . .	74
III.3.5 Short summary . . . . .	76
<b>III.4 Numerical results</b> . . . . .	<b>76</b>
III.4.1 Parallel computing . . . . .	76
III.4.2 Effect of rheological coupling coefficient $N_p$ on flow and fiber orientation . . . . .	79
III.4.3 Effect of interaction coefficient $C_I$ on fiber orientation . . . . .	87
III.4.4 Short summary . . . . .	89
<b>III.5 Conclusion</b> . . . . .	<b>90</b>

Injection process modelling requires the construction of a general constitutive equation that represents the behaviour of the material for the different flow cases encountered. In the case of a fiber-reinforced thermoplastic composite, it is necessary to express the stress field of the material according to the orientation distribution, the deformation rate and the parameters of the reinforced polymer such as the density fraction of fiber, the fiber-to-shape ratio and the viscosity of the matrix. The chapter will first focus on the different rheological laws that apply to fiber suspensions. The macroscopic behaviour of a material is obtained after a homogenization step which consists in averaging quantities obtained by means of a micro-mechanical formalism. Once the numerical tool is in place, a numerical validation of the computational code is performed. This numerical tool will be tested within the framework of simple geometries of academic types in order to evaluate the contribution of rheology/orientation coupling on the results of the numerical simulation. Thus, the numerical methods and the calculation code that have been developed to simulate the flow of reinforced fiber thermoplastics are presented. Chapter III describes the numerical methods used to solve the global problem. The coupling between the

fibers and the kinematics is taken into account via a constitutive equation for the stress field which has been solved by a mixed P1+/P1 finite element method. The orientation tensor is then assumed to be known through the resolution of FPE and the coupling is explicitly considered, that is to say that the viscous flow problem and the orientation problem are solved successively.

### III.1 Introduction

Several studies have pointed out the complexity of fiber orientation phenomena. The formation of a core-skin structure characteristic of discontinuous fiber-reinforced composites was highlighted. During the filling of an injection mould, the glass fibers orient themselves under the influence of the flow. Conversely, the rheological properties of the shaped material are very largely influenced by the orientation state of the fibers and this in turn affects the flow profile. The overall behaviour of the fiber suspension is therefore a complex problem. Therefore the origin of these arrangements is complex, linked to a number of interactions that appear during the flow. The challenge lies in exposing these interactions. In fact, hydrodynamic fiber-fluid interactions, fiber-to-wall interactions, the nature of the flow, the concentration of particles are all phenomena that can be the cause of the final orientation of the particles. Fiber suspensions are model suspensions capable of imitating composite materials filled with reinforcement. Considerable efforts have been made by many researchers to try to provide an understanding of the phenomena of the flow of suspensions, whether from an experimental or theoretical point of view.

Therefore the numerical simulation of fiber orientation has been the subject of much work over the past twenty years [67]. Advances in computing power have allowed large-scale problems to be simulated. Mainly, the studies have been done on two types of calculations on very different spatial scales. The first approach is about the macroscopic simulation of existing models, notably those of Jeffery or Folgar and Tucker with or without coupling with kinematics. The second approach is built based on the micromechanical scale simulation. The work involves the direct simulation of the orientation of a single fiber or a population of fibers. This includes predicting the orientation of solid particles in a Newtonian fluid, while quantifying all hydrodynamic interactions in a fluid-particle flow. Thus, there are many studies in the literature concerning the numerical calculation of the orientation of fibers in a given flow. Various types of shaping processes were studied: extrusion [109], flow around a sphere [110], squeeze flows [111], flows in a channel or radial between disks [112, 113], and finally injection [114, 104]. The number of publications on this subject is very abundant. In the literature, the works have been developed mainly on three categories of numerical models. First, the decoupled models where the equations of the kinematics are solved without the consideration of the fibers. Once the speed field is obtained, the equation for the orientation of the fibers is resolved for each iteration in time. The literature is full of articles on the simulation of the orientation of fibers not coupled to the flow [77, 40]. Various types of flows and geometries were used by this model such as in the case of injection process. Then a number of research [115] dealt with models coupled with the assumption that fibers are aligned along current lines. And finally there are the coupled models [116] where

the equations of kinematics are function of the orientation of the fibers, the latter being governed by an evolutionary equation.

For an extrusion flow case, a research work done in [117] studies the insulated extrusion of a semi-diluted solution of fibers in a Newtonian fluid. Coupling is taken into account via a Dinh and Armstrong constitutive law (see section III.2) and the resolution incorporates a 2D finite element method. The orientation of the fibers is calculated after the resolution of the orientation distribution function following specific current lines. The method used pairs the calculation of the velocity field and the current lines with the calculation of the fiber orientation by a Newton algorithm. A study carried out in [118] also uses an anisotropic behaviour law to model the flow of liquid crystalline polymers in the chain. They describe the orientation state of the fibers from the Ericksen and Jeffery equations. A finite difference calculation method is used to resolve the problem. For the case of flow with recirculation zones, a research [119], an extension of what has been done in [84] where the coupling between orientation and kinematics was taken into account via a constitutive equation and the stress field is thus reduced to a nonlinear function of the velocity field, studies the case of a diluted suspension using a finite difference method. The numerical results obtained corroborate the trends gotten in [84] and thus emphasise the importance of rheological coupling. However, it should be borne in mind that the local fiber alignment hypothesis is very reductive, since for elongational flows, the fiber orientation is not carried out along current lines. For case of flows in a complex geometry, a finite element solver for fiber suspension [120] were developed for the benchmark 4:1 contraction problem, where an enhancement in the magnitude of the zone of recirculation has been reproduced with an increasing concentration of fibers. A model introduced in [121], have used a fully coupled solution to predict the flow of fiber suspensions across a variety of complex geometries, including expansion, center-grid disk, and the axisymmetric contractions. In the case of injection flow, a work done in [122] have studied the filling of a 2D cavity. Its originality stems from the fact that the matrix is no longer considered Newtonian but is governed by a law of pseudoplastic anisotropic behaviour. The determination of the orientation is made after the resolution of the evolutionary equation of the written orientation in the Lagrangian form, valid for diluted concentrations of fibers. Another study was also carried out for the injection of 3D parts [68], disregarding the hypothesis of Hele and Shaw. The behaviour law refers to the model of Dinh and Armstrong coupled with Folgar and Tucker equation. The advection equation is solved using a SUPG method while the Stokes problem uses a continuous finite element technique. The numerical model thus developed is valid in the context of axisymmetric flows for application to the filling of a disk injected by the centre as well as a threshold plate.

However, as it is mentioned before, at the time of injection phase, there is a strong coupling between the distribution of the fibers and the flow of the suspension formed by the fibers scattered in the polymer matrix in the liquid state. Therefore, a constitutive law or rheological equation mathematically expresses stresses based on the history of deformation and/or the reaction rates for a given material [123]. In order to properly model a molding process, it is important to have a global constitutive equation, which best represents the behaviour of the material for a multitude

of stresses (single shear, elongation or combination of the two) and for particular regimes (steady state or transient). In the case of axisymmetrical particle suspensions, it seems important to consider the effects of fiber orientation. Thereby, there are two steps to obtaining a law of behaviour for the case of reinforced thermoplastic materials. The first one is to get the macroscopic quantities associated with the microscopic behaviour of the material. It is a classic step of spatial homogenisation that allows to obtain average quantities from a micromechanical formalism. And the second step is a statistical homogenisation that allows the average macroscopic quantities to be obtained from the particle orientation state obtained through statistical formalism. Some works done on the approach frequently used to obtain a model of macroscopic behaviour using a micromechanical approach can be found in [124]. So considering the incompressible composite (fiber and fluid), the total stress  $\sigma$  in the material is the contribution of a hydrostatic pressure  $P$  and a deviatoric part representing the field of the extra stresses  $\tau$ . Generally, hydrostatic pressure is negligible. For a composite, it is customary to break the field of the stresses down to a sum of the contributions from the polymer (a Newtonian or non-Newtonian matrix fluid) and the fibers.

## III.2 Rheological models of fiber suspensions

Fiber suspensions are model suspensions capable of imitating composite materials filled with reinforcement. Considerable efforts have been made by many researchers to try to provide an understanding of the phenomena of the flow of suspensions, from a theoretical point of view. Thus, building a model of suspension behaviour law, is like finding a relationship between the total suspension stress tensor and the shear rate tensor. Moreover, the total stress of the suspension is the result of the contribution of the stress due to the suspended fluid, and of the contribution of the fibers themselves. So the purpose of this section is to present a bibliographic study on the main rheological models taking into account the contribution of fibers to the tensor of macroscopic stresses.

### III.2.1 Newtonian matrix suspensions

Several behavioural laws have been proposed for suspensions of rigid fibers placed in a fluid. Nevertheless, it should be noted that most of the work encountered refers to behaviour laws that take into account a Newtonian matrix for diluted to semi-diluted concentration regimes.

#### III.2.1.1 A generic model

In all theories, the particle is assumed to be small compared to the flow dimensions. Several behaviour models have been proposed for rigid fiber suspensions in a Newtonian fluid. These models are derived from a micromechanical approach. So as it is explained before, the behaviour law is obtained by conventional homogenisation techniques: the macroscopic quantities are defined as the spatial averages, on a certain representative volume  $V$ , of the associated microscopic quantities. Thus the

field of macroscopic velocities  $\mathbf{u}$  and its strain rate  $\mathbf{E}$  are written:

$$\begin{aligned}\mathbf{u} &= \langle \mathbf{v} \rangle = \frac{1}{V} \int_V \mathbf{v} dv \\ \mathbf{E}(\mathbf{u}) &= \frac{1}{2}(\nabla \mathbf{u} + \nabla \mathbf{u}^T) = \frac{1}{V} \int_V \mathbf{E}(\mathbf{v}) dv = \frac{1}{2V} \int_V (\nabla \mathbf{v} + \nabla \mathbf{v}^T) dv\end{aligned}\quad (\text{III.1})$$

where  $\mathbf{v}$  represents the microscopic velocity and  $\mathbf{E}(\mathbf{v})$  is the associated strain rate, as the microscopic velocity field is expressed by:

$$\mathbf{v} = \mathbf{u} + \mathbf{v}' \quad (\text{III.2})$$

where the  $\mathbf{v}'$  symbolises velocity fluctuations such as  $\langle \mathbf{v}' \rangle = 0$ , then the macro stress tensor is defined as follows:

$$\boldsymbol{\sigma} = \frac{1}{V} \int_V (\boldsymbol{\tau} - \rho \mathbf{v}' \otimes \mathbf{v}') dv \quad (\text{III.3})$$

where  $\boldsymbol{\tau}$  the tensor of the microscopic constraints and  $\rho$  the mean density of the suspension considered. If the matrix of viscosity  $\eta$  has a Newtonian behaviour, then the microscopic stress in the fluid is expressed as:

$$\boldsymbol{\tau} = 2\eta \mathbf{E}(\mathbf{v}) - p \mathbf{I} \quad (\text{III.4})$$

where  $p$  is the microscopic pressure, then the rate of macroscopic deformation is expressed in terms of contributions due to the fluid and the contribution of fibers:

$$\mathbf{E}(\mathbf{u}) = \frac{1}{V} \int_V \mathbf{E}(\mathbf{v}) dv = \frac{1}{V} \int_{V-\sum V_i} \mathbf{E}(\mathbf{v}) dv + \sum_i \int_{V_i} \mathbf{E}(\mathbf{v}) dv \quad (\text{III.5})$$

where  $V_i$  is the volume occupied by fiber  $i$ . Since the fibers are assumed to be rigid, (III.5) is simplified and written:

$$\mathbf{E}(\mathbf{u}) = \frac{1}{V} \int_{V-\sum V_i} \mathbf{E}(\mathbf{v}) dv \quad (\text{III.6})$$

Using equations (III.3), (III.4), (III.6) and assuming that the Reynolds number is smaller than 1 (which is generally the case in polymer implementation), the macroscopic stress tensor writes:

$$\boldsymbol{\sigma} = -P \mathbf{I} + 2\eta \mathbf{E}(\mathbf{u}) + \boldsymbol{\tau}_f \quad (\text{III.7})$$

where  $P$  represents the macroscopic pressure,  $\eta$  refers to the viscosity of the neat matrix without charge and  $\boldsymbol{\tau}_f$  is the contribution of particles (fibers) to the tensor of the macroscopic stresses. Thus, the difficulty lies in expressing the particle-related stress,  $\boldsymbol{\tau}_f$ , which contains the essential information about the nature of the fiber-fluid and fiber-fiber interaction and involves the orientation tensors of the fibers,  $\mathbf{a}_2$  and  $\mathbf{a}_4$  (see section I.4.3.3). Thus, in order to obtain an estimate of the fiber contribution to the macroscopic stress tensor, it is necessary to make assumptions about the shape of the particles and the concentration of the solution. Classic models are presented in the following sections. In all cases, the relationship between

the stress tensor and macroscopic strain rates for axisymmetric particle suspension can be set as follows according to [125]:

$$\boldsymbol{\sigma} = -P\mathbf{I} + 2\eta(\mathbf{E} + N_s[\mathbf{E} \cdot \mathbf{a}_2 + \mathbf{a}_2 \cdot \mathbf{E}] + N_p\mathbf{E} : \mathbf{a}_4) \quad (\text{III.8})$$

The terms  $\eta$ ,  $N_p$ , and  $N_s$  are rheological parameters representing the viscosity of the fluid, the concentration of the suspension and the shape factor of the fibers, respectively. The last term describes the coupling between hydrodynamic forces and fiber orientation. For large shape factors, the parameter  $N_s$  is negligible with respect to  $N_p$ .

### III.2.1.2 Slender-body theory

Many suspension models incorporate in their development the results of the slender body theory [126, 124]. The results of this theory are used to calculate the perturbation due to the presence of a body in a low Reynolds number viscous fluid flow, Stokes flow. The basic hypothesis of this theory is that the perturbation due to the presence of particles in the fluid is described by an adequate linear force distribution of the Stokes singularities. A Stokes singularity represents the effect of a force applied at a point in the fluid on the flow. In slender body theory, the main effect of the body on the surrounding fluid is due to the distribution of the resultant forces on the contour of the section of a length element. In the approximations based on this theory, the term  $\eta$  is equal to the viscosity of the fluid and the rheological parameter  $N_s$  is zero.

#### Batchelor model

Batchelor [124] proposes a law of rheological behavior for rigid particles of ellipsoidal shape in a dilute suspension. It is an extension to the case of particles of non-circular section of the work of Cox [126]. Thus, the approach used is divided into two main steps, where the perturbation due to the presence of the particle is replaced by a linear density of intensity forces to be determined and the intensity of the forces is calculated so as to best verify the boundary conditions. Thus in this model, the contribution of the particles to the macroscopic stress field is calculated in the particular case of a dilute solution of fibers having the same orientation, where it considers that the particles are independent from a hydrodynamic point of view and that there is no contact between fibers. Therefore, the law of constitutional behavior states:

$$\boldsymbol{\sigma} = -P\mathbf{I} + 2\eta(\mathbf{E} + N_p\mathbf{E} : \mathbf{a}_4) \quad (\text{III.9})$$

$$N_p = \frac{\phi\beta^2}{3 \ln \beta}$$

where  $\beta$  is the aspect ratio of the fibers and  $\phi$  is their volume fraction. This relationship is valid only in the case of dilute suspensions of rigid particles. In order to extend this behavior law to more concentrated suspensions, it is essential to take into consideration interactions of the hydrodynamic type which are predominant for this type of concentration regime. Still considering the theory of slender bodies,

Batchelor [124] models stresses in a semi-dilute suspension of fibers during elongational flow, and in the case where the fibers are aligned in the elongation direction of the fluid. An empirical relationship, expressing the rheological parameter  $N_p$ , is found in the form:

$$N_p = \frac{\phi\beta^2}{9[\ln(2\beta) - \ln(1 + 2\beta\sqrt{\frac{\phi}{\pi}}) - 1.5]} \quad (\text{III.10})$$

Hydrodynamic interactions between particles are represented by an effective medium. Each fiber is within a "cell" created by the surrounding environment. In order to determine the evolution of a hydrodynamic perturbation, this study introduces the concept of the screen effect of hydrodynamic interactions. The basic hypothesis of this approach is to assume that the perturbation created by a fiber will decrease with an order distance of the mean distance between the particles, as if at this distance the other fibers in the presence formed a "screen" that prevents the propagation of the perturbation. In particular, it shows that there is a screening length beyond which a hydrodynamic disturbance has no effect on the surrounding fluid.

### Dinh-Armstrong model

The model developed in [127] is based on the works done in [124] to get extended to semi-diluted suspensions. A test fiber is considered to be in an effective medium that includes the influence of other fibers, where the hydrodynamic interactions between the fibres are always taken into account. Also, the average distance between two neighbouring particles determines the size of the cell. Thus, the final behaviour law takes the following form:

$$\begin{aligned} \boldsymbol{\sigma} &= -P\mathbf{I} + 2\eta(\mathbf{E} + N_p\mathbf{E} : \mathbf{a}_4) \\ N_p &= \frac{\phi\beta^2}{3\ln(\frac{2h}{D})} \end{aligned} \quad (\text{III.11})$$

where  $h$  represents the characteristic distance between two neighbor fibers. This distance depends on the orientation of the particles and has the value:

$$\begin{aligned} h_{\text{aligned}} &= \frac{D}{2} \sqrt{\frac{\pi}{\phi}} \quad \text{for aligned orientation} \\ h_{\text{random}} &= \frac{\pi D}{4\phi\beta} \quad \text{for random orientation} \end{aligned} \quad (\text{III.12})$$

For intermediate fiber orientation situations, a study done in [128] determines the average distance in this form:

$$\begin{aligned} h &= (1 - f)h_{\text{random}} + fh_{\text{aligned}} \quad \text{for } \frac{\pi}{4\beta^2} < \phi < \frac{\pi}{4\beta} \\ h &= h_{\text{aligned}} \quad \text{for } \frac{\pi}{4\beta} < \phi < \frac{\pi}{4} \end{aligned} \quad (\text{III.13})$$

so  $h$  is assumed to be linear in terms of the scalar measure of orientation  $f$ , as the latter is expressed as:

$$f = 1 - N\det(\mathbf{a}_2) \quad (\text{III.14})$$

where  $N=4$  and  $N=27$  in a two-dimensional and three-dimensional case, respectively.

### Shaqfeh-Fredrickson model

A theory has been developed in [129] to describe the effective transport properties of a fiber suspension. It determines the contribution to the tensor of the macroscopic stresses for dilute and semi-dilute regions. The approach is based on the calculation of a propagation tensor that describes the average velocity field created by a point force in the suspension. Using this theory, it has been demonstrated that there is a screening effect corresponding to a rapid damping of the hydrodynamic perturbation created by a test fiber due to the presence of the neighboring fibers. In contrast to the Dinh-Armstrong model, the hydrodynamic interactions between the fibers are calculated explicitly and summed by a diagrammatic method. The law of behavior retains a form similar to the preceding laws and the rheological parameter  $N_p$  is expressed:

$$N_p = \frac{2\phi\beta^2}{3[\ln(\frac{1}{\phi}) + \ln(\ln(\frac{1}{\phi})) + \zeta]} \quad (\text{III.15})$$

where  $\zeta = -0.664$  for an isotropic fiber orientation and  $\zeta = 0.158$  for an aligned orientation. For the dilute suspensions, the use of this model retrieves the results of Batchelor. In the semi-diluted case, the explicit calculation refines the results of Dinh and Armstrong showing, among other things, that the influence of the orientation state of the particles on the rheological parameters is small.

#### III.2.1.3 Slender ellipsoidal theory

Using Jeffery's work [47] which gives the solution of the velocity field around an ellipsoidal particle, the latter is used to compute the shear viscosity of a dilute suspension [50, 130]. Based on their results, the work is extended by [131, 84] in order to establish a behavioral relationship for diluted solutions. Thus the constitutive equation has the following form:

$$\begin{aligned} \boldsymbol{\sigma} &= -P\mathbf{I} + 2\eta_I(\mathbf{E} + N_s[\mathbf{E} \cdot \mathbf{a}_2 + \mathbf{a}_2 \cdot \mathbf{E}] + N_p\mathbf{E} : \mathbf{a}_4) \\ \eta_I &= \eta(1 + \phi) \end{aligned} \quad (\text{III.16})$$

The exact but complex expressions of the coefficients  $N_p$  and  $N_s$  are given in [124, 130]. Based on ellipsoidal particles theory [131, 84], the following asymptotic forms are used:

$$\begin{aligned} N_p &= \frac{\phi\beta^2}{[1 + 2\phi][2(\ln(2\beta) - 1.5)]} \\ N_s &= \frac{6\phi \ln(2\beta) - 11\phi}{\beta^2[1 + 2\phi]} \end{aligned} \quad (\text{III.17})$$

These asymptotic forms of rheological parameters give good results for large aspect ratio (less than 1% error for  $\beta = 50$ ). For an aspect ratio  $\beta = 10$ , the error is in the order of 15%. Moreover, for this model, the term  $N_s$  is smaller than the term  $N_p$  as the aspect ratio gets greater. Extensions of this model have also been proposed in order to refine the results when approaching the semi-diluted concentration regimes.

Particularly, a study done in [132] developed a phenomenological constitutive equation that states that, at high volume fraction, the effective viscosity diverges, leading them to obtain the coefficients empirically:

$$\begin{aligned} \eta_I &= \eta \\ N_s &= 0 \\ N_p &= \frac{\phi\beta^2 \left[2 - \frac{\phi}{\phi_m}\right]}{2\left(1 - \frac{\phi}{\phi_m}\right)^2 [\ln(2\beta) - 1.5]} \end{aligned} \quad (\text{III.18})$$

where  $\phi_m$  describes the maximum volume packing ( $\phi_m = 0.53 - 0.013\beta$ ). This law is valid for an aspect ratio ( $5 < \beta < 30$ ).

### III.2.2 Non-Newtonian matrix suspensions

It should be noted that there are also few models that take into account the non-Newtonian behavior and the shear thinning nature of the polymer matrix.

#### III.2.2.1 Pseudoplastic matrix

According to the same principle of dividing the total volume in volume occupied by the matrix plus a volume occupied by the fibers, the stress field in a pseudoplastic fluid is of the type:

$$\boldsymbol{\sigma} = -P'\mathbf{I} + 2K|2I_2|^{\frac{m-1}{2}}\mathbf{E} + \boldsymbol{\tau}_f \quad (\text{III.19})$$

where  $P'$  is the contribution of the matrix to the homogenized pressure,  $K$  denotes the consistency of the neat matrix,  $m$  is the pseudoplasticity index, and  $I_2$  is the second invariant of  $\mathbf{E}$ .

#### Souloumiac model

Using the same steps as in [127], [133] has built a stress expression, represented by a power-law, that takes into account the shear-thinning behavior of the matrix. Using the cell model [134], the contribution of the fibers to the stress field is determined, as the hydrodynamic interactions between the fibers are assumed to be weak. The total stress field is the sum of the contributions of the matrix and the fibers. In this work [133], it is noted that the homogenization of the matrix contribution with a nonlinear power-law is not straightforward, where the power-law index is assumed to be the same as that used for the matrix. Thus, for a fiber suspension, the total stress of a power-law fluid is expressed as follows:

$$\boldsymbol{\sigma} = -P\mathbf{I} + \mathbf{K}|\dot{\boldsymbol{\gamma}}|^{m-1}\dot{\boldsymbol{\gamma}} + \mathbf{K}\phi\eta_1 \int_{\mathbf{p}} \varphi(\mathbf{p}, t)|\dot{\boldsymbol{\gamma}} : \mathbf{p} \otimes \mathbf{p}|^{m-1}(\dot{\boldsymbol{\gamma}} : \mathbf{p} \otimes \mathbf{p})\mathbf{p} \otimes \mathbf{p} d\mathbf{p} \quad (\text{III.20})$$

where  $\mathbf{K}$  is the matrix consistency and  $\eta_1$  is the coupling effect, written as:

$$\eta_1 = \frac{\beta^{m+1}}{2^{m-1}(m+2)} \left[ \frac{1-m}{m\left[1 - \left(\frac{D}{2h}\right)^{\frac{1-m}{m}}\right]} \right]^m \quad (\text{III.21})$$

where  $h$  is the size of the cell, beyond which the velocity is no longer disturbed by the fiber.

### Other models

Among the models, we can mention the Goddard's model [135] which is an extension of the work of Batchelor [136]. However, these models only address only the problem of matrices whose behavior is non-linear through a power law. A study in [137] also presented a non-local relationship for stress generation in a planar rod suspension, characterized by power-law drag laws governing local interactions. Literature equations for fiber suspensions typically involve local stress fields, in other words, stresses at a material point are only influenced by deformation rates at the same point. In the case of homogeneous flows of statistically homogeneous suspensions, the result can be reduced to the equation (III.20). On the other hand, based on the written works, equation (III.20) is seldom used, presumably because of its limited computational interest due to the impractical inclusion of the strain rate tensor in the orientation integral. According to the research done in [138], simple shear flows involving fibers with an isotropic orientation have some analytical solutions.

#### III.2.2.2 Viscoelastic matrix

Due to the complexity of modeling such suspensions, the constitutive equations discussed above are unable to accurately describe the viscoelastic properties of melt polymer composites. Numerous theoretical investigations have shown that the Jeffery equation (I.8) is no longer accurate for fiber suspensions in viscoelastic fluids. In the analysis of the motion of a single fiber suspended in a second-order fluid [139], it has been demonstrated that the fiber rotation orbit deviates from the Jeffery orbit and that this deviation is inversely proportional to the second normal-stress coefficient. In order to extend the Jeffery equation, [140] developed a rheological model for fiber suspensions in viscoelastic fluids using Poisson bracket formalism for both the matrix and the fiber. Understanding these complex behaviors is expected to be aided by mathematical modeling of viscoelastic suspensions using fundamental equations governing particle and fluid dynamics [141, 142]. Several studies on the modeling of the rheological characteristics of suspensions in viscoelastic matrices [143, 144, 145] have demonstrated that in this case the stress tensor can be written in the following form:

$$\boldsymbol{\sigma} = \boldsymbol{\sigma}_{sol} + \boldsymbol{\tau}_p + \boldsymbol{\tau}_f \quad (\text{III.22})$$

in which, the fluid's contribution to the stress tensor of suspension is represented as the sum of the contributions from the solvent  $\boldsymbol{\sigma}_{sol}$  and the polymer  $\boldsymbol{\tau}_p$  and the fiber contribution  $\boldsymbol{\tau}_f$  is calculated by taking the whole viscosity (solvent and polymer) as in for taking into consideration of non-Newtonian part. Other models can be stated that take into account the viscoelastic nature of the suspension. Petrie [146] presents a description of these models, Olroyd B fluid, FENE-CR model [147], Giesekus model [147]. Also, the multimode Giesekus model [96] was utilized by studies made in [148, 149] to predict the strain rate-dependent viscoelastic behavior of the polymer matrix.

### III.2.3 Short summary

- ✓ It turns out that the calculation of the contribution of the fibers to the tensor of the macroscopic stresses represents a delicate point.
- ✓ Several empirical models are proposed to describe the rheological behavior of fiber-filled suspensions in dilute or semi-dilute cases.
- ✓ The theory of slender bodies makes it possible to construct macroscopic models valid for suspensions in a semi-dilute regime but, on the other hand, the thickness of the particles are being neglected.
- ✓ The model based on the theory of slender body is derived from Jeffery's work and could be generally limited to the dilute regime.
- ✓ There are not many models in the literature that consider the nonlinear behavior of the suspending fluid.

## III.3 Multiscale modeling for injection molding process

Multiscale modeling is a simulation technique used to study injection molding processes. It involves the development of models that capture the interaction of various physical phenomena, from the macroscopic scale of the entire injection molding process down to the microscopic scale of the material microstructure. This allows for a more detailed and accurate prediction of the process behavior, as well as the ability to optimize process parameters for improved efficiency and quality. This section presents the various numerical simulation techniques that can be used to solve the overall problem of injecting fiber-filled materials. In particular, the chosen numerical methods for solving the mechanical problem are described, typically here the solution of the generalized Stokes problem and numerical techniques for solving the advection equation (evolution of the fiber orientation).

### III.3.1 Generalities on the resolution of the flow-fiber coupling problem

The resolution of the flow-fiber coupling problem involves the development of mathematical models and simulation techniques that can accurately predict the behavior of the fluid flow and fiber structure, and how they influence each other. This can be a complex task, as it involves multiple length scales, from the microscopic scale of the individual fibers to the macroscopic scale of the composite material and the use of the DNS which is a simulation technique used to solve the flow-fiber coupling problem in fiber-reinforced composite materials.

#### III.3.1.1 Change of scales: from macro to microscopic and vice versa

In the context of the flow-fiber coupling problem, it is often necessary to consider multiple length scales in order to accurately predict the behavior of the system. At

the macroscale, the fluid flow through the composite material is typically modeled using traditional fluid dynamics equations, such as the Navier-Stokes equations. At the microscale, the orientation and deformation of the individual fibers within the material must also be taken into account, as this is done by solving FPE and then redefining the stress constitutive equation in order to consider the influence of fibers on the flow at macroscale. Thus, to solve the flow-fiber coupling problem at both the macroscale and microscale, it is necessary to change scales between the two levels of modeling.

### III.3.1.2 DNS technique

DNS involves the direct solution of the governing equations of fluid flow and fiber structure, without the need for any simplifying assumptions or approximations. This allows for a highly accurate prediction of the behavior of the fluid and fibers, and how they influence each other. So this numerical approach consists of solving exactly the Stokes equations for the fluid, and the FPE for the fibers. Direct simulation methods allow to reproduce the intrinsic physics of fluid-fiber flows by taking into account all interactions that occur during the flow. Therefore the advantage of this approach is that the velocity and pressure fields of the fluid phase are calculated exactly without any simplifying hypothesis. In other words, the fluid's flow is directly modified by the presence of the particles.

## III.3.2 Construction of the physical model

The physical model of the fluid-fiber coupling problem refers to the mathematical description of the system being studied, including the governing equations and the associated boundary and initial conditions. The construction of this model is an important step in the simulation of the flow-fiber coupling problem, as it allows for the prediction of the behavior of the system based on the underlying physical phenomena at play. Thus, these phenomena are typically described using a set of governing equations, which can be derived from fundamental physical principles. In addition, the model must also account for the boundary and initial conditions of the system, which define the state of the system at the start of the simulation and the constraints on its behavior.

### III.3.2.1 Governing equations

The resin flow around the fibers can be described by the Navier-Stokes equations [150] at macroscale level. The latter provide the best mathematical description, known to date, of the flows of real fluids. On the domain of the material  $\Omega \in \mathbb{R}^2$  and the time interval  $[0, t]$ , the Navier-Stokes problem consists of two equations:

- The first stems from the application of the fundamental principle of dynamics and is written as follows:

$$\rho \left( \frac{\partial \mathbf{u}}{\partial t} + \mathbf{u} \cdot \nabla \mathbf{u} \right) = f + \nabla \cdot \boldsymbol{\sigma} \quad \text{in } \Omega \times [0, t] \quad (\text{III.23})$$

with  $f$  the sum of the volumetric forces,  $\boldsymbol{\sigma}$  the Cauchy stress tensor,  $\rho$  the density and  $\mathbf{u}$  the velocity vector of the fluid.

- The second comes from the conservation of mass principle and guarantees the continuity of the solutions obtained. In the case of incompressible fluids, the density is constant in time and space. The conservation equation for incompressible fluid of constant density is reduced to:

$$\nabla \cdot \mathbf{u} = 0 \quad \text{in } \Omega \times [0, t] \quad (\text{III.24})$$

In addition, in injection molding, polymers have a high viscosity and flow slowly. In this case, the viscous effects dominate the inertial effects and we can consider a simplified form of the Navier-Stokes equations. This form is known in the literature as Stokes equations. Considering a steady state and neglecting volumetric forces, this system takes the following form:

$$\begin{aligned} \nabla \cdot \mathbf{u} &= 0 \quad \text{in } \Omega \\ \nabla \cdot \boldsymbol{\sigma} &= 0 \quad \text{in } \Omega \end{aligned} \quad (\text{III.25})$$

Equation (III.25) can be adopted for different behavioral laws introduced through the term  $\boldsymbol{\sigma}$ . So the system is closed by a constitutive equation between stresses and deformations given by the law introduced in equation (III.9). This behavior law reveals a descriptor of the orientation via the tensor  $\mathbf{a}_4$ . It is then necessary to compute it by using the evolution equation of the fiber orientation (FPE). By substituting the expression of  $\boldsymbol{\sigma}$  in the system (III.25), and using the definition of strain rate tensor in (II.3), it is shown that the flow problem to be solved is reduced to a generalized Stokes problem:

$$\begin{aligned} \eta \nabla^2 \mathbf{u} - \nabla p + 2\eta N_p \nabla \cdot (\mathbf{E} : \mathbf{a}_4) &= 2\eta \nabla \cdot \mathbf{E} - \nabla p + 2\eta N_p \nabla \cdot (\mathbf{E} : \mathbf{a}_4) = 0 \quad \text{in } \Omega \\ \nabla \cdot \mathbf{u} &= 0 \quad \text{in } \Omega \end{aligned} \quad (\text{III.26})$$

The first equation of system (III.26) expresses well the balance of the different forces present in a viscous fluid by linking of the pressure forces  $\nabla p$  and the viscous forces resulting from the characterization of fluid itself  $\eta \nabla^2 \mathbf{u}$  and  $\eta N_p \nabla \cdot (\mathbf{E} : \mathbf{a}_4)$  derived from the contribution of fibers to the fluid viscosity. It can be seen from the Stokes equation that the influence of the fiber contribution of the injection process can be significant, because the fibers can affect the flow behavior of the polymer and the filling of the mold. For example, if the fibers are oriented in a particular direction, they may exert a force on the fluid in that direction. It is worth recalling that FPE is used to compute the fiber orientation tensor at each time step and then the fibers are being advected by the flow of the fluid employing an advection equation that can be written as follows:

$$\frac{\partial \varphi}{\partial t} + \mathbf{u} \nabla \varphi = 0 \quad (\text{III.27})$$

Equation (III.27) describes the transport of a quantity by the fluid. In the context of the injection process, it can be used to describe the transport of fibers in the melt polymer as it is injected into the mold. During the injection process, the fibers can rotate as they are transported. So it can be modeled using an advection equation,

which describes how the fibers move through the plastic while also rotating. To use equation (III.27) to model the transport of rotating fibers during the injection process, it is necessary to specify the velocity field  $\mathbf{u}$  of the polymer, by solving the Stokes equations (III.26).

### III.3.2.2 Boundary conditions

In order to complete the Stokes problem, the system (III.26) is accompanied by a set of boundary conditions. These conditions can be of the Dirichlet type, i.e. assigning a value to the velocity  $\mathbf{u}$  (or to certain of its components) on the boundary  $\Gamma_D \subset \partial\Omega$ , and/or of the Neumann type, i.e. imposing the stress exerted by the external medium  $\boldsymbol{\sigma}\cdot\mathbf{n}$  on the boundary  $\Gamma_N \subset \partial\Omega$ . In a single-phase context, these conditions are imposed at the boundaries of the computational domain to define the nature of the flow (see figure III.1). The boundary conditions are as follows:

- on  $\Gamma_{in}$ , a pressure condition is imposed:  $(\boldsymbol{\sigma}\mathbf{n})\cdot\mathbf{n} = -p_{in}$  where  $\mathbf{n}$  is the external unit normal and  $p_{in}$  is the pressure at the inlet.
- on  $\Gamma_{in}$ , an planar random orientation of fiber is imposed:  $\mathbf{a}_4 = \mathbf{a}_4^{t_0}$  where  $\mathbf{a}_4^{t_0}$  is computed from equation (I.6) by taking  $\varphi = \frac{1}{2\pi}$ .
- on  $\Gamma_{end}$ , a pressure condition is imposed:  $(\boldsymbol{\sigma}\mathbf{n})\cdot\mathbf{n} = -p_{end} = 0$ , where  $p_{end}$  is the pressure at the right end of the domain.
- on  $\Gamma_{bord}$ , no-slip boundary condition is imposed, which results in  $\mathbf{u} = 0$ .

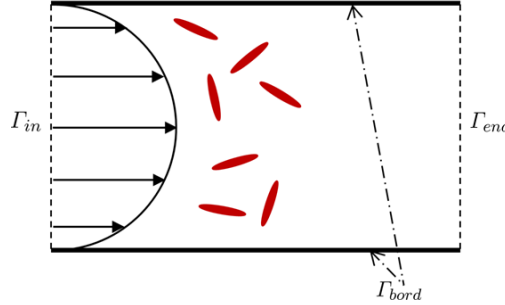


Figure III.1: Representation of different boundaries

where  $\Gamma_{in}$ ,  $\Gamma_{bord}$  and  $\Gamma_{end}$  respectively designate the boundaries of the domain corresponding to the injection zone and to the zone of contact with the walls of the injection mold with  $\Gamma_{in} \cup \Gamma_{bord} \cup \Gamma_{end} = \partial\Omega$ . It is noted also that Eulerian approach is used in this case. Similar to the work done in [151], the free surface condition is eliminated by extending the Stokes equations to the entire domain. This allows for the resolution of a confined Stokes flow problem.

### III.3.3 Finite element approach to resolving a flow-fiber coupling model

In order to develop the finite element method used to solve the velocity/pressure problem, it is necessary to proceed with a weak formulation of the equations.

### III.3.3.1 Classical mixed formulation

A Finite-Element approach is used to solve the system (III.26). Initially, the distinct spaces required to articulate the weak formulation of the Stokes physical problem while taking into account within its equation the effect of fiber orientation are introduced. Thus, the spaces are recalled as follows:

- $\mathcal{C}^0(\Omega)$ : the space of functions continuous on  $\Omega$
- $\mathcal{P}^1(\Omega)$ : the space of polynomials of degree 1 on  $\Omega$
- $\mathcal{L}^2(\Omega)$ : the Lebesgue space of square-integrable functions on  $\Omega$

$$\mathcal{L}^2(\Omega) = \left\{ w, \int_{\Omega} w^2 d\Omega \right\} \quad (\text{III.28})$$

- $\mathcal{H}^1(\Omega)$ : the Sobolev space of functions whose order 1 derivatives belong to  $\mathcal{L}^2(\Omega)$

$$\mathcal{H}^1(\Omega) = \{ w \in \mathcal{L}^2(\Omega), Dw \in \mathcal{L}^2(\Omega) \} \quad (\text{III.29})$$

The function spaces for velocity, pressure, and velocity weighting are defined as follows:

$$\begin{aligned} \mathcal{V} &= \{ \mathbf{u} \in \mathcal{H}^1(\Omega), \mathbf{u}|_{\Gamma_D} = \mathbf{g} \} \\ \mathcal{Q} &= \{ p \in \mathcal{L}^2(\Omega) \} \\ \mathcal{V}_0 &= \{ \mathbf{v} \in \mathcal{H}^1(\Omega), \mathbf{v}|_{\Gamma_D} = 0 \} \end{aligned} \quad (\text{III.30})$$

After applying the divergence theorem and considering the aforementioned boundary conditions, the Galerkin variational formulation (or weak formulation) of the problem is constructed by multiplying the equations of the (III.26) system by the test functions  $(\mathbf{v}, q) \in \mathcal{V}_0 \times \mathcal{Q}$  and integrating over the domain  $\Omega$ . The result is as follows:

$$\begin{aligned} (2\eta \mathbf{E}(\mathbf{u}) : \mathbf{E}(\mathbf{v})) + (\eta N_p [\mathbf{E}(\mathbf{u}) : \mathbf{a}_4] : \mathbf{E}(\mathbf{v})) - (p, \nabla \cdot \mathbf{v}) &= 0 \\ (\nabla \cdot \mathbf{u}, q) &= 0 \end{aligned} \quad (\text{III.31})$$

where the notation  $(\cdot, \cdot)$  defines the scalar product in the sense of the  $\mathcal{L}^2(\Omega)$ :

$$\forall (u, v) \in \mathcal{L}^2(\Omega), (u, v) = \int_{\Omega} uv d\Omega \quad (\text{III.32})$$

To solve this problem, the domain is discretized and broken down into simplices  $\mathcal{K}$  formed by tetrahedral elements in 3D (triangular elements in 2D). Thus, the aforementioned spaces of continuous functions are approximated on  $\mathcal{K}$  by discrete subspaces of finite dimensions consisting of piecewise continuous functions.

$$\begin{aligned} \mathcal{V}_h &= \{ \mathbf{u}_h | \mathbf{u}_h \in \mathcal{C}^0(\Omega), \forall \mathcal{K}, \mathbf{u}_h|_{\mathcal{K}} \in \mathcal{P}^1(\mathcal{K}) \} \\ \mathcal{Q}_h &= \{ p_h | p_h \in \mathcal{C}^0(\Omega), \forall \mathcal{K}, p_h|_{\mathcal{K}} \in \mathcal{P}^1(\mathcal{K}) \} \\ \mathcal{V}_{h,0} &= \{ \mathbf{v}_h | \mathbf{v}_h \in \mathcal{V}_h, \mathbf{v}_h = 0 \} \end{aligned} \quad (\text{III.33})$$

Thus, the discrete Galerkin problem consists of finding  $(\mathbf{u}_h, p_h) \in \mathcal{V}_h \times \mathcal{Q}_h$  such that  $(\mathbf{v}_h, q_h) \in \mathcal{V}_{h,0} \times \mathcal{Q}_h$  for the following mixed problem:

$$\begin{aligned} (2\eta \mathbf{E}(\mathbf{u}_h) : \mathbf{E}(\mathbf{v}_h)) + (\eta N_p[\mathbf{E}(\mathbf{u}_h) : \mathbf{a}_4] : \mathbf{E}(\mathbf{v}_h)) - (p_h, \nabla \cdot \mathbf{v}_h) &= 0 \\ (\nabla \cdot \mathbf{u}_h, q_h) &= 0 \end{aligned} \quad (\text{III.34})$$

The approximation of the solution on an element is determined using the values at the nodes. Then the solution is approached by:

$$\begin{aligned} \mathbf{u}_{h|\mathcal{K}} &= \sum_{i=1}^{D_{\mathcal{K}}} \mathbf{u}_i N^i \\ p_{h|\mathcal{K}} &= \sum_{i=1}^{D_{\mathcal{K}}} p_i N^i \end{aligned} \quad (\text{III.35})$$

where  $i$  represents the node,  $N_i$  is the shape function at that node, and  $D_{\mathcal{K}}$  is the number of nodes of simplex  $\mathcal{K}$ . In the context of such a mixed formulation, the choice of element types and interpolation function orders is never random since this choice affects both the accuracy of the results and the stability of the approach. It is also worth noting that in order for the formulation to be well-posed and stable, the pair of finite elements chosen for the velocity-pressure approximation must satisfy a compatibility condition leading to the Ladyzhenskaya-Babuška-Brezzi condition (discrete inf-sup condition)[152]:

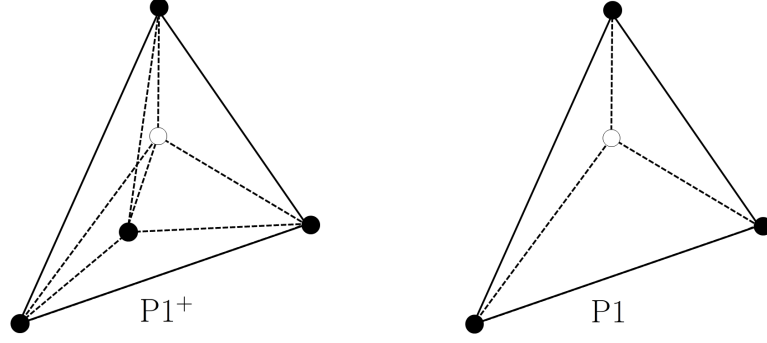
$$\inf_{q_h \in \mathcal{Q}_h} \sup_{\mathbf{u}_h \in \mathcal{V}_{h,0}} \frac{(\nabla \cdot \mathbf{u}_h, q_h)}{\|\mathbf{u}_h\|_{\mathcal{V}_{h,0}} \|q_h\|_{\mathcal{Q}_h}} \geq C > 0 \quad (\text{III.36})$$

with  $C$  being a constant independent of the discretization. For example, if P1/P1 elements (linear and continuous per element) are used, the standard Galerkin formulation of equations (III.34) will suffer from instability. Thus, low-order elements do not satisfy condition (III.36). The instability of this approximation is manifested by the appearance of a spurious pressure mode in the computed solution. However, low-order finite elements, particularly those of equal order, are widely used since they are the easiest to implement in practice. To address the issue of condition (III.36), several stabilization methods have been proposed in the literature [153, 154, 155].

### III.3.3.2 Stable mixed variational formulation

An existing Stokes finite element solver at ICI-tech has been integrated into our numerical scheme. One approach, already implemented at ICI-tech, to stabilize the solution of the Stokes equation involves the use of a modified finite element method, known as the MINI-element or P1+/P1 element [154]. In this method, the function space for velocity is enriched with a bubble function, which is defined at the element level and takes the value of 1 at the barycenter of the element and 0 at its edges. This modification aims to satisfy the discrete inf-sup condition, which is necessary for the stability of the Galerkin method, by introducing additional degrees of freedom in the velocity approximation. So the velocity and pressure fields are considered as follows:

- the pressure is linear and continuous.
- the velocity is broken down into a linear part  $\mathbf{u}$  and a bubble part  $\mathbf{b}$ . This decomposition is unique.


 Figure III.2: Element  $P1^+/P1$ 

Like in the previous section, the finite element discretization of the Stokes problem (III.26) involves computing the solution of its variational formulation (III.31) in subspaces of finite-dimensional approximations  $\mathcal{V}_h$  and  $\mathcal{Q}_h$ , whereas  $\mathcal{V}_h$  can be written in form of:

$$\mathcal{V}_h = V_h \oplus \mathcal{B}_h \quad (\text{III.37})$$

and then the approximation subspaces  $(V_h, \mathcal{Q}_h, \mathcal{B}_h)$  are expressed in the following form:

$$\begin{aligned} V_h &= \{\mathbf{u}_h | \mathbf{u}_h \in \mathcal{C}^0(\Omega), \forall \mathcal{K}, \mathbf{u}_h|_{\mathcal{K}} \in \mathcal{P}^1(\mathcal{K})\} \\ \mathcal{B}_h &= \{\mathbf{b}_h | \mathbf{b}_h \in \mathcal{C}^0(\Omega), \mathbf{b}_h|_{\partial\mathcal{K}} = 0, \mathbf{b}_h|_{\mathcal{K}} \in \mathcal{P}^1(\mathcal{K}_i), 1 \leq i \leq 3\} \\ \mathcal{Q}_h &= \{p_h | p_h \in \mathcal{C}^0(\Omega), \forall \mathcal{K}, p_h|_{\mathcal{K}} \in \mathcal{P}^1(\mathcal{K})\} \end{aligned} \quad (\text{III.38})$$

Hence, the discrete Galerkin Stokes-fiber problem can be formulated as the search for a triplet of finite-dimensional approximation spaces  $(V_h, \mathcal{B}_h, \mathcal{Q}_h)$  to obtain a trio solution  $(\mathbf{u}_h, \mathbf{b}_h, p_h) \in V_h \times \mathcal{B}_h \times \mathcal{Q}_h$  such that  $(\mathbf{v}_h, \mathbf{b}_h^*, q_h) \in V_h \times \mathcal{B}_h \times \mathcal{Q}_h$ :

$$\begin{aligned} (2\eta \mathbf{E}(\mathbf{u}_h) : \mathbf{E}(\mathbf{v}_h)) + (\eta N_p[\mathbf{E}(\mathbf{u}_h) : \mathbf{a}_4] : \mathbf{E}(\mathbf{v}_h)) - (p_h, \nabla \cdot \mathbf{v}_h) &= 0 \\ (2\eta \mathbf{E}(\mathbf{b}_h) : \mathbf{E}(\mathbf{b}_h^*)) + (\eta N_p[\mathbf{E}(\mathbf{b}_h) : \mathbf{a}_4] : \mathbf{E}(\mathbf{b}_h^*)) - (p_h, \nabla \cdot \mathbf{b}_h^*) &= 0 \\ (\nabla \cdot \mathbf{u}_h, q_h) + (\nabla \cdot \mathbf{b}_h, q_h) &= 0 \end{aligned} \quad (\text{III.39})$$

It should be noted that the bubble functions possess the following properties [156]:

$$\begin{aligned} (\nabla \cdot \mathbf{b}_h, q_h) &= -(\mathbf{b}_h, \nabla q_h) \\ (\mathbf{C} : \nabla \mathbf{b}_h) &= 0, \text{ for all constant tensor } \mathbf{C} \end{aligned} \quad (\text{III.40})$$

The aforementioned properties have enabled the decoupling of the first two equations of the system (III.39).

### III.3.3.3 Algebraic formulation

Traditionally, the system arising from the discrete weak formulation can be expressed locally in the form of an algebraic system:

$$\begin{bmatrix} A_{uu} & 0 & B_{up} \\ 0 & A_{bb} & B_{bp} \\ B_{up}^T & B_{bp}^T & 0 \end{bmatrix} \cdot \begin{bmatrix} U \\ U_b \\ P \end{bmatrix} = \begin{bmatrix} F \\ F_b \\ 0 \end{bmatrix} \quad (\text{III.41})$$

where  $U$  denotes the vector containing the velocity components at each vertex of the triangular element (2D) or the tetrahedron (3D),  $U_b$  is the vector containing the bubble velocity components at each barycenter of the triangular element (2D) or the tetrahedron (3D) and  $P$  is the vector of pressure degrees of freedom. Notably,  $A_{uu}$  and  $A_{bb}$  respectively denote the symmetric matrices associated with the discrete form of the terms:

$$\begin{aligned} A_{uu} &= (2\eta \mathbf{E}(\mathbf{u}_h) : \mathbf{E}(\mathbf{v}_h)) + (\eta N_p [\mathbf{E}(\mathbf{u}_h) : \mathbf{a}_4] : \mathbf{E}(\mathbf{v}_h)) \\ A_{bb} &= (2\eta \mathbf{E}(\mathbf{b}_h) : \mathbf{E}(\mathbf{b}_h^*)) + (\eta N_p [\mathbf{E}(\mathbf{b}_h) : \mathbf{a}_4] : \mathbf{E}(\mathbf{b}_h^*)) \end{aligned} \quad (\text{III.42})$$

Finally, the matrices  $B_{up}$  and  $B_{bp}$  are associated with the terms  $\mathbf{b}(u_h, p_h)$  and  $\mathbf{b}(b_h, p_h)$ , respectively. Since the bubble is local to each triangle, it can be substituted using the standard technique of static condensation:

$$A_{bb}U_b + B_{bp}P = F_b \Rightarrow U_b = A_{bb}^{-1}(F_b - B_{bp}P) \quad (\text{III.43})$$

Thus, a classic mixed velocity-pressure formulation is obtained, in which the unknown vector is solely composed of the velocity and pressure fields at the nodes:

$$\begin{bmatrix} A_{uu} & B_{up} \\ B_{up}^T & C_{up} \end{bmatrix} \cdot \begin{bmatrix} U \\ P \end{bmatrix} = \begin{bmatrix} F \\ F_p \end{bmatrix} \quad (\text{III.44})$$

with  $C_{up} = -B_{bp}^T A_{bb}^{-1} B_{bp}$  and  $F_p = -B_{bp}^T A_{bb}^{-1} F_b$ . Then similar to what was done in the previous chapter II, the system obtained (III.44) is solved using the library of PETSc, which offers useful methods such as preconditioners in the resolution of partial differential equations.

### III.3.4 Solution algorithm

The flowchart presented in figure III.3 illustrates the sequence of steps involved in the algorithm. Initially, the orientation tensor is set to an isotropic state, and the probability distribution function  $\varphi$  is initialized at time  $t = 0$ . Subsequently, the orientation tensor is integrated into the Stokes equation to solve the fiber-flow coupling problem. Following the computation of the Stokes equation, the gradient of velocity  $\nabla \mathbf{u}$  and the norm of the generalized shear rate  $\dot{\gamma}$  are determined. These values, along with the initial probability distribution function  $\varphi^{t_n}$ , serve as input field for solving the Fokker-Planck equation. In turn, the resolution of the Fokker-Planck equation generates a new distribution function  $\varphi^{t_{n+1}}$  and computes the new orientation tensor  $\mathbf{a}_4^{t_{n+1}}$  at time  $t_{n+1} = t_n + \Delta t$ .

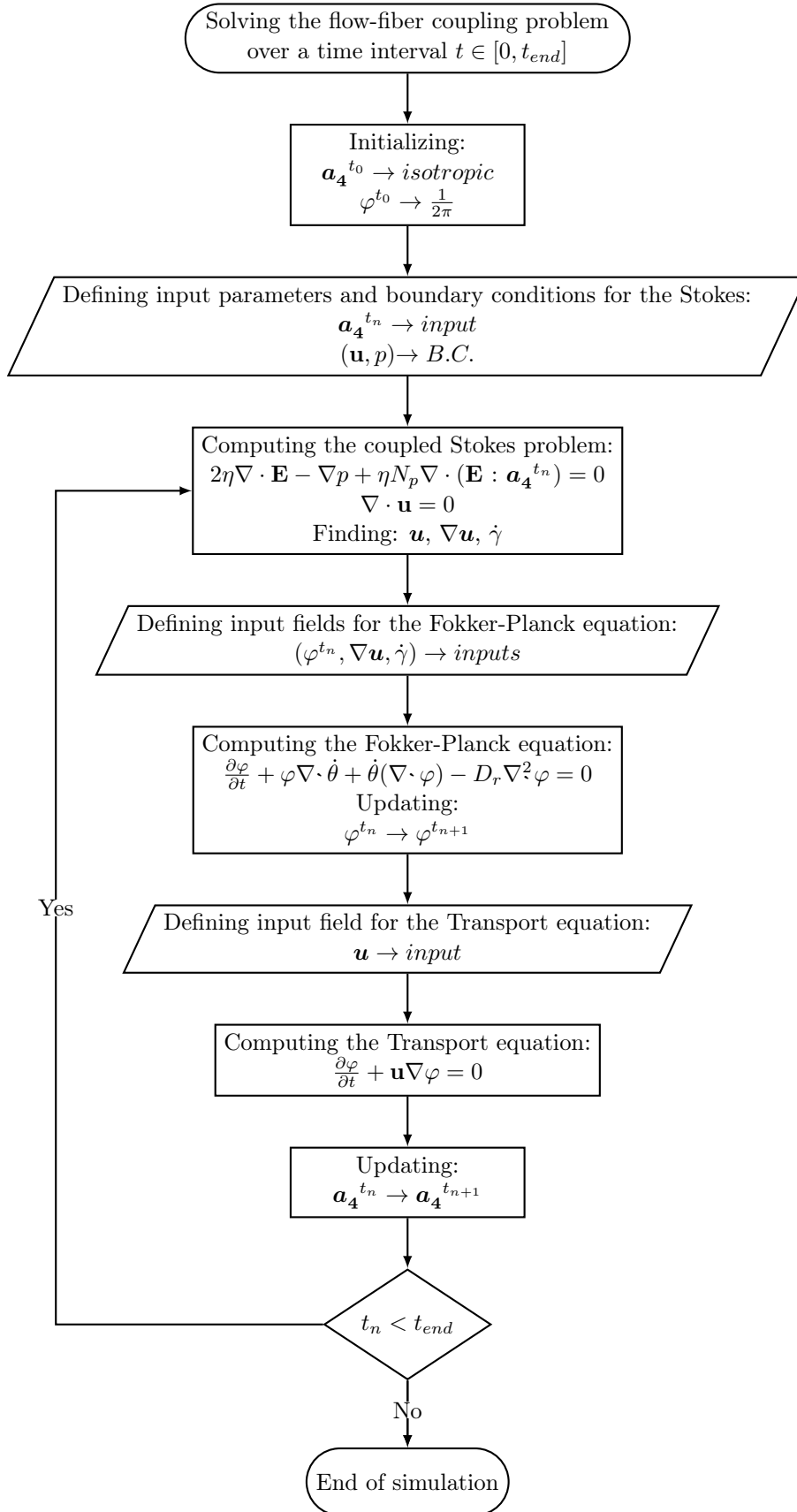


Figure III.3: Algorithm scheme

An advection equation is then calculated for the probability distribution, taking the velocity of the Stokes fluid  $\mathbf{u}$  as a input in order to transport the fibers. The newly computed orientation tensor  $\mathbf{a}_4^{t_{n+1}}$ , obtained from the solution of the Fokker-Planck equation, is again used as a input field in the calculation of the Stokes equation. This iterative process continues until the final time is reached.

### III.3.5 Short summary

- ✓ Multiscale modeling is a well-established simulation technique used to study injection molding processes, which involves considering various length scales (Macro-Micro).
- ✓ The constitutive equation of the Stokes equation is modified to account for fiber orientation by integrating a fourth-order orientation tensor into it in order to capture the influence of fiber orientation on the fluid flow.
- ✓ A transport (advection) equation is incorporated into the set of equations, comprising the Fokker-Planck equation and the Stokes equation, in order to account for the fiber advection based on the fluid velocity field.
- ✓ The MINI-element or P1+/P1 element method is used for approximating the velocity and pressure fields in the Stokes equation in order to provide a stable and accurate discretization of the equations.
- ✓ The algorithm is based on linking three solvers (Stokes, Fokker-Planck and Transport) that run consecutively, where the outputs of one solver are used as inputs for the next solver in the sequence.

## III.4 Numerical results

### III.4.1 Parallel computing

Parallel computing is an advanced technology that has revolutionized scientific research, allowing for faster and more efficient computations. By harnessing the power of multiple processors or computing nodes, parallel computing enables tasks to be executed simultaneously, resulting in improved performance and the ability to handle large-scale datasets. This approach involves breaking down complex computational problems into smaller, independent tasks, where the workload is enabled through parallel computing to be distributed among the available processing units, allowing for concurrent processing and reducing the overall computational time. This method is particularly advantageous when dealing with computationally intensive tasks or large amounts of data that would be impractical or time-consuming to process sequentially. As it is aforementioned in chapter II, the MPI technique using Open MPI library is implemented to effectively distribute the computational workload, optimizing efficiency.

Therefore the MPI technique is employed to solve the fiber-flow coupling problem, a computational task that can be time-consuming, often taking several hours or even days to complete, particularly when employing fine meshes for the Fokker-Planck (II.16) equation and the Stokes (III.26) and advection (III.27) equations. It is important to note that the individual solvers for the Fokker-Planck, Stokes, and advection equations independently do not require significant computation time, with results available within seconds. However, the coupling between these solvers involves significantly higher computation time. As it is discussed in the previous chapters, to accurately predict fiber orientation throughout the configurational domain in the context of solving the Stokes problem, the Fokker-Planck equation must be resolved at each node within this domain. To speed up this process and improve computational efficiency, the use of MPI technique is essential. By leveraging the power of multiple cores, the computations are distributed among them. For instance, if the configurational domain of the Stokes problem is discretized into ( $\mathbf{nb}_{\text{Stokes}} = 900$  nodes) and there are ( $\mathbf{n}_f = 4$  available cores), each core will handle the computation of the Fokker-Planck equation for a subset of nodes ( $900/4$ ) in parallel. This parallelization effectively reduces the computational burden by enabling multiple cores to simultaneously solve the Fokker-Planck equation, significantly speeding up the overall process compared to using a single core to solve the equation for all ( $\mathbf{nb}_{\text{Stokes}} = 900$  nodes) sequentially.

In order to simulate the translational motion of fibers within the flow, the advection equation needs to be solved. This equation is computed for each component of the probability distribution function across the entire configurational domain, utilizing the results obtained from solving the Fokker-Planck equation. Similarly to what has been done above and to speed up this process, the MPI technique is also employed to distribute the computations across multiple cores. For instance, if the probability distribution function consists of ( $\mathbf{nb}_{\text{Fokker}} = 1024$  components) and there are ( $\mathbf{n}_a = 4$  available cores), each core will handle the computation of the advection equation for a subset of ( $1024/4$ ) components in parallel. This parallelization significantly reduces the overall computation time, enhancing the efficiency of the fiber-flow coupling simulation.

$\mathbf{nb}_{\text{Stokes}} \backslash \mathbf{nb}_{\text{Fokker}}$	24	128	256	1024	2048
9	t(1,1)=1mn6s t(1,4)=41s t(4,4)=22s	t(1,1)=4mns33s t(1,4)=1mn29s t(4,4)=1mn15s	t(1,1)=8mns37s t(1,8)=1mn41s t(8,8)=1mn31ss	t(1,1)=33mns6s t(1,16)=2mns39s t(16,16)=2mns29s	t(1,1)=1h4mns52s t(1,16)=5mns5s t(16,16)=4mns50s
146	t(1,1)=5mns33s t(4,1)=2mns10s t(4,4)=1mn36s	t(1,1)=9mns49s t(4,4)=2mns36s t(8,8)=1mn32s	t(1,1)=12mns48s t(4,8)=2mns30s t(8,8)=1mn56s	t(1,1)=36mns58s t(4,16)=3mns49s t(16,16)=3mns3s	t(1,1)=1h9mns9s t(4,16)=6mns14s t(16,16)=5mns26s
825	t(1,1)=30mns52s t(8,4)=3mns56s t(8,8)=3mns40s	t(1,1)=34mns18s t(8,4)=5mns22s t(8,8)=4mns49s	t(1,1)=38mns7s t(8,4)=6mns21s t(8,8)=5mns27s	t(1,1)=1h9mns53s t(8,16)=6mns42s t(16,16)=4mns45s	t(1,1)=1h35mns18s t(8,16)=9mns29s t(16,16)=7mns16s
2092	t(1,1)=1h14mns41s t(16,4)=5mns12s t(16,16)=5mns12s	t(1,1)=1h18mns32s t(16,4)=6mns15s t(16,8)=5mns52s	t(1,1)=1h23mns4s t(16,8)=8mns5s t(16,16)=7mns7s	t(1,1)=1h47mns38s t(16,8)=12mns26s t(16,16)=11mns31s	t(1,1)=2h13mns48s t(16,8)=18mns30s t(16,16)=12mns37s

(..):(number of cores used for fokker-planck, number of cores used for advection)

Table III.1: Computation time for fiber-flow coupling: Impact of varying number of cores

To assess the impact of utilizing the MPI technique in the implementation of solvers for full fiber-flow coupling simulations, the complete code linking all the solvers was executed for a single time step across various scenarios. The problem was formulated with specific parameter values for solving the Stokes equation in the fiber-flow coupling simulations. The fluid viscosity  $\eta$  and the pressure drop  $\Delta p$  were set to 1 Pa.s and 2 Pa, respectively. The initial orientation tensor  $\mathbf{a}_4$  was assumed to be isotropic, and the number of fibers  $N_p$  in the system was set to 100. For the Fokker-Planck equation, the chosen parameters were a lambda value  $\lambda$  of 0.98 and a coefficient of interaction  $C_I$  of 0.1. By altering the number of nodes used in solving the Fokker-Planck and advection equations, and adjusting the number of cores dedicated for each case, the effect of parallel computing could be evaluated. It is worth noting that these two equations require a significant amount of computation time within the fiber-flow coupling problem.

The total time taken to resolve the full fiber-flow coupling problem for one iteration was then determined, allowing for the deduction of the parallel technique's influence on computational efficiency and speed. By conducting these analyses, the benefits and effectiveness of parallel computing in improving the overall performance and time efficiency of the fiber-flow coupling simulations can be quantitatively assessed as it is illustrated in table III.1. The results presented in the table III.1 clearly demonstrate that the total computational time required to solve a fiber-flow coupling problem increases with mesh refinement for both the Fokker-Planck and Stokes equations. For instance, in the first case, the Fokker-Planck equation and advection equation were solved 9 and 24 times, respectively, for a single iteration. In contrast, in the last case, the Fokker-Planck equation and advection equation were solved 2092 and 2048 times, respectively, for a single iteration. It is noteworthy that each run of either the Fokker-Planck or advection equation took approximately 2 seconds. This is evident in the total computation time for solving the fiber-flow coupling problem, which was 1 minute and 6 seconds for the first case ( $\mathbf{nb}_{\text{Fokker}}=24$ ,  $\mathbf{nb}_{\text{Stokes}}=9$ ) with a single core used, and increased to 1 hour, 4 minutes, and 52 seconds for the last case of the first row in the table ( $\mathbf{nb}_{\text{Fokker}}=2048$ ,  $\mathbf{nb}_{\text{Stokes}}=9$ ) with the same number of cores employed. Furthermore, the results presented in table III.1 highlight the significance of utilizing multiple cores to reduce the overall computational time. It is evident that the total computation time can be significantly decreased by a factor equal to the number of cores used. For example, in the last case ( $\mathbf{nb}_{\text{Fokker}}=2048$ ,  $\mathbf{nb}_{\text{Stokes}}=2092$ ), where the reduction in computation time is most pronounced, employing 16 cores for both the Fokker-Planck and advection equations resulted in a decrease in total time from 135 minutes to 12 minutes. This represents a substantial gain in computational efficiency. Similarly, using a higher number of cores demonstrated a consistent decrease in computation time across all the cases presented in the table III.1. These findings highlight the impact of mesh refinement on the computational time and emphasize the importance of parallel computing in accelerating the solution of fiber-flow coupling problems and demonstrate its potential for significantly reducing computation time.

### III.4.2 Effect of rheological coupling coefficient $N_p$ on flow and fiber orientation

The investigation of the influence of the rheological coupling coefficient,  $N_p$ , on both the fiber orientation within the flow and the flow itself represents a central component of this study. To comprehensively address this influence, simulations were conducted under Poiseuille flow conditions, employing the Stokes equation. The computational domain adopted for these simulations featured a rectangular

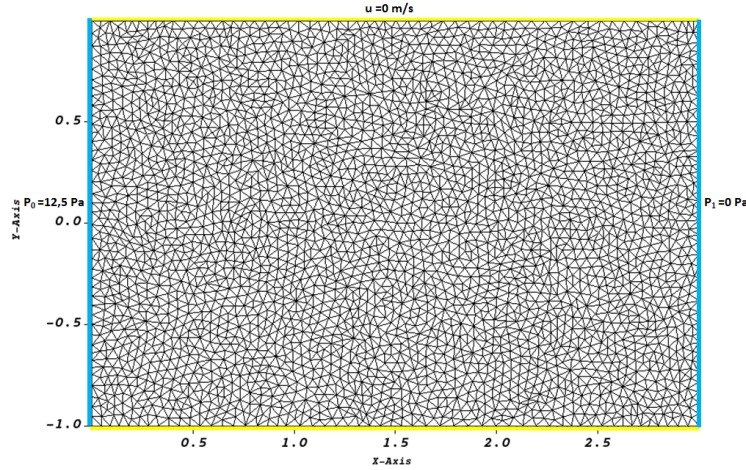


Figure III.4: Rectangular domain: FE mesh

configuration with a height of 2 m and a length of 4 m, discretized into 3123 nodes, as depicted in Figure III.4. Boundary conditions were precisely defined: the pressure at the inlet, denoted as  $P_0$ , was set to 12.5 Pa, while the outlet pressure,  $P_1$ , was established at 0 Pa. A non-slip boundary condition was imposed along the top and bottom walls. The dynamic viscosity of the fluid,  $\eta$ , was assigned a value of 1 Pa·s. In terms of the advection equation, a fully randomized fiber orientation distribution was enforced at the inlet, constituting a Dirichlet boundary condition ( $\varphi = \frac{1}{2\pi}$ ), while an initial planar random orientation was also mandated across the entire domain. Within the framework of the Fokker-Planck equation, the angular domain underwent discretization with a mesh size  $h$  of  $\frac{2\pi}{1024}$ . Temporal discretization was executed via the Rosenbrock-W scheme, employing a time step  $\Delta t$  of  $5 \times 10^{-2}$  s. Additional parameters included a shape factor  $\lambda$  set at 1 and an interaction coefficient  $C_I$  established at 0.001. Notably, these simulations encompassed a range of rheological coupling coefficients, specifically  $N_p$  values of 0, 10, 20, 30, and 40, allowing for a comprehensive exploration of the coupling effect's impact.

#### III.4.2.1 Uncoupled flow case

The exploration of fiber orientation predictions begins within the framework of an uncoupled flow field scenario, specifically when  $N_p = 0$ . In this case, as mentioned above, a steady flow under Poiseuille flow conditions is assumed, where streamlines remain consistently parallel both to each other and to the channel walls. Simulations were conducted until a state of steady flow was reached, indicating that all fiber ori-

entations within the domain have settled into a stable equilibrium. As illustrated in figure III.5, this scenario reveals the evolution of fiber orientation within the flow over time. It is noteworthy that in the absence of coupling effects, the velocity profile remains unchanged throughout the simulation, preserving the characteristic parabolic distribution along the  $y$ -direction (vertical) in the fluid domain. The el-

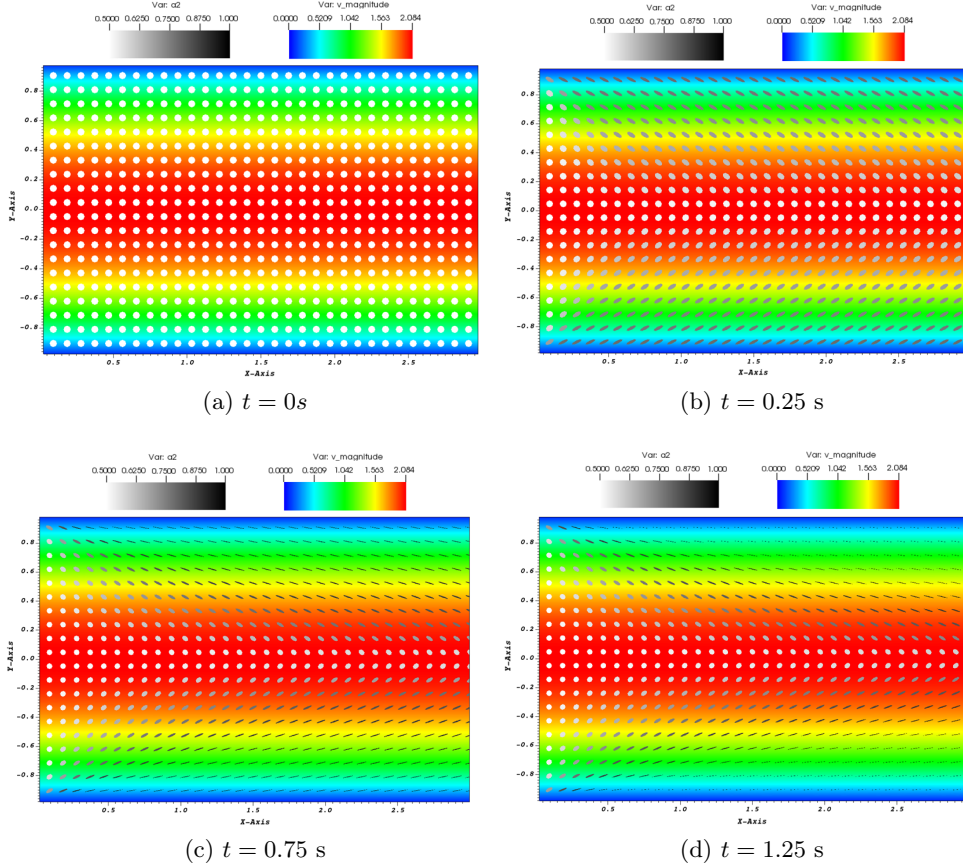


Figure III.5: Evolution of fiber orientation within flow: time-dependent changes in fiber alignment and distribution with  $N_p = 0$

lipses, serving as representations of average fiber orientations, are derived from the second-order orientation tensor  $\mathbf{a}_2$ . The eigenvalues and eigenvectors of  $\mathbf{a}_2$  govern the major axes of these ellipses in the  $xy$ -plane, signifying the degree of orientation along these axes. The coloration of the ellipses indicates the magnitude of the eigenvalue in the  $\theta$ -direction, with white signifying isotropic conditions ( $a_{xx} = a_{yy} = 0.5$ ) and black representing full fiber alignment. Interestingly, in proximity to the centerline axis, fiber orientation appears quasi-random due to the absence of  $\nabla \mathbf{u}$ , while closer to the wall, the ellipses progressively flatten and align. Additionally, partial alignment arises due to the nonzero value of  $C_I$ , which prevents the achievement of perfect fiber alignment along the streamlines. This observation is consistent with the predictions of the Folgar-Tucker model [59]. Moreover, in the absence of coupling effects ( $N_p = 0$ ), a fiber suspension flowing between plates can be considered spatially uniform, enabling the calculation of dynamic orientation history along a

streamline when moving with the fluid.

### III.4.2.2 Coupled flow case

The investigation examines the influence of the rheological coupling coefficient  $N_p$  when considering the coupling effect ( $N_p \neq 0$ ) on both the fiber orientation and the velocity profile within the simulation domain. It is important to note that all previous numerical and boundary conditions remained consistent throughout these simulations, with the sole alteration being the adjustment of  $N_p$  to observe its impact in the context of coupled flow.

### Temporal evolution of fiber orientation with varying $N_p$

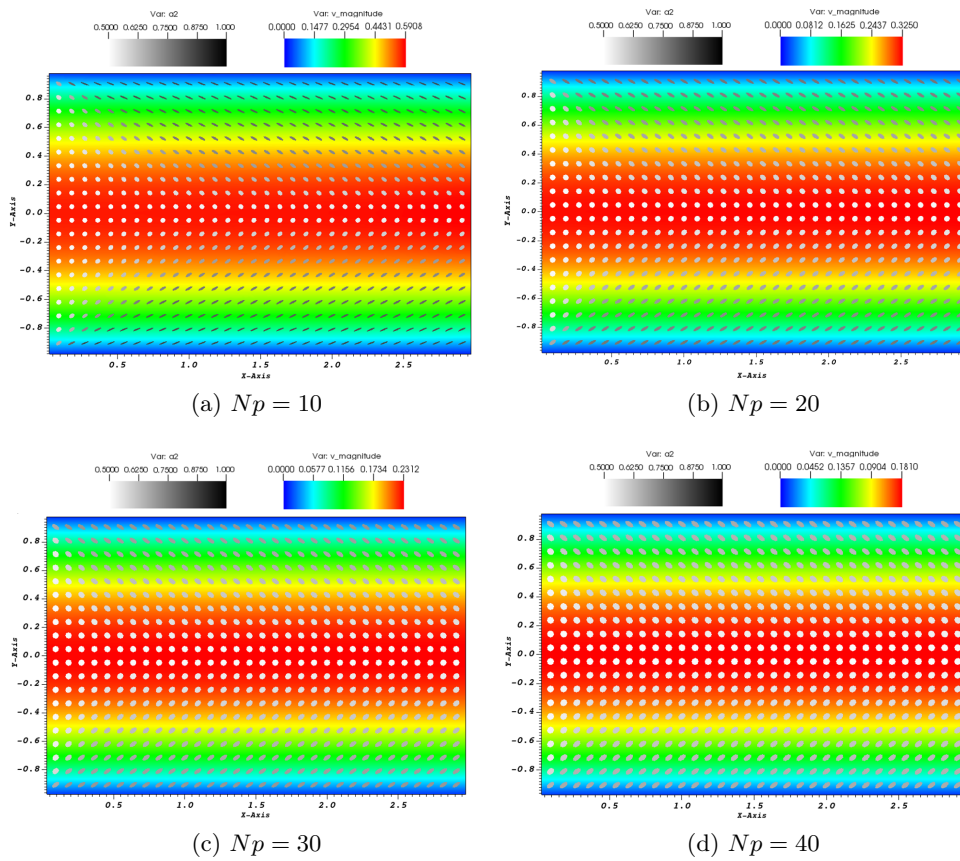


Figure III.6: Fiber orientation evolution over time at  $t = 0.75$  s for various  $N_p$

Notably, one significant effect becomes apparent as fiber concentration increases with higher  $N_p$  values, which implies a more substantial coupling between the fibers and the fluid. This, in turn, potentially leads to longer relaxation times required for the fibers to align with the flow. To illustrate this phenomenon, we examine the time evolution of fiber orientation at different time intervals for various  $N_p$  values, including the time at which they reach a steady state. As observed in figures III.6 through III.9, it becomes apparent that achieving a steady state in fiber orientation

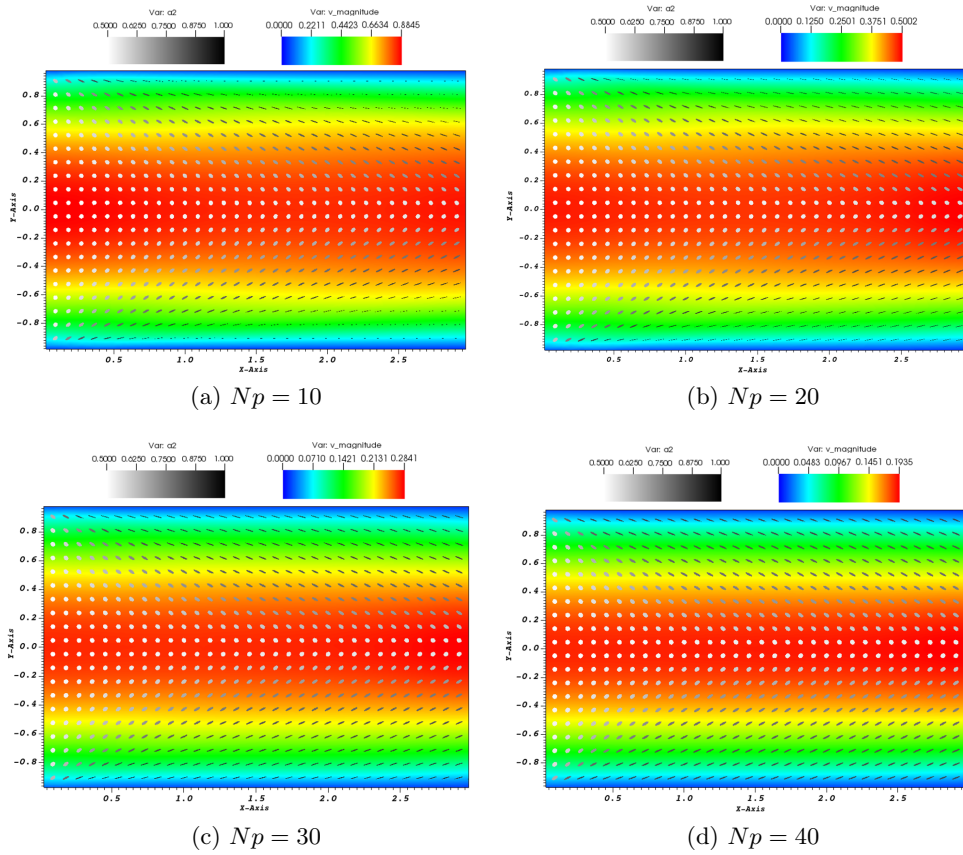


Figure III.7: Fiber orientation evolution over time at  $t = 2.5$  s for various  $N_p$

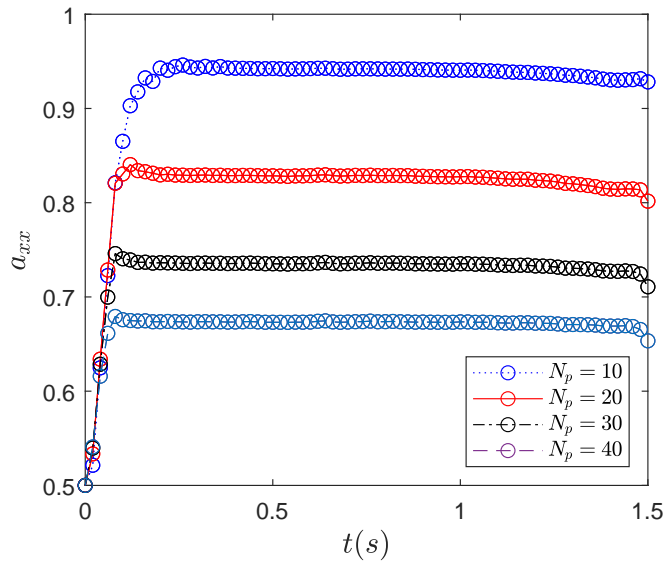


Figure III.8: Time evolution of  $a_{xx}$  for different  $N_p$  at  $y = 0.95$ m

requires significantly more time as  $N_p$  increases. For example, in the case of  $N_p = 10$ , it took approximately 7.5 seconds to reach a steady state. In contrast, for  $N_p = 20$  and  $N_p = 30$ , this duration extended to around 12 and 15 seconds, respectively.

Notably, for  $N_p = 40$ , the steady state took roughly 20 seconds to establish. In addition, figure III.8 illustrates the time-dependent evolution of the first component of the orientation tensor,  $a_{xx}$ , for various  $N_p$  values near the upper wall. It is evident that as  $N_p$  increases, fibers require more time to fully align with the flow direction. These observations highlight the substantial influence of the coupling coefficient  $N_p$  on the dynamics of fiber orientation and the time required for these orientations to stabilize under varying conditions. Similar to the previous section (section III.4.2.1), the ellipses, which depict the average fiber orientations, are determined using the second-order orientation tensor  $\mathbf{a}_2$ . These ellipses' coloration corresponds to the magnitude of eigenvalues in the  $\theta$ -direction. White color denotes isotropic conditions ( $a_{xx} = a_{yy} = 0.5$ ), while black signifies complete alignment of the fibers representing the highest level of anisotropy.

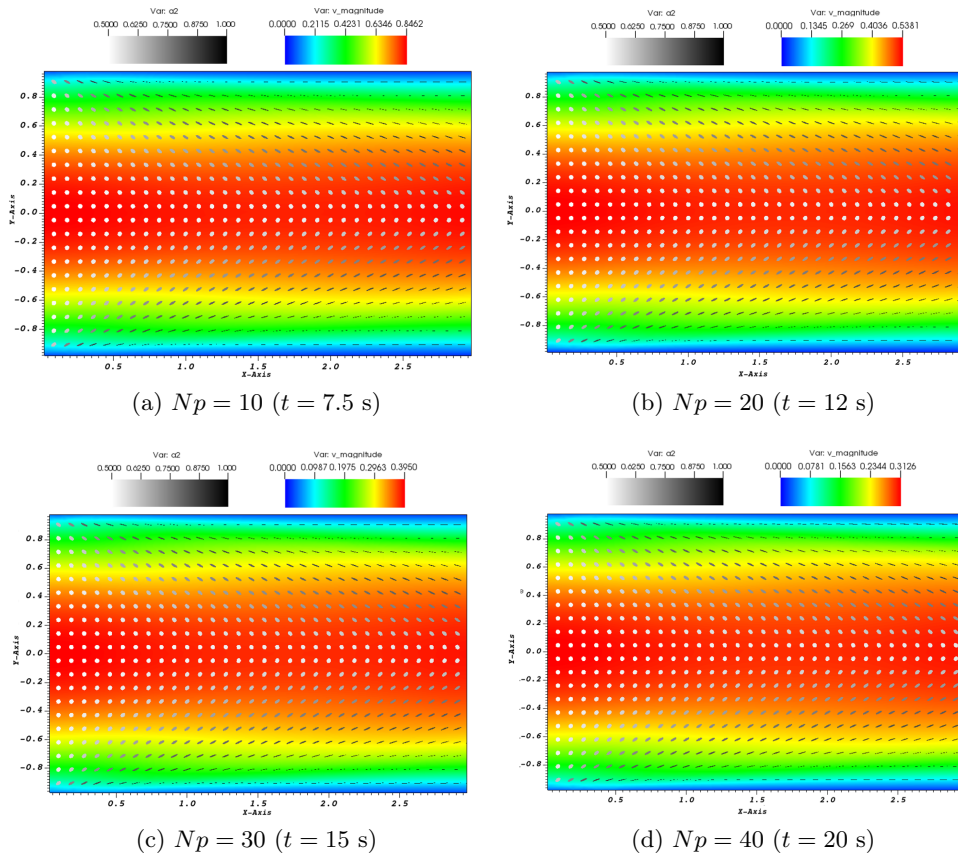


Figure III.9: Fiber orientation at steady state for various  $N_p$

### Impact of $N_p$ on the velocity profile

Moreover, the consideration of the coupling effect ( $N_p \neq 0$ ) has also a noticeable impact on the velocity profile. This transformation occurs as the fiber suspension transitions into a non-Newtonian fluid due to the introduction of particle stress contributions in the momentum equation (III.26). In fact, anisotropic viscosities are obtained once average fiber orientations deviate from their initial 2D random

configuration. Consequently, the total viscosity, particularly within the core region, increases, leading to changes in flow behavior. In all figures III.6 to III.9, a Newtonian profile is observed at the inlet due to the imposed boundary condition. Since an isotropic orientation is assumed at the inlet ( $x = 0$ ), the equivalent viscosity remains homogeneous. However, beyond the entrance, streamlines experience slight disturbances for all different  $N_p$  values, gradually returning to parallel alignment as they approach the outlet. The transition to non-Newtonian behavior becomes evident across figures III.6 to III.9, with increasing  $N_p$  corresponding to a reduction in maximum velocity and a flatter velocity profile within the core, compared to the result obtained from the decoupled problem. This is clearly illustrated in figure III.10, which depicts the velocity profiles at the outlet ( $x = 3\text{m}$ ) for all different  $N_p$  values.

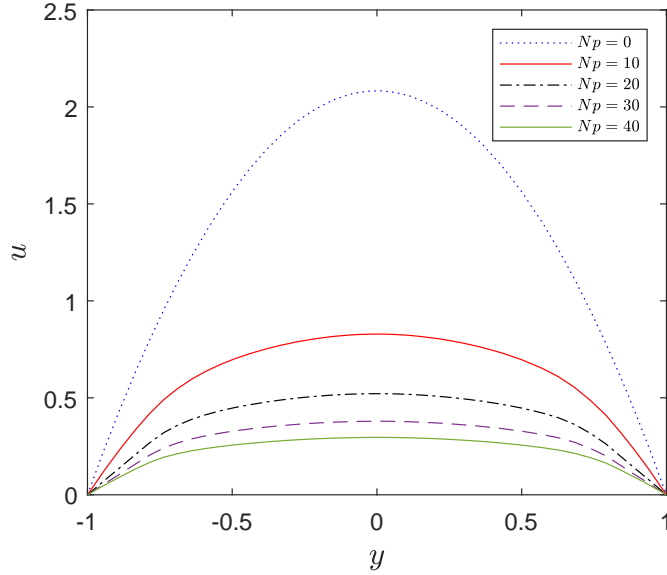


Figure III.10: Velocity profile variations at the outlet ( $x = 3\text{m}$ ) for different  $N_p$

### Fiber orientation changes with increasing $N_p$

Furthermore, the interaction between the flow and fibers introduces another significant influence on the pattern of the fiber orientation. To illustrate this phenomenon, we examine the evolution of the first component of the second-order orientation tensor,  $a_{xx}$ , across the domain for various values of  $N_p$ . These results are presented in figure III.11. It is notable that as  $N_p$  increases, a distinctive shift in fiber orientation patterns happens, particularly within the core region. This shift results in fibers gradually aligning transversely to the flow direction. The emergence of a vertical velocity component,  $u_y$ , is important in this process. Interestingly, even under Poiseuille flow conditions, a slight increase in the vertical velocity  $u_y$  is observed due to the coupling problem. This increase in vertical velocity exerts an influence on the fibers, causing them to align in the  $y$ -direction.

In figure III.12, an analysis of the variation in  $a_{xx}$  at  $x = 1.5$  between the coupled

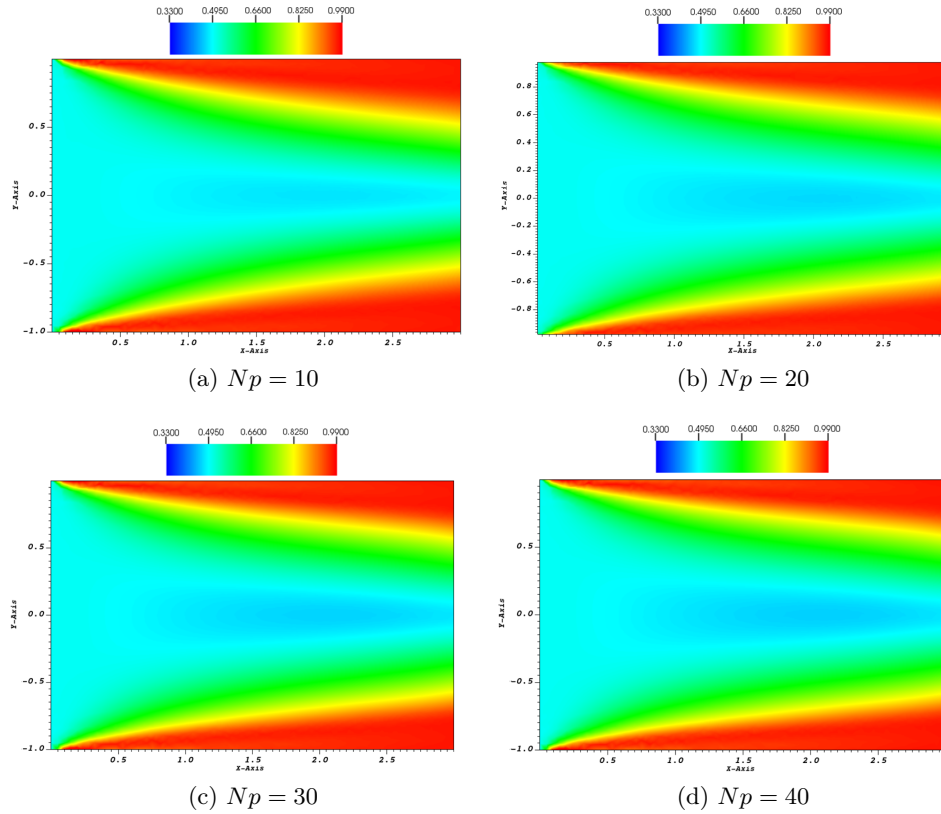


Figure III.11: Fiber orientation  $a_{xx}$  at steady state for various  $N_p$

and decoupled solutions ( $\Delta a_{xx} = a_{xx}^{coupled} - a_{xx}^{decoupled}$ ) is presented. The results reveal that  $\Delta a_{xx}$  exhibits the most significant decrease in the shell region between the skin and the core regions, with a comparatively smaller reduction observed in the central core region. Interestingly, this difference is not notably evident in the vicinity of the channel walls. These findings are in line with those obtained in figure III.11. Several factors contribute to these outcomes. Firstly, in the context of the coupled solution, the continuity equation drives a flattening of the velocity profile (as depicted in figure III.10), leading to a mass flow relocation towards the channel walls. Consequently, the shear components of  $\nabla \mathbf{u}$  promote changes in  $a_{yy}$ , resulting in a decrease in  $a_{xx}$  from the centerline towards the shell region, as evident in figure III.11. Conversely, the flattening of the velocity profile decreases the shear component  $E_{12}$  in the central region, as reported in [157], which subsequently leads to a slower alignment in the horizontal direction. Importantly, the asymptotic state remains unaltered by the coupling effect. As a consequence, the difference  $\Delta a_{xx}$  becomes negligible in the wall region and even in the limiting case of an infinitely long channel. The variation in fiber orientation attributed to coupling falls within the range of -13.5% and 0.5% on the [0.33, 0.99] scale.

#### Influence of $N_p$ on generalized shear rate $\dot{\gamma}$

Figure III.13 presents the variation of the generalized shear rate  $\dot{\gamma}$  along the  $y$ -axis, specifically at the center of the domain ( $x = 1.5$  m). It shows a substantial

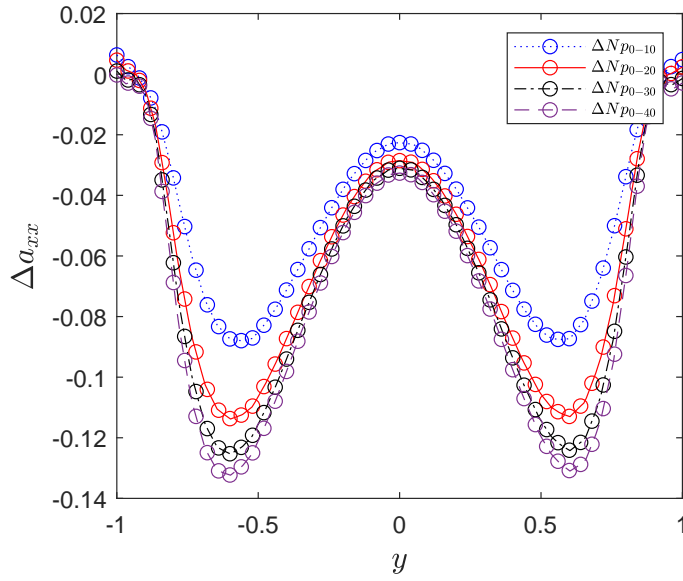


Figure III.12: Variation of  $a_{xx}$  difference at  $x = 1.5$ : coupled vs uncoupled solutions for different  $N_p$

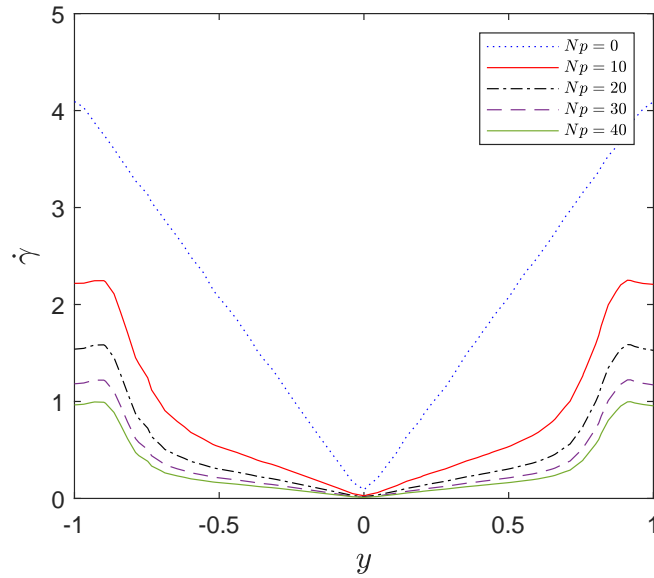


Figure III.13: Variation of  $\dot{\gamma}$  at the center ( $x = 1.5\text{m}$ ) for different  $N_p$

reduction in  $\dot{\gamma}$  for the coupled solution ( $N_p \neq 0$ ) in comparison to the uncoupled solution ( $N_p = 0$ ), with the most pronounced decline occurring in the skin and shell regions. The results also reveal that as the rheological coupling coefficient  $N_p$  increases, the  $\dot{\gamma}$  profile widens significantly within the core region. In contrast, for the case of  $N_p = 0$ , the profile exhibits a distinct triangular sharp edge, which is clearly demonstrated in figure III.13. An interesting observation is a minor reduction in the shear rate for the case of the coupled solution, particularly near the boundary wall. This drop can be attributed to the fountain flow effect.

### III.4.3 Effect of interaction coefficient $C_I$ on fiber orientation

In a manner similar to the approach employed in the previous section, simulations were conducted for a channel flow case within the domain illustrated in figure III.4, while maintaining the same boundary conditions. This investigation focuses, while

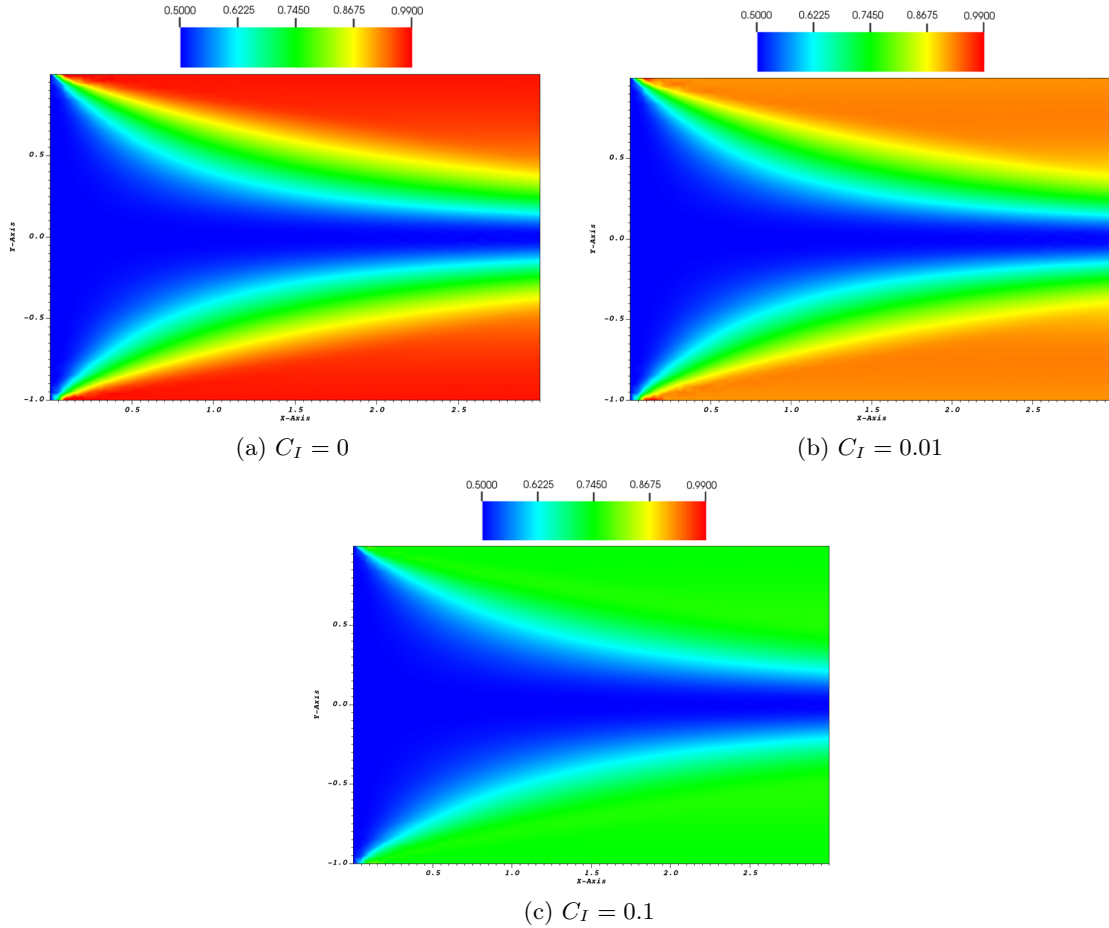


Figure III.14: Evolution of  $a_{xx}$  in flow for different  $C_I$

setting  $N_p = 0$ , on the critical analysis of the influence of the interaction coefficient  $C_I$  on fiber orientation within the flowing medium. To ensure consistency and rigor, the numerical parameters will remain as follows: a Rosenbrock-W scheme will be used for time integration, and a time step of  $\Delta t = 5 \times 10^{-2}$  s will be employed for resolving both the Fokker-Planck and spatial advection equations. This setup ensures a robust and controlled environment for the exploration of the relationship between the interaction coefficient  $C_I$  and fiber orientation in the context of fluid flow. Figure III.14 offers a comprehensive insight into the influence of the interaction coefficient  $C_I$  on fiber orientation, particularly after a prolonged period during which the fiber orientation reaches a steady state. This examination involved three distinct simulations, varying the interaction coefficient from 0 to 0.1, with a primary focus on tracking the evolution of the first component of the second-order orientation tensor,  $a_{xx}$ . Notably, when  $C_I = 0$ , corresponding to the elimination of the

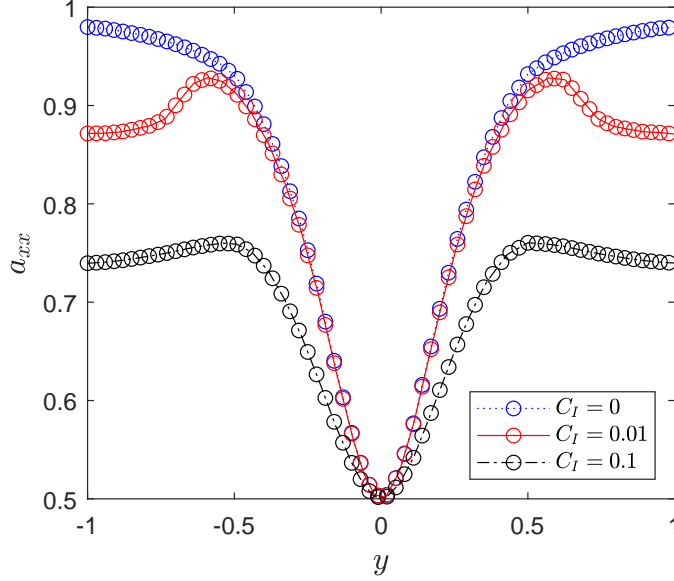


Figure III.15: Variation of  $a_{xx}$  at the outlet ( $x = 3\text{m}$ ) for different  $C_I$

diffusion term within the Fokker-Planck equation, a distinctive pattern emerges. Fibers tend to align themselves predominantly along the flow direction near the walls, whereas within the core region where the generalized shear rate  $\dot{\gamma}$  approaches zero, fiber orientation becomes more random. In this regime, the orientation dynamics are primarily governed by the advection term of the Fokker-Planck equation. As we increase  $C_I$ , the diffusion term plays a more prominent role, leading to observable changes. Figures III.14b and III.14c vividly illustrate this transition. As  $C_I$  increases, the alignment of fibers near the walls is hindered, and the orientation distribution becomes more isotropic. Particularly, in Figure III.14c with a higher  $C_I$  value, the zone of isotropic orientation expands further into the core region. In order to thoroughly clarify the influence of the interaction coefficient  $C_I$ , a detailed examination of the evolution of  $a_{xx}$  was conducted along the outlet's  $y$ -axis, as demonstrated for varying  $C_I$  values in figure III.15. The findings reveal a discernible pattern: as the interaction coefficient increases, the alignment of fibers along the wall with the direction of flow progressively decreases, as the value of  $a_{xx}$  goes down from 0.99 to 0.75, for  $C_I$  values of 0 and 0.1 respectively. Conversely, the orientation of the fibers within the core region appears to be much less sensitivity to fluctuations in the interaction coefficient. Intriguingly, there is an observable increase in the value of  $a_{xx}$  within the transitional zone situated between the wall and the core. This phenomenon can be explained as a result of the interplay between the advection and diffusion terms inherent to the Fokker-Planck equation. Consequently, it can be inferred that within this intermediate region, the advection term plays a central role in influencing the state of the fiber orientation. Conversely, closer to the wall, the diffusion term tends to slightly dominate, reflecting the involved dependence of both terms on the generalized shear rate  $\dot{\gamma}$ . A similar trend was observed in the studies conducted both numerically and experimentally as reported in [158, 159]. These intricate observations contribute to a more thorough understanding of the

interrelationship between the interaction coefficient and the spatial distribution of fiber orientation across the domain.

#### III.4.4 Short summary

- ✓ Parallel computing using the MPI library is employed in the code to reduce computational time.
- ✓ Distributing the computation of the fiber-flow coupling problem across multiple nodes results in a time reduction of up to 25 times per iteration.
- ✓ The rheological coupling coefficient  $N_p$  plays a central role in the velocity profile as it causes the fluid to transition into a non-Newtonian state due to the contribution of fibers to the fluid's viscosity.
- ✓ Increasing  $N_p$  induces a notable shift in fiber orientation, particularly in the core region, driven by the emergence of a vertical velocity component,  $u_y$ , even under Poiseuille flow conditions, influencing fibers to align in the  $y$ -direction.
- ✓ As expected, a higher interaction coefficient leads to less alignment of fibers near the wall in the direction of flow. An increase in the  $C_I$  factor results in a greater average misalignment of fibers. However, the orientation of fibers within the core region is much less influenced by the value of the interaction coefficient.

### III.5 Conclusion

In conclusion, this study addresses a 2D fiber-flow coupling problem employing a multiscale modeling approach, which finds applications in understanding complex processes like injection molding, encompassing macro to micro interactions. A modified constitutive equation for the Stokes equation is introduced, incorporating a fourth-order orientation tensor to capture fiber orientation's influence on fluid flow. Additionally, an advection equation is integrated into the governing equations to account for fiber spatial motion within the fluid domain at the macroscale. These components link three solvers (Stokes, Fokker-Planck, and Transport) operating consecutively. Parallel computing via the MPI library significantly enhances computational efficiency, distributing tasks across multiple nodes, thus accelerating simulations.

Our investigation into the rheological coupling coefficient  $N_p$  and the interaction coefficient  $C_I$  reveals their substantial impact on both the fluid behavior and fiber orientation evolution within the fluid domain. Specifically,  $N_p$  emerges as a critical determinant of the velocity profile, transforming the fluid into a non-Newtonian state due to fiber-induced viscosity alterations. Conversely, higher  $C_I$  values result in reduced fiber alignment near the wall in the direction of flow, leading to greater average misalignment. Notably, the orientation of fibers within the core region remains relatively unaffected by changes in  $C_I$ . These findings highlight the central role of the coupling coefficient in controlling the fiber alignment within the flow, crucial for modeling complex fluid-fiber interactions.

# Application: complex geometries

---

## Contents

---

<b>IV.1 Introduction</b> . . . . .	<b>91</b>
<b>IV.2 Configurations of fluid-fiber coupling in diverse geometries</b>	<b>93</b>
IV.2.1 Complex shape models . . . . .	93
IV.2.2 Numerical results . . . . .	95
IV.2.3 Short summary . . . . .	114
<b>IV.3 Problem setup for a real-case injection molding scenario</b> . .	<b>114</b>
IV.3.1 Two-phase flow model . . . . .	114
IV.3.2 Numerical results . . . . .	117
IV.3.3 Short summary . . . . .	124
<b>IV.4 Conclusion</b> . . . . .	<b>124</b>

---

In the previous chapter, the investigation of the fiber-flow coupling problem focused on a simple rectangular geometry. While this provided valuable insights, it is necessary to extend the analysis to more complex domains that better represent real-world scenarios encountered in injection molding processes. Thus, the present chapter is dedicated to conducting simulations on complex geometries, such as a contraction and L-shaped regions that roughly emulates the geometry of a mold used in actual injection molding processes, and then extending the study to develop a foundational model for describing an overmolding process. The objective of this chapter is to describe the obtained results, specifically examining the impact of different geometries on fiber motion during the injection phase, and to extend the analysis to a two-phase model, considering the injected thermoplastic, which is considered as a complex fluid. By exploring these different models and their descriptions of the complex behavior of the injected thermoplastic, a more comprehensive understanding of the fiber-flow coupling phenomenon and its behavior in realistic injection molding scenarios can be achieved.

## IV.1 Introduction

Understanding the motion of fibers within the injected fluid during the injection phase is crucial for optimizing the manufacturing process and enhancing the mechanical properties of the final product. The distribution and alignment of fibers significantly influence the mechanical strength, stiffness, and other functional properties of fiber-reinforced composite materials. Moreover, the interaction between

fibers and the surrounding fluid can impact the filling behavior, flow front advancement, and pressure drop during injection molding.

By simulating fiber-flow coupling in complex geometries that closely resemble real injection molding scenarios, we can obtain a comprehensive understanding of the underlying mechanisms governing the behavior of fiber-reinforced composites. This understanding is vital for constructing accurate predictive models that can be used to optimize the injection process, predict fiber alignment, estimate the mechanical properties of the final product such as strength, stiffness, and other functional properties of composite materials, and guide the design of composite materials for specific applications. Thus, the study of fiber-flow coupling in injection molding processes plays a crucial role in comprehending the dynamics of complex fluid systems and their influence on the overall manufacturing process.

Consequently, one of the objective of this chapter is to emphasize the importance of applying fiber-flow coupling in complex geometries to investigate fiber motion during the injection phase and its effect on the surrounding fluid. In the past years, researchers have developed numerical techniques for predicting fiber orientation within intricate geometries by addressing the coupling between fluid flow and fiber orientation distribution. The work done in [84] developed a numerical methodology to analyze streamlines in a 4.5:1 axisymmetric contraction at low Reynolds numbers, using a Newtonian fluid with sparse, high aspect ratio fibers. Remarkably, their results correlated quantitatively with experimental observations despite using the aligned-fiber approximation. A fully coupled solution is employed in [121] to predict fiber suspension flow in various complex geometries, encompassing axisymmetric contractions, expansions, and center-gated disks. Another work done in [160] emphasized the impact of three-dimensional flow and fountain flow on fiber orientation during the injection molding of thick wall parts. Ranganathan and Advani [40] explored fiber-fiber interactions based on the Folgar-Tucker model [59] in axisymmetric diverging radial flow.

Through computational simulations and comprehensive analysis, we aim to construct a robust model capable of accurately capturing the intricate dynamics involved in real-world injection molding processes. The knowledge derived from this research is expected to advance manufacturing techniques, facilitate improved material designs, and enhance the overall performance of fiber-reinforced composites in diverse industrial sectors.

This chapter's second section outlines a model tailored to emulate a real-case scenario encountered in the injection molding process. The primary objective of this research endeavor was to develop a versatile model capable of simulating overmolding processes—a frequently encountered application involving the injection of short fiber-reinforced thermoplastics over a thermoformed insert filled with continuous fiber-reinforced thermoplastics.

In practice, this process presents various complexities and challenges, including the potential occurrence of defects such as insert displacement, insert displacement, and polymer penetration. These defects, which have been comprehensively detailed in chapter I, can significantly impact the quality and integrity of the final product. To gain a deeper understanding of these issues and their implications, numerical simulations were conducted. These simulations allow for the interpretation of the

observed defects and their correlation with experimental results from previous studies. Numerically, this complex problem was addressed through the development of a comprehensive two-phase flow model. Within this model, one phase distinctly represents the insert, while the other characterizes the injected thermoplastic materials, capturing their dynamic interplay.

Thus, by simulating this intricate scenario, valuable insights into the physical interactions at the interface between these two phases can be gained. Computational analyses encompass critical parameters such as stress and displacement occurring at this interface. This knowledge, in turn, is critical to understanding the mechanical properties of the final product once the injection molding process is complete. Additionally, the study involves a detailed analysis of how variations in phase properties, achieved through parameter adjustments like viscosity  $\eta$  and the fiber interaction coefficient  $C_I$ , impact the overall process and product outcomes. This investigation further enhances our understanding of the complexities inherent in real-world injection molding scenarios.

## **IV.2 Configurations of fluid-fiber coupling in diverse geometries**

This section initiates an in-depth investigation into the dynamic behavior of fiber orientation and the substantial influence of fiber-flow coupling within two complex geometrical contexts: the 2D contraction and the L-shape domains, as depicted in figure IV.1. Through rigorous analyses and simulations, the aim is to explain the underlying mechanisms that dictate fiber orientation and coupling phenomena in these challenging spatial configurations.

### **IV.2.1 Complex shape models**

#### **IV.2.1.1 2D planar contraction model**

The study of contraction flow has gained significant attention due to its crucial industrial applications. So this type of flow frequently manifests in practical molding processes, thus serving as vital benchmark scenarios of notable significance. Consequently, numerous numerical investigations have focused on fluid suspensions flowing through channels featuring sudden contractions [161, 162, 157] or expansions [163, 164, 165]. In the numerical simulations, a model similar to the one detailed for standard planar channel flow in section III.3.2 is employed. Consequently, the governing equations for continuity and momentum, applicable to fiber suspension flows within a 2D planar contraction domain, remain unchanged and are presented in the system of equations (III.26). Additionally, for the spatial advection of fibers into the domain, equation (III.27) is also used. Within the numerical results section, the behavior of fiber suspensions within a 4:1 contraction geometry is explored.

#### **IV.2.1.2 2D L-shaped model**

Solving the fiber-flow coupling problem in L-shaped injection molding domains is crucial for understanding mechanical properties, such as residual stress. The final

orientation state of fibers plays a significant role in studies related to these properties within such domains. The complex geometry of an L-shape can set down some challenges not found in simpler cases, making it a valuable representation of real-world scenarios. Accurate simulation of fiber orientation in such complex shapes validates our numerical approach, providing a foundation for advanced studies and enhancing applicability in practical molding simulations. The same model used in previous cases is employed, maintaining continuity and momentum and spatial advection equations outlined for fiber suspension flows in a 2D planar contraction domain (section IV.2.1.1). It is worth noting that there is limited numerical research concerning this specific domain, making this study valuable for validating numerical approaches.

### IV.2.1.3 Boundary conditions

Similarly to the discussion in section III.3.2.2 concerning boundary conditions for simple channel flow domains, the consideration of complex flow domains (whether contraction or L-shape) introduces a similar necessity for defining appropriate boundary conditions to complete the Stokes problem. Thus, the governing system of equations for these both complex domains must also be supplemented with boundary conditions. These conditions are necessary in specifying the behavior of the flows

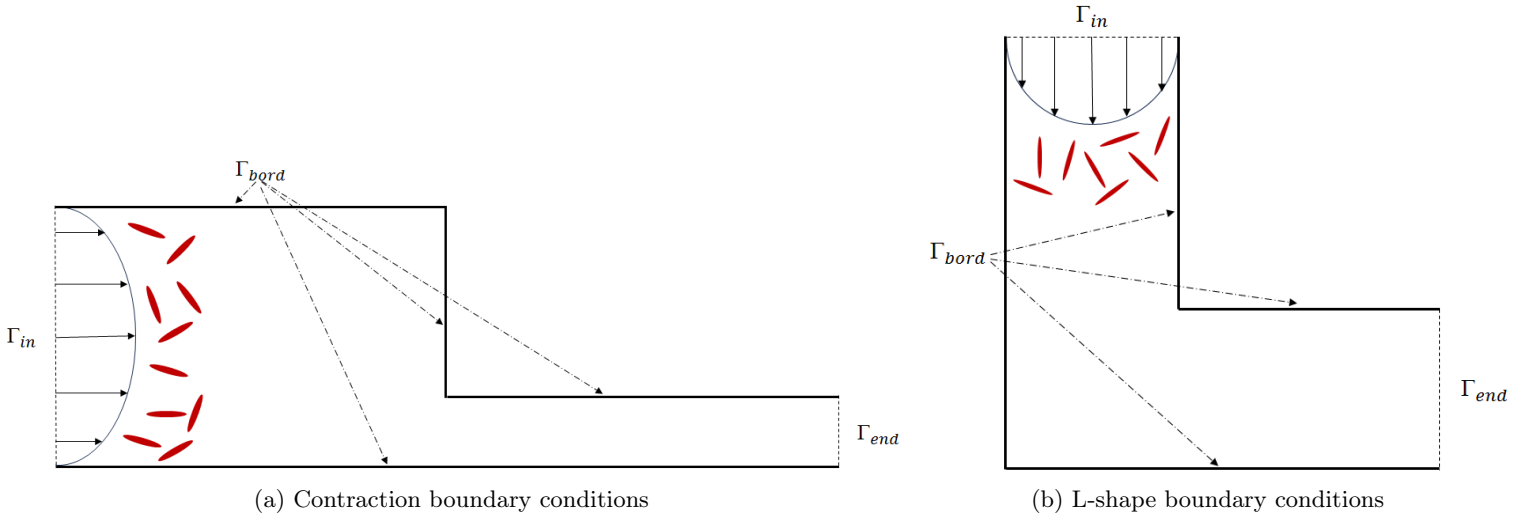


Figure IV.1: Representation of different boundaries and domains

at the boundaries of the computational domains and they are detailed as follows:

- on  $\Gamma_{in}$ , a pressure condition is imposed:  $(\boldsymbol{\sigma} \cdot \mathbf{n}) \cdot \mathbf{n} = -p_{in}$  where  $\mathbf{n}$  is the external unit normal and  $p_{in}$  is the pressure at the inlet.
- on  $\Gamma_{in}$ , an isotropic orientation of fiber is imposed:  $\mathbf{a}_4 = \mathbf{a}_4^{t_0}$  where  $\mathbf{a}_4^{t_0}$  is computed from equation (I.6) by taking  $\varphi = \frac{1}{2\pi}$ .
- on  $\Gamma_{end}$ , a pressure condition is imposed:  $(\boldsymbol{\sigma} \cdot \mathbf{n}) \cdot \mathbf{n} = -p_{end} = 0$ , where  $p_{end}$  is the pressure at the right end of the domain.

- on  $\Gamma_{edge}$ , no-slip boundary condition is imposed, which results in  $\mathbf{u} = 0$ .

where  $\Gamma_{in}$ ,  $\Gamma_{edge}$  and  $\Gamma_{end}$  respectively designate the boundaries of the domain corresponding to the injection zone and to the zones of contact with the walls of the injection mold with  $\Gamma_{in} \cup \Gamma_{edge} \cup \Gamma_{end} = \partial\Omega$ .

## IV.2.2 Numerical results

### IV.2.2.1 Contraction flow domain

In the simulations, pressure-driven flow conditions were initiated by solving the Stokes equation. The computational domain, considered for these simulations was designed to represent a contraction geometry by assembling two rectangles, where the left rectangle section measuring 4 m of height and 6 m of length connects to the right rectangular section with a height of 1 m and a length of 6 m. For analysis purposes, simulations were conducted using two types of meshes: a coarse mesh with 1139 nodes and a fine mesh with 6066 nodes, as depicted in figure IV.2. Boundary

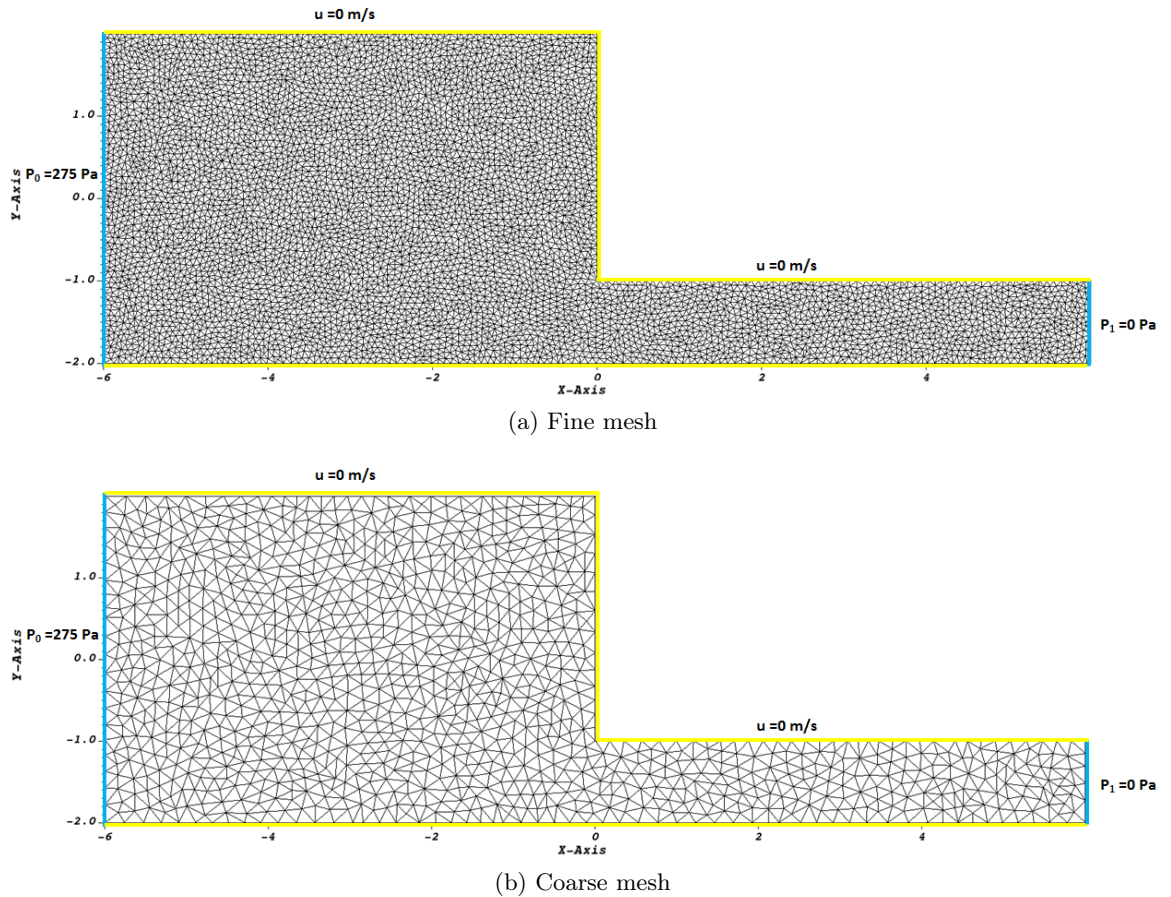


Figure IV.2: Contraction domain: FE mesh

conditions were rigorously defined to accurately model the physical system. At the inlet ( $x=-6$ ), we specified the pressure as  $P_0$ , set to 275 Pa, while at the outlet ( $x=6$ ), the pressure was established as  $P_1$ , which was set to 0 Pa. Along the four

walls, non-slip boundary conditions were imposed. The dynamic viscosity of the fluid, denoted as  $\eta$ , was assigned a value of 1 Pa·s. Concerning the advection equation for fibers, a completely randomized fiber orientation distribution was enforced at the inlet, serving as a Dirichlet boundary condition ( $\varphi = \frac{1}{2\pi}$ ). Additionally, an initial isotropic orientation was applied across the entire computational domain. Within the framework of the Fokker-Planck equation, the angular domain underwent discretization, featuring a mesh size  $h$  of  $\frac{2\pi}{1024}$ . Temporal discretization was accomplished through the use of the Rosenbrock-W scheme, employing a time step  $\Delta t$  of  $75 \times 10^{-3}$ s. Other essential parameters included a shape factor  $\lambda$  set at 1 and an interaction coefficient  $C_I$  established at 0.01. These simulations also included different values of  $N_p$ , namely 0, 10, and 30.

### Influence of $N_p$ on fluid streamlines (coarse mesh)

Numerical results at steady state for both the uncoupled solution ( $N_p = 0$ ) and coupled solutions ( $N_p = 10$  and 30) using a Newtonian suspending fluid are illustrated in figure IV.3. In this visualization, the background color corresponds to the magnitude of the  $x$ -component of velocity  $u_x$ , and select streamlines are drawn to provide further interpretation. Additionally, ellipses represent the average fiber orientation, as explained in the previous chapter.

Figure IV.4 representing, a closer examination of the zoomed-in region outlined by the red dashed-line rectangle in figure IV.3, reveals the presence of a recirculation zone (vortex) near the top corner of the contraction zone at  $x=0$ . When considering fiber-fluid coupling, it becomes evident that the size of this corner vortex increases as  $N_p$  varies from 0 to 30. This observation highlights that the introduction of fibers, even at relatively low concentrations, significantly influences the size of these recirculation zones. This finding is consistent with the results reported in [166] by Yasuda et al., who employed polymeric fibers made from cellulose acetate propionate in a suspension made of glycerin and polyethylene glycol. Consequently, the vortex boundary takes on a more convex shape relative to the main flow in the case of coupled fiber flow ( $N_p \neq 0$ ), in contrast to the pure Newtonian flow ( $N_p = 0$ ), where it exhibits a more concave shape, as reported in some studies done in [167, 168]. Similar conclusions were drawn from the experimental work presented in [84], where it was observed an enlargement of the vortex when slender fibers were introduced into a Newtonian fluid, even at low Reynolds numbers.

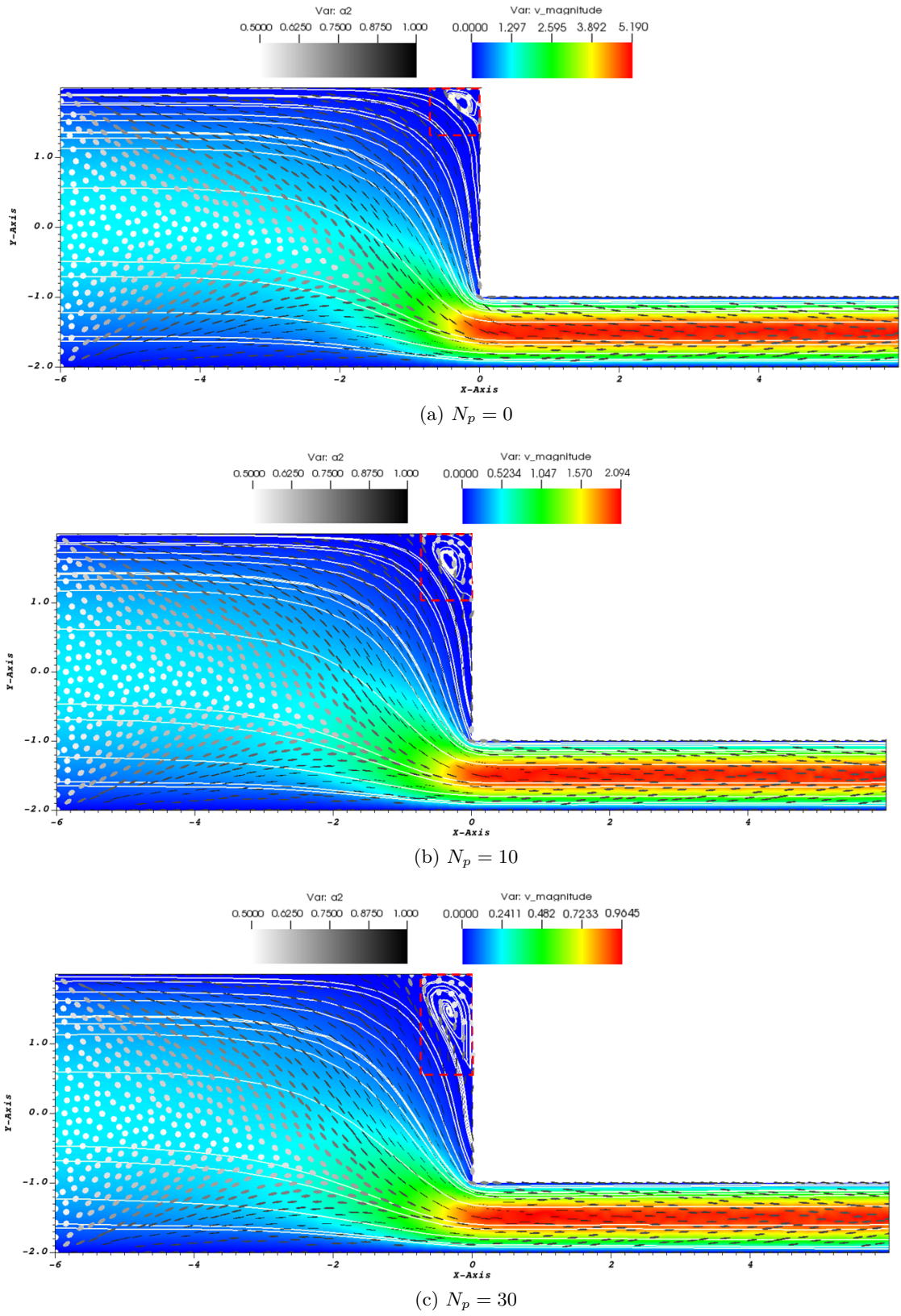


Figure IV.3: Velocity distribution and streamline patterns for different  $N_p$

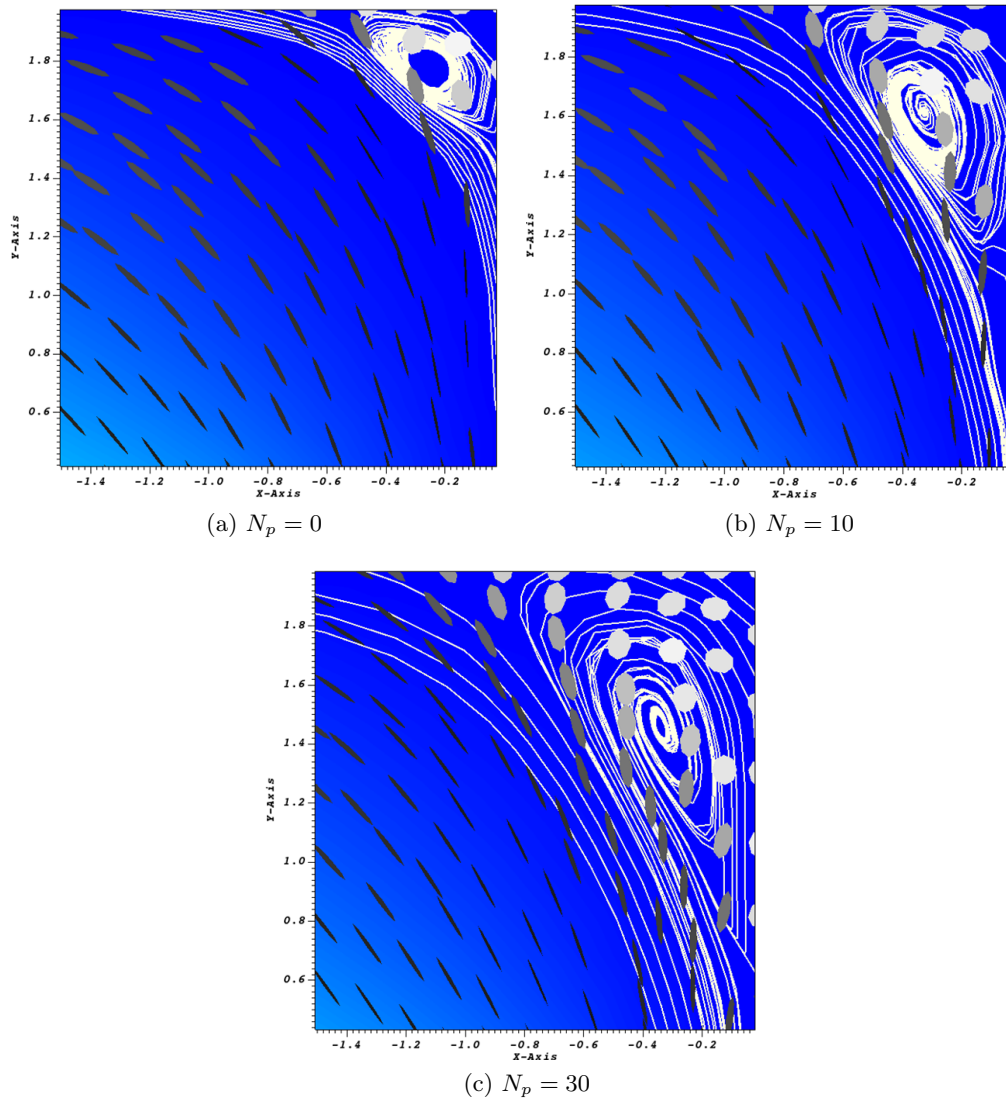
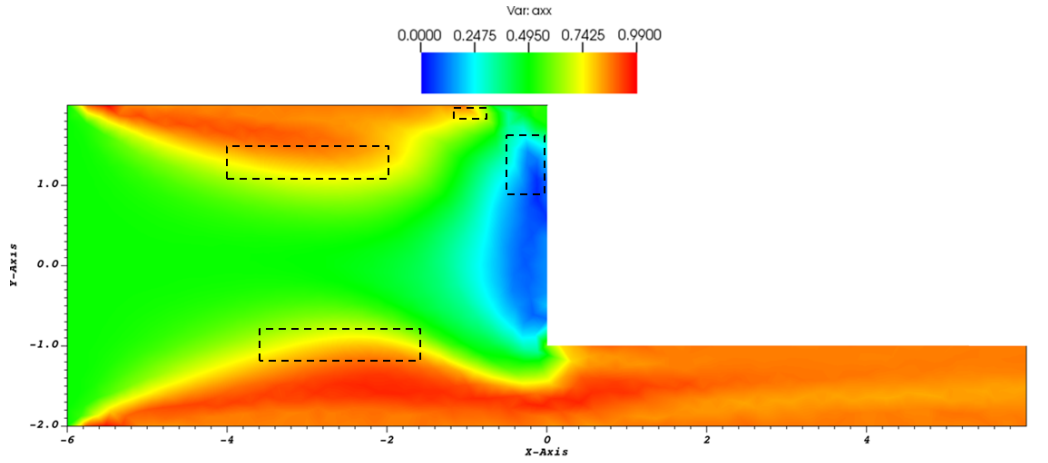
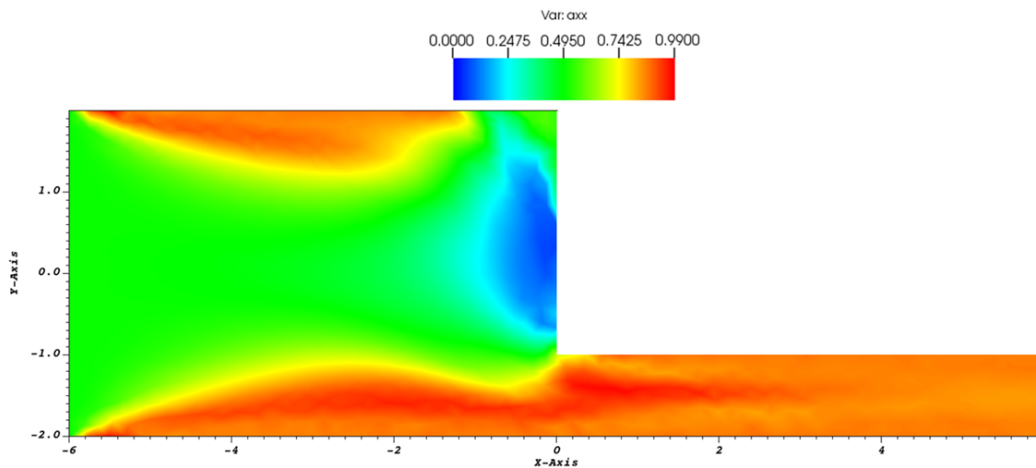


Figure IV.4: Zoomed-in view of streamline patterns in vortex zone for various  $N_p$

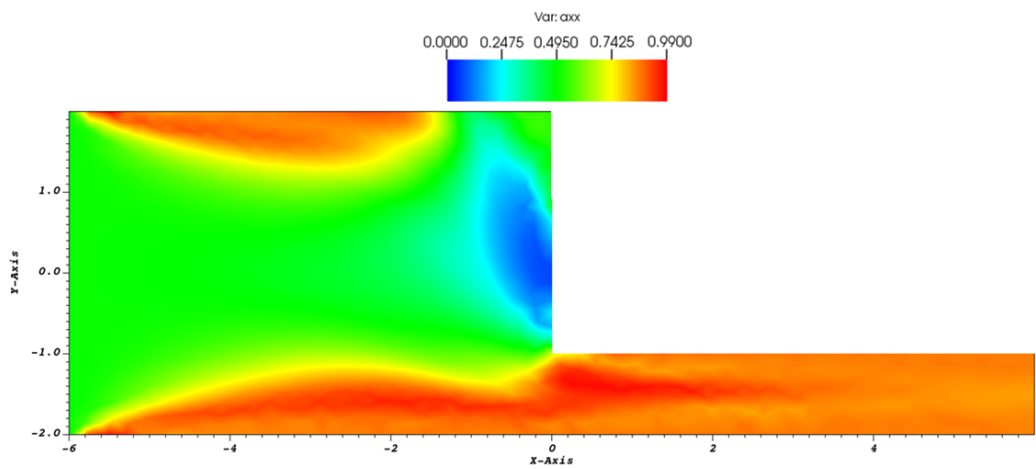
Impact of  $N_p$  on fiber orientation and fluid velocity(coarse mesh)



(a)  $N_p = 0$



(b)  $N_p = 10$



(c)  $N_p = 30$

Figure IV.5: Variation of  $a_{xx}$  for different  $N_p$

Furthermore, it is evident that the presence of the vortex has a clear impact on the fiber orientation. In this region, most fibers align themselves parallel to the streamlines, as indicated in figures IV.3 and IV.4. However, the alignment is not perfect, primarily due to the nonzero fiber-fiber interaction coefficient ( $CI = 0.01$ ). As the

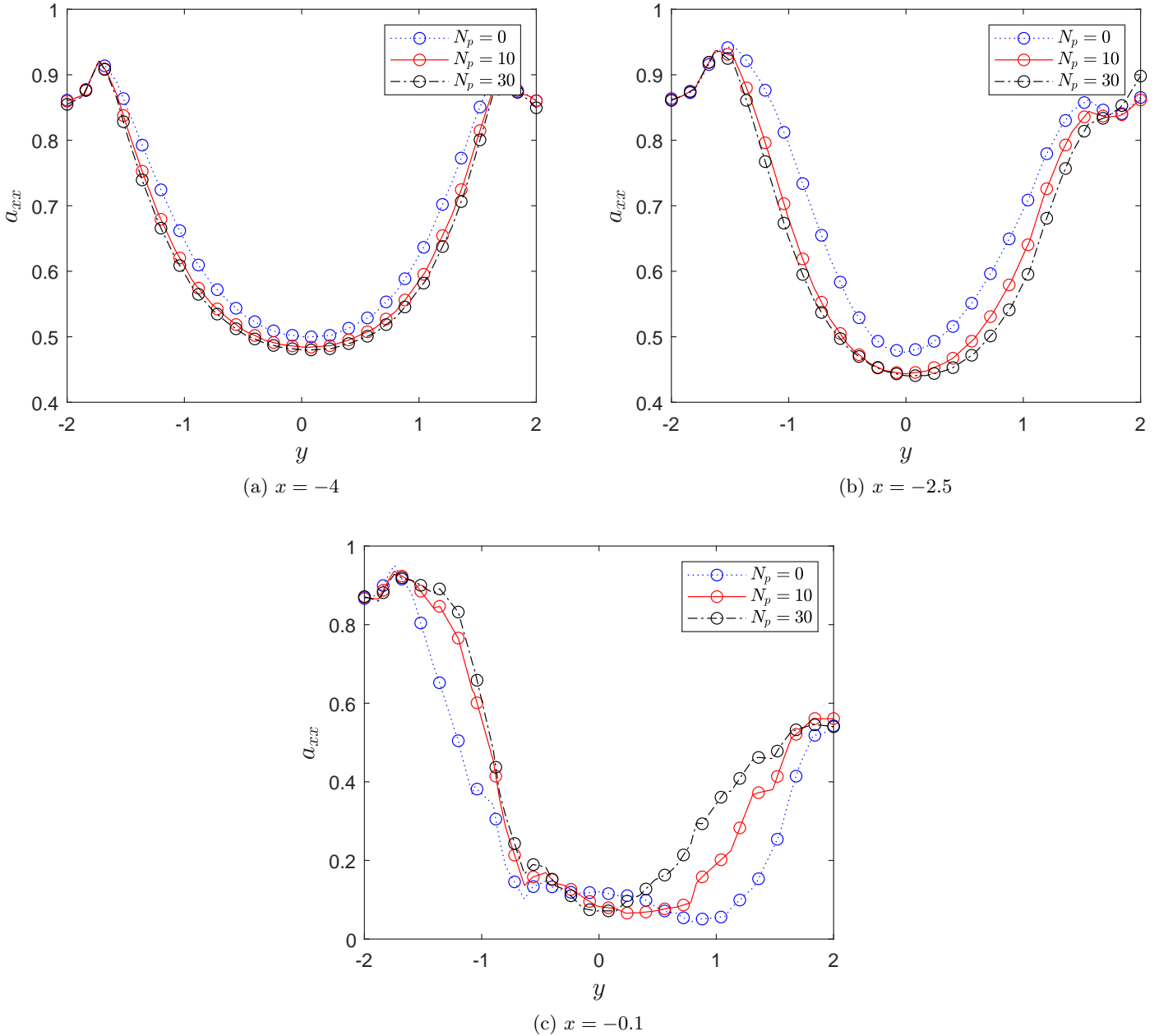


Figure IV.6: Variation of  $a_{xx}$  along  $y$ -axis at different positions  $x$  for different  $N_p$

value of  $N_p$  increases, the anisotropy of fiber distribution in both the main flow and vortex regions decreases. In figure IV.5, it is clear that the area characterized by an anisotropic fiber distribution (as precisely indicated by the black dashed-line boxes) gradually shrinks as  $N_p$  rises from smaller values (indicative of dilute/semi-dilute

conditions) to higher concentrations (indicative of a more concentrated state), as this evolution is consistent with the findings reported in [169]. It can be also clearly seen by plotting the variation of  $a_{xx}$  at different  $x$ -positions near the observed regions, as depicted in figure IV.6. This trend can be attributed to the strengthening random interactions between fibers, particularly pronounced with increasing  $N_p$ , which decreases the influence of flow velocity on fiber orientation. Simultaneously, the fibers' distribution tends to be more isotropic towards the center of the vortex, as shown in figure IV.4.

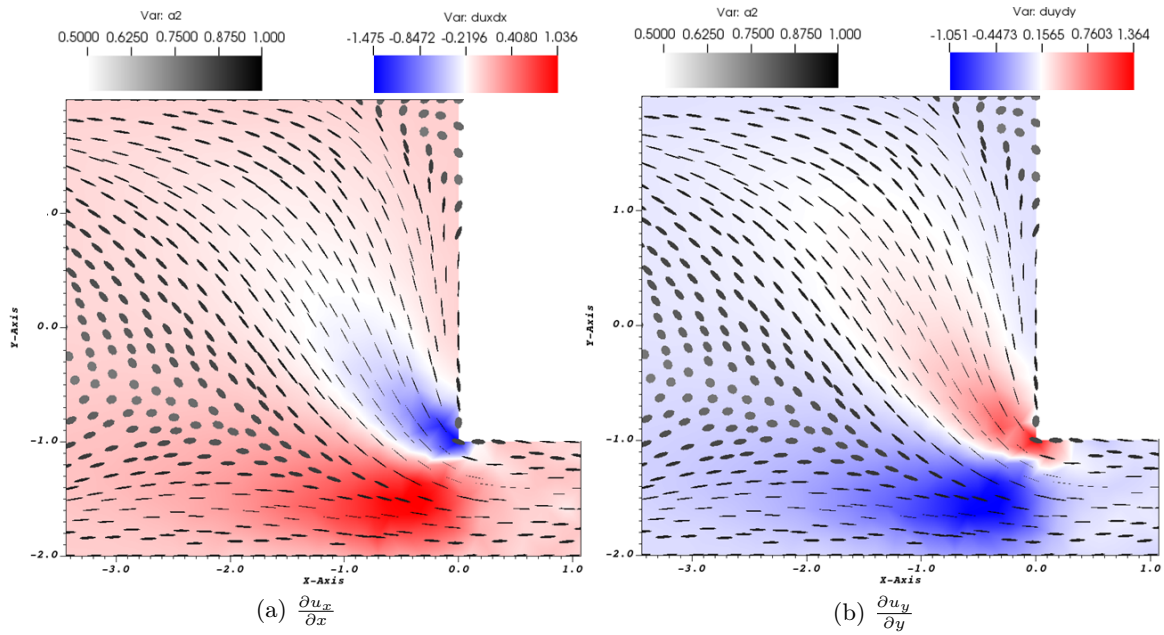
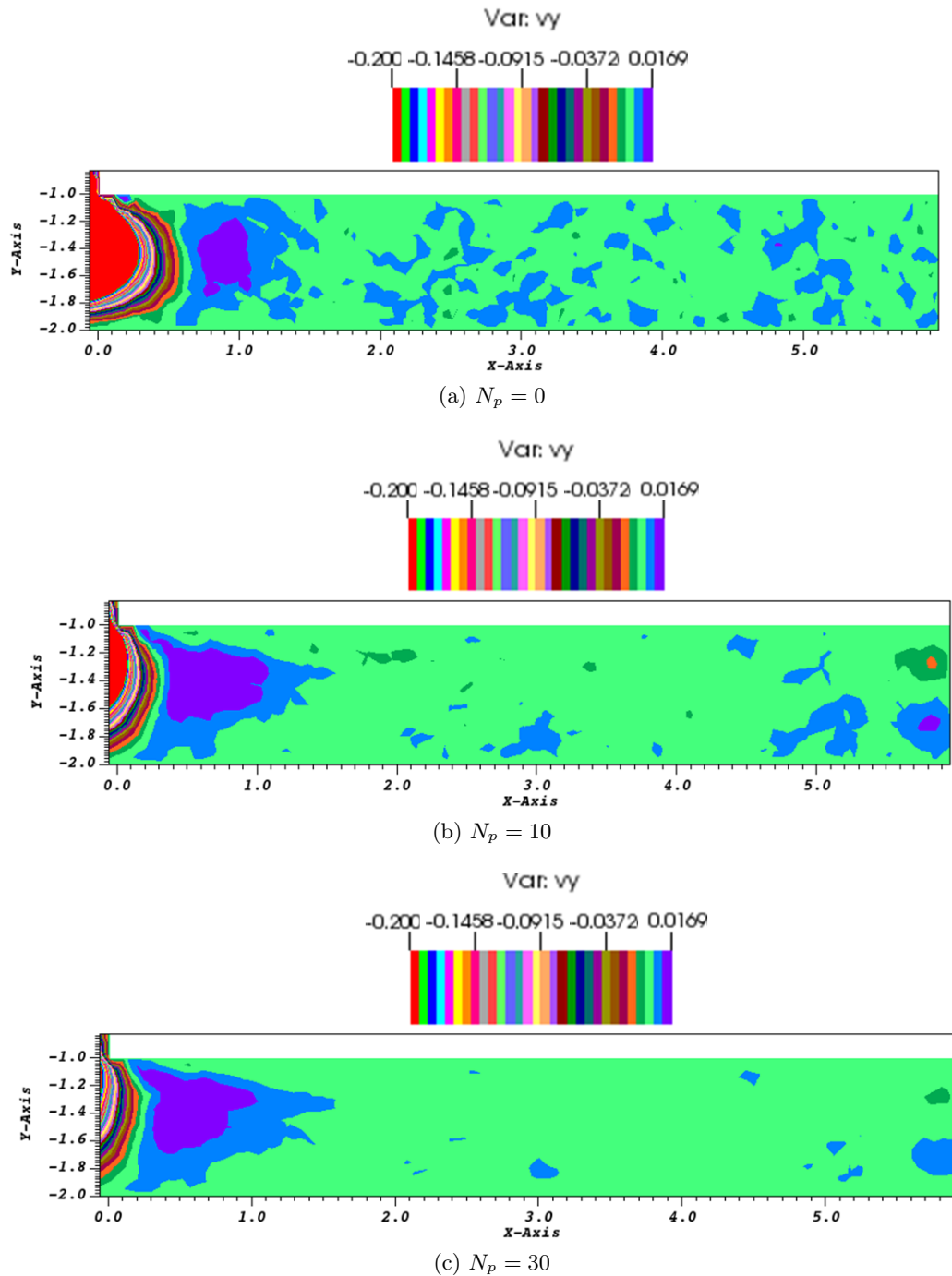


Figure IV.7: Variation of velocity gradient diagonal components in the throat region for  $N_p=10$

It is important to note that fibers at the entrance of the contraction region experience elongational flow. This can be interpreted through the plotting of the diagonal terms of the velocity gradients ( $\frac{\partial u_x}{\partial x}$ ,  $\frac{\partial u_y}{\partial y}$ ) in this region, as depicted in figure IV.7. Another observation from the simulations (figure IV.8) reveals that as  $N_p$  increases, the vertical velocity in the narrow channel becomes more consistent and uniform. Thus, the interaction between fibers and the flow, influenced by higher  $N_p$ , results in a more even distribution of vertical velocity  $u_y$ .

Figure IV.8: Variation of  $u_y$  for different  $N_p$ 

### Mesh refinement analysis: influence on solution accuracy

A mesh analysis has been undertaken to investigate its influence on the dynamic motion of fibers and the coupling dynamics between fibers and the flow. It is well acknowledged that refining the angular domain directly affects the solution of the Fokker-Planck equation, and hence the accuracy of fiber orientation prediction. Therefore, it is also important to examine mesh dependency in the spatial domain for solving the full coupling problem, particularly in complex geometries.

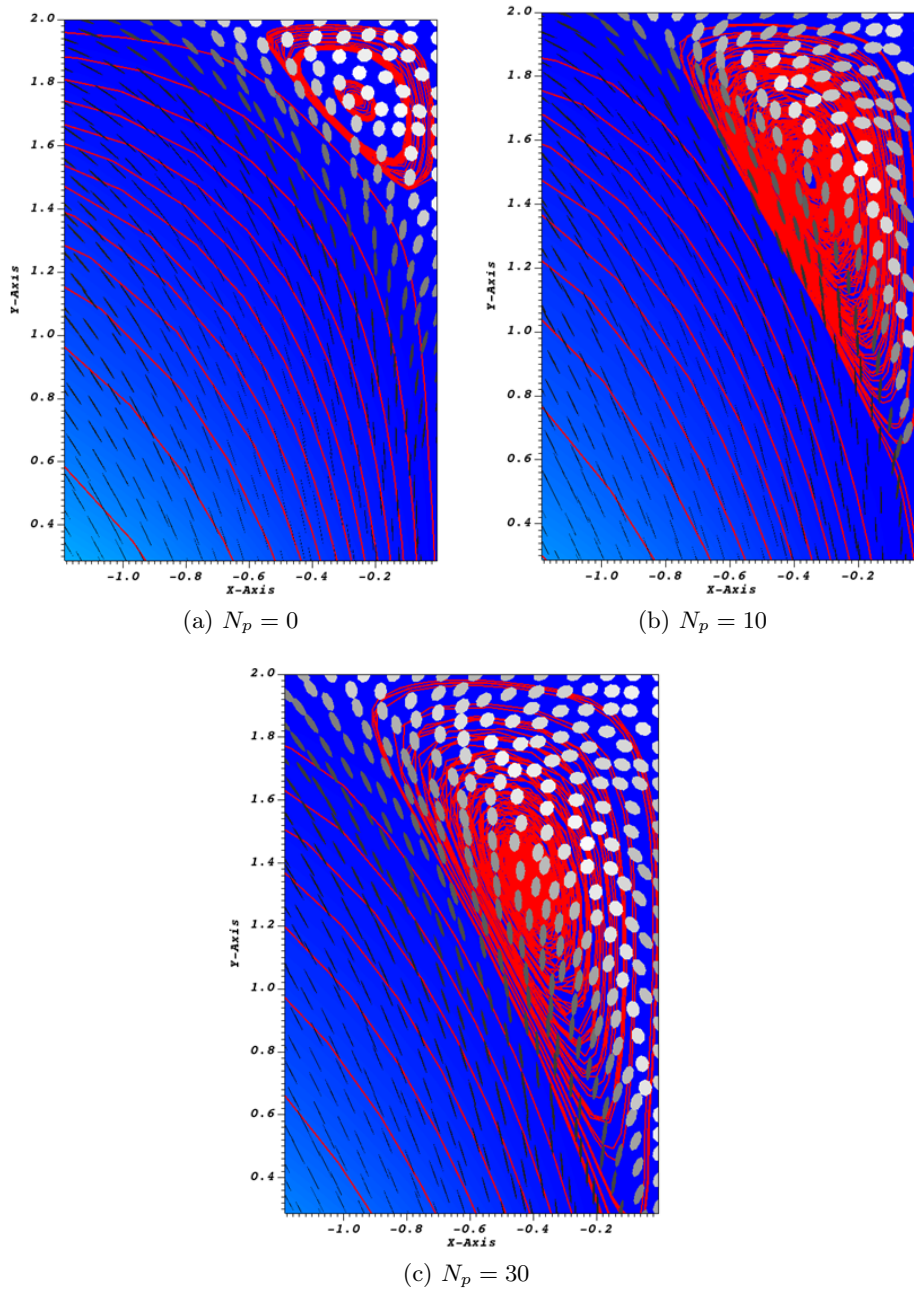


Figure IV.9: Vortex zone for different  $N_p$  (fine mesh)

The first noticeable effect can be seen by plotting the recirculation zone, as shown in figure IV.9. Notably, the vortices intensity increases with a finer mesh, thus the vortices exhibit larger sizes and a more convex shape compared to those obtained with a coarser mesh (see figure IV.4). This effect is consistently proportional to the value of  $N_p$ . Consequently, the vortex centers expand, and the fibers tend to orient more randomly within these regions.

Another impact of the mesh refinement on the solution of the fiber-flow coupling problem is the effect on the variation of the velocity profile. It was deduced in the previous chapter III that the presence of fibers in the flow causes the fluid to

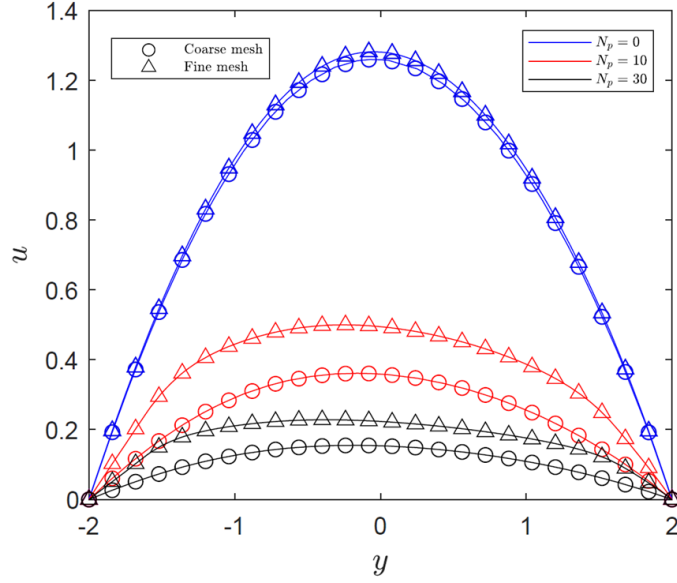


Figure IV.10: Effect of mesh size on velocity profile at  $x = -4$  for different  $N_p$

adopt non-Newtonian behavior. Figure IV.10 illustrates a comparison of the variation of velocity profile at  $x = -4$  between a coarse and a fine mesh for coupled and decoupled solutions. As shown, for a coarse mesh in the contraction domain, this transition was not well captured. On the other hand, when decreasing the mesh size, the coupling effect can be seen more obviously as the velocity profile starts to flatten when increasing  $N_p$ . However, even with a coarse mesh, it can be observed that the overall flow velocity has decreased, taking into account the drag force on the fluid exerted by the fibers on the flow, while approximately maintaining its parabolic profile. Thus, it can be said that to capture the full effect of fibers on the flow, especially in complex domains like the contraction domain, sufficient spatial nodes should be used. Despite the limitations of a coarse mesh, essential information regarding the influence of fibers on the flow can still be obtained.

The use of a smaller mesh size can also exert an influence on the evolution of fiber orientation within the domain. Figure IV.11 shows the variation of  $a_{xx}$  in the narrow channel region. Analyzing the behavior of fibers at the entry of the throat region orientation can be divided into four zones, starting from the upper and lower wall zones where fibers exhibit similar behavior. In these regions, fibers initially align with the flow direction before gradually relaxing slightly towards the exit zone. This behavior is driven by the effect of  $C_I$  and is observed for both coupled and uncoupled solutions.

In the lower shell region, fibers display similar horizontal orientation at the entry but tend to shift their orientation slightly above the  $x$ -axis due to the influence of positive shear rate. Increasing  $N_p$ , delays this effect as fibers are advected in the narrow channel, attributed to the lower shear rate when  $N_p$  is non-zero. A similar interpretation can be drawn for the upper shell region, where the high and rapid twist in the magnitude of the components of  $\nabla \mathbf{u}$  results in less oriented fibers entering the flow direction. For  $N_p \neq 0$ , fibers tend to orient more in the  $y$ -direction, but as they flow in the channel, the negative shear rate counteracts this orientation,

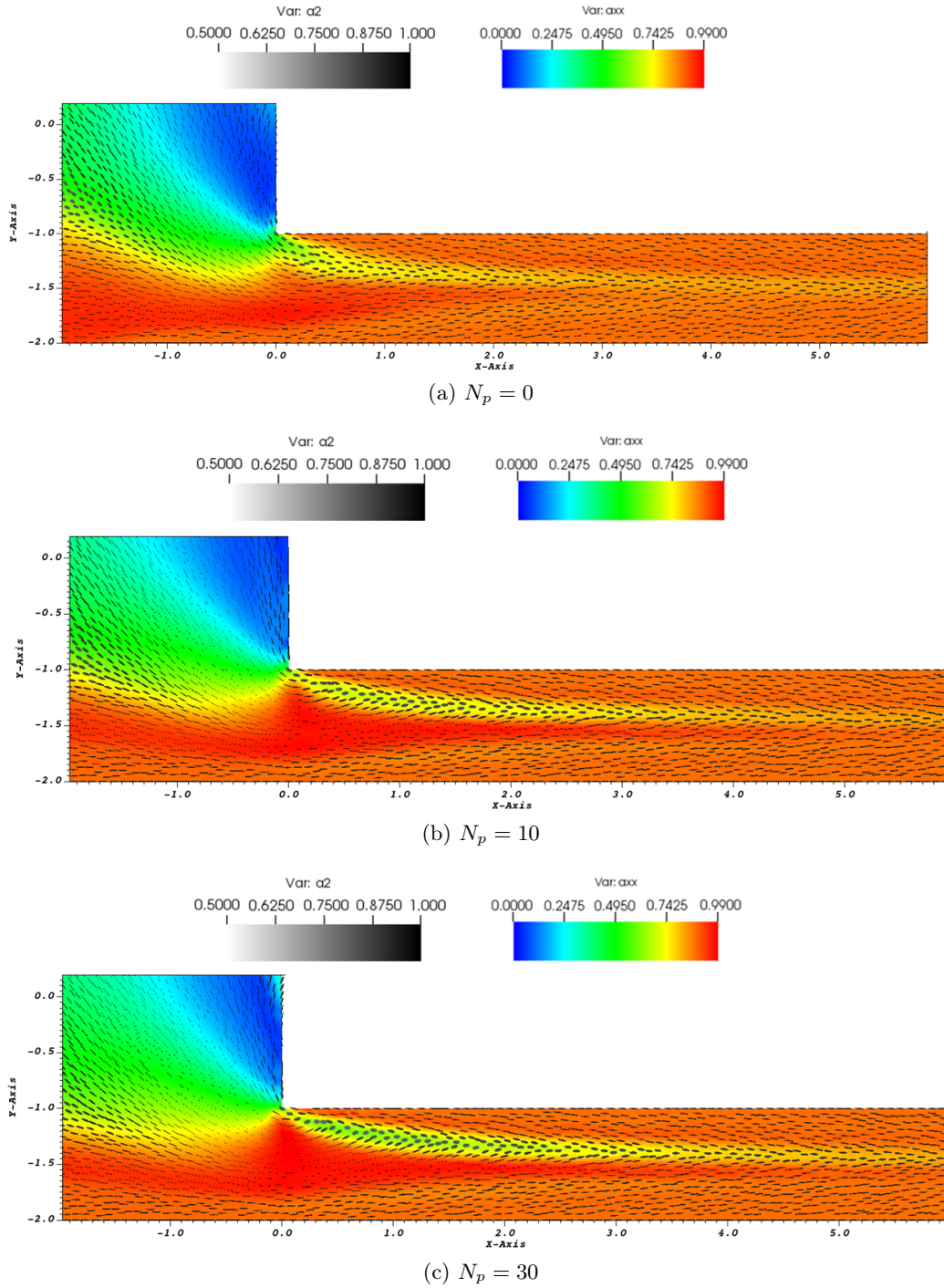


Figure IV.11: Variation of  $a_{xx}$  for different  $N_p$  in the narrow channel (fine mesh)

aligning them more with the  $x$ -direction. Notably, fibers take a longer time to reach a steady orientation state for the coupled solution compared to the uncoupled solution.

Compared to the results presented in Figure IV.5, the variation of  $a_{xx}$  in the narrow channel region exhibits distinct behavioral patterns, particularly in the upper shell region, for the two different mesh sizes. This can be inferred from the fact

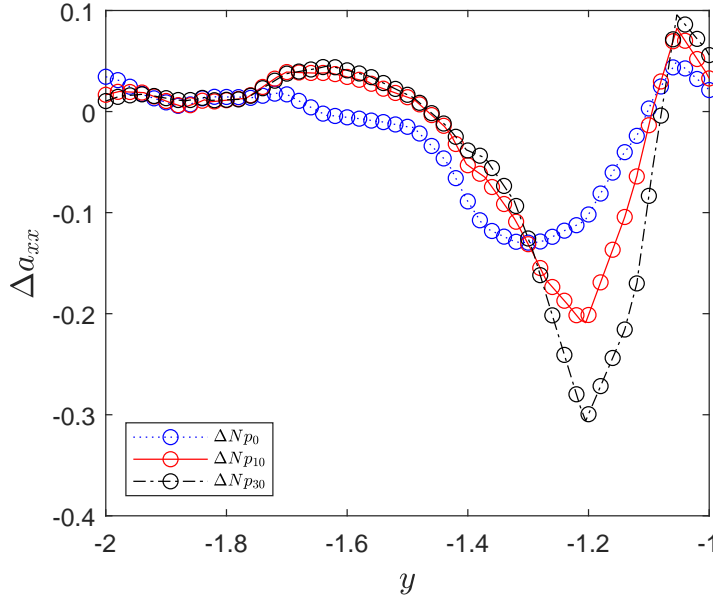


Figure IV.12: Variation of  $a_{xx}$  difference at  $x = 0.5$ : coarse vs fine mesh for different  $N_p$

that a significant shift in shear components of  $\nabla \mathbf{u}$  occurs in this region, leading consequently to a rapid change in the evolution of fiber orientation. As a result, a refined mesh is required in this region to accurately capture these variations, as a coarse mesh with insufficient nodes cannot provide an accurate solution through interpolation. To quantify the error, an analysis of the variation in  $a_{xx}$  along  $y$ -axis between the two mesh sizes is done by plotting  $\Delta a_{xx} = a_{xx}^{fine} - a_{xx}^{coarse}$  at a position near the entry of the throat region ( $x=0.5$ ), as depicted in figure IV.12. The results reveal that  $\Delta a_{xx}$  exhibits the most pronounced decrease in the upper shell region, as previously mentioned. Interestingly, the error becomes comparatively higher when increasing  $N_p$ . The difference  $\Delta a_{xx}$  is considered negligible in the wall region. The variation in fiber orientation attributed to the choice of mesh size falls within the range of -30% and 10%.

#### IV.2.2.2 L-shaped flow domain

To address this problem, similarly to the previous section, simulations were initialized under Poiseuille flow conditions. The computational domain for these simulations was designed in the shape of an "L", composed of two connected rectangles. The horizontal rectangle featured dimensions of 1 m in height and 3 m in length, while the vertical rectangle had dimensions of 2 m in height and 1 m in length. This complex domain was discretized into 4077 nodes, as illustrated in figure IV.13. For the boundary conditions, the flow is expected to enter from the top, with the pressure  $P_0$  set to 100 Pa at the inlet ( $y=3$ ), with the flow direction going downwards. At the outlet ( $x=3$ ), the pressure  $P_1$  was 0 Pa. Non-slip boundary conditions were imposed along all other walls. The dynamic viscosity of the fluid,  $\eta$ , was given a value of 1 Pa·s. Similar to our approach in the 2D contraction flow model, a fully

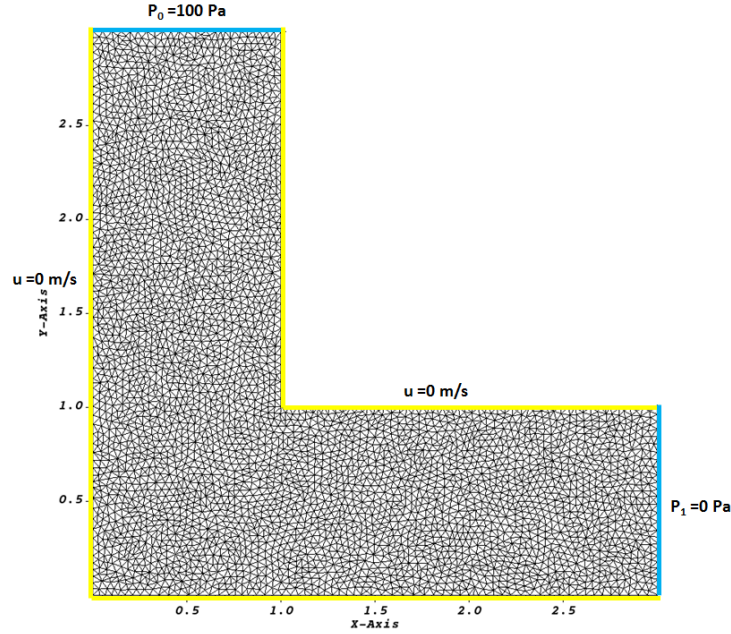


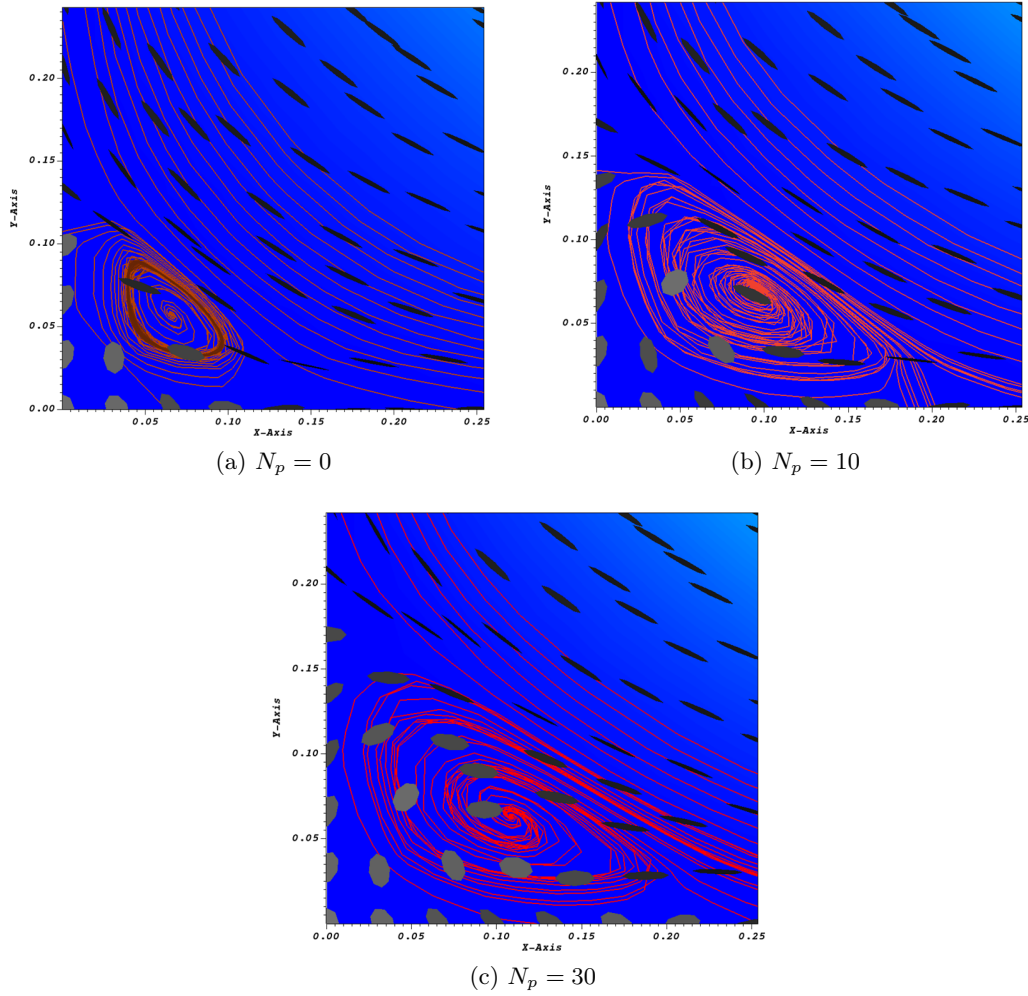
Figure IV.13: L-shape domain: FE mesh

randomized fiber orientation distribution was prescribed at the inlet and maintained across the entire domain. The angular domain for fibers is discretized using a mesh size  $h$  of  $\frac{2\pi}{1024}$  and performed temporal discretization with a Rosenbrock-W scheme using a time step  $\Delta t$  of  $75 \times 10^{-3}$ s. We also kept the values of  $\lambda$  and  $C_I$  consistent at 1 and 0.01, respectively, while solutions were also obtained for  $N_p$  values of 10, 20, and 30.

### Influence of $N_p$ on vortex and fiber orientation

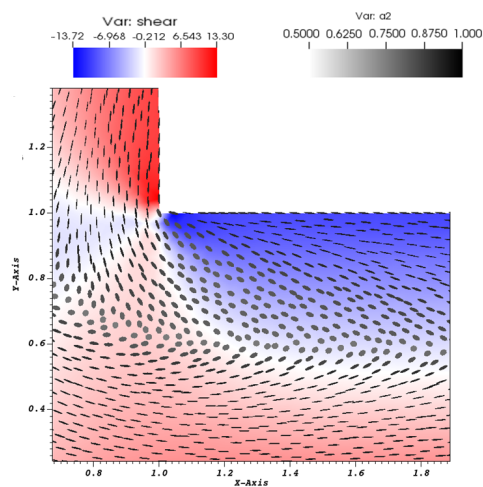
The first numerical result that can be discussed for this geometry is related to the phenomenon of recirculation zone formation and the influence of  $N_p$  on this zone. As shown in figure IV.14, a vortex zone emerges at the lower-left corner of the domain for the three different selected  $N_p$  values. The obtained result is consistent with the findings in the previous study (case of contraction domain), which suggest that higher  $N_p$  contributes to the expansion of the vortex zone. Within this region, the fibers exhibit a more isotropic orientation state.

The fiber orientation state around the lower-right corner, designated as a zone of interest, is important to understanding and explaining the effect of flow dynamics on fibers. Similar to the observations in the contraction domain, the velocity gradient, particularly its shear components, varies rapidly within the shell zone. Figure IV.15 illustrates the variation of total shear stress ( $\tau_{total} = \mu(\frac{\partial u_x}{\partial y} + \frac{\partial u_y}{\partial x})$ ) in this zone, represented by color intensity, and the ellipses depicting the average fiber orientation. While the ellipses for all  $N_p$  cases, especially for  $N_p=0$ , suggest a gradual relaxation of fibers before reorienting to favor the  $x$ -direction, this representation is somewhat challenging to interpret due to the complexity of this problem for this type of domain, where numerous interacting physical parameters influence fiber orientation. Nevertheless, one plausible interpretation of this phenomenon is that in the region

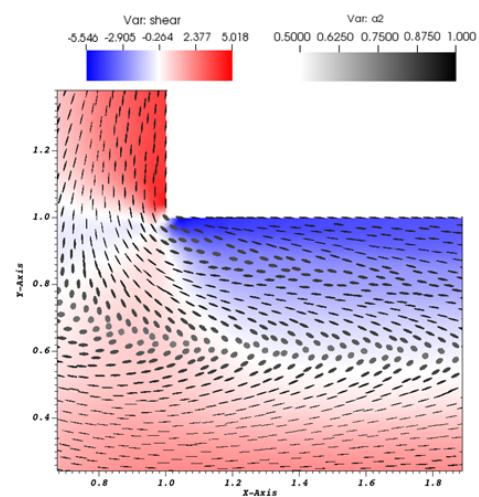
Figure IV.14: Vortex zone for different  $N_p$ 

surrounding this corner, the effect of fibers being advected by the fluid's velocity has a more significant impact on fiber orientation, particularly for  $N_p=0$ . In other words, fibers have less time to reorient along the  $x$ -direction. Conversely, this effect has less influence on  $N_p \neq 0$  cases, where an increase in fiber concentration leads to a reduction in velocity magnitude. As a result, the shear rate has a more pronounced impact on fiber orientation in this zone when  $N_p$  increases. Additionally, it is worth noting from figure IV.15 that fibers tend to relax slightly before entering the horizontal channel for the uncoupled case compared to the coupled cases.

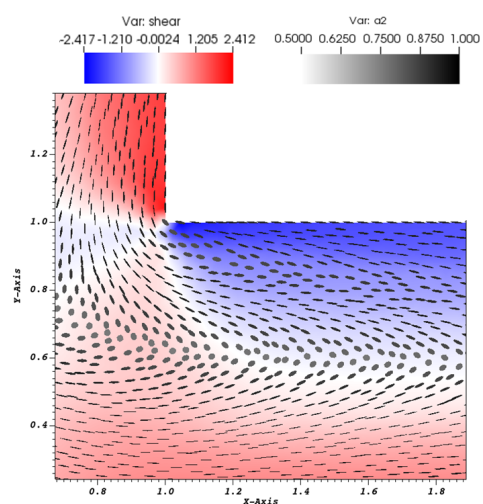
To illustrate the distribution of fiber orientation near the zone of interest, figure IV.16 shows the variation of  $a_{xx}$  along the  $y$ -axis at two positions:  $x = 1.05$  (close to the entry of the horizontal channel) and  $x = 1.5$  (near the center). This allows us to observe the difference in fiber orientation between a critical and a non-critical position. In the lower region,  $a_{xx}$  varies expectedly, with fibers aligned near the wall and gradually reorienting into an isotropic state as they move towards the center. This profile is similar for all  $N_p$  values. In the upper region, however, the corner effect becomes apparent. Fibers remain in an isotropic state for a longer  $y$ -distance, particularly for  $N_p=0$ , before starting to reorient and align in the  $x$ -direction. At  $x$



(a)  $N_p = 0$



(b)  $N_p = 10$



(c)  $N_p = 30$

Figure IV.15: Shear stress and fiber orientation distribution for different  $N_p$

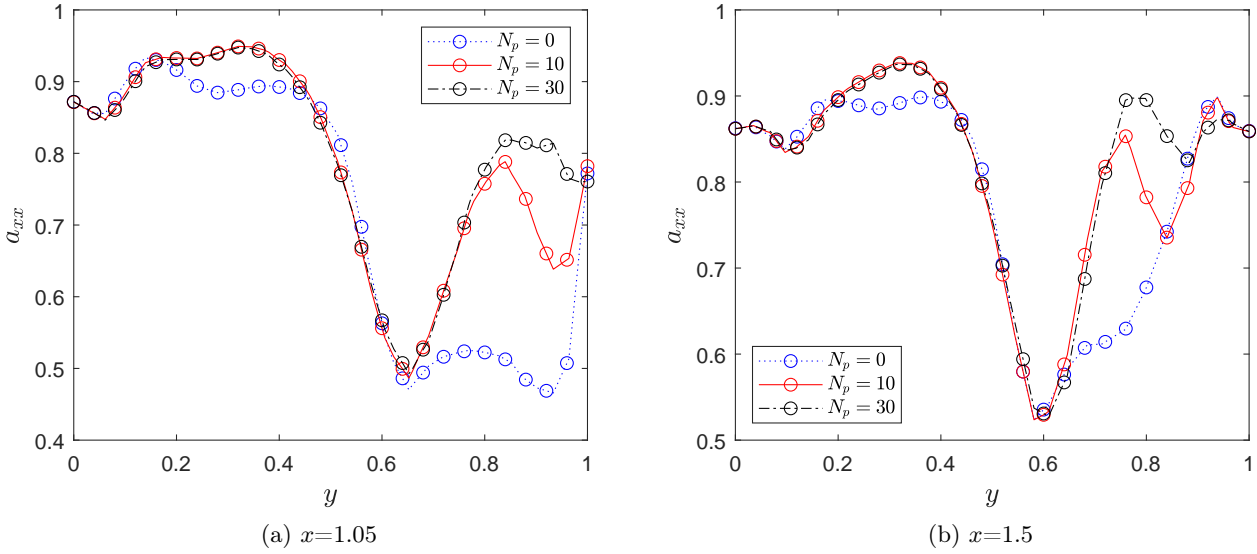
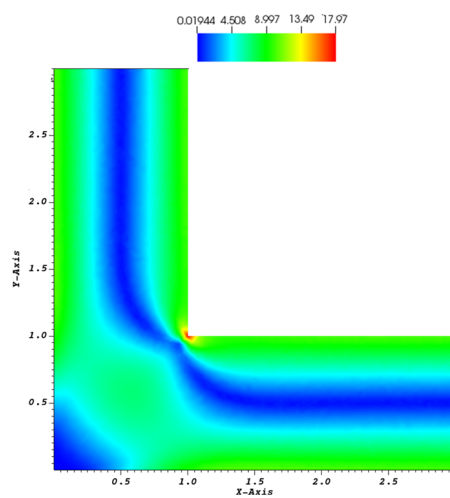
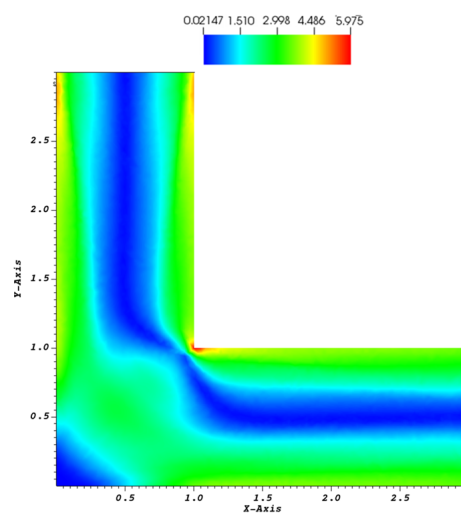


Figure IV.16: Variation of fiber orientation along the  $y$ -axis at two different  $x$ -positions for various  $N_p$

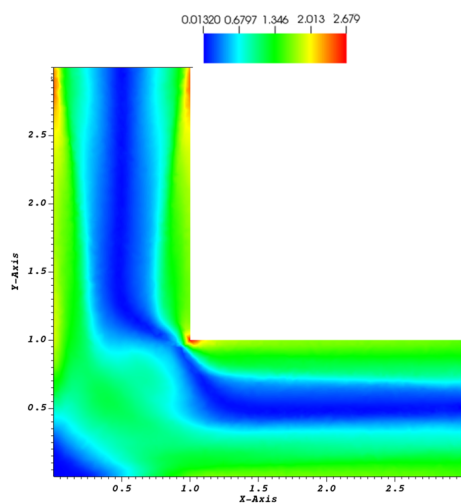
$= 1.5$ , the fiber orientation distribution starts to take its standard variation along the  $y$ -axis, as seen in figure IV.16b for all different  $N_p$ . This variation is characteristic of channel flow in rectangular domains. Thus, as the flow moves downstream, the fiber orientation distribution gradually transitions to its standard profile. It is worth noting that the core region, where most fibers are randomly oriented, is shifted slightly higher. The latter phenomenon can be explained by plotting the distribution of generalized shear rate  $\dot{\gamma}$  within the domain. As shown in figure IV.17, the region of zero shear rate has also shifted slightly upwards in the  $y$ -direction. This shift coincides with the upward shift of the core region in fiber orientation distribution. The evolution of fiber orientation along the entry channel in the L-shaped domain is also noteworthy. Figure IV.18 depicts the variation of  $a_{xx}$  along the  $x$ -axis for different  $N_p$ , with the velocity flowing downward. This indicates that the shear rate varies perpendicular to the flow direction along the  $x$ -axis, as shown in figure IV.17. The left-hand side plot, IV.18a, illustrates the variation of  $a_{xx}$  near the entry zone at  $y=2.5$ . It is evident that at this distance from the entry, most of the fibers still retain a random orientation. However, as  $a_{xx}$  begins to decrease below 0.5 towards the region near the wall, it suggests that the fibers are starting to align in the  $y$ -direction. This trend for  $a_{xx}$  is similar for all  $N_p$  cases. The right-hand side plot depicts the variation of  $a_{xx}$  near the corner at  $y=1.05$ . Interestingly, no particular behavior is observed in this zone. The region where the fibers are in an isotropic state has decreased as the distance from the entry zone has increased. The only notable feature is that the core region for  $N_p=0$  is slightly shifted compared to the cases of  $N_p \neq 0$ .



(a)  $N_p = 0$



(b)  $N_p = 10$



(c)  $N_p = 30$

Figure IV.17: Shear rate distribution

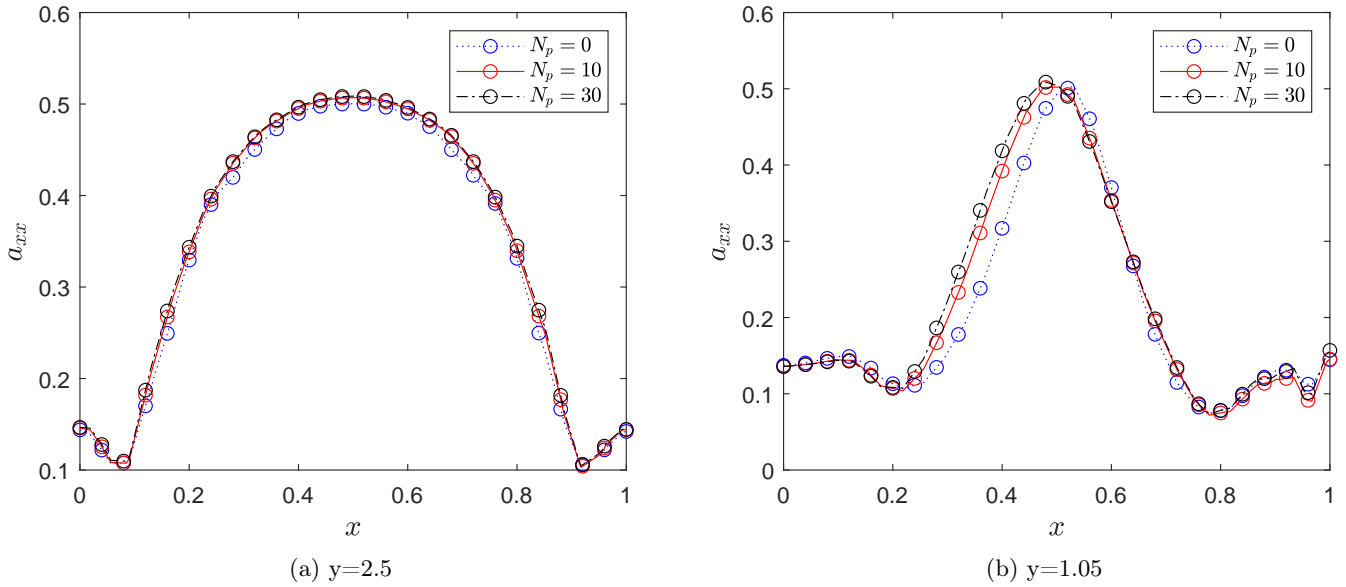


Figure IV.18: Variation of fiber orientation along the  $x$ -axis at two different  $y$ -positions for various  $N_p$

#### Impact of $N_p$ on velocity profile

Another analysis that can be performed for this domain is to investigate the coupling effect on the fluid velocity. As depicted in figure IV.19, the evolution of the velocity profiles for diverse  $N_p$  values at various positions has been plotted. Figures IV.19a and IV.19b illustrate the velocity profiles at different positions along the entry channel, one close to the flow inlet and the other near the corner region. It has been observed that the influence of increasing  $N_p$  on the velocity is evident at both positions. As anticipated, the velocity peak decreases due to the drag force exerted by the fibers on the flow, causing the fluid to transition into a non-Newtonian state by flattening the velocity profile's peak. Moreover, this flattening becomes more pronounced when the velocity profile is plotted near the corner zone. Similarly, figures IV.19c and IV.19d depict the variation of the velocity profiles through the horizontal channel at two distinct positions: one near the corner zone and the other close to the exit zone. Notably, it has been observed that the velocity profile appears to revert to its parabolic shape towards the exit, while the velocity magnitude remains reduced due to the presence of fibers in the flow.

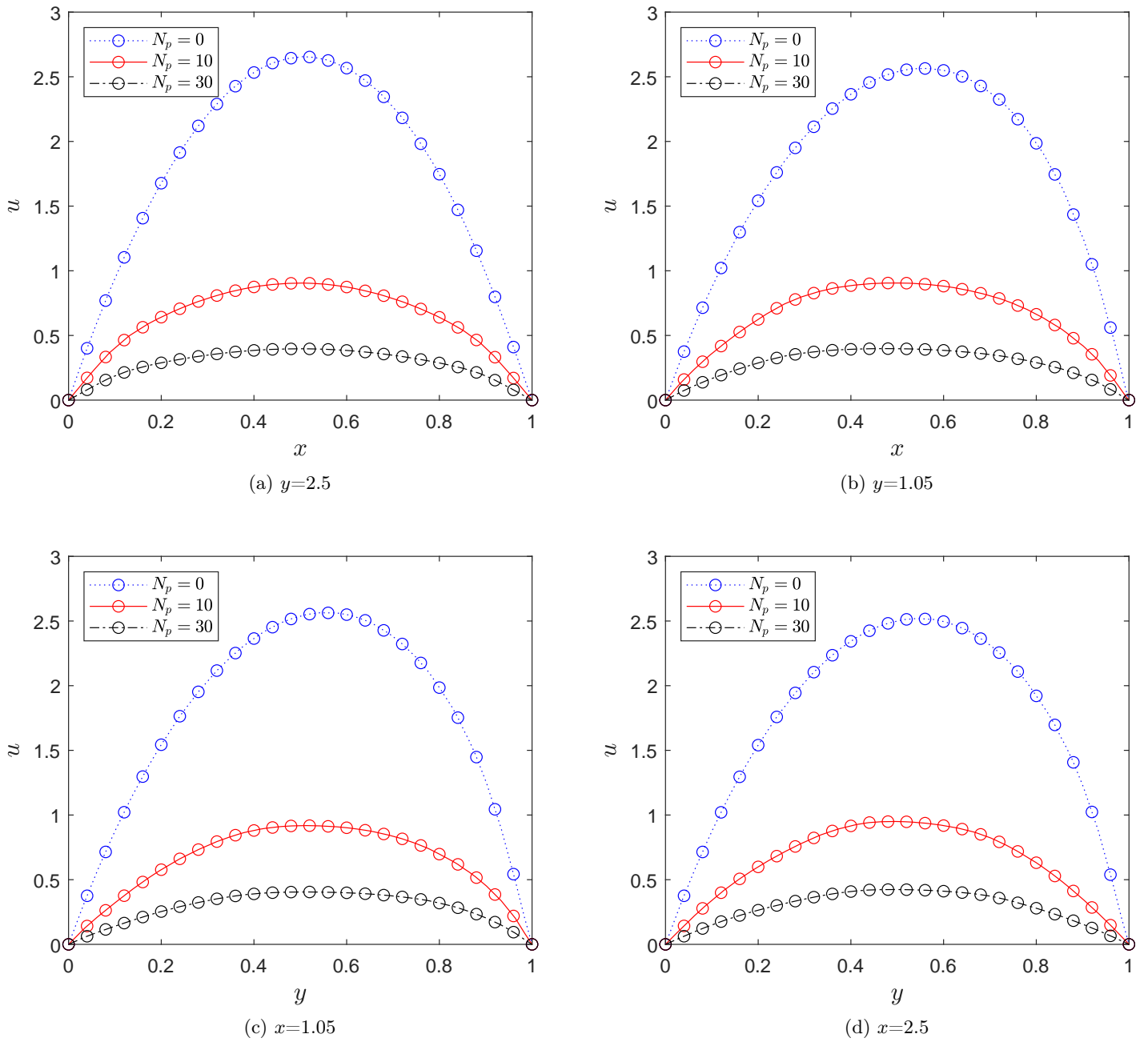


Figure IV.19: Variation of velocity profile at different positions for various  $N_p$

### IV.2.3 Short summary

- ✓ Contraction and L-shaped domains are used to test the validity of the developed method in solving fiber-flow coupling problems in complex geometries.
- ✓ The rheological coupling coefficient  $N_p$  widens the size of the vortex zone that can be formed in complex geometries, thus affecting the fibers orientation within this zone.
- ✓ The high shear rates caused by the acceleration of the flow near the throat in the contraction region cause the fibers to experience elongational flow.
- ✓ Refining the spatial mesh can capture the effects of high shear rates on fiber orientation distribution, particularly near the throat region of a contraction domain. This, in turn, can affect the transition of the fluid from Newtonian to non-Newtonian behavior.
- ✓ Fiber relaxation in an L-shape domain near the throat zone, acknowledging the difficulty of interpretation it due to the complexity of the problem and the numerous interacting physical parameters.
- ✓ It is noticed that in L-shaped domain, the effect of  $N_p$  in transitioning the fluid into non-Newtonian is more prominent through the entry vertical channel than the horizontal exit channel.

## IV.3 Problem setup for a real-case injection molding scenario

### IV.3.1 Two-phase flow model

We first recall that the initial goal of this work is to develop a comprehensive simulation framework that closely mirrors real-world scenarios encountered in the overmolding process. To achieve this, a detailed analysis of the dynamic behavior of fibers is incorporated into a two-phase model. This model allows us to gain critical insight into the complex interactions that occur at the interface between the molten thermoplastic material being injected and the pre-molded or thermoformed insert composed of fiber-reinforced thermoplastics. By delving into the intricate dynamics of this interface, our goal is to improve our understanding of the overmolding process and its potential impact on various applications.

Therefore, different perspectives have been considered to emulate the overmolding process problem. One well-established approach is the fluid-structure interaction (FSI) model, where the fluid component represents the injected material and the solid component represents the insert. This model involves solving two sets of equations: one for fluid viscosity and another for elasticity. However, an alternative method has been adopted in which a two-phase flow model is used instead of the

FSI model. In this approach, both the injected and the preformed parts are represented as one fluid phase, which significantly reduces the complexity of the equations to be solved. Specifically, this is achieved by solving a full-domain viscous problem for the two phases. The solid component is represented by simply setting a very high viscosity when solving the viscous equations for that phase, while a low viscosity is used for the fluid phase. This approach effectively introduces a substantial difference in viscosity between the two phases, thereby facilitating an accurate representation of the solid component.

#### IV.3.1.1 Governing equations

In the specific context of the two-phase flow model developed to describe the overmolding process problem, the Stokes equations are used to characterize the flow behavior. It is important to note that in this particular scenario, the interfacial exchange terms within the Stokes equations are typically considered to be significantly smaller than the other terms, indicating the dominance of viscous forces over inertial forces. This predominance allows to neglect the interfacial exchange terms, leading to the decoupling of the equations (IV.1). Consequently, the Stokes equations can be solved independently for each phase, allowing a more tractable and efficient approach to simulating the system.

$$\begin{aligned} \nabla \cdot \mathbf{u}_k &= 0 \quad \text{in } \Omega \\ \nabla \cdot \boldsymbol{\sigma}_k &= 0 \quad \text{in } \Omega \\ \boldsymbol{\sigma}_k &= 2\eta_k \mathbf{E}_k - p_k \mathbf{I} + \eta_k N_p(\mathbf{E}_k : \mathbf{a}_{4k}) = 0 \quad \text{in } \Omega \end{aligned} \tag{IV.1}$$

where  $k = 1, 2$  denotes the two phases,  $p_k$  is the pressure of phase  $k$ ,  $\eta_k$  is the dynamic viscosity of phase  $k$ ,  $\mathbf{u}_k$  is the velocity vector of phase  $k$ ,  $\boldsymbol{\sigma}_k$  is the stress tensor of phase  $k$  and  $\mathbf{a}_{4k}$  is the orientation tensor of phase  $k$ .

A fully implicit approach is adopted in the simulations, where the interface is defined using a level set function, denoted as  $\Phi$ . In addition, a convection equation for the level set is needed to be solved to analyze and capture the displacement at the interface throughout the simulation. This is done by tracking the evolution of the interface between the two phases.

$$\frac{\partial \Phi}{\partial t} + \mathbf{u} \cdot \nabla \Phi = 0 \tag{IV.2}$$

The level set function  $\Phi$  smoothly spans the interface with a characteristic thickness represented by  $E$ . To identify the materials on either side of the interface and account for their distinct properties, such as viscosity  $\eta$ , within this finite thickness  $E$ . A discontinuous Heaviside function  $H$  is introduced, defined as 1 in one phase and 0 in the other phase, in order to distinguish between the two phases. While it is inherently discontinuous, a smoothed representation is employed to avoid numerical instabilities. The Heaviside function  $H$  is defined as follows:

$$H = \begin{cases} 1 & \text{if } \Phi > E \\ \frac{1}{2}(1 + \frac{\Phi}{E}) & \text{if } -E < \Phi < E \\ 0 & \text{if } \Phi < -E \end{cases} \tag{IV.3}$$

where in this case, the level set function  $\Phi_E$  is approximated as:

$$\Phi_E \simeq \Phi = E \tanh\left(\frac{\Phi}{E}\right) \quad (\text{hyperbolic tangent level set function}) \quad (\text{IV.4})$$

Any properties that transition between phases, denoted as  $\xi$ , can be represented as a variable field within the mesh, using the Heaviside function to ensure that they vary appropriately between phases:

$$\xi = \xi_{\text{phase1}}H + \xi_{\text{phase2}}(1 - H) \quad (\text{IV.5})$$

It is worth noting that we used the Adaptive Mesh Refinement feature within the ICI-Tech library to optimize the mesh. In this approach, finer resolution is applied specifically around the interface level set, while coarser mesh is used in the remaining domain. A finer mesh is necessary at the interface to reduce the width of the transition region where properties of the two phases mix when employing hyperbolic tangent interpolation.

#### IV.3.1.2 Boundary conditions

Parallel to the discussion of boundary conditions for single-phase flow in section III.3.2.2, the consideration of two-phase flow introduces a similar requirement for defining appropriate boundary conditions to complete the Stokes problem. As shown in equation (IV.1), the governing system of equations for this two-phase flow must be supplemented with boundary conditions. These conditions are critical in specifying the behavior of the two flows at the boundaries of the computational domain, as depicted in figure IV.20. The prescribed boundary conditions for this scenario are detailed below:

- on  $\Gamma_{in,k}$ , a pressure condition is imposed:  $(\boldsymbol{\sigma}_k \cdot \mathbf{n}) \cdot \mathbf{n} = -p_{in,k}$  where  $\mathbf{n}$  is the external unit normal and  $p_{in,k}$  is the pressure at the inlet of phase  $k$ .
- on  $\Gamma_{in,k}$ , an isotropic orientation of fiber is imposed:  $\mathbf{a}_{4k} = \mathbf{a}_{4k}^{t_0}$  in which  $\mathbf{a}_{4k}^{t_0}$  is in phase  $k$ , where an isotropic and an alignment orientation are prescribed for  $k=1$  and  $k=2$ , respectively.
- on  $\Gamma_{end,k}$ , a pressure condition is imposed:  $(\boldsymbol{\sigma}_k \cdot \mathbf{n}) \cdot \mathbf{n} = -p_{end,k} = 0$ , where  $p_{end,k}$  is the pressure of phase  $k$  at the right end of the domain.
- on  $\Gamma_{edge,k}$ , no-slip boundary condition is imposed, which results in  $\mathbf{u}_k = 0$ .
- on  $\Gamma_{interf}$ , a continuity condition for the velocity field and normal stress is imposed:  $[\mathbf{u}]_{\Gamma_{interf}} = 0$ ,  $[\mathbf{n} \cdot \boldsymbol{\sigma} \cdot \mathbf{n}]_{\Gamma_{interf}} = 0$ , and a zero level-set function is imposed:  $\Phi_{\Gamma_{interf}} = 0$ , where  $\Phi_{\Gamma_{interf}}$  is the level set function at the interface.

where  $\Gamma_{in,k}$ ,  $\Gamma_{edge,k}$  and  $\Gamma_{end,k}$  respectively designate the boundaries of the domain corresponding to the injection zone for each phase  $k$  and to the zone of contact with the walls of each injection mold, and  $\Gamma_{interf}$  refers to the boundary at the interface zone, with  $\Gamma_{in,k} \cup \Gamma_{edge,k} \cup \Gamma_{end,k} \cup \Gamma_{interf} = \partial\Omega$ .

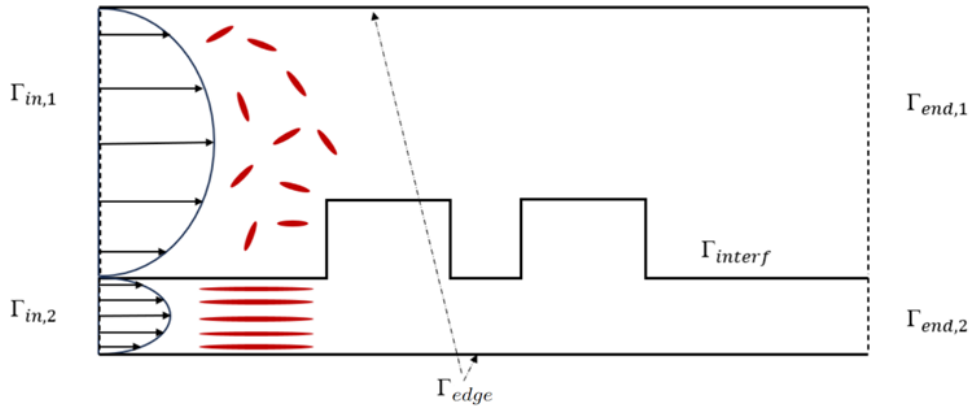


Figure IV.20: Representation of different boundaries and domains.

### IV.3.2 Numerical results

A comprehensive investigation into the influence of fiber concentration and fiber orientation on the displacement behavior at the interface between two phases was conducted using numerical simulations. The Stokes equation was employed to model the fluid flow over the two phases, which were discretized into 5397 nodes to form a rectangular computational domain with a height of 2 m and a length of 3 m. The lower phase represented the insert domain, as depicted in figure IV.21. The thickness of the refined mesh around the interface region was set to 0.14. Boundary conditions were carefully defined: the inlet pressure  $P_0$  for both phases was set to 40 Pa, while the outlet pressure,  $P_0$ , was established at 0 Pa. Non-slip boundary conditions were imposed along the top and bottom walls. A significant viscosity

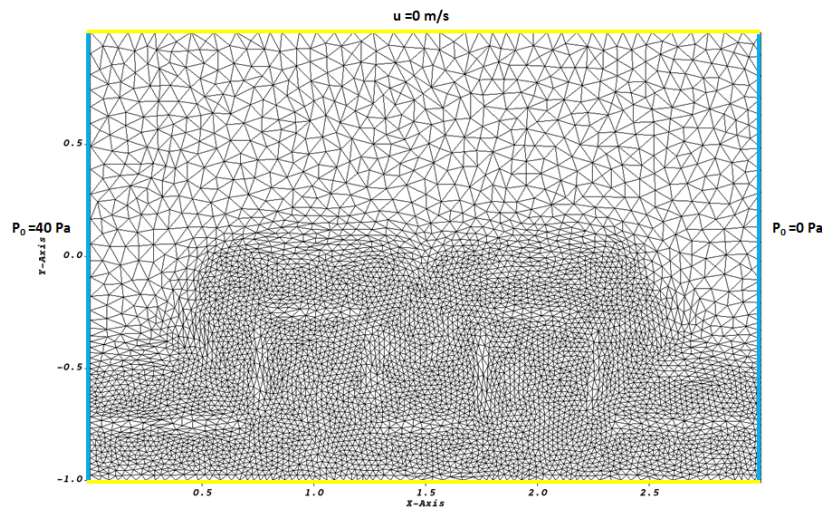


Figure IV.21: FE mesh

difference was introduced between the two phases: the upper phase had a viscosity of 1 Pa·s, while the lower phase was assigned a viscosity of 250 Pa·s, representing a more solid-like behavior. At the inlet of the upper phase, a fully randomized fiber orientation distribution was imposed. For the lower phase inlet, two cases were studied, with probability distribution functions favoring alignment of fibers in the

$x$ -direction for the first case and in the  $y$ -direction for the second case. Within the framework of the Fokker-Planck equation, the angular domain was discretized with a mesh size  $h$  of  $\frac{2\pi}{1024}$ , and the temporal discretization was executed via the Rosenbrock-W scheme, employing a time step  $\Delta t$  of  $5 \times 10^{-2}$  s. Figure IV.22 shows a representation of the key parameters change across the two phases in the numerical simulations. Two different shape factors  $\lambda$  and interaction coefficient  $C_I$  were set:

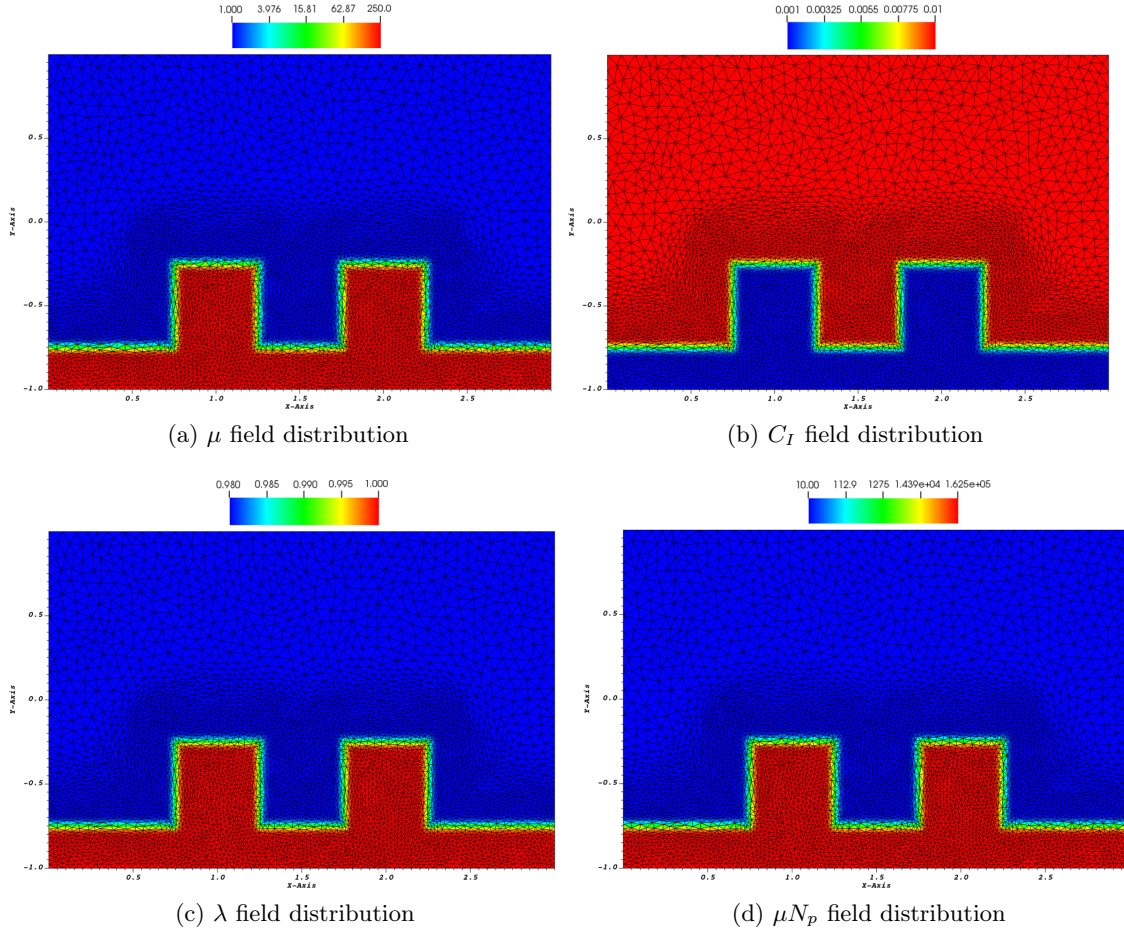


Figure IV.22: Representation of material scalar fields across the two phase using level set

for phase 1,  $\lambda=0.98$  and  $C_I=0.01$  to allow fibers to orient more freely, and for phase 2, representing the insert with unidirectional orientation,  $\lambda=1$  and  $C_I=0.001$  to limit fiber orientation. Notably, these simulations encompassed three different fiber volume fractions for phase 2, specifically  $\phi$  values of 40% 50% and 65%, and one  $\phi$  for phase 1 with a value of 15%, allowing for a comprehensive exploration of the impact of concentration. It should be noted that figure IV.22d represents the case of  $\phi=50\%$ , and the value of  $N_p$  is calculated based on the equation III.9 for phase 1 (dilute suspension) and the equation III.11 for phase 2 (semi-dilute suspension).

## IV.3.2.1 Effect of concentration on interface displacement behavior

Before getting into the analysis of the displacement behavior at the interface, it is also important to study the effect of the presence of the fibers in the flow on the velocity profile, and conversely the influence of the fluid flow on the fiber orientation in the two phase flow case, as it has been done in all previous cases, while maintaining a good stability of level set to track the changes across the two phases. Figure IV.23

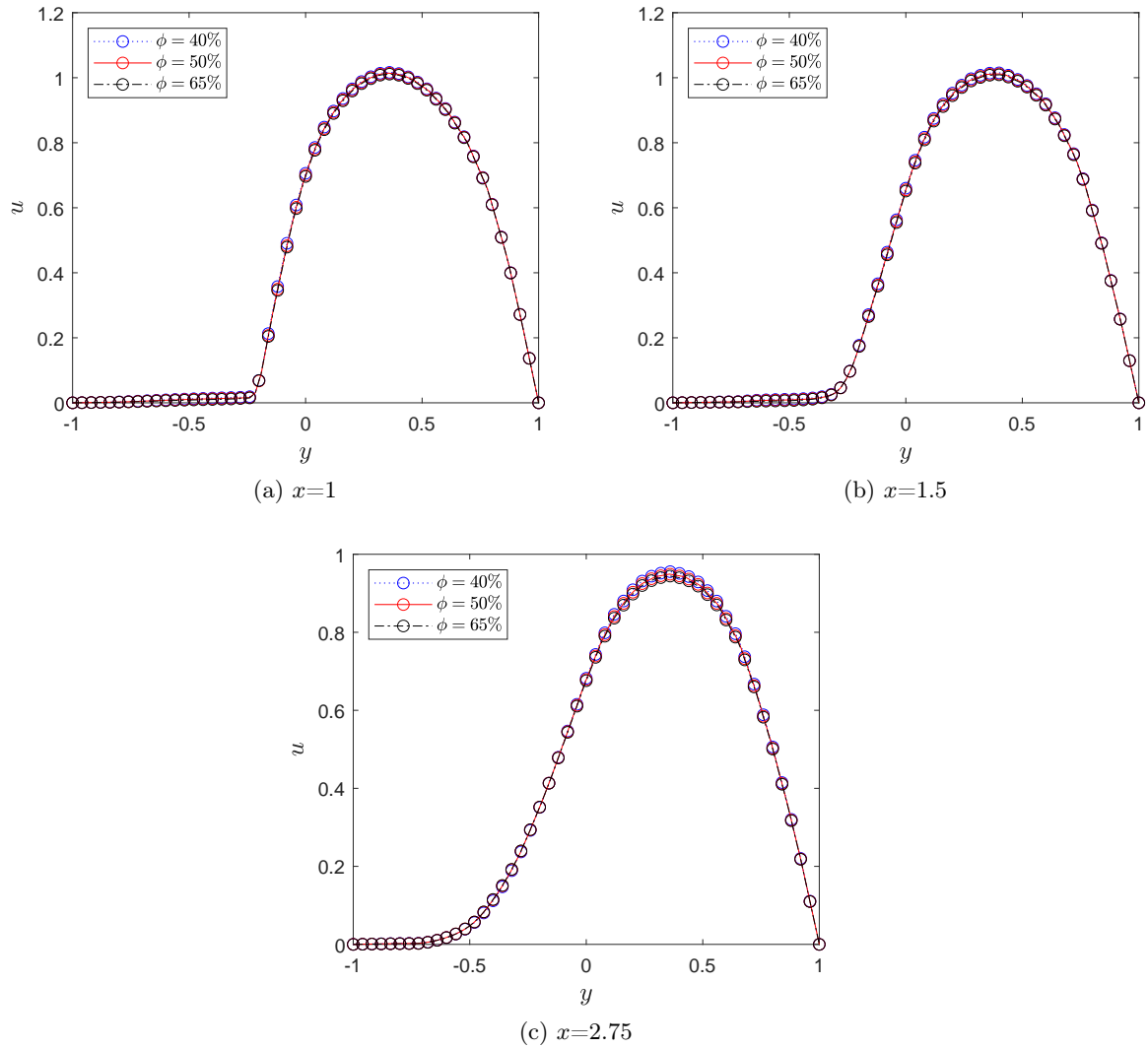


Figure IV.23: Velocity profile at different  $x$ -positions for various  $\phi$

illustrates the variation of velocity profiles along  $y$ -axis for various  $\phi$  at three distinct  $x$  locations. Interestingly, it can be seen that the profiles are nearly identical for all three cases of fiber concentration. This observation can be attributed to the high viscosity of phase 2 (insert) with a  $\mu$  set to 250 Pa.s, which approximates a solid-like behavior. Consequently, even slight changes in  $\phi$  are unlikely to significantly alter the flow characteristics of the phase 1 (injected thermoplastics). In other words, the simulations resemble a fluid flowing over a solid, where the changes in the solid properties primarily affect its own behavior due to the external force (originating

from phase 1) exerted on it.

It can be also noted that the velocity profiles obtained are consistent with the conditions imposed in the problem in order to build a model that can represent an overmolding process scenario. The velocity in the insert phase is indeed almost zero, representing the solid-like behavior of the insert. In contrast, the injected thermoplastics phase exhibits a standard parabolic velocity profile, as expected for a low-viscosity fluid flowing through a confined channel. This parabolic profile arises from the relatively low fiber volume concentration employed for the injected thermoplastics, with  $\phi=15\%$  corresponding to  $N_p \simeq 10$ . As  $N_p$  increases, the viscosity of the injected thermoplastics increases transforming the fluid into non-newtonian behavior as discussed in all previous results. Furthermore, the velocity profile exhibits slight variations for different  $x$  positions. As seen in figure IV.23c, the zero-velocity distance covered along the  $y$ -axis appears to be less than that depicted in figure IV.23b. This difference can be attributed to the presence of a "dead zone" ( $\mathbf{u} \simeq 0$ ) at  $x=1.5$  (region between the two ribs). At  $x=1$ , the zero-velocity covered distance along the  $y$ -axis is expected to be the greatest, as it encompasses the entire height of the rib. In addition, it is worth noting that numerically, the level set function ensures continuity in the velocity profile across the two phases.

Figure IV.24 showcases the variation of  $a_{xx}$  along  $y$ -axis for different  $\phi$  at three various  $x$  positions. First, it is noteworthy that the plots for different  $\phi$  values are also superposed, which is consistent with the findings in the velocity profiles. This observation is consistent with the previously discussed mutual influence of fiber orientation and fluid velocity.

A notable distinction emerges in the evolution of  $a_{xx}$  across different  $x$  locations. Figure IV.24a clearly demonstrates that the imposed unidirectional fiber orientation condition is accurately maintained within the insert domain, where  $a_{xx}$  remains consistently equal to 1 along the rib's height. When traversing the insert area, a distinct region called the "interphase" is created due to penetration phenomena at the interface. Within this relatively narrow region, a mixed fiber orientation state exists, exhibiting a coexistence of fibers aligned with the fiber flow and randomly oriented fibers. This is visually evidenced by the zigzag variation of  $a_{xx}$  across the interface as shown in Figure IV.24a.

In figure IV.24b, near the interface of the injected thermoplastic phase,  $a_{xx}$  shows a slight decrease below 0.5. This phenomenon can be attributed to the appearance of tiny vertical velocity fluctuations in the dead zone at  $x=1.5$  as seen in figure IV.25. Conversely, at  $x=2.75$ , the fiber orientation remains in an isotropic state near the interface, as shown in figure IV.24c. Moving away from the interface zone and into the upper phase, the evolution of  $a_{xx}$  follows a consistent pattern for different  $x$  positions. Fiber orientation remains isotropic near the core region, where the generalized shear rate approaches zero. As we progress towards the skin-shell region, fibers tend to align parallel to the fluid direction. Finally, akin to the continuity observed in the velocity profile, the level set function effectively ensures a seamless transition in the evolution of fiber orientation throughout the two-phase system.

Figure IV.26 visualizes the level set displacement at the interface relative to the initial position and the calculated maximum displacement for different  $\phi$ . It is evident that with increasing  $\phi$ , the level set shifts less towards the right, implying

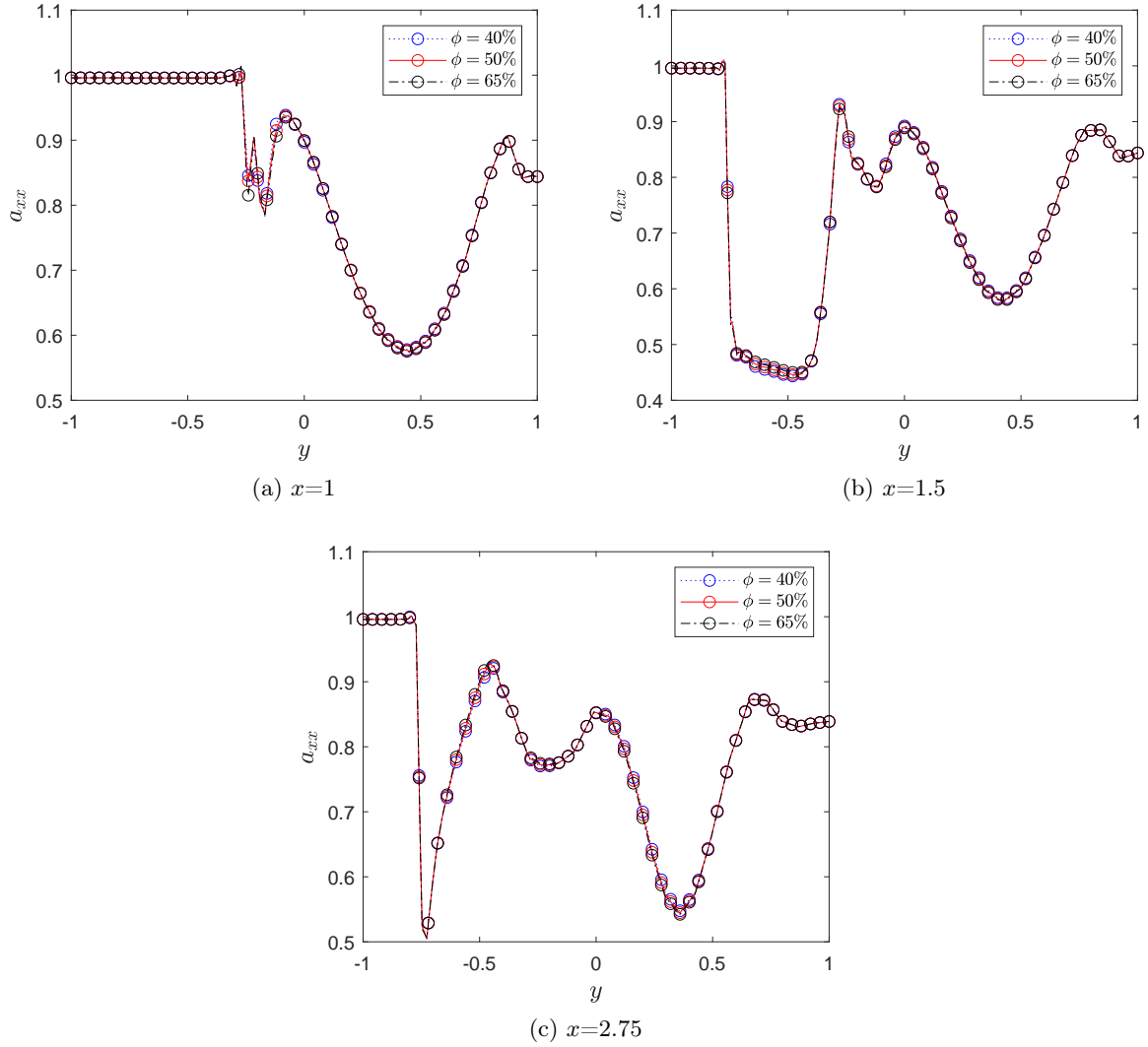


Figure IV.24: Evolution of  $a_{xx}$  at different  $x$ -positions for various  $\phi$

that the insert phase experiences a diminished impact from the force exerted by the fluid phase. This translates to a more rigid lower phase in physical terms. This observation can be attributed to the heightened stiffness and strength reached by incorporating a higher fiber volume concentration, which effectively slows down the displacement. Figure IV.26b quantifies the variation of maximum displacement with respect to  $\phi$ . Notably, as  $\phi$  increases from 40% to 65%, the maximum displacement  $\Delta x$  decreases from 92.875 mm to 78.5 mm. Interestingly, the rate of decrease does not remain constant with a higher slope observed when  $\phi$  is between 40% and 50% compared to when it increases from 50% to 65%. This suggests that there exists a limit to stiffness, implying that after a certain  $\phi$  value, the material's stiffness and strength will no longer exhibit significant improvement. This realization aligns with the common industrial practice of employing fiber volume concentrations within the range of 40% to 65% for unidirectional composites.

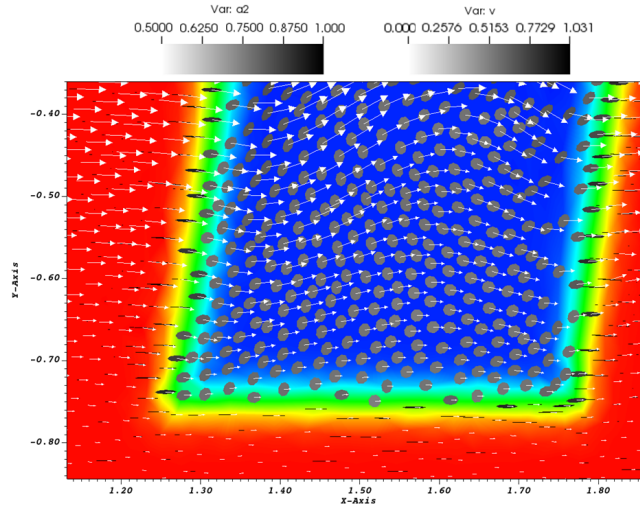
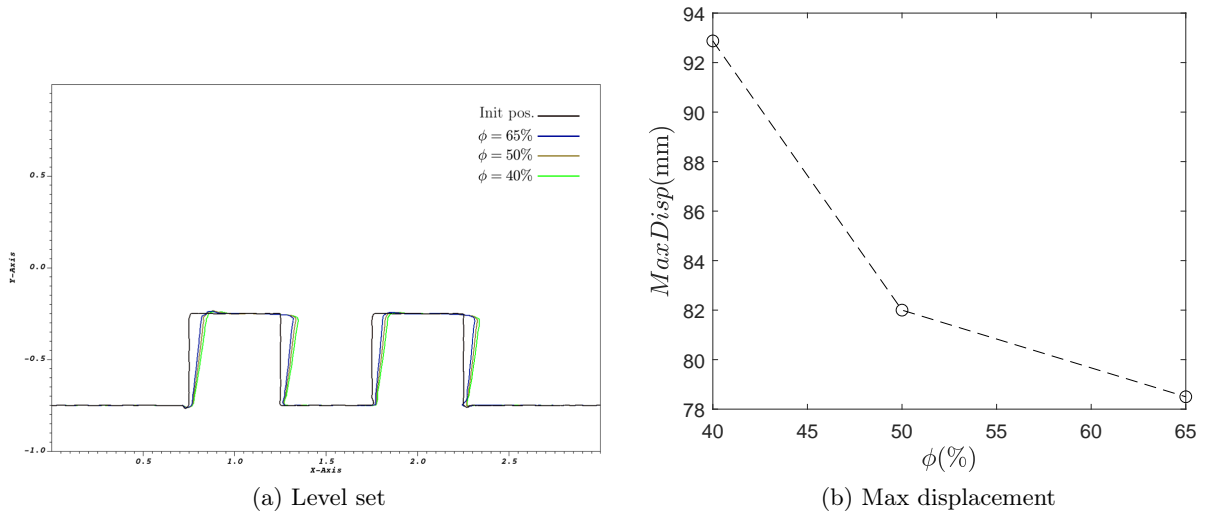


Figure IV.25: Representation of velocity field in the dead zone

Figure IV.26: Measuring the evolution of interface geometry under varying  $\phi$ 

#### IV.3.2.2 Influence of fiber orientation on interface displacement

Another study was conducted to validate the developed model by investigating the influence of fiber orientation on the insert displacement. Seven simulations were carried out, each with a different initial fiber orientation represented by  $\mathbf{a}_4$ . All simulations were conducted with a constant fiber volume fraction of  $\phi=50\%$ . The fiber orientations considered were 0, 10, 30, 45, 60, 80, and 90 degrees. Figure IV.27 shows the level set displacement relative to the initial position and the computed maximum displacement for different  $\theta$ . The results showed that the variation of displacement followed a parabolic pattern with respect to  $\theta$  (angle of fiber orientation), as depicted in figure IV.27b. The maximum displacement occurred when the fibers were oriented parallel to the flow direction, with a value of  $\Delta x=82$  mm. This is attributed to the smoother flow of the fluid in this configuration compared to other cases. Interestingly, the displacement was significantly reduced as  $\theta$  increased to

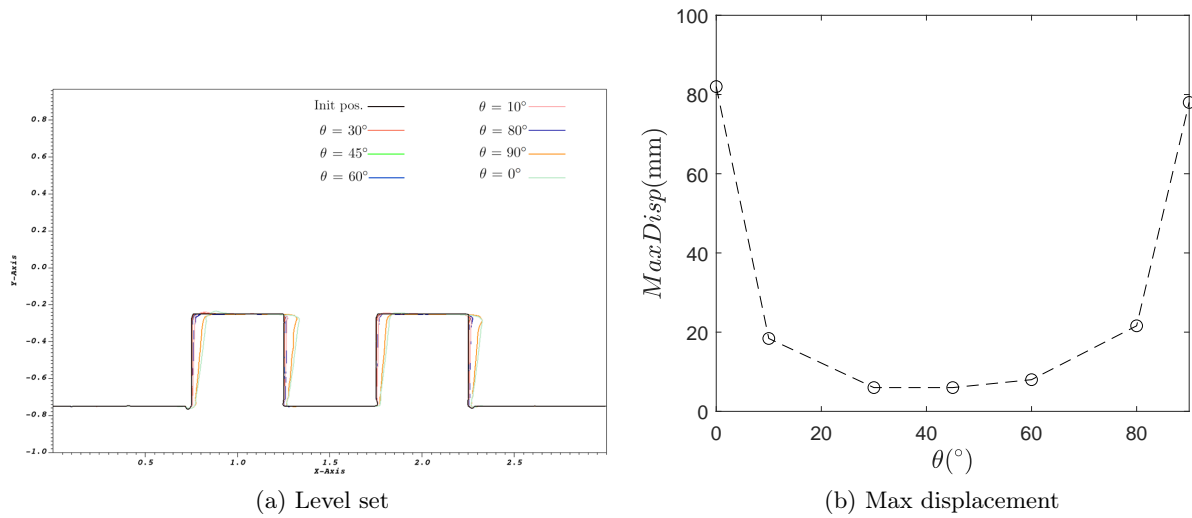


Figure IV.27: Measuring the evolution of interface geometry under varying  $\theta$

wards  $45^\circ$ , reaching a minimum value of  $\Delta x=6$  mm. Intriguingly, it is worthy noted that case of fibers oriented at  $\theta=45^\circ$  with respect to the flow direction demonstrated the most robust resistance to displacement. Then as  $\theta$  increases towards  $90^\circ$ , the displacement started to increase again, reaching a value of  $\Delta x=78$  mm. These findings demonstrate that the arrangement of fibers significantly impacts the flow behavior and the displacement of the insert. The fibers act as physical barriers to the flow, and their orientation modulates the flow resistance, which in turn affects the layer displacement at the interface.

### IV.3.3 Short summary

- ✓ Instead of a standard fluid-solid interaction model, a two-phase flow model is used to simulate an overmolding process by treating the solid phase as a very viscous fluid. This simplification reduces the number of equations required to be solved, making the simulation more computationally efficient.
- ✓ The study for this model mainly focuses on the displacement of the interface in relation to two factors: fiber volume concentration  $\phi$  and the initial fiber orientation in the insert phase.
- ✓ Increasing fiber volume concentration leads to enhancing the stiffness and strength of the insert phase resulting in reduced interface displacement, but this improvement is limited up to a certain fiber volume concentration.
- ✓ The layer displacement at the interface is influenced by the initial orientation of fibers within the insert phase, as their arrangement shapes the flow resistance and velocity distribution within the insert phase, ultimately affecting the displacement at the interface.

## IV.4 Conclusion

This study presents two main contributions. Firstly, the flow-fiber coupling model was validated in more complex geometries, specifically 2D contraction and L-shaped flow domains. The simulations revealed that increasing the rheological coupling parameter  $N_p$  leads to an expansion of recirculation zones where fibers align their streamlines, except in the vortex center where they tend to orient randomly. For the contraction domain, the velocity profile flattens as  $N_p$  increases, resembling the patterns observed in a standard 2D channel flow domain. For L-shaped domain, the effect of  $N_p$  on the transition of the fluid into non-Newtonian behavior was more pronounced through the entry vertical channel than the exit channel. Mesh refinement studies demonstrated that finer meshes better capture the size of vortices and fiber orientation evolution with greater precision, particularly at the throat region with high shear rates.

Secondly, a two-phase flow model was constructed for simulating overmolding processes. The model uses a Newtonian fluid for the fluid phase and a highly viscous fluid for the solid phase, representing the injected thermoplastic and the thermoformed insert, respectively. This simplification reduces computational complexity compared to conventional fluid-solid interaction (FSI) models that require solving two sets of equations. The distinction between the two phases properties was achieved using the level set function. The model was validated by investigating the impact of fiber concentration and fiber orientation on the displacement behavior of the insert. The results showed that increasing fiber volume fraction  $\phi$  resulted in the formation of a barrier within the lower phase, which disrupted the smooth

flow of the fluid, ultimately leading to a decrease in interface displacement. This is attributed to the increased rigidity of the insert, enabling it to better withstand the flow force. Similarly, varying the initial orientation of fibers in the rigid phase through  $\mathbf{a}_4$  significantly influenced the layer displacement. Remarkably, an orientation of  $\theta=45^\circ$  with respect to the flow direction exhibited the strongest resistance to displacement.

All test cases done in this chapter can provide a robust foundation for conducting more sophisticated simulations, encompassing complex scenarios involving both mono- and two-phase systems.



# Conclusion and perspectives

---

## Contents

---

<b>V.1 Synthesis and conclusion</b> . . . . .	<b>127</b>
<b>V.2 Perspectives and improvements</b> . . . . .	<b>130</b>

---

Chapter V of this thesis is dedicated to the conclusions and future perspectives of the work conducted on solving the Fokker-Planck equation to comprehend and predict fiber orientation, as it also addresses the integration of fiber orientation into the Stokes equation in the form of an orientation tensor, with the aim of constructing a model for simulating fiber orientation and motion within fluid flow. The developed model has potential applications in real-world scenarios, particularly in simulating processes such as injection molding, which facilitates the understanding of defects that occur during the fabrication of parts.

## V.1 Synthesis and conclusion

### Resolution of Fokker-Planck equation

A new numerical model is designed to investigate the dynamic motion of fibers, specifically targeting its rotation during the injection phase of molten thermoplastics within a mold cavity. The developed approach (DNS) is focused on the resolution of the Fokker-Planck equation, offering insight into fiber orientation at the mesoscopic level, rather than relying on pre-averaged quantities such as the second and fourth order orientation tensors ( $\mathbf{a}_2, \mathbf{a}_4$ ) which introduces inaccuracies and information loss due to the utilization of closure approximations. The proposed numerical model is implemented within a finite element framework.

A modified version of the Fokker-Planck equation has been formulated, enabling a simplified solution approach. In this reformulation, a simplification is introduced by replacing the vector  $\mathbf{p}$ , which represents the unit vector describing fiber orientation, with a single angle  $\theta$ . This angle can effectively capture the rotation of the fiber and serves as a concise descriptor of its orientation. As a result, the original two-dimensional Fokker-Planck equation is reduced to a simpler one-dimensional advection-diffusion equation, where the angular velocity  $\dot{\theta}$  at which the fibers rotate is easily calculated rather than explicitly considering the two-dimensional orbital velocity  $\dot{\mathbf{p}}$ .

Thus, in the initial formulation, the configurational domain for solving the Fokker-Planck equation was represented by a 2D unit circle. However, to simplify the computational process, a transformation is applied to convert this 2D domain into a 1D domain. This transformation involves projecting the unit circle onto a 1D segment, specifically a segment of length  $2\pi$ . This new 1D domain serves as the basis for discretization.

In order to address the challenges posed by the Fokker-Planck equation, the SUPG approach is employed as an alternative to the standard Galerkin method. As the Fokker-Planck equation is characterized as an advection-diffusion equation, using the standard Galerkin method alone can lead to undesirable effects such as excessive numerical diffusion or non-physical oscillations in the computed solution. By adopting the SUPG approach, a stabilization term is introduced that explicitly considers the advective nature of the equation. This additional term enhances the accuracy and stability of the numerical solution.

Validation tests were performed to ensure the accuracy of the Fokker-Planck equation solver. The normalization condition, indicating that the probability distribution function's integral remains 1, was satisfied. Investigations into parameter influences ( $\lambda$ ,  $D_r$ ) yielded logical and expected results. A convergence study determined optimal mesh sizes and time steps for accurate solutions with minimal computational cost. Comparisons with existing literature, including analytical solutions, showed the solver's higher accuracy and similarity to analytical results, confirming its reliability and effectiveness.

### Resolution of Stokes-fiber coupled problem

In order to incorporate the effects of fibers on the macroscopic stresses in the constitutive equation and establish a flow-fiber coupling problem, various empirical models have been developed in the literature to describe the rheological behavior of fiber-filled suspensions. In this study, the theory of slender bodies is employed, specifically the Batchelor model, which enables the construction of a macroscopic model applicable to suspensions in a dilute or semi-dilute regime. All simulations have been conducted based on this model, providing a comprehensive understanding of the flow behavior and interactions between the fibers and the surrounding fluid.

Numerically, the compressible Stokes-fiber coupled problem was solved using the mixed finite element method. The computational domain was discretized employing triangular elements in two dimensions (2D), and a continuous approximation of velocity and pressure was considered, with velocity enriched by bubbles. It has been demonstrated that this interpolation satisfies the stability conditions of the problem, even in the incompressible limit.

The utilization of the MPI technique in solving the fiber-flow coupling problem proved to be highly advantageous. By distributing the computational workload across multiple cores, parallel processing enabled by MPI significantly enhances com-

putational efficiency and reduces the overall computation time. With the ability to simultaneously solve the Fokker-Planck equation at each node of the configurational domain and compute the advection equation for multiple components of the probability distribution function, the MPI technique effectively accelerates the simulation of fiber orientation and translational motion within the flow.

2D channel flow simulations were performed to investigate the impact of fiber presence on fluid flow and the influence of fluid flow on fiber orientation. Specifically, the rheological coupling coefficient  $N_p$  and interaction coefficient  $C_I$  were controlled to observe how changes in these parameters affected the system. The results showed that when  $N_p=0$ , the fibers preferentially aligned near the wall region and maintained random orientation in the core region. Increasing  $N_p$  led to longer relaxation times for the fibers to align with the flow, a flatter velocity profile due to a transition into non-Newtonian fluid behavior, a shift of fiber orientation patterns from the flow direction to the transverse direction around the core, a slight decrease in generalized shear rate  $\dot{\gamma}$  for both the skin and shell regions, and a widening of the  $\dot{\gamma}$  profile within the core region. Further, increasing  $C_I$  resulted in a decrease in fiber alignment near the walls and an expansion of the isotropic orientation zone.

### Up to applications (Injection molding/Overmolding)

In this study, simulations were performed first using the constructed flow-fluid coupling model on 2D complex domains like contractions and L-shaped, to emulate real-world scenarios encountered in the injection molding process. The aim was to capture the intricate flow behavior and fiber-fluid interaction within these representative geometries.

The study for the 2D contraction flow domain focused on the impact of  $N_p$  and the mesh size on the solution of the coupling problem from both physical and numerical perspectives. It was found that increasing  $N_p$  led to an expansion of the recirculation zones, as fibers align with the vortex streamlines, except in the vortex center where they tend to orient randomly. Additionally, the velocity profile flattens as  $N_p$  increases, demonstrating similar trends to those observed in a standard 2D channel flow domain. Moreover, increasing  $N_p$  resulted in more uniform vertical velocity distribution in the narrow channel region at the throat of the domain. From a numerical standpoint, mesh refinement plays a crucial role in this domain. Finer meshes produce larger, more convex vortices with increased intensity compared to those obtained with coarser meshes. Refining spatial mesh improved representation of high shear rate effects on fiber orientation distribution, particularly near throat region.

For the L-shaped domain, similar effects of  $N_p$  on the vortex zone and fiber orientation in this zone were observed compared to the contraction domain. The focus was mainly on the throat region, where fiber orientation was studied. It was interpreted that in this region, the effect of fibers being advected by the fluid's velocity had a more significant impact on fiber orientation, particularly for  $N_p=0$ . Conversely, this

effect had less influence on  $N_p \neq 0$  cases, where an increase in fiber concentration resulted in a reduction in velocity magnitude. As a result, the shear rate had a more pronounced impact on fiber orientation in this zone when  $N_p$ . An investigation on the coupling effect on the fluid velocity has been done, and it was noticed that in the L-shaped domain, the effect of  $N_p$  in transitioning the fluid into non-Newtonian was more prominent through the entry vertical channel than the horizontal exit channel.

To accurately simulate the overmolding process, the used approach deviates from the conventional fluid/solid interaction model in favor of a fluid/fluid interaction model. This innovative choice streamlines the computational process by solving a single equation across the entire domain with only varying viscosities in the two phases, contrasted with the more typical approach of solving two equations. In this model, the insert part (thermoformed) is depicted as a phase with high viscosity, while the injected short fiber reinforced thermoplastic is represented by a phase with lower viscosity.

To validate the two-phase model, simulations were conducted to investigate the impact of fiber concentration and fiber orientation on the displacement behavior at the interface between the two phases. The level set method was employed to assign different parameters ( $\lambda$ ,  $C_I$ ,  $\mu$ ,  $\phi$ ,  $\mathbf{a}_4$ ) to each phase to replicate the respective behaviors of the injected thermoplastics and the unidirectional composite insert. The results revealed that an increase in fiber volume fraction  $\phi$  within the insert phase resulted in enhanced stiffness and strength, leading to a reduction in interface displacement. This is attributed to the increased rigidity of the insert phase, enabling it to better withstand the force exerted by the flow upon the insert surface. In addition, the arrangement of fibers within the insert phase significantly impacts the layer displacement, as their orientation influences the flow resistance and velocity distribution within the insert phase. This, in turn, affects the displacement at the interface. A counter-intuitive observation has been made, as fibers oriented at  $\theta=45^\circ$  with respect to the flow direction exhibit the strongest resistance to displacement can be attributed to the fact that fibers at this angle effectively impede the flow.

## V.2 Perspectives and improvements

### Resolution of Fokker-Planck equation

In the context of solving the Fokker-Planck equation, an improvement can be achieved by exploiting the symmetric property of the problem. Instead of fully discretizing the angular domain from 0 to  $2\pi$ , it is possible to limit the angular discretization to the range of  $-\pi/2$  to  $\pi/2$ . This approach effectively reduces the computational effort and saves valuable computation time. By leveraging the symmetric nature of the problem, accurate results can still be obtained while optimizing the computational resources required for solving the Fokker-Planck equation.

In this study, the Fokker-Planck equation has been successfully solved in a 1D domain to represent a 2D configuration. However, further development can be un-

dertaken to extend the approach to higher dimensions, specifically by solving the Fokker-Planck equation in a 2D domain that can better represent a 3D configuration. This can be accomplished by representing the orbital velocity  $\dot{\mathbf{p}}$  as a function of two angular velocities  $(\dot{\theta}, \dot{\phi})$ . By considering additional dimensions, the model can capture the intricate dynamics of fibers in a more realistic and accurate manner, paving the way for enhanced simulations and predictions in complex 3D systems.

### Resolution of Stokes-fiber coupled problem

While this study has made significant progress in understanding the dynamics of the flow-fiber coupling problem, it's important to note that certain aspects remain unexplored. Specifically, the influence of changing the fiber shape factor  $\lambda$  on the behavior of the fluid within the flow-fiber coupling problem has not been thoroughly investigated in this study. Future research endeavors could focus on systematically varying the fiber shape factor  $\lambda$  to comprehensively assess its impact on the coupling dynamics.

Moreover, a promising avenue for future research involves delving into the dynamics of non-Newtonian fluids within the context of the flow-fiber coupling problem. These fluids showcase distinct rheological behaviors, introducing intriguing complexities into the system and offering a captivating area of study. Additionally, considering the thermal impact on the fluid, where viscosity responds to temperature fluctuations, adds another layer of intricacy and practical relevance. Integrating thermal effects into the flow-fiber problem holds significant potential, especially in fields like industrial processes (injection or overmolding process).

### Up to applications (Injection molding/Overmolding)

An interesting perspective for future work is the creation of realistic 3D shapes resembling complex geometries found in actual injection molding processes. For example using computer-aided design (CAD) software enables accurate representation of these shapes. Importing these 3D shapes into the solver allows extensive testing and validation of the fiber-flow coupling model. Comparing simulation results with experimental tests assesses the model's accuracy and reliability. Research in this direction aims to refine and optimize the fiber-flow coupling model, enhancing its practical applicability and advancing understanding in fiber-filled composite manufacturing.

A potential avenue for further work involves the study of the interphase region between the two phases, which is formed due to the penetration phenomenon that occurs during the overmolding process. Within this small region, a complex mixture of different fiber orientations is observed. The developed direct numerical simulation DNS method in this work for solving Fokker-Planck equation can be used to examine the fiber orientation within this region, enabling a more thorough understanding of the fiber-fiber interactions in a two phase problem and their impact on the mechanical properties of the final composite. This information can be used to optimize the overmolding process and produce composites with enhanced properties.

Another prospective work can involve constructing and integrating a new model into the current model using tensor-based anisotropic constitutive behavior to predict the various viscosity components of an anisotropic two-phase fluid. This would enable a more realistic simulation of the behavior of a unidirectional composite during the overmolding process.

# Bibliography

- [1] S. Hossain, “Applications of composite materials in automobile.” University Presentation, 2017.
- [2] M. Kaufmann, D. Zenkert, and P. Wennhage, “Integrated cost/weight optimization of aircraft structures,” *Structural and Multidisciplinary Optimization*, vol. 41, pp. 325–334, 03 2009.
- [3] R. RIM, “What are composites?,” 2021.
- [4] J. M. Stickel and M. Nagarajan, “Glass fiber-reinforced composites: from formulation to application,” *International Journal of Applied Glass Science*, vol. 3, no. 2, pp. 122–136, 2012.
- [5] M. S. Moawad, “Effect of short glass fiber on shear capacity for shallow wide reinforced concrete beams,” *Journal of Engineering and Applied Science*, vol. 68, no. 1, pp. 1–16, 2021.
- [6] S. C. SE, “Sigrafil® continuous carbon fiber tows,” 2022.
- [7] S. Manoharan, B. Suresha, G. Ramadoss, and B. Bharath, “Effect of short fiber reinforcement on mechanical properties of hybrid phenolic composites,” *J. Mater.*, vol. 2014, pp. 1–9, 2014.
- [8] M. Ali, A. Soliman, and M. Nehdi, “Hybrid-fiber reinforced engineered cementitious composite under tensile and impact loading,” *Materials & Design*, vol. 117, pp. 139–149, 2017.
- [9] A. Goldberg and C. Burstone, “The use of continuous fiber reinforcement in dentistry,” *Dental materials*, vol. 8, no. 3, pp. 197–202, 1992.
- [10] R. Conner, H. Choi-Yim, and W. Johnson, “Mechanical properties of zr57nb5al10cu15. 4ni12. 6 metallic glass matrix particulate composites,” *Journal of Materials Research*, vol. 14, no. 8, pp. 3292–3297, 1999.
- [11] M. M. Thwe and K. Liao, “Effects of environmental aging on the mechanical properties of bamboo–glass fiber reinforced polymer matrix hybrid composites,” *Composites Part A: Applied Science and Manufacturing*, vol. 33, no. 1, pp. 43–52, 2002.
- [12] F. H. Gojny, M. H. Wichmann, B. Fiedler, and K. Schulte, “Influence of different carbon nanotubes on the mechanical properties of epoxy matrix composites—a comparative study,” *Composites science and technology*, vol. 65, no. 15-16, pp. 2300–2313, 2005.
- [13] V. Chaudhary and F. Ahmad, “A review on plant fiber reinforced thermoset polymers for structural and frictional composites,” *Polymer Testing*, vol. 91, p. 106792, 2020.

- [14] J.-P. Pascault and R. J. Williams, "Thermosetting polymers," *Handbook of Polymer Synthesis, Characterization, and Processing*, pp. 519–533, 2013.
- [15] R. Pantani, I. Coccorullo, V. Speranza, and G. Titomanlio, "Modeling of morphology evolution in the injection molding process of thermoplastic polymers," *Progress in polymer science*, vol. 30, no. 12, pp. 1185–1222, 2005.
- [16] M. Hecke and W. Schomburg, "Review on micro molding of thermoplastic polymers," *Journal of Micromechanics and Microengineering*, vol. 14, no. 3, p. R1, 2003.
- [17] S. S. . All, "Polymer structure and intermolecular forces," 2014.
- [18] J. Lamon, "Properties of characteristics of sic and sic/sic composites," 2019.
- [19] S. Zhandarov and E. Mäder, "Characterization of fiber/matrix interface strength: applicability of different tests, approaches and parameters," *Composites Science and Technology*, vol. 65, no. 1, pp. 149–160, 2005.
- [20] L. Greszczuk, "Theoretical studies of the mechanics of the fiber-matrix interface in composites," 1969.
- [21] M. Mohan, M. Ansari, and R. A. Shanks, "Review on the effects of process parameters on strength, shrinkage, and warpage of injection molding plastic component," *Polymer-Plastics Technology and Engineering*, vol. 56, no. 1, pp. 1–12, 2017.
- [22] D. O. Kazmer, *Injection mold design engineering*. Carl Hanser Verlag GmbH Co KG, 2016.
- [23] H. Fu, H. Xu, Y. Liu, Z. Yang, S. Kormakov, D. Wu, and J. Sun, "Overview of injection molding technology for processing polymers and their composites," *ES Materials & Manufacturing*, vol. 8, no. 4, pp. 3–23, 2020.
- [24] D. V. Rosato and M. G. Rosato, *Injection molding handbook*. Springer Science & Business Media, 2012.
- [25] C. Kaynak and S. D. Varsavas, "Performance comparison of the 3d-printed and injection-molded pla and its elastomer blend and fiber composites," *Journal of Thermoplastic Composite Materials*, vol. 32, no. 4, pp. 501–520, 2019.
- [26] G. Group, "Two-shot injection molding solutions," 2022.
- [27] R. Direct, "Overmolding vs insert molding: Selecting the better manufacturing process for your product," 2022.
- [28] E. Anczurowski, R. Cox, and S. Mason, "The kinetics of flowing dispersions: Iv. transient orientations of cylinders," *Journal of Colloid and Interface Science*, vol. 23, no. 4, pp. 547–562, 1967.
- [29] B. Trevelyan and S. Mason, "Particle motions in sheared suspensions. i. rotations," *Journal of Colloid Science*, vol. 6, no. 4, pp. 354–367, 1951.

- [30] M. Vincent, Y. Germain, and J. Agassant, "Numerical and experimental study of the fiber motion in reinforced thermoplastic flows," in *Progress and Trends in Rheology II*, pp. 144–146, Springer, 1988.
- [31] G. De Bonhomme and T. De Brouwer, "Etude de l'orientation des fibres courtes lors de la mise en oeuvre des matériaux composites," tech. rep., Research report, Université Catholique de Louvain, 1990.
- [32] M. Arif, F. Meraghni, Y. Chemisky, N. Despringre, and G. Robert, "In situ damage mechanisms investigation of pa66/gf30 composite: Effect of relative humidity," *Composites Part B: Engineering*, vol. 58, pp. 487–495, 2014.
- [33] P. Bright, R. Crowson, and M. Folkes, "A study of the effect of injection speed on fibre orientation in simple mouldings of short glass fibre-filled polypropylene," *Journal of Materials Science*, vol. 13, no. 11, pp. 2497–2506, 1978.
- [34] P. Bright and D. MW, "Factors influencing fibre orientation and mechanical properties in fibre reinforced thermoplastics injection mouldings," 1981.
- [35] M. Folkes and D. Russell, "Orientation effects during the flow of short-fibre reinforced thermoplastics," *Polymer*, vol. 21, no. 11, pp. 1252–1258, 1980.
- [36] A. Bernasconi, F. Cosmi, and D. Dreossi, "Local anisotropy analysis of injection moulded fibre reinforced polymer composites," *Composites Science and Technology*, vol. 68, no. 12, pp. 2574–2581, 2008.
- [37] M. Vincent and J. Agassant, "Experimental study and calculations of short glass fiber orientation in a center gated molded disc," *Polymer composites*, vol. 7, no. 2, pp. 76–83, 1986.
- [38] P. Shokri and N. Bhatnagar, "Effect of packing pressure on fiber orientation in injection molding of fiber-reinforced thermoplastics," *Polymer Composites*, vol. 28, no. 2, pp. 214–223, 2007.
- [39] R. Bay, C. Tucker, and R. Davis, "Effect of processing on fiber orientation in simple injection moldings," in *Annual Technical Conference-Society of Plastics Engineers*, pp. 539–542, 1989.
- [40] S. Ranganathan and S. G. Advani, "A simultaneous solution for flow and fiber orientation in axisymmetric diverging radial flow," *Journal of Non-Newtonian Fluid Mechanics*, vol. 47, pp. 107–136, 1993.
- [41] D. Spahr, K. Friedrich, J. Schultz, and R. Bailey, "Microstructure and fracture behaviour of short and long fibre-reinforced polypropylene composites," *Journal of Materials Science*, vol. 25, no. 10, pp. 4427–4439, 1990.
- [42] A. Megally, *Etude et modélisation de l'orientation de fibres dans des thermoplastiques renforcés*. PhD thesis, École Nationale Supérieure des Mines de Paris, 2005.

- [43] M. Fujiyama, H. Awaya, and S. Kimura, "Mechanical anisotropy in injection-molded polypropylene," *Journal of Applied Polymer Science*, vol. 21, no. 12, pp. 3291–3309, 1977.
- [44] T. Coupez and S. Marie, "From a direct solver to a parallel iterative solver in 3-d forming simulation," *The International Journal of Supercomputer Applications and High Performance Computing*, vol. 11, no. 4, pp. 277–285, 1997.
- [45] J. W. Gillespie Jr, J. A. Vanderschuren, and R. B. Pipes, "Process induces fiber orientation: Numerical simulation with experimental verification," *Polymer composites*, vol. 6, no. 2, pp. 82–86, 1985.
- [46] R. S. Bay and C. L. Tucker III, "Fiber orientation in simple injection moldings. part ii: Experimental results," *Polymer composites*, vol. 13, no. 4, pp. 332–341, 1992.
- [47] G. B. Jeffery, "The motion of ellipsoidal particles immersed in a viscous fluid," *Proceedings of the Royal Society of London. Series A, Containing papers of a mathematical and physical character*, vol. 102, no. 715, pp. 161–179, 1922.
- [48] S. Prager, "Stress-strain relations in a suspension of dumbbells," *Transactions of the Society of Rheology*, vol. 1, no. 1, pp. 53–62, 1957.
- [49] S. G. Advani and C. L. Tucker III, "The use of tensors to describe and predict fiber orientation in short fiber composites," *Journal of rheology*, vol. 31, no. 8, pp. 751–784, 1987.
- [50] G. L. Hand, "A theory of anisotropic fluids," *Journal of Fluid Mechanics*, vol. 13, no. 1, pp. 33–46, 1962.
- [51] M. Grmela and P. Carreau, "Conformation tensor rheological models," *Journal of Non-Newtonian Fluid Mechanics*, vol. 23, pp. 271–294, 1987.
- [52] K. Breuer, M. Stommel, and W. Korte, "Analysis and evaluation of fiber orientation reconstruction methods," *Journal of Composites Science*, vol. 3, no. 3, p. 67, 2019.
- [53] D. Kuzmin, "Planar and orthotropic closures for orientation tensors in fiber suspension flow models," *SIAM Journal on Applied Mathematics*, vol. 78, no. 6, pp. 3040–3059, 2018.
- [54] M. Kontopoulou, *Applied Polymer Rheology: Polymeric Fluids with Industrial Applications*. Wiley, 2011.
- [55] A. Redjeb, *Simulation numérique de l'orientation de fibres en injection de thermoplastique renforcé*. PhD thesis, École Nationale Supérieure des Mines de Paris, 2007.
- [56] L. Orgéas, P. Dumont, and S. L. Corre, "5 - rheology of highly concentrated fiber suspensions," in *Rheology of Non-Spherical Particle Suspensions* (F. Chinesta and G. Ausias, eds.), pp. 119 – 166, Elsevier, 2015.

- [57] M. Doi, “Molecular dynamics and rheological properties of concentrated solutions of rodlike polymers in isotropic and liquid crystalline phases,” *Journal of Polymer Science: Polymer Physics Edition*, vol. 19, no. 2, pp. 229–243, 1981.
- [58] R. B. Pipes, D. W. Coffin, S. F. Shuler, and P. Šimáček, “Non-newtonian constitutive relationships for hyperconcentrated fiber suspensions,” *Journal of composite materials*, vol. 28, no. 4, pp. 343–351, 1994.
- [59] F. Folgar and C. L. Tucker III, “Orientation behavior of fibers in concentrated suspensions,” *Journal of reinforced plastics and composites*, vol. 3, no. 2, pp. 98–119, 1984.
- [60] F. Chinesta, G. Chaidron, and A. Poitou, “On the solution of fokker–planck equations in steady recirculating flows involving short fiber suspensions,” *Journal of Non-Newtonian Fluid Mechanics*, vol. 113, no. 2, pp. 97–125, 2003.
- [61] J. Férec, M. Heniche, M. Heuzey, G. Ausias, and P. Carreau, “Numerical solution of the fokker–planck equation for fiber suspensions: application to the folgar–tucker–lipscomb model,” *Journal of non-newtonian fluid mechanics*, vol. 155, no. 1-2, pp. 20–29, 2008.
- [62] J. Thomasset, P. J. Carreau, B. Sanschagrin, and G. Ausias, “Rheological properties of long glass fiber filled polypropylene,” *Journal of non-newtonian fluid mechanics*, vol. 125, no. 1, pp. 25–34, 2005.
- [63] J. Wang, J. F. O’Gara, and C. L. Tucker III, “An objective model for slow orientation kinetics in concentrated fiber suspensions: Theory and rheological evidence,” *Journal of Rheology*, vol. 52, no. 5, pp. 1179–1200, 2008.
- [64] J. H. Phelps and C. L. Tucker III, “An anisotropic rotary diffusion model for fiber orientation in short-and long-fiber thermoplastics,” *Journal of Non-Newtonian Fluid Mechanics*, vol. 156, no. 3, pp. 165–176, 2009.
- [65] H.-C. Tseng, R.-Y. Chang, and C.-H. Hsu, “Phenomenological improvements to predictive models of fiber orientation in concentrated suspensions,” *Journal of Rheology*, vol. 57, no. 6, pp. 1597–1631, 2013.
- [66] H.-C. Tseng, R.-Y. Chang, and C.-H. Hsu, “The use of principal spatial tensor to predict anisotropic fiber orientation in concentrated fiber suspensions,” *Journal of Rheology*, vol. 62, no. 1, pp. 313–320, 2018.
- [67] S. K. Kugler, A. Kech, C. Cruz, and T. Osswald, “Fiber orientation predictions—a review of existing models,” *Journal of Composites Science*, vol. 4, no. 2, p. 69, 2020.
- [68] D. H. Chung and T. H. Kwon, “Invariant-based optimal fitting closure approximation for the numerical prediction of flow-induced fiber orientation,” *Journal of rheology*, vol. 46, no. 1, pp. 169–194, 2002.
- [69] J. S. Cintra Jr and C. L. Tucker III, “Orthotropic closure approximations for flow-induced fiber orientation,” *Journal of Rheology*, vol. 39, no. 6, pp. 1095–1122, 1995.

- [70] G. Marrucci and N. Grizzuti, "Predicted effect of polydispersity on rodlike polymer behaviour in concentrated solutions," *Journal of non-newtonian fluid mechanics*, vol. 14, pp. 103–119, 1984.
- [71] N. ul Qadir and D. A. Jack, "Modeling fibre orientation in short fibre suspensions using the neural network-based orthotropic closure," *Composites Part A: Applied Science and Manufacturing*, vol. 40, no. 10, pp. 1524–1533, 2009.
- [72] T. Karl, D. Gatti, B. Frohnappel, and T. Böhlke, "Asymptotic fiber orientation states of the quadratically closed folgar–tucker equation and a subsequent closure improvement," *Journal of Rheology*, vol. 65, no. 5, pp. 999–1022, 2021.
- [73] W. Ogierman, "Novel closure approximation for prediction of the effective elastic properties of composites with discontinuous reinforcement," *Composite Structures*, vol. 300, p. 116146, 2022.
- [74] H.-C. Tseng, "A constitutive equation for fiber suspensions in viscoelastic media," *Physics of Fluids*, vol. 33, no. 7, p. 071702, 2021.
- [75] E. Hinch and L. Leal, "Constitutive equations in suspension mechanics. part 1. general formulation," *Journal of Fluid Mechanics*, vol. 71, no. 3, pp. 481–495, 1975.
- [76] D. H. Chung and T. H. Kwon, "Improved model of orthotropic closure approximation for flow induced fiber orientation," *Polymer composites*, vol. 22, no. 5, pp. 636–649, 2001.
- [77] V. Verleye *et al.*, "Modelling the flow of fiber suspensions in narrow gaps," in *Rheology series*, vol. 8, pp. 1347–1398, Elsevier, 1999.
- [78] A. Andriyana, N. Billon, and L. Silva, "Mechanical response of a short fiber-reinforced thermoplastic: Experimental investigation and continuum mechanical modeling," *European Journal of Mechanics-A/Solids*, vol. 29, no. 6, pp. 1065–1077, 2010.
- [79] C. Unterweger, O. Brüggemann, and C. Fürst, "Synthetic fibers and thermoplastic short-fiber-reinforced polymers: Properties and characterization," *Polymer Composites*, vol. 35, no. 2, pp. 227–236, 2014.
- [80] J. Martin-Herrero and C. Germain, "Microstructure reconstruction of fibrous c/c composites from x-ray microtomography," *Carbon*, vol. 45, no. 6, pp. 1242–1253, 2007.
- [81] M. Gupta and K. Wang, "Fiber orientation and mechanical properties of short-fiber-reinforced injection-molded composites: Simulated and experimental results," *Polymer Composites*, vol. 14, no. 5, pp. 367–382, 1993.
- [82] E. Zainudin, S. Sapuan, S. Sulaiman, and M. Ahmad, "Fiber orientation of short fiber reinforced injection molded thermoplastic composites: A review," *Journal of Injection Molding Technology*, vol. 6, no. 1, pp. 1–10, 2002.

- [83] B. E. VerWeyst, C. Tucker, P. H. Foss, and J. F. O’Gara, “Fiber orientation in 3-d injection molded features,” *International Polymer Processing*, vol. 14, no. 4, pp. 409–420, 1999.
- [84] G. Lipscomb II, M. M. Denn, D. Hur, and D. V. Boger, “The flow of fiber suspensions in complex geometries,” *Journal of Non-Newtonian Fluid Mechanics*, vol. 26, no. 3, pp. 297–325, 1988.
- [85] W. C. Jackson, S. G. Advani, and C. L. Tucker, “Predicting the orientation of short fibers in thin compression moldings,” *Journal of Composite Materials*, vol. 20, no. 6, pp. 539–557, 1986.
- [86] F. P. Bretherton, “The motion of rigid particles in a shear flow at low reynolds number,” *Journal of Fluid Mechanics*, vol. 14, no. 2, pp. 284–304, 1962.
- [87] J. L. Doob, “The brownian movement and stochastic equations,” *Annals of Mathematics*, pp. 351–369, 1942.
- [88] D. Jack and D. Smith, “The effect of fibre orientation closure approximations on mechanical property predictions,” *Composites Part A: Applied Science and Manufacturing*, vol. 38, no. 3, pp. 975–982, 2007.
- [89] D. Dray, P. Gilormini, and G. Régnier, “Comparison of several closure approximations for evaluating the thermoelastic properties of an injection molded short-fiber composite,” *Composites Science and Technology*, vol. 67, no. 7-8, pp. 1601–1610, 2007.
- [90] S. G. Advani and C. L. Tucker III, “Closure approximations for three-dimensional structure tensors,” *Journal of Rheology*, vol. 34, no. 3, pp. 367–386, 1990.
- [91] J. D. Eldredge, “Numerical simulation of the fluid dynamics of 2d rigid body motion with the vortex particle method,” *Journal of Computational Physics*, vol. 221, no. 2, pp. 626–648, 2007.
- [92] B. Mokdad, E. Pruliere, A. Ammar, and F. Chinesta, “On the simulation of kinetic theory models of complex fluids using the fokker-planck approach,” *Applied Rheology*, vol. 17, no. 2, pp. 26494–1, 2007.
- [93] S. R. Strand, S. Kim, and S. J. Karrila, “Computation of rheological properties of suspensions of rigid rods: stress growth after inception of steady shear flow,” *Journal of Non-Newtonian Fluid Mechanics*, vol. 24, no. 3, pp. 311–329, 1987.
- [94] J. Gillissen, B. Boersma, P. Mortensen, and H. Andersson, “On the performance of the moment approximation for the numerical computation of fiber stress in turbulent channel flow,” *Physics of Fluids*, vol. 19, no. 3, p. 035102, 2007.
- [95] T. Johnson, P. R oytt , A. Mark, and F. Edelvik, “Simulation of the spherical orientation probability distribution of paper fibers in an entire suspension using immersed boundary methods,” *Journal of Non-Newtonian Fluid Mechanics*, vol. 229, pp. 1–7, 2016.

- [96] R. B. Bird, C. F. Curtiss, R. C. Armstrong, and O. Hassager, *Dynamics of polymeric liquids, volume 2: Kinetic theory*. Wiley, 1987.
- [97] R. Weinstock, *Calculus of variations: with applications to physics and engineering*. Courier Corporation, 1974.
- [98] S. Gottlieb and D. I. Ketcheson, “Time discretization techniques,” in *Handbook of Numerical Analysis*, vol. 17, pp. 549–583, Elsevier, 2016.
- [99] T. J. Hughes, L. P. Franca, and G. M. Hulbert, “A new finite element formulation for computational fluid dynamics: Viii. the galerkin/least-squares method for advective-diffusive equations,” *Computer methods in applied mechanics and engineering*, vol. 73, no. 2, pp. 173–189, 1989.
- [100] S. Balay, S. Abhyankar, M. Adams, J. Brown, P. Brune, K. Buschelman, L. Dalcin, A. Dener, V. Eijkhout, W. Gropp, *et al.*, “Petsc users manual,” 2019.
- [101] M. C. Altan and L. Tang, “Orientation tensors in simple flows of dilute suspensions of non-brownian rigid ellipsoids, comparison of analytical and approximate solutions,” *Rheologica acta*, vol. 32, pp. 227–244, 1993.
- [102] P. Perrochet and D. Bérod, “Stability of the standard crank-nicolson-galerkin scheme applied to the diffusion-convection equation: Some new insights,” *Water Resources Research*, vol. 29, no. 9, pp. 3291–3297, 1993.
- [103] J. Lang and J. Verwer, “Ros3p—an accurate third-order rosenbrock solver designed for parabolic problems,” *BIT Numerical Mathematics*, vol. 41, no. 4, pp. 731–738, 2001.
- [104] J. M. Park and S. J. Park, “Modeling and simulation of fiber orientation in injection molding of polymer composites,” *Mathematical Problems in Engineering*, vol. 2011, 2011.
- [105] P. Laure, L. Silva, and M. Vincent, “20 - modelling short fibre polymer reinforcements for composites,” in *Composite Reinforcements for Optimum Performance* (P. Boisse, ed.), Woodhead Publishing Series in Composites Science and Engineering, pp. 616–650, Woodhead Publishing, 2011.
- [106] C. L. Tucker III, “Planar fiber orientation: Jeffery, non-orthotropic closures, and reconstructing distribution functions,” *Journal of Non-Newtonian Fluid Mechanics*, vol. 310, p. 104939, 2022.
- [107] S. K. Kugler, G. M. Lambert, C. Cruz, A. Kech, T. A. Osswald, and D. G. Baird, “Macroscopic fiber orientation model evaluation for concentrated short fiber reinforced polymers in comparison to experimental data,” *Polymer Composites*, vol. 41, no. 7, pp. 2542–2556, 2020.
- [108] J. Kattinger, S. Joas, F. Willems, M. Kreutzbruck, and C. Bonten, “Application of the folgar-tucker model to predict the orientation of particles of different aspect ratios in polymer suspensions,” *Journal of Polymer Engineering*, vol. 41, no. 7, pp. 528–536, 2021.

- [109] J. J. Martin, M. S. Riederer, M. D. Krebs, and R. M. Erb, "Understanding and overcoming shear alignment of fibers during extrusion," *Soft matter*, vol. 11, no. 2, pp. 400–405, 2015.
- [110] N. Phan-Thien and R. Zheng, "Macroscopic modelling of the evolution of fibre orientation during flow," in *Flow-Induced Alignment in Composite Materials*, pp. 77–111, Elsevier, 1997.
- [111] S. G. Advani and C. L. Tucker III, "A numerical simulation of short fiber orientation in compression molding," *Polymer composites*, vol. 11, no. 3, pp. 164–173, 1990.
- [112] L. Jianzhong and K. Xiaoke, "Fiber orientation distributions in a suspension flow through a parallel plate channel containing a cylinder," *Journal of Composite Materials*, vol. 43, no. 12, pp. 1373–1390, 2009.
- [113] J. Férec, P. Laure, L. Silva, and M. Vincent, "Short fiber composite reinforcements," in *Composite Reinforcements for Optimum Performance*, pp. 627–669, Elsevier, 2021.
- [114] M. Vincent, T. Giroud, A. Clarke, and C. Eberhardt, "Description and modeling of fiber orientation in injection molding of fiber reinforced thermoplastics," *Polymer*, vol. 46, no. 17, pp. 6719–6725, 2005.
- [115] K. Chiba and F. Chinesta, "Simulation numérique et observation de l'écoulement d'une suspension de fibres dans une filière à géométrie complexe," *Revue des composites et des matériaux avancés*, vol. 12, no. 3, pp. 499–513, 2002.
- [116] J. Férec, E. Bertevas, G. Ausias, and N. Phan-Thien, "Macroscopic modeling of the evolution of fiber orientation during flow," in *Flow-induced alignment in composite materials*, pp. 77–121, Elsevier, 2022.
- [117] T. C. Papanastasiou and A. N. Alexandrou, "Isothermal extrusion of non-dilute fiber suspensions," *Journal of Non-Newtonian Fluid Mechanics*, vol. 25, no. 3, pp. 313–328, 1987.
- [118] W. Vanderheyden and G. Ryskin, "Computer simulation of flow and molecular orientation in liquid crystal polymers," *Journal of Non-Newtonian Fluid Mechanics*, vol. 23, pp. 383–414, 1987.
- [119] K. Chiba, K. Nakamura, and D. Boger, "A numerical solution for the flow of dilute fiber suspensions through an axisymmetric contraction," *Journal of Non-Newtonian Fluid Mechanics*, vol. 35, no. 1, pp. 1–14, 1990.
- [120] B. Reddy and G. Mitchell, "Finite element analysis of fibre suspension flows," *Computer methods in applied mechanics and engineering*, vol. 190, no. 18-19, pp. 2349–2367, 2001.
- [121] B. E. VerWeyst and C. L. Tucker III, "Fiber suspensions in complex geometries: Flow/orientation coupling," *The Canadian Journal of Chemical Engineering*, vol. 80, no. 6, pp. 1093–1106, 2002.

- [122] B. Souloumiac, *Etude rhéologique, modélisation et simulation numérique de l'écoulement des thermoplastiques chargés de fibres courtes*. PhD thesis, 1996.
- [123] P. Carreau, D. De Kee, and R. Chhabra, "Rheology of polymeric systems, principles and applications. hanser," *American Institute of Chemical Engineers: New York, NY, USA*, 1997.
- [124] G. Batchelor, "Slender-body theory for particles of arbitrary cross-section in stokes flow," *Journal of Fluid Mechanics*, vol. 44, no. 3, pp. 419–440, 1970.
- [125] C. L. Tucker III, "Flow regimes for fiber suspensions in narrow gaps," *Journal of Non-Newtonian fluid mechanics*, vol. 39, no. 3, pp. 239–268, 1991.
- [126] R. Cox, "The motion of long slender bodies in a viscous fluid part 1. general theory," *Journal of Fluid mechanics*, vol. 44, no. 4, pp. 791–810, 1970.
- [127] S. M. Dinh and R. C. Armstrong, "A rheological equation of state for semiconcentrated fiber suspensions," *Journal of Rheology*, vol. 28, no. 3, pp. 207–227, 1984.
- [128] S. Chung and T. Kwon, "Coupled analysis of injection molding filling and fiber orientation, including in-plane velocity gradient effect," *Polymer Composites*, vol. 17, no. 6, pp. 859–872, 1996.
- [129] E. S. Shaqfeh and G. H. Fredrickson, "The hydrodynamic stress in a suspension of rods," *Physics of Fluids A: Fluid Dynamics*, vol. 2, no. 1, pp. 7–24, 1990.
- [130] H. Giesekus, "Elasto-viskose flüssigkeiten, für die in stationären schichtströmungen sämtliche normalspannungskomponenten verschieden groß sind," *Rheologica Acta*, vol. 2, no. 1, pp. 50–62, 1962.
- [131] E. Hinch and L. Leal, "Time-dependent shear flows of a suspension of particles with weak brownian rotations," *Journal of Fluid Mechanics*, vol. 57, no. 4, pp. 753–767, 1973.
- [132] N. Phan-Thien and A. Graham, "A new constitutive model for fibre suspensions: flow past a sphere," *Rheologica acta*, vol. 30, no. 1, pp. 44–57, 1991.
- [133] B. Souloumiac and M. Vincent, "Steady shear viscosity of short fibre suspensions in thermoplastics," *Rheologica acta*, vol. 37, no. 3, pp. 289–298, 1998.
- [134] G. Batchelor, "The stress system in a suspension of force-free particles," *Journal of fluid mechanics*, vol. 41, no. 3, pp. 545–570, 1970.
- [135] J. D. Goddard, "Tensile stress contribution of flow-oriented slender particles in non-newtonian fluids," 1976.
- [136] G. Batchelor, "The stress generated in a non-dilute suspension of elongated particles by pure straining motion," *Journal of Fluid Mechanics*, vol. 46, no. 4, pp. 813–829, 1971.

- [137] A. Gibson and S. Toll, "Mechanics of the squeeze flow of planar fibre suspensions," *Journal of non-newtonian fluid mechanics*, vol. 82, no. 1, pp. 1–24, 1999.
- [138] J. Férec, A. Perrot, and G. Ausias, "Toward modeling anisotropic yield stress and consistency induced by fiber in fiber-reinforced viscoplastic fluids," *Journal of Non-Newtonian Fluid Mechanics*, vol. 220, pp. 69–76, 2015.
- [139] L. Leal, "The slow motion of slender rod-like particles in a second-order fluid," *Journal of Fluid Mechanics*, vol. 69, no. 2, pp. 305–337, 1975.
- [140] M. Grmela, A. Ait-Kadi, and P. G. Lafleur, "Suspensions of fibers in viscoelastic fluids: Rheology," *The Journal of chemical physics*, vol. 109, no. 16, pp. 6973–6981, 1998.
- [141] F. Snijkers, G. D'Avino, P. L. Maffettone, F. Greco, M. Hulsen, and J. Vermant, "Effect of viscoelasticity on the rotation of a sphere in shear flow," *Journal of Non-Newtonian Fluid Mechanics*, vol. 166, no. 7-8, pp. 363–372, 2011.
- [142] G. D'Avino and P. L. Maffettone, "Particle dynamics in viscoelastic liquids," *Journal of Non-Newtonian Fluid Mechanics*, vol. 215, pp. 80–104, 2015.
- [143] A. Ait-Kadi and M. Grmela, "Modelling the rheological behaviour of fibre suspensions in viscoelastic media," *Journal of non-newtonian fluid mechanics*, vol. 53, pp. 65–81, 1994.
- [144] A. Ramazani, A. Ait-Kadi, and M. Grmela, "Rheological modelling of short fiber thermoplastic composites," *Journal of non-newtonian fluid mechanics*, vol. 73, no. 3, pp. 241–260, 1997.
- [145] A. Ramazani SA, A. Ait-Kadi, and M. Grmela, "Rheology of fiber suspensions in viscoelastic media: Experiments and model predictions," *Journal of Rheology*, vol. 45, no. 4, pp. 945–962, 2001.
- [146] C. J. Petrie, "The rheology of fibre suspensions," *Journal of Non-Newtonian Fluid Mechanics*, vol. 87, no. 2-3, pp. 369–402, 1999.
- [147] J. Azaiez, "Constitutive equations for fiber suspensions in viscoelastic media," *Journal of Non-Newtonian fluid mechanics*, vol. 66, no. 1, pp. 35–54, 1996.
- [148] C. Kagarise, J. Xu, Y. Wang, M. Mahboob, K. W. Koelling, and S. E. Bechtel, "Transient shear rheology of carbon nanofiber/polystyrene melt composites," *Journal of non-newtonian fluid mechanics*, vol. 165, no. 3-4, pp. 98–109, 2010.
- [149] C. Kagarise, K. Miyazono, M. Mahboob, K. W. Koelling, and S. E. Bechtel, "A constitutive model for characterization of shear and extensional rheology and flow induced orientation of carbon nanofiber/polystyrene melt composites," *Journal of Rheology*, vol. 55, no. 4, pp. 781–807, 2011.
- [150] J. Donea and A. Huerta, *Finite element methods for flow problems*. John Wiley & Sons, 2003.

- [151] E. Pichelin and T. Coupez, "Finite element solution of the 3d mold filling problem for viscous incompressible fluid," *Computer methods in applied mechanics and engineering*, vol. 163, no. 1-4, pp. 359–371, 1998.
- [152] F. Brezzi and M. Fortin, *Mixed and hybrid finite element methods*, vol. 15. Springer Science & Business Media, 2012.
- [153] E. Hachem, *Stabilized finite element method for heat transfer and turbulent flows inside industrial furnaces*. PhD thesis, Citeseer, 2009.
- [154] D. N. Arnold, F. Brezzi, and M. Fortin, "A stable finite element for the stokes equations," *Calcolo*, vol. 21, no. 4, pp. 337–344, 1984.
- [155] R. Codina, "Stabilization of incompressibility and convection through orthogonal sub-scales in finite element methods," *Computer methods in applied mechanics and engineering*, vol. 190, no. 13-14, pp. 1579–1599, 2000.
- [156] T. Coupez, "Stable-stabilized finite element for 3d forming calculation," *CE-MEF. Rapport interne*, 1996.
- [157] D. Mezi, G. Ausias, S. G. Advani, and J. Férec, "Fiber suspension in 2d nonhomogeneous flow: The effects of flow/fiber coupling for newtonian and power-law suspending fluids," *Journal of Rheology*, vol. 63, no. 3, pp. 405–418, 2019.
- [158] H.-C. Tseng, R.-Y. Chang, and C.-H. Hsu, "Improved fiber orientation predictions for injection molded fiber composites," *Composites Part A: Applied Science and Manufacturing*, vol. 99, pp. 65–75, 2017.
- [159] Y. Lizama-Camara, C. Pinna, Z. Lu, and M. Blagdon, "Effect of the injection moulding fibre orientation distribution on the fatigue life of short glass fibre reinforced plastics for automotive applications," *Procedia CIRP*, vol. 85, pp. 255–260, 2019.
- [160] K. Kabanemi, J. F. Héту, and A. García-Réjon, "Numerical simulation of the flow and fiber orientation in reinforced thermoplastic injection molded products," *International Polymer Processing*, vol. 12, no. 2, pp. 182–191, 1997.
- [161] J. Azaiez, R. Guenette, and A. Ait-Kadi, "Investigation of the abrupt contraction flow of fiber suspensions in polymeric fluids," *Journal of Non-Newtonian Fluid Mechanics*, vol. 73, no. 3, pp. 289–316, 1997.
- [162] A. Latz, U. Strautins, and D. Niedziela, "Comparative numerical study of two concentrated fiber suspension models," *Journal of non-newtonian fluid mechanics*, vol. 165, no. 13-14, pp. 764–781, 2010.
- [163] J. P. Rothstein and G. H. McKinley, "Extensional flow of a polystyrene boger fluid through a 4: 1: 4 axisymmetric contraction/expansion," *Journal of non-newtonian fluid mechanics*, vol. 86, no. 1-2, pp. 61–88, 1999.

- 
- [164] X.-k. Ku and J.-z. Lin, “Fiber orientation distributions in slit channel flows with abrupt expansion for fiber suspensions,” *Journal of Hydrodynamics, Ser. B*, vol. 20, no. 6, pp. 696–705, 2008.
- [165] T. Karl, D. Gatti, T. Böhlke, and B. Frohnäpfel, “Coupled simulation of flow-induced viscous and elastic anisotropy of short-fiber reinforced composites,” *Acta Mechanica*, vol. 232, no. 6, pp. 2249–2268, 2021.
- [166] K. Yasuda, S. Henmi, and N. Mori, “Effects of abrupt expansion geometries on flow-induced fiber orientation and concentration distributions in slit channel flows of fiber suspensions,” *Polymer composites*, vol. 26, no. 5, pp. 660–670, 2005.
- [167] A. Baloch and M. Webster, “A computer simulation of complex flows of fibre suspensions,” *Computers & fluids*, vol. 24, no. 2, pp. 135–151, 1995.
- [168] Z. Lu, B. C. Khoo, H.-S. Dou, N. Phan-Thien, and K. S. Yeo, “Numerical simulation of fibre suspension flow through an axisymmetric contraction and expansion passages by brownian configuration field method,” *Chemical engineering science*, vol. 61, no. 15, pp. 4998–5009, 2006.
- [169] H. Q. Nguyen and C.-D. Tran, “Simulation of non-dilute fibre suspensions using rbf-based macro–micro multiscale method,” *Korea-Australia Rheology Journal*, vol. 34, no. 1, pp. 1–15, 2022.

**Titre :** Modélisation multi-échelle de l'orientation des fibres dans des systèmes polymères visqueux renforcés de fibres

**Mots clés :** Méthode des éléments finis, Orientation des fibres, Modélisation multi-échelle, Matériaux composites

**Résumé :** Les thermoplastiques renforcés par des fibres courtes ont acquis une notoriété croissante en ingénierie, notamment dans les applications automobiles. La prédiction précise de l'orientation des fibres est cruciale car elle influence les caractéristiques mécaniques. Les travaux de recherche antérieurs dans ce domaine ont mis en exergue la complexité inhérente à l'orientation des fibres au sein d'un écoulement. La majorité des simulations industrielles s'appuient sur des modèles macroscopiques qui font usage de quantités préalablement moyennées et d'approximations de fermeture, engendrant fréquemment des inexactitudes dans la prédiction de l'orientation des fibres. Afin de relever ce défi, la présente étude propose une nouvelle approche reposant sur la résolution de l'équation de Fokker-Planck à l'échelle mésoscopique.

La méthode des éléments finis (MEF) est utilisée pour calculer l'orientation des fibres, permettant une représentation plus précise du comportement des fibres. Le tenseur d'orientation ainsi calculé est intégré aux équations de Stokes, engendrant un modèle multi-échelle de l'interaction entre les fibres et l'écoulement environnant, ce qui enrichit considérablement notre compréhension de cette dynamique complexe. Finalement, un modèle d'écoulement à deux phases est étudié, reproduisant fidèlement des situations réelles telles que le processus de surmoulage. En exploitant ce modèle multi-échelle, cette étude vise à améliorer la précision des simulations dans les applications industrielles, offrant de nouvelles perspectives pour l'optimisation des processus et la conception.

**Title :** Multi-scale modeling of fiber orientation in coupled fiber-reinforced viscous polymer systems

**Keywords :** Finite Element Method, Fiber orientation, Multi-Scale Modeling, Composites

**Abstract :** Thermoplastics reinforced with short fibers have gained prominence in engineering, notably in automotive applications. Accurate prediction of fiber orientation is crucial, as it profoundly influences mechanical characteristics. Previous research in this field has highlighted the complexity of fiber orientation within a flow. Most industrial simulations rely on macroscopic models that use pre-averaged quantities and closure approximations, often resulting in inaccuracies in predicting fiber orientation. To address this challenge and enhance accuracy, this study presents a novel approach based on resolving the Fokker-Planck equation at the meso-scale level, offering a more detailed and accurate model for predicting fiber orientation.

In this work, the finite element method (FEM) is used to compute fiber orientation, providing a more precise representation of fiber behavior. Subsequently, the computed orientation tensor is integrated into the Stokes equations, creating a multi-scale fiber-flow model which enhances our understanding of the dynamic interaction between fibers and the surrounding flow. Furthermore, the research extends its scope to develop a two-phase flow model, reflecting real-world scenarios such as overmolding process. By leveraging the multi-scale model, this work aims to improve the accuracy of simulations in industrial applications, providing valuable insights for process optimization and design.